A COMPUTATIONAL STUDY OF SURFACE-DIRECTED PHASE SEPARATION IN POLYMER BLENDS UNDER TEMPERATURE GRADIENT

by

Mohammad Tabatabaieyazdi

Master of Chemical Engineering
Technical University of Denmark, Denmark, 2006

A dissertation
presented to Ryerson University

in partial fulfillment of the
requirements for the degree of
Doctor of Philosophy
in the Program of
Chemical Engineering

Toronto, Ontario, Canada, 2014

Author's Declaration

I hereby declare that I am the sole author of this thesis. This is a true copy of the dissertation, including any required final revisions, as accepted by my examiners. I authorize the Ryerson University to lend this dissertation to other institutions or individuals for the purpose of scholarly research.

_____

Mohammad Tabatabaieyazdi

I further authorize Ryerson University to reproduce this thesis by photocopying or by any other means, in total or in part, at the request of other institutions or individuals for the purpose of scholarly research. I understand that my dissertation may be made electronically available to the public.

_____

Mohammad Tabatabaieyazdi

Acknowledgements

I would like to express my appreciation to my supervisors, Dr. Philip K. Chan, and Dr. Jenny Wu for their assistance and encouragement.

In addition, my sincere gratefulness goes out to Dr. Philip K. Chan for providing me with a stipend during my studies as well as the excellent research environment.

Thanks to Ryerson University School of Graduate Studies for providing me with scholarship during my studies.

I would also like to thank my parents for their inspiration and many friends who have acted as my support when I needed most, and for that I am truly grateful.

Finally, I would like to thank my wife Mehrak. She has always been there to help, encourage, and assist me when I really needed it.

Abstract

A COMPUTATIONAL STUDY OF
SURFACE-DIRECTED PHASE SEPARATION
IN POLYMER BLENDS UNDER TEMPERATURE GRADIENT

Mohammad Tabatabaieyazdi, PhD, 2014

Department of Chemical Engineering, Ryerson University
350 Victoria Street, Toronto, Ontario M5B 2K3 Canada.

To apprehend the real industrial behavior of polymeric materials phase separation phenomenon, the nonlinear Cahn-Hilliard theory incorporating the Flory-Huggins-de Gennes free energy theory was used to study the non-uniform thermal-induced phase separation phenomenon in a symmetric binary polymer blend in which surface(s) with short- and long-range attraction to one polymer component compete with temperature gradient effects. The numerical results indicate that an increase of diffusion coefficient value will increase the rate of phase separation in the bulk but will decrease the growth rate of the wetting layer on the surface regardless of the surface potential strength. Also, the morphology transition from complete to partial wetting of the surface with short-range surface attraction is successfully demonstrated. However, no partial wetting is observed for the surface with long-range potential. For shallow quenches, first, a growth rate of $t^{0.5}$ is observed in the early stage of spinodal decomposition phase separation at the surface and then a decline in the growth rate to $t^{0.13}$ in the intermediate stage occurred. For short- and long-range surface potential, the growth rate value of $t^{0.33}$ obtained in the bulk. The morphology results of temperature gradient effect on surface directed spinodal decomposition in short-range, long- range and multiple-surface attraction cases have been presented for the first time.

It is realized that regardless of surface potential magnitude, surface enrichment is increased by higher temperature gradient (deep quenches on the side with no surface attraction). The studied models would provide more in depth understanding of polymer blend processes.

Table of Contents

Chapter 1

Chapter 2

Chapter 3

Chapter 4

Chapter 5

Chapter 6

Chapter 7

List of Figures

List of Tables

Nomenclature

Symbols	Description
b	Bond length [m]
c	Solvent concentration (volume fraction) [-]
c_0	Initial solvent concentration (volume fraction) [-]
D	Mutual diffusion coefficient [$m^2\ s^{-1}$]
$f(c)$	Flory-Huggins free energy of mixing [$kg\ m^2\ s^{-2}$]
F	Total free energy of mixing [$kg\ m^2\ s^{-2}$]
ΔG_{max}	Gibbs free energy of mixing [$kg\ m^2\ s^{-2}$]
ΔH	Enthalpy of mixing [$kg\ m^2\ s^{-2}$]
J_A	Inter-diffusional flux [$mol\ m^{-2}\ s^{-1}$]
k_B	Boltzmann constant [$m^2\ kg\ s^{-2}\ K^{-1}$]
M	Mobility [$m^5\ J^{-1}\ s^{-1}$]
N_i	Polymerization index [-]
p_i	Geometrical factor [-]
r_i	Entropic coefficient [-]
s_i	Number of lattice sites occupied by a single monomer [-]
ΔS	Entropy of mixing [$kg\ m^2\ s^{-2}\ K^{-1}$]
t	Time
T	Temperature [K]

T_c	Critical temperature [K]
V	Long-range surface interaction term [-]
V_0	Potential field at the surface [-]
x	Distance at x axis [m]
z	Lattice coordination number [-]

Greek Letters Description

α	Entropy contribution
β	Enthalpy contribution
χ	Flory-Huggins interaction parameter [-]
Ω	Partition function [-]
θ	Theta temperature [K]
κ	Gradient energy coefficient [J m^{-1}]
ψ	Entropy of dilution parameter [-]
υ	Volume of a cell or segment [m^3]
ϵ	Blend exchange energy [kg m^2 s^{-2}]
λ	Chain occupancy index ratio [-]
μ	Chemical potential [J mol^{-1}]
Λ	Kinetic factor (Onsager coefficient) [-]
γ	Surface tension [J m^{-2}]
η	Noise term [s^{-1}]
ξ	Frictional coefficient of a component

n	Director

Acronyms	**Description**
ABS	Acrylonitrile butadiene styrene
AFM	Atomic force microscopy
ANSI	American National Standards Institute
BDF	Backward Differentiation Formulas
CHC	Cahn-Hillard-Cook
DPB	Perdeuterated polybutadiene
dPEP	Deuterated polyethylene propylene
dPS/hPS	Deuterated/hydrogenated polystyrene
EVAc	Ethylene-*co*-vinyl acetate
FDM	Finite-Difference Method
FH	Flory-Huggins
FHdG	Flory-Huggins-de Gennes
FTA	Fourier transform analysis
GMRES	Generalized Minimal Residual
HIPs	High impact polystyrene
LCP	Liquid crystalline polymer
LCST	Lower critical solution temperature
LLNL	Lawrence Livermore National Laboratory
MOL	Method of lines
MPS	Morphological phase separation

NG	Nucleation and growth
NR	Neutron reflection
ODE	Ordinary differential equation
OTS	Octadecyltrichlorosilane
P2CS	Poly(2-chlorosytrene)
PC	Polycarbonate
PDE	Partial differential equations
PDLC	Polymer dispersed liquid crystal
PE	Polyethylene
PEP	Poly(ethylene propylene)
PI	Polyisoprene
PIPS	Polymerization induced phase separation
PMMA	Polymethyl methacrylate
PP	Polypropylene
PPO	Poly(phenylene oxide)
PS	Polystyrene
PVC	Poly(vinyl chloride)
PVME	Poly(vinyl methyl ether)
PαMS	Poly(α-methylstyrene)
PVP	Poly(vinylpyridine)
SAM	Self-assembled monolayers
SD	Spinodal decomposition

SDPS	Surface directed phase separation
SDSD	Surface-directed spinodal decomposition
SIMS	Secondary ion mass spectroscopy
SIPS	Solvent induced phase separation
SLCT	Simplified lattice cluster theory
SUNDIALS	Suite of nonlinear and differential algebraic equation solver
THF	Tetradrofurane
TIPS	Thermal induced phase separation
UCST	Upper critical solution temperature
UHMWPE	Ultrahigh molecular weight polyethylene

Chapter 1

1. General Introduction

1.1 Polymer Blends

Humankind has been combining different materials together since the beginning of written history to manufacture products with developed engineering properties [1]. The polymer industry dates only from nineteenth century, where the main industrial polymers aside from wood were natural rubber (cis-1,4-polyisoprene) from Brazil, gutta-percha (trans-1,4-polyisoprene) from Singapore and Malaya, and natural fibers, including cellulose (cotton, linen), protein (wool) fibers and leather. Polymer blends were made as mixtures of two or more polymers and possibly an additional component to enhance polymer compatibility. The first commercial polymer blends, which were naturally forming, were polyisoprenes (natural rubber and gutta-percha) and then cellulose derivatives. From the early twentieth century, numerous fully synthetic polymer blends were introduced.

Perhaps the first widely used synthetic polymer blend was the NBR–poly(vinyl chloride) system more popularly known as NBR–PVC which was extensively used in under the hood applications in automobiles [2]. Since 1960s, there have been broad explorations of polymer blends in both manufacturing and academic laboratories all over the world on improving the properties of polymers by blending. Polymer blending is one of the most

significant and simple techniques to make different improved-performance polymeric materials such as easier processability, better final properties and competitive pricing [3]. Morphology of the polymeric material has significant impact on their properties and it is well known that phase separation of polymer blends at a range of conditions could lead to variety of structural morphology. Therefore it is important to understand phase separation behavior of polymer materials and also effect of different external fields (such as surface effect and temperature gradient) that could lead to the formation of structural anisotropy in polymer blends and could help to produce new products with enhanced properties and functionalities. Few examples of industrial applications include preparation of membrane with anisotropic morphology under temperature gradient [4–7] and formation of patterned polymer surfaces [8] and micro-optical devices [9]. The need for making new polymeric materials with novel properties requires in-depth understanding of real-world polymeric materials production processes. In most polymer blend production processes, confined geometry, presence of the external surface and temperature change within the domain are inevitable. The ability to control these properties could be inspiring for further research on their effect in morphology formation of polymer blends.

1.2 Polymer Blends Morphology

Polymer melt blends may be miscible or immiscible. Miscible blends form solutions with no significant phase morphology. Immiscible blends are categorized by two or more phases separated by interfaces. Most polymer blend systems are immiscible due to the low entropies of mixing related to mixing chain-like molecules to create homogeneous solutions.

The interface between two phases in a liquid system is described by an interfacial tension, which seeks to control the interface shape and join with other dispersed phase. This interfacial tension is commonly resisted by the melt viscosity, which decelerates the changes the interfacial tension seeks to achieve. Particularly, interfacial tension in two-phase low viscosity systems has been acknowledged and reviewed since the nineteenth century. In fact, Clerk Maxwell [10] discussed it in an 1879 Encyclopedia Britannica review. Several researchers developed techniques and performed calculations on the interfacial tension in the nineteenth and early twentieth century. Measurements for combinations of polymer melts, however, date back only to the 1960s [11–14] and commonly acknowledged values were accessible by the 1990s [15–18]. When the interfacial tension goes to zero, the blend becomes miscible. Large interfacial tensions cause interfaces to become unstable, mainly when the viscosity is low, leading to coalescence phenomena as in “salad dressing” which also appear in polymer melt blends. The possibility to change the interfaces between liquids using specific additives was discovered by ancient and medieval researchers and applied in the form of soaps, in food technology and in the application of dyes. The mechanisms of these additives only came to be achieved in about 1900. Such additives are commonly molecules with hydrophobic and hydrophilic parts that align along interfaces between the two liquid phases and stabilize phase morphology to smaller dispersed phase sites through reducing interfacial tension. This phenomenon was later used to produce synthetic rubber.

By the 1960s, understanding the interfaces between the individual polymers in the blends was of an interest. It was recognized that in some blend systems including high impact polystyrene (HIPS) and acrylonitrile butadiene styrene (ABS) resins, there were considerable quantities of graft copolymer products at the interface between the polymer phases [2]. This

caused broad studies of polymeric interfacial agents, gradually identified as compatibilizing agents in polymer blends [17,19–24]. These agents reduced dispersed phase size, enhanced phase stability, and increased mechanical properties (Figure 1.1).

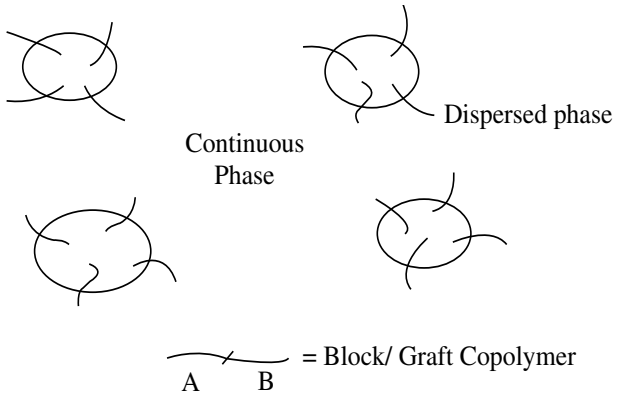

Figure 1.1: Compatibilized dispersed polymer blend phase showing compatibilizing agents [1].

These were consistently block and graft copolymers. The property development is because of their lodging the blend interface and having long chains in each phase. Later, some researchers [17,25] measured the interfacial tensions in these compatibilized blends and found that they were considerably decreased when proper compatibilizing agent was used. Usually, phase morphologies shaped in blending contain disperse phase sizes that change with interfacial tension and viscosity [26,27].

1.3 Polymer Blends Applications

Polymer blend technology has received significant attention since 1970s in the field of

polymer science [28]. As academic and industrial research interest in polymer blend technology increases, its applications in commercial utilities have been developed drastically. Today, polymer science programs at universities such as University of Massachusetts and University of Texas have employed main focus on polymer blend technology particularly related to miscible polymer blends" [28]. Miscible polymer blends used to be very rare with unpredicted performance [29–31]. Yet, within 1970s, a large number of miscible systems were produced [32,33]. "Particular interactions such as hydrogen bonding between interacting groups on various polymeric structures were identified to provide an adequate thermodynamic driving force (i.e., negative energy of mixing) for miscibility between high molecular weight polymer chains [28].

The adaptation of Flory-Huggins's equation of state to the thermodynamics of polymer blends noted the prediction of lower critical solution temperature (LCST) behavior for polymer blends [34]. Evidence for this behavior [34] and the potential of spinodal decomposition as a method of phase separation in polymeric blends have been provided experimentally [35]. Additional work by different groups included the two-dimensional solubility parameter approach to miscibility of polymer blends [36], the advantage of the inverse gas chromatography method in studying polymer blends [37], crystallization characteristics of polymer blends [32,38], and employment of glass transition shift to determine the level of crystallization in miscible polymer blends [32,39].

The field of polymer blend functions is now so huge that only a brief review will be possible. A number of reviews have been formerly published regarding applications of polymer blends in the form of polymeric alloys [32,40–44], elastomer blends [45–48],

polyolefin blends [49], polymeric plasticizers for wire and cable insulation, food contact, and pond liners used for oil containment [50,57,58], fiber blends [51], rubbery thermoplastic blends [52], block copolymers in blends [53], interpenetrating networks [54], and polyelectrolyte complexes [55,56]. Also, plasticized poly(vinyl chloride) (PVC) has been added to nitrile rubber to result in improved ozone, thermal aging, and chemical resistance leading to applications including fuel hose covers, gaskets, conveyor belt covers, and printing roll covers [28]. Particular applications mentioned for PVC plasticized with these materials are upholstery, automotive interior, food packaging film, wire and cable insulation, and agricultural insecticide hose jackets. ABS/PVC blends add the flame resistance of PVC with the toughness and processability of ABS for a number of injection molding, extrusion, and thermoforming applications [28]. Certain applications involve interior truck panels, communication relays, electrical housings, appliance housings, mass transit interiors, and television housings [42]. Poly(methyl methacrylate) (PMMA)/PVC blends (including impact modifiers) add the heat resistance of PMMA and the chemical and flammability resistance of PVC into a material for injection molding and extrusion applications. Interior paneling, trim, and seat backs are main applications of this blend in mass transit vehicles [42].

The miscible polymer blend of polystyrene and poly(2,6-dimethyl phenylene oxide) (PPO) has been commercialized by General Electric since the late 1960s under the trade name Noryl. Applications for these blends contain appliance housings, business machine housings, automotive dashboards, pump components, and television components [59]. Blends of ABS and polycarbonate, that are two-phase and display weak weld-line strength, are used in automotive interior trim, electrical housings, and recreational vehicle and mass transit applications [28]. Thermoplastic polyurethane/ABS blends have been developed for

automotive filler panels, rock shield applications, aircraft seat tracks, and snowmobile modular drive belts [60]. Semi-flexible PP/EPR blends (60 to 80 wt. percent EPR) were commercialized for wire and cable insulation, automotive bumpers and fascia, hose, gaskets, seals, and weather stripping. These blends exchanged plasticized PVC and cross-linked rubbers where improved low temperature flexibility, rubbery properties, and thermoplastic character were preferred [61,62]. The leading application of polymer blends, however, is in the tire market [48]. AB styrene-diene block copolymers have commercial value in numerous elastomers applications in wire and cable, adhesives, battery separators, shoe soles and heels, and rug underlay [63]. Potential applications of polyelectrolyte complexes include photo-resistant films, electrical conductive coatings, antistatic coatings, wound and burn dressings, cornea substitutes and soft contact lenses, environmental sensors and chemical detectors, non-fogging, transparent window coating, matrix for slow release of implantable drugs, membranes for artificial kidneys and lungs, battery separators and fuel cell membranes [55,56,64,65].

Recently, there has been abundant interest in using polymer blends in nanocomposites [66,75], gas separation membranes [67], and pharmaceutical and medical applications [68,71], which will be out of the scope of this thesis due to the extensiveness of their practices and diversity of polymer blend types.

1.4 Surface Adsorption

Polymers in blends may eagerly adsorb onto different surfaces where there is an attractive interaction between sections of the polymer and the surface, which

overcompensates for the conformational entropy loss of the polymer upon adsorption [69].

The adsorption of polymers onto surfaces, whether preferred or not, has great consequences in many areas of research. Moreover, understanding and controlling such processes is significant and is necessary in many technological features varying from paper industry and paint formulation to pharmaceutical applications [68,71], biophysics [72–74], and nanocomposite materials [66,75]. The adsorption process of polymers onto a surface is mainly controlled by the fundamental conditions under which polymer, solvent, and surface interact [70]. The equilibrium-adsorbed layer in terms of surface coverage and layer thickness is often of interest from a technical viewpoint, where a surface is physically or mechanically modified to meet particular needs. Due to the huge number of applications for polymer adsorption, there has historically been a large interest in characterizing layers of adsorbed polymers [76–80]. Yet, often kinetics is so slow that true equilibrium of the adsorbed polymers may never be reached on realistic time scales. Determining the various time scales involved through the whole adsorption process, from diffusional transport to a surface followed by later attachment and spreading on it, hence remains an important task and a big challenge inside the field [70].

Several techniques have been used to theoretically analyze the nature of polymer adsorption onto surfaces from bulk solution. Adsorption profiles close to adsorbing surfaces have been characterized by mean-field methods [81,82] in addition to using different simulation techniques [83–86]. The dynamics of polymer adsorption has also been examined by dynamic mean-field arrangements [87] along with dynamic Monte Carlo [88–94], molecular dynamics [95–99], and Brownian dynamics methods [100,101]. Some of the

dynamic studies were performed on individual polymers at a surface [91,94,100] while others contained adsorption from solution varying from semi-dilute conditions [88–93] to polymer melts [95–98]. Several static and dynamic properties of polymer adsorption have been studied as a function of strength of the polymer-surface interaction [83,86,90,92,100] and only a few have examined polymer models with changing intrinsic stiffness [83,85,100]. Moreover, some consideration has been given to diffusion and exchange in an adsorbed layer [90,92,95,96,101].

Linse and Kallrot [70] investigated the adsorption of single polymers in good solvent onto solid surfaces using a coarse-grained model. “The transition from bulk to entirely relaxed equilibrium structures is a complicated process including three distinct phases comprising different time scales: (i) an initial distortion phase, where the polymer becomes deformed by its weak interaction with the solid surface; (ii) an attachment phase, where the polymer begins to physically join to the surface and partly spread on it; (iii) a relaxation phase, during which the polymer continues to spread on the surface until it reaches full equilibrium” [70]. In their second contribution [101], adsorption of flexible polymers in good solvent onto a planar and solid surface for different polymer lengths and densities was studied. “When the adsorption occurs from a polymer blend, the situation becomes more difficult due to the polymer-polymer interaction between adsorbed polymers” [70].

Kallrot *et al*. [101] also identified a fourth relaxation phase near the end of the adsorption process, involving shape and conformational reordering of adsorbed polymers driven by repulsive polymer-polymer interactions. They examined a coarse-grained polymer model by employing Brownian and Monte Carlo simulations. In particular, they widely

studied the fourth relaxation phase for flexible polymers, and described another slow relaxation phase of the adsorption of rod-like polymers. Moreover, the integration time needed to completely integrate polymers into the adsorbed polymer layer was described. Integration and residence times of entirely integrated polymers were found to increase with growing polymer stiffness and increasing bead-surface attraction [70].

In this study, simulation is extended over the adsorption of polymer blends onto solid surfaces by numerically considering surface-directed phase separation phenomenon with varying temperature and with varying polymer-surface interaction strength.

1.4.1 Short Range and Long Range Surface Potentials

"Interactions at interfaces control our life and the way we experience our environment extensively. Intermolecular forces may lead physical behavior at interfaces and properties of polymer films. Properties of composite materials, many biological sensors, or chemical reactions are influenced or even governed by the behavior of materials at interfaces and interfacial interactions. The stability of polymer films is necessary in many technological applications, such as in coatings (paints) or in microelectronic devices (insulating layers). Thus, one would like to prevent spontaneous pattern formation and the break-up of such films. In polymer films, due to the large surface-to-volume ratio, interfacial properties become increasingly significant" [102]. Especially if the film thickness becomes much thinner than 1-μm or approaches molecular dimensions, intermolecular forces begin to control the system [103–112]. A polymer film characterizes a system of two parallel interfaces. These interfaces know about their mutual existence within short-range interactions

or at such large separations via long-range interactions. It is then significant to understand and predict what results from such interactions.

As a first effort to prevent such instabilities one may think of treating the substrate to increase the interactions between film and substrate. Short-range surface interaction, related to forces acting primarily on contact between molecules, greatly controls interfacial tensions. Therefore, surface modifications may develop wettability, adhesion, or friction, but they have little impact on long-range surface dispersion forces at large distances. Though, it is not apparent if dispersion forces are still adequately strong to be related (e.g., for the stability of polymer films up to 100 nm or more) [102].

Short-range surface interactions may be enough to compete with consequences resulting from long-range interactions, even if these forces are not strong [110–113]. At a distance of 100 nm, these forces (per unit area) are already at least 4-5 orders of magnitude weaker than atmospheric pressure. Short-range forces may change individually and even may have distinctive signs as they are derived from dissimilar sorts of interactions. Systematic experiments on the impact of antagonistic short- and long-range surface forces on film stability have been already presented. Such systems have already been examined theoretically by 2- and 3-dimensional computer simulations [113–115].

The wetting and phase separation are more involved with short-range surface interactions of capillarity compared to long-range surface interactions, which include van der Waals forces [116]. These short and long-range interactions alone, which play the major role in spinodal dewetting, have been widely studied [111,117,118]. The interfacial energy (per unit area) of a bulk interface is its interfacial tension. A limited thickness domain has an

excess energy since the long-range interactions are cut off at a finite thickness [105]. These long- range interactions lead to the Gibbs' theory of the interfacial tension when integrated over a semi-infinite domain. There are as many additive components of the excess free energy as the variety of the underlying intermolecular interactions [103–112]. Most noticeable of these interactions are apolar (and ubiquitous) van der Waals interactions, polar acid-base, and interactions of entropic origin, with the hydration repulsion and hydrophobic attraction (for aqueous media on hydrophilic and hydrophobic surfaces, respectively), electrostatic double-layer interactions (for charged surfaces in ionic solutions), and more complicated shorter range attraction/repulsion produced by the entropic effects in polymer blends near a limiting wall or because of chain-adsorption/grafting [119–121].

A properly typical excess intermolecular interaction free energy (ΔG) is composed of antagonistic (attractive/repulsive) long-and (fairly) short-range interactions, which decay with the local thickness [107,108,110–112]. For unstable systems, there are four universal classes of the form of the free energy [110,111,114]. Type I systems are where both long-range apolar and short-range polar surface potential forces are attractive. Type II systems are those where a long-range surface attraction couples with a shorter-range repulsion. Type III systems (stable ones) are where both long- and short-range interactions are repulsive. Type IV systems are where a long-range repulsion couples with a shorter-range attraction. Figure 1.2 is a schematic representation of possible interactions of a liquid with a solid and its relation to drop spreading and film stability. Based on a specific interaction potential (C), B and D give the equilibrium state after initial situations A and E, respectively. A, describes a drop of finite volume located on the solid, after possible initial fast relaxations because of the deposition; B reflects the final equilibrium state on a finite solid surface; C is the thickness

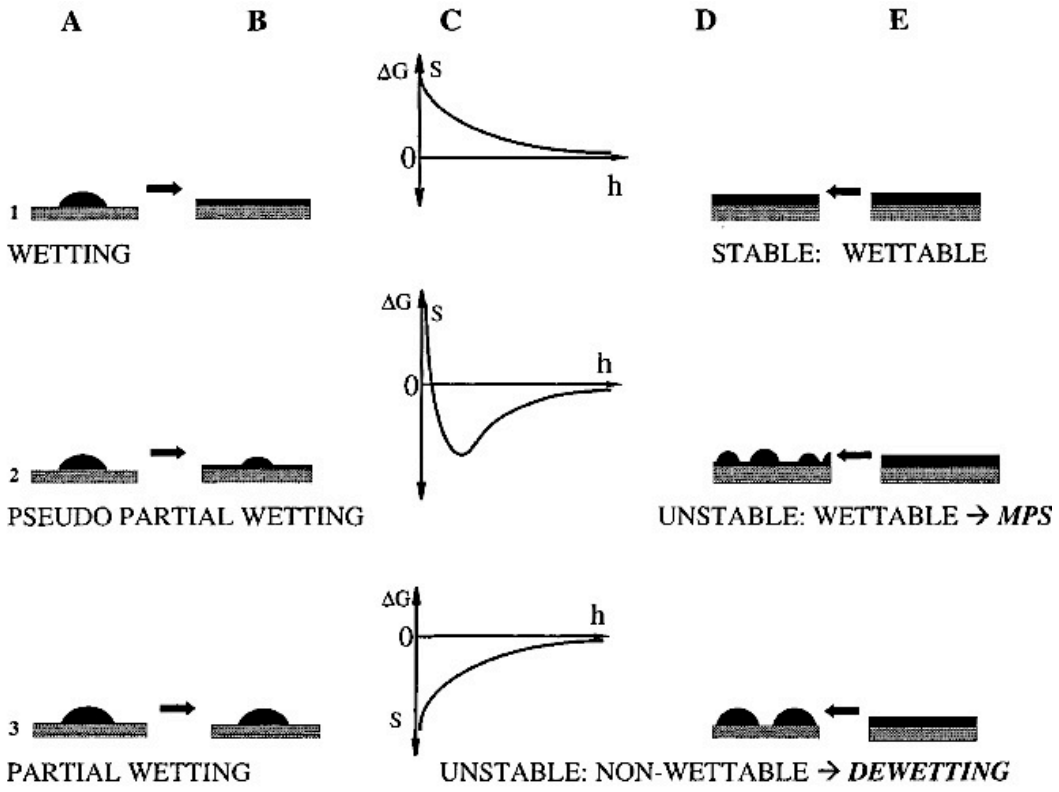

Figure 1.2: Schematic drawing of different possible interactions of a liquid with a solid and its relation to drop spreading and film stability. S, h and ΔG are representing spreading parameter, film thickness and excess free energy of the system respectively [102].

variation of the excess free energy (ΔG) of the system with a spreading parameter and the substrate; E stands for a film forced to spread uniformly on the substrate; and finally, D gives the possible final patterns after relaxation towards equilibrium. Line 1 is for complete spreading/complete wetting for positive spreading parameter and purely repulsive interaction forces. In this case, an absolute minimum at a finite distance from the substrate results in pseudo-partial wetting (A to B) and morphological phase separation (MPS) (E to D) for drops and films above some critical thickness, respectively. In line 3, a drop never spreads,

and films of all thicknesses are basically unstable causing true dewetting (dry patch formation) due to purely attractive forces [102].

1.5 Thesis Objectives

As mentioned before, the necessity for manufacturing novel polymeric materials with unique properties, demands profound understanding of real-world polymeric materials fabrication developments. In most polymer blend production methods, confined geometry, existence of the outside surface and temperature change within the domain are unavoidable. The capability to control these properties would be motivating for additional research on their influence in morphology formation of polymer blends for simple and complex geometries.

Based on previous literature, the effect of both temperature gradient profile and surface potential on phase separation morphology of polymer blends has not been studied yet. These two external fields affect morphology of blends drastically and have numerous industrial applications such as preparation of micro-optic and microelectronic devices [8,9,122–125].

The sequential objectives of the research thesis are as follows:

1) To develop mathematical models (two-dimensional) to describe the TIPS process of phase separation in a binary polymer blend sample under an externally imposed spatial linear temperature gradient and in the presence of short-range surface potential field. The theories which will be taken into account during the development of the mathematical model for the research thesis, are the non-linear Cahn-Hilliard theory describing the TIPS method via the

spinodal decomposition (SD) mechanism and the Flory-Huggins-de Gennes theory describing the thermodynamics of polymer blends with number of monomers $N > 200$ in each chain.

2) To implement, solve and validate the two dimensional models as specified and developed in objective 1 for the TIPS method for both critical and off critical quenches in simple geometries with finite difference numerical technique for a polymer blend system with short range surface potential.

3) To implement, solve and validate the two dimensional models as specified and developed in objective 1 for more complex geometries that better reflect situations in industrial polymer processes, both for critical and off critical quenches with multiple surface effects.

4) To implement, solve and validate the two dimensional models as specified and developed in objective 1 for the TIPS method for both critical and off critical quenches in simple geometries with finite difference numerical technique for a polymer blend system with long range surface potential.

1.6 Thesis Methodology and Approach

Computer simulation provides a way from the microscopic factors such as atomic masses and atomic charges to the macroscopic aspects such as state equations, and properties of materials [126]. It also enables the direct description of details at the microscopic scale, which may be difficult, if not impossible, to investigate from experiment. For example, a

fluid structure can be simply figured out from simulation but with rather more effort from the experiment. In addition, it offers a direction to define properties in conditions out of the scope of experiment (high pressures or temperatures, for instance) [127]. Yet, in all situations, properties predictions are relied on a suitable model of the interactions between particles and efficient computer modeling methods.

This thesis has focused on the computational modeling and mathematical simulation of surface-directed phase separation in polymer blends undergoing temperature gradient. The objectives of the thesis in fulfilling the above mentioned parameters shown in Figure 1.3 and described below. The flowchart is designed for better understanding the phase separation process of polymer blends with the help of mathematical modeling.

The flowsheet specifies that the prime step in the simulation of a physical experience is suggesting objectives. A model can then be developed and implemented based on the objectives, existing theories, and experimental results. This model is then solved using the proper computational methods and computer hardware. Lastly, the numerical results obtained from the simulations are processed so that they can be validated with available published experimental data.

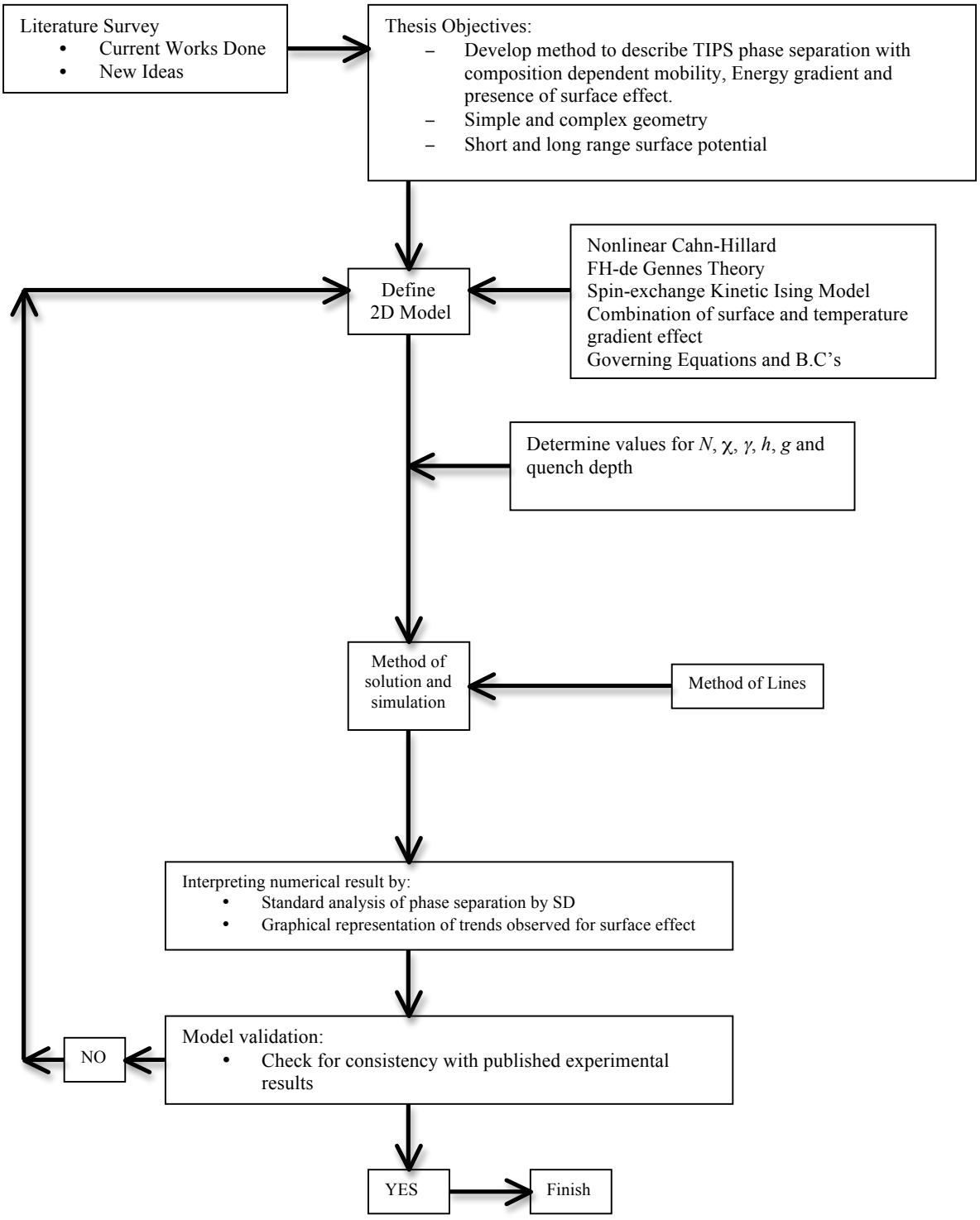

Figure 1.3: Computational modeling flowchart of the thesis objectives.

1.7 Thesis organization

This thesis contains six chapters that are organized in the following way:

Chapter 1: This chapter is an introduction and overview of polymer blends and their applications. Surface attraction, which plays a prominent role in surface-directed phase separation, would be introduced with its short-range and long-range surface potentials. The thesis objectives, the methodology approach and the thesis organization are also introduced.

Chapter 2: This chapter will present a literature review about the history of phase separation phenomenon mechanisms and the published findings of surface-directed phase separation method under thermal quenching. It will furthermore outline the new experimental and numerical work and research that have been done. This chapter is also an introduction and overview of phase separation phenomenon with its different methods and mechanisms. The focus of this thesis is on thermally induced phase separation induced by surface effect.

Chapter 3: This chapter discusses the theoretical background of phase separation thermodynamics along with its governing equations. Cahn-Hilliard theory, Flory-Huggins free energy, spinodal decomposition theory and reptation theory are also introduced and applied. Moreover, it is shown how a phase diagram of a polymer blend is determined as well as investigating the entropy and enthalpy of polymer blends.

Chapter 4: In this chapter, models with short-range surface potential are developed and the results are discussed. This chapter deals with the short-range model development technique and the numerical method of applied solution. Initial and boundary conditions are

also presented. The model is then derived in two dimensions. Structure factor calculations are also presented to validate the observed morphology. The simulation is also validated by comparison to relevant published experimental and numerical work.

Chapter 5: In this chapter, models with multiple-surface potential are developed and discussed. Structure factor results are also analyzed. The concentration profiles are presented in two-dimensional contour plots. The model is also validated by comparison to the analogous experimental and numerical work.

Chapter 6: In this chapter, models with long-range surface potential are developed and the results are discussed. This chapter deals with the long-range model development technique and the numerical method of applied solution. Initial and boundary conditions are also presented. The model is then derived in two dimensions. Structure factor results are also presented to validate the observed morphology. The model is also confirmed by comparison to comparable experimental and numerical work.

Chapter 7: This chapter discusses the conclusions on all numerical findings on surface-directed phase separation under temperature gradient and contributions of this work have been summarized.

Chapter 2

2. Literature Review

2.1 Phase Separation

The phenomena of phase separation have always attracted a great deal of interest [128–137]. Understanding the phase behavior and the phase separation dynamics of polymer blends is significant for numerous processes in regard to polymer production, refinement, processing, and modifications. Phase separation of polymer blends is one of the most significant methods to produce many useful polymeric materials that can be extensively applied in engineering industries [138]. Phase separation in polymer blends has attracted great interests of scientists and engineers in recent years [139–142]. Due to long relaxation time and large scale of polymer molecules, the morphology of phase separation in polymer blend systems can exhibit many special features such as volume shrinking and phase inversion phenomenon compared with that in small molecule systems [143].

The kinetics of phase separation in polymer blends that follow a transfer of the system from a thermodynamically stable to a thermodynamically metastable or unstable state is the focus of many theoretical and experimental studies [140–147]. Changing parameters such as temperature, pressure or concentration can cause phase separation to occur. The phase separation can progress through either spinodal decomposition (SD) or nucleation and growth (NG) when a homogenous mixture is brought into the heterogeneous state [148].

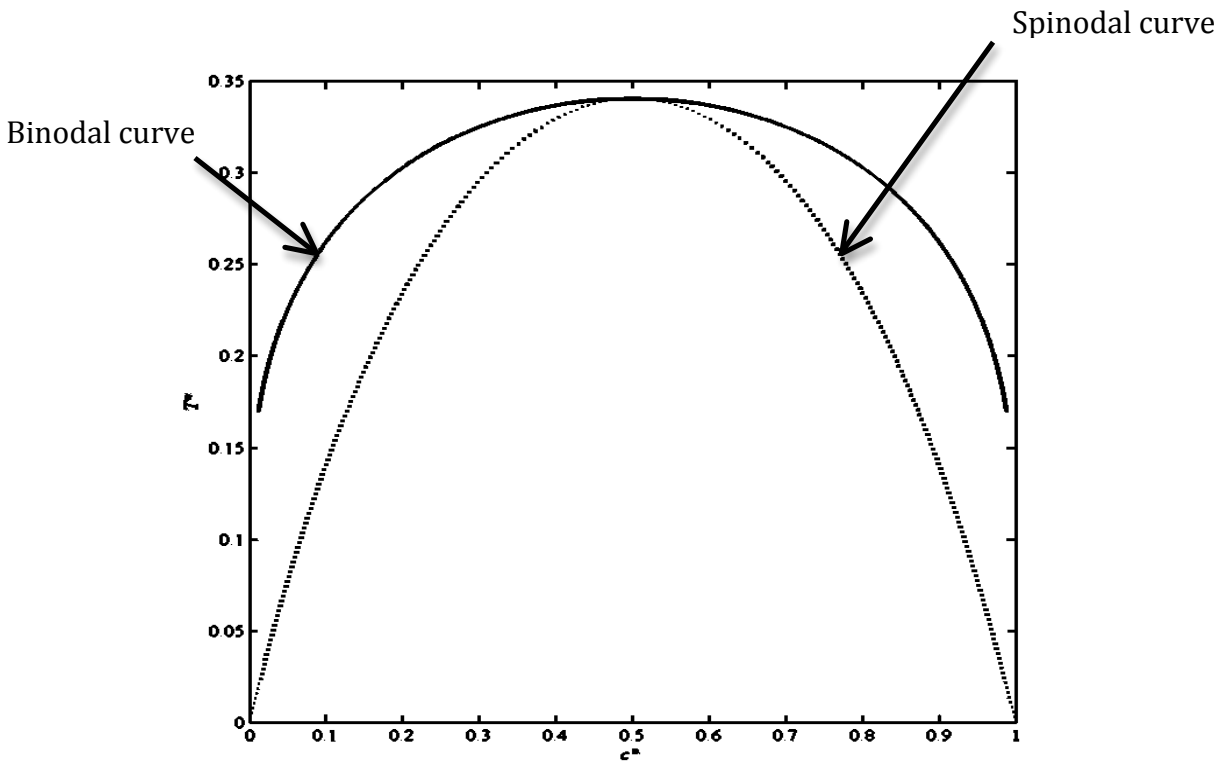

Figure 2.1: Schematic dimensionless temperature (T^*) versus dimensionless concentration (c^*) phase diagram for a symmetric polymer blend with polymer degree of polymerization $N_1 = N_2 = 1000$. The solid (dot) line represents the binodal (spinodal) line.

The phase separation route relies on the quench depth (ε) into the two-phase region [149–151]. Figure 2.1 shows a schematic phase diagram of a binary polymer blend. When the system is cooled down into the thermodynamical unstable region under the spinodal line, spinodal decomposition happens. If the system is cooled down into the metastable region confined by the binodal and spinodal lines, droplets form via the nucleation and growth mechanism. The morphologies resulting from the two processes are completely different in polymer blends [135,136,138,145,146]. There has been an increasing interest in controlling morphology of phase separation of thin polymer blend films because of their significant

applications in different fields, such as opto-electronic devices and lithographic processes [152–154]. Patterned surfaces with imprinted structures have been made by experimental techniques to control structure development in polymer blend films. These surfaces considerably alter the phase separation in polymer blend films by breaking the symmetry of polymer blend and favoring one of the blend components in attraction [155–157].

Phase separation techniques, however, fall into three major categories; i) through thermally-induced phase separation (TIPS) process; ii) by polymerization-induced phase separation (PIPS); iii) by evaporation of a common solvent dissolving the polymer blend known as solvent-induced phase separation (SIPS). As the names suggest, the phase separation is induced by the change in temperature, polymerization of the monomer and the evaporation of a common solvent, respectively. “TIPS process, however, is considered as an inexpensive, easy to handle and convenient method, while the PIPS process is useful when pre-polymer materials are miscible in low molecular weight solvents” [158].

2.2 Phase Separation Methods

2.2.1 Thermally-Induced Phase Separation Method

Phase separation is commonly induced through a temperature jump (for polymer blends with a lower critical solution temperature) or quench (for polymer blends with an upper critical solution temperature) into the unstable region of the phase diagram known as thermally induced phase separation (TIPS) [159]. Phase separation in TIPS method often occurs via spinodal decomposition (SD) [135,136,160,161]. This particular process of phase

separation does not require an activation energy like in the NG mechanism, but proceeds spontaneously in the presence of minimal concentration fluctuations or thermal noise. The phase separation mechanism for spinodal decomposition may be classified into the following three regimes: (a) early stage, (b) intermediate stage, and (c) late stage. These stages are schematically represented in Figure 2.2 for polymer blends with an upper critical solution temperature (explained in Chapter 3). In the early stage (a) which occurs immediately after the temperature lowers from the single-phase region into the two-phase region (see Figure 2.3, route 1 to 2), fluctuations in the average concentration, c_0, lead to a change in the Gibbs free energy, ΔG_M, that can only decrease due to the fact $[\partial^2 \Delta G_M / \partial c^2] < 0$ which will be explained in detail in Chapter 3. During the early stage of SD, the characteristic wavelength λ of the domain size does not change with time, only the concentration difference of the polymers in polymer A-rich phase and polymer B-rich phase increases with time. The phase separation at this stage can be predicted by the Cahn-Hilliard theory [135,136,138,145,146,160–163].

In the intermediate stage (b), the concentration difference and the characteristic wavelength both increase with time. The nonlinear effects on the time evolution of the average concentration fluctuations become increasingly important with time. The droplet size on the other hand and composition as well increase gradually with time. As a consequence, growth of the fluctuations is governed by the nonlinear time evolution equation. In the late stage (*c*), the concentration fluctuation reaches the equilibrium concentration (c_u and c_l) and the domain size is coarsening without a change in concentration, therefore phase separation is

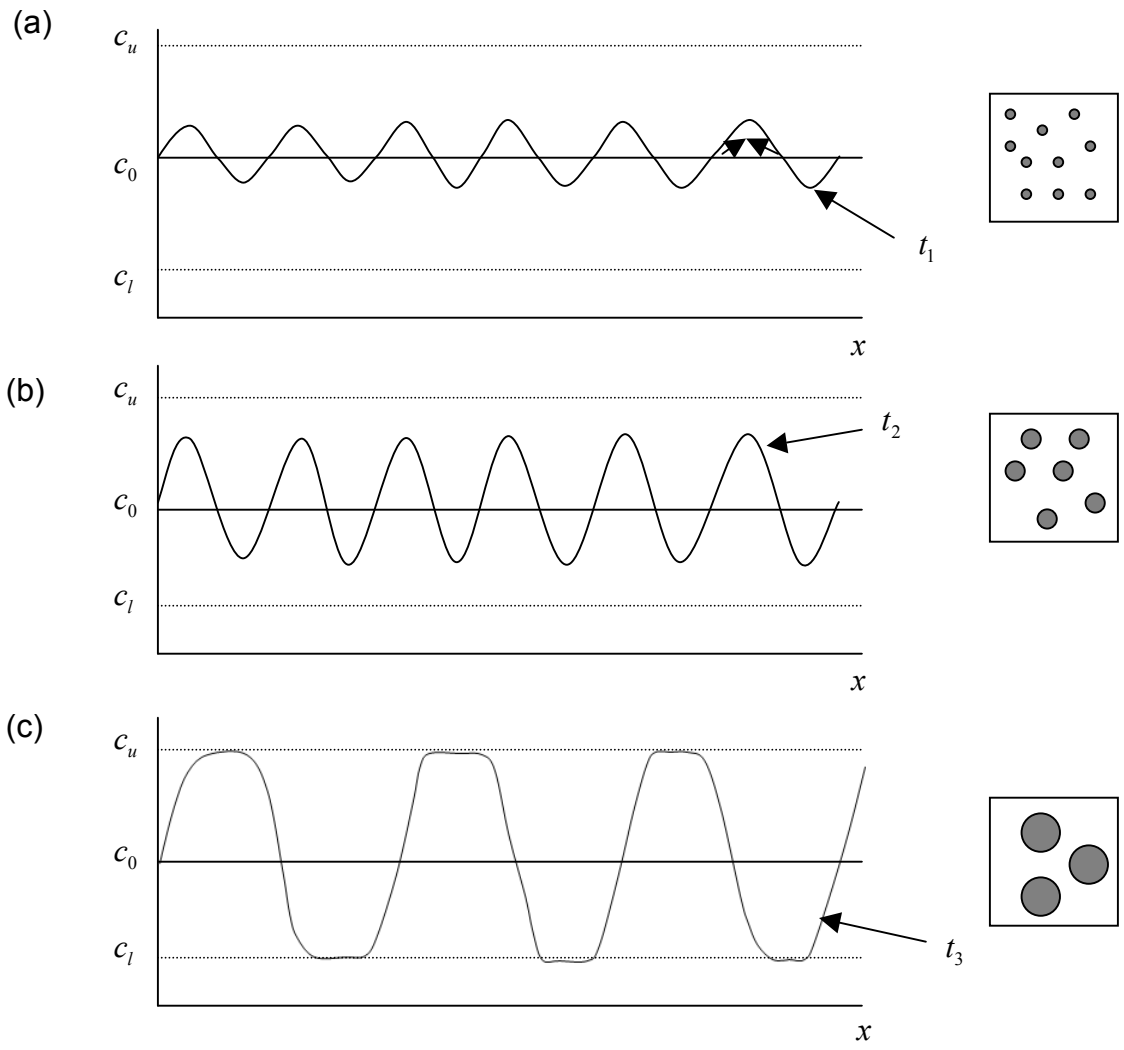

Figure 2.2: Schematic one-dimensional illustration of phase separation by spinodal decomposition mechanism for (a) early stage, (b) intermediate stage and (c) late stage where $t_3 > t_2 > t_1$. c_0 is the average concentration, c_u and c_l are upper and lower equilibrium concentrations, respectively and x is the horizontal distance. The diagrams on the right side are depicting the corresponding morphology in each stage [164].

terminated by the minimization condition of the Gibbs free energy of mixing and the wavelength of the droplets is fixed by the scale of phase-separated structure.

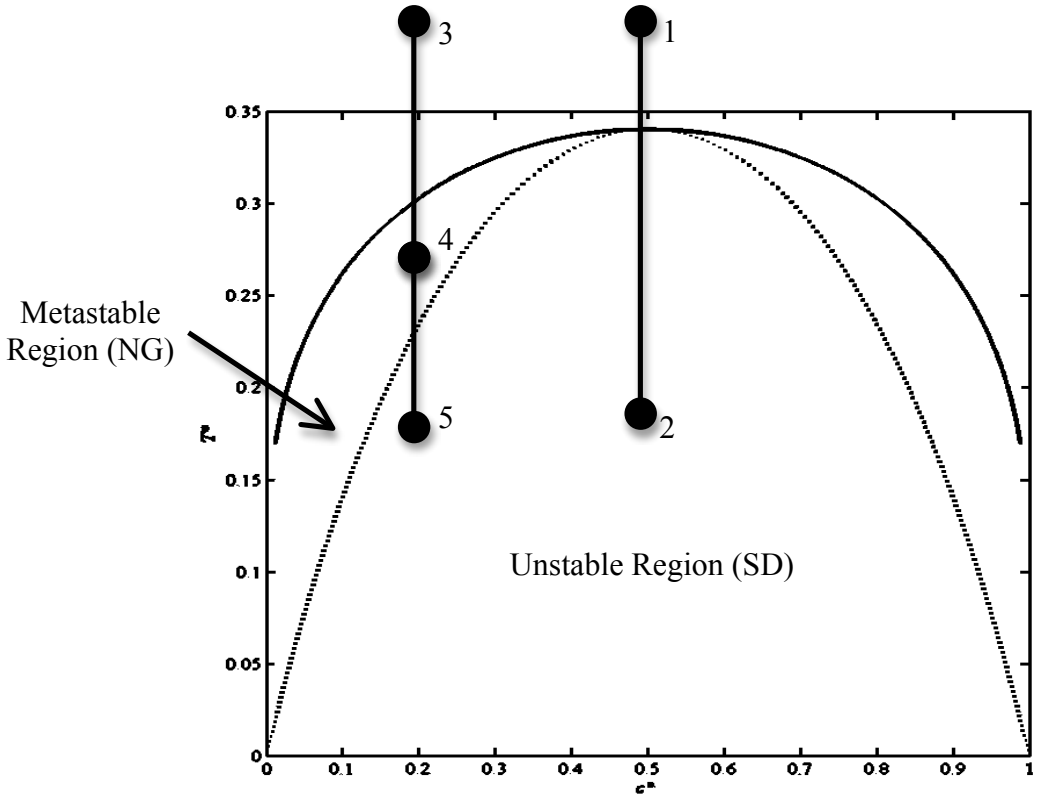

Figure 2.3: Schematic illustration of dimensionless temperature (T^*) versus dimensionless concentration (c^*) phase diagram for a symmetric polymer blend undergoing phase separation by spinodal decomposition mechanism (1 to 2 or 3 to 5) and nucleation and growth (3 to 4) in TIPS process, showing metastable and unstable region with binodal and spinodal lines.

In SD, the diffusion coefficient determined by the sign of the curvature $\partial^2 \Delta G_M / \partial c^2$ is negative. Thus, molecules diffuse up toward higher concentrations from lower concentration known as "uphill diffusion" depicted in Figure 2.2 (a) by arrows, causing the concentration fluctuations to grow gradually in magnitude. The mechanism of phase separation depends on the location of the solution composition relative to the binodal and spinodal compositions.

For mixtures between the binodal and spinodal compositions, small concentration fluctuations actually increase the free energy (e.g. point 4 in Figure 2.3), and phase separation cannot proceed until a finite nucleus with a composition close to the binodal composition spontaneously forms. With time, the initial nucleus grows while additional nuclei continue to form at random locations throughout the system. Phase separation that occurs in this way is referred to as nucleation and growth. When these nuclei are made, the system decomposes with a reduction in free energy, and the nuclei increase in size [165]. This growing procedure and the corresponding phase structure are depicted in Figure 2.4.

During nucleation and growth, pore growth occurs at a constant composition as material diffuses down the concentration gradient (downhill diffusion). Phase separation is typically the result of a deep quench, and evidence suggests that spinodal decomposition is the dominant phase separation mechanism over much of the phase diagram [135,136,160–163]. The experimental study of spinodal decomposition in some polymer blends is also a challenging task. The diffusion constant D in these blends is normally several orders of magnitude larger than the others, and so the time scale for the SD mechanism in these blends is very small, though, close to the critical point the SD mechanism happens on an experimentally observable time scale due to the low diffusion rate [166]. Therefore, most of the experimental studies on polymer mixtures [167–172] were performed by staying close to the critical temperature. The phase separation in polymer blends is mostly based on temperature and concentration in addition to the rate of polymerization (in PIPS), rate of cooling (in TIPS) and rate of evaporation (in SIPS). The competition between two contributions to the existing free energy, that are fully described in Chapter 3, is the reason

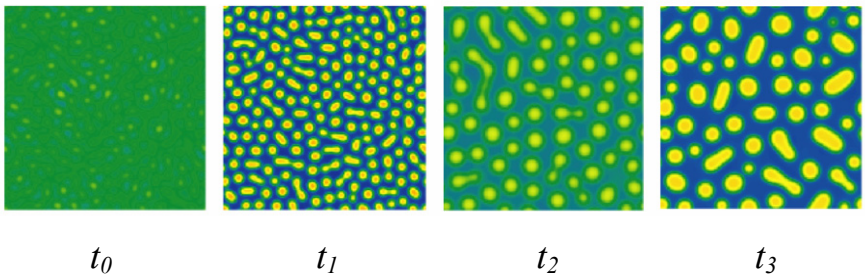

Figure 2.4: Schematic two-dimensional illustration of phase separation by nucleation and growth mechanism; $t_0 < t_1 < t_2 < t_3$ [173].

for the mechanism involved in all these phase separation processes. The separated state after phase separation has lower entropy. "The entropy is lower because the molecules of the same kind often interact between themselves more than with the molecules of other type. In the case of homogeneous state it has higher entropy. At lower temperature, enthalpy plays a more important role than entropy, but at higher temperature the situation is the reverse. Applying these postulates, the phase transition can be predicted at some intermediate temperature, and this gives the frame of the TIPS process" [158].

"In the case of PIPS, the minimum of entropy is reached when polymerizing the polymers as the bounded polymers have lower degree of freedom. The reduction of entropy is much larger in the case of homogeneous state than that of separate state. In recent years many groups have worked on such systems similarly on different phenomenological continuous models, which were utilized in the coupling of the Landau-de Gennes and Flory-Huggins free energy densities with the same microscopic techniques" [158]. In this thesis, however, the surface-directed phase separation process (SDPS) has been studied through thermal quenching (TIPS) (Figure 2.5).

Figure 2.5 is a typical representation of SDPS in a blend film of polystyrene/ polybutadiene (PS/PB) annealed with the mold located on the film. The morphology obtained by Lee *et al*. [174] takes thermodynamics into consideration, where "PB segments move to the air-polymer interface to minimize the interfacial free energy since PB segments have a lower surface tension than PS segments" [174]. However, a surface structure similar to that resulting from spinodal decomposition forms due to a very high rate of short- and long-range surface attraction taking place in between the mold and favored polymer. "As a result, a local rearrangement makes the PS-rich segments protrude from the film surface as seen in Figure 2.5" [174,175–177].

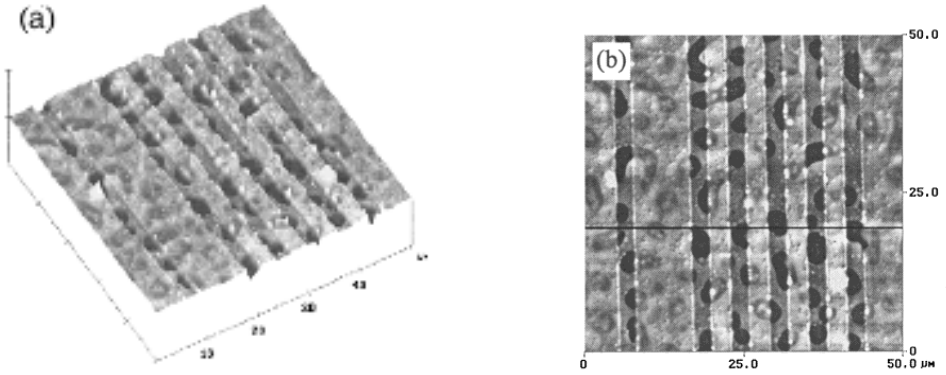

Figure 2.5: (a) Three-dimensional and (b) two-dimensional cross-section AFM images of polystyrene/polybutadiene (PS/PB, 65/35) blend film 120 nm thick with recessed strips undergoing surface-directed phase separation process [174].

TIPS can be applied when the polymer binder melting temperature is lower than its decomposition temperature [135–138,145,146,160–163,178]. In this approach, a

homogeneous mixture of solvent and a melted polymer is created. The mixture with an upper critical solution temperature is cooled at a specific rate to initiate phase separation. Solvent droplets start to shape when the polymer solidifies. The droplets continue to develop until the glass transition temperature of the polymer is passed. Droplet size is mostly influenced by the cooling rate of the polymer blend. Quick cooling rates tend to yield small droplets since there is not enough time for large particles to shape through coalescence in the later stages of SD. Thus, droplet size and cooling rate are connected inversely [178].

The phase diagram for the TIPS process is a plot of concentration as a function of temperature (Figures 2.6 and 2.7). In the TIPS process, a single-phase mixture is prepared at a certain temperature. When the mixture is thrust into the unstable or metastable region due to temperature variation, usually one component separates from the other. Figure 2.6 shows schematically a typical phase diagram for a binary symmetric polymer with an upper critical solution temperature (UCST) along with Figure 2.7 representing two-dimensional morphology of each thermal quenching case. The dashed (dotted) curve represents the binodal (spinodal) line. The area between binodal and spinodal curves is called the metastable region, where phase separation occurs by nucleation and growth (route 1). At the beginning, a polymer blend in a homogeneous phase is formed at an initial temperature and some average concentration. When the mixture is cooled to a lower temperature, phase separation takes place. When the polymer solidifies, the phase separation is terminated. Two types of morphology can be obtained in the unstable region according to the average concentration.

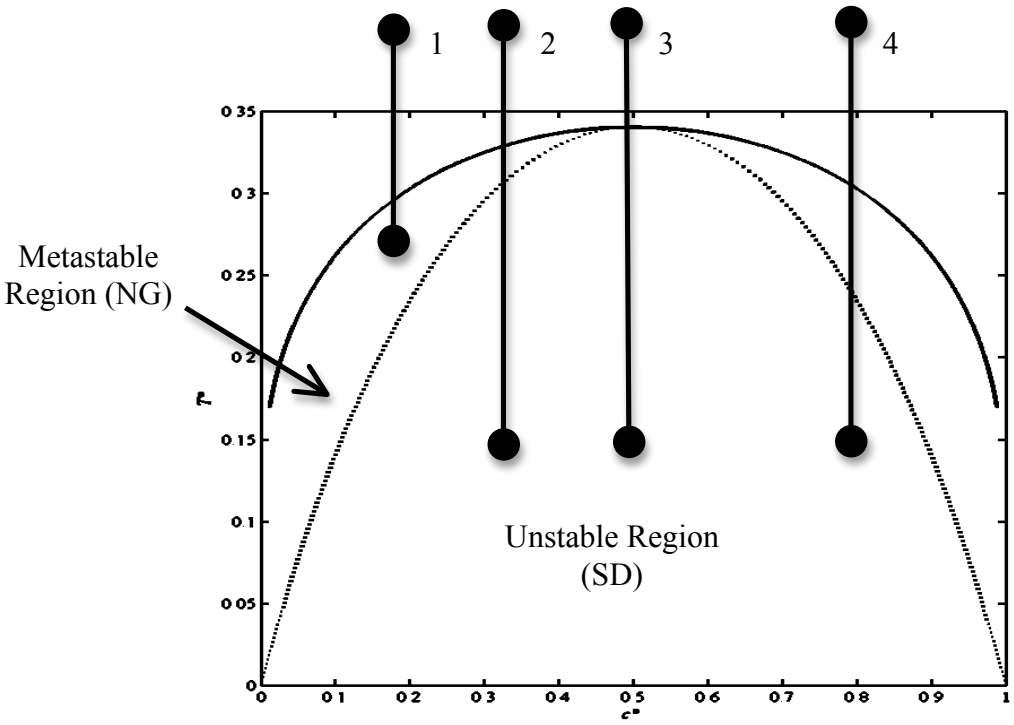

Figure 2.6: A dimensionless temperature (T^*) vs. polymer volume fraction (c^*) phase diagram of TIPS process showing the various types of quenching into spinodal region, off-critical (2 and 4) and critical (3). Route 1 is a quench into metastable region.

For an off-critical quench (route 2 or 4); where the average concentration is not the same as critical concentration, c_c^*; the droplet-type morphology forms (Figure 2.7). In route 2, the black droplets belong to polymer 1 phase dispersed in the white matrix of polymer 2, while in 4, white droplets are representing polymer 2 phase dispersed inside the blac continuous polymer 1 phase. Performing a critical quench (route 3) where the average concentration is the same as critical concentration will result in the interconnected structure consisting of a phase, which is rich in one component of the binary solution, interwoven in a matrix that is rich in the other component [179].

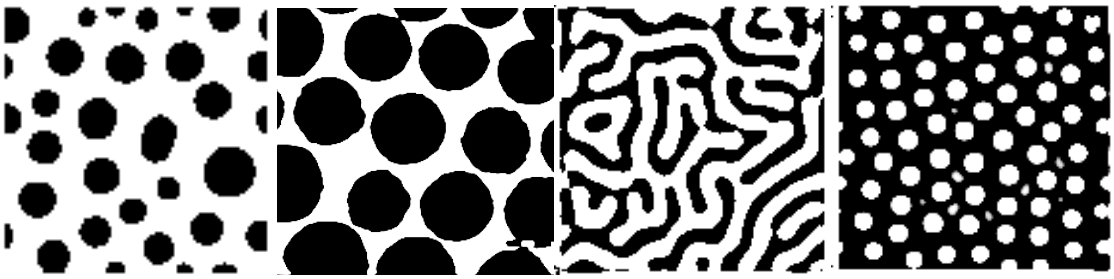

(a) (b) (c) (d)

Figure 2.7: Morphology pattern for (a) nucleation and growth quench [180] (route 1), (b) off-critical quench spinodal decomposition [179] (route 2), (c) critical quench spinodal decomposition [181] (route 3), and (d) off-critical quench spinodal decomposition [182] (route 4) in a typical polymer solution. The black (white) regions in each pattern represent solvent-rich (solute-rich) regions.

Besides the morphology, the droplet size in the TIPS process can also be controlled by the rate of cooling. In addition, there are other factors affecting the droplet sizes, such as the rate of diffusion, viscosity, and chemical potential of both components. Although the TIPS method seems simple, care must be taken to consider the process history and high temperature due to the unstable region in SD.

2.2.2 Polymerization-Induced Phase Separation Method

Polymerization-induced phase separation, or PIPS, occurs when a solvent is mixed with a solution that has not yet undergone polymerization (a prepolymer) [178,179,183–186]. Once a homogeneous solution is formed, the polymerization reaction is initiated. The

polymerization is triggered by either heat or ultraviolet exposure in the presence of initiator or crosslinking agent, depending on the chemistry of the system. Polymerization decreases the miscibility of the two components because of the increased molecular weight of the prepolymer [183].

At a certain point, phase separation occurs via either nucleation and growth mechanism, if the system is in the metastable region, or spinodal decomposition mechanism, if the system is within the unstable region. The morphology further evolves with polymerization until the system is "frozen" by chemical gelation. A large range of morphologies can be obtained by PIPS in a controlled manner, with the two major types being interconnected, and droplet morphology, as predicted by the two-phase separation mechanisms. However, in reality, the situation is complicated by the competition of reaction rate and phase separation kinetics as well as the interplay of multiple sub-factors such as viscosity, temperature, non-covalent interactions, and viscoelasticity [184].

Another way to interpret the polymerization induced phase separation is to use the phase diagram illustrated in Figure 2.8. Here, c_0, T_i and N_2 are the system composition (volume fraction), temperature and polymer degree of polymerization, respectively. Considering a system with an upper critical solution temperature (UCST, Figure 2.1), since most polymer mixtures exhibit UCST behavior, the system with an initial composition, c_0, is initially miscible at the polymerization temperature T_i. While the polymerization proceeds, the miscible mixture becomes less stable as the phase boundary curve shifts upwards. When it reaches the curing (system) point (c_0, T_i), phase separation begins.

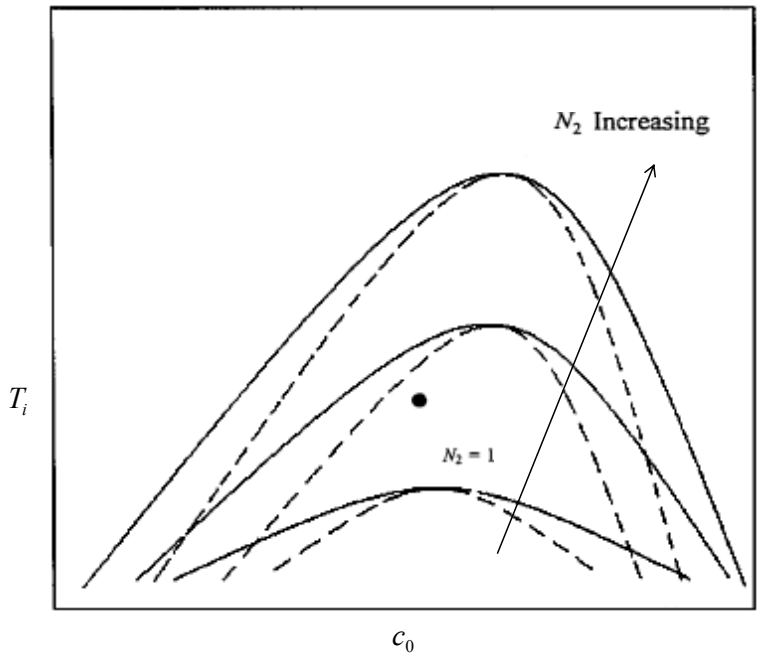

Figure 2.8: Schematic phase diagram of PIPS process. The solid (dashed) curves represent the binodal (spinodal) lines. c_0 and T_i are average concentration and initial temperature respectively. N_2 is the polymer degree of polymerization which increases with polymerization. Note that the phase diagram becomes asymmetric and the system point is thrust into the unstable spinodal decomposition region [160,179].

As the system point thrusts quickly (the reaction happens fast) into the unstable region, phase separation occurs via spinodal decomposition (nucleation and growth is inducing the phase separation mechanism within metastable region) and the phase diagram becomes asymmetric. This point is also defined as the "cloud point" (the point when phase separation begins) [160,179]. The two main factors that influence the size of solvent droplets in PIPS are the cure temperature and the type and proportions of materials used. The cure temperature affects the speed of the polymerization as well as the diffusion rate and solubility of the

solvent in the polymer. These factors can greatly influence the size of the solvent droplets, which translates into different macroscopic optical properties [184–186].

2.2.3 Solvent-Induced Phase Separation Method

"The third common type of phase separation is called solvent-induced phased separation, or SIPS. This process requires both the solvent and polymer to be dissolved in a solvent" [179,187–190]. "The solvent is then removed (typically by evaporation) at a controlled rate to begin the phase separation. Droplets start growing as the polymer and solvent come out of solution and stop when all of the solvent has been removed. The main factor affecting droplet size in SIPS is the rate of solvent removal. Like TIPS, droplet size increases as the rate of solvent removal decreases" [188]. The SIPS method has received the least attention by researchers. The main reason for this is that some thermoplastics require strong solvents. If these solvents are not recovered, environmental problems will arise and if they are recycled, additional equipment is needed [189].

2.3 Surface Directed Phase Separation

"When a binary polymer blend is quenched into the immiscible gap on the phase diagram by reducing the temperature, the spinodal decomposition can be self-induced from a system with a small composition fluctuation. Generally, the immiscible polymers will separate into A- and B-rich domains and coarsen with time" [204]. The presence of a surface may alter the course of phase separation in polymer blends by breaking translational and

rotational symmetry [191]. Surface induced spinodal decomposition has been intensively studied in the last decade [191,197–205,208,217,218,224,228,232,236,245]. Depending on the strength of interactions exerted by both external surfaces, different kinetic pathways of phase coarsening are observed for blend films leading to different final phase domain structures. “In the absence of surface effects, the initial bulk homogeneity is destroyed by the growth of fluctuations of the order parameter (concentration difference). Near a free surface, the homogeneity of the system is already disturbed by the presence of the surface and this could result in quite different pattern formation. Such “surface-directed” phase separation behavior can lead to interesting mechanical properties in polymer blends” [191]. It has been found experimentally [155,192] that “preferential attraction of one of the components to a free surface causes the spinodal wave to grow with a dominant wave vector directed normal to the surface. Another realization of surface effects is seen when a solid wetting wall is present. If a binary fluid (simple liquid or polymer) blend is quenched in the presence of such a solid surface, preferential wetting of the surface by one of the components becomes relevant.

Previous experiments [193,194] indicate that this wetting behavior affects the phase separation dynamics near the surface. If hydrodynamic effects can be neglected, the main mechanism for the growth of the wetting layer (B phase) is the diffusion of the B molecules through the A-rich phase to the B phase in contact with the wall. The same mechanism for growth of a A-rich layer is also expected to hold when A molecules are preferentially attracted to a free surface. The late stages of this diffusion-limited growth process have been studied theoretically by Lipowsky and Huse [195] for the case of stable or metastable bulk solutions of simple binary liquids. They have developed a theory in which the growth of the

wetting-layer thickness is characterized by an asymptotic power-law behavior with time" [191].

2.3.1 Numerical Studies

The power law exponent is found by two factors: (1) the interaction potential between the wall and (2) the molecules of the mixture [196]. Brown and Chakrabarti [191] numerically studied a model describing the growth of wetting layers following a critical quench of a binary mixture in contact with a wall (or with a free surface) that favors one of the two components. "They presented results from a two-dimensional simulation of surface-directed spinodal decomposition with both short-ranged and long-ranged surface fields. They modelled bulk phase separation by the Cahn-Hillard-Cook (CHC) equation with a surface potential term. The surface was represented by two boundary conditions; one fixing the order parameter at the surface to its value in the preferred phase, and the other one related to the usual no-flux condition" [198]. Having studied the dependence of the layer thickness and the density profile function on the quench location, they found that the density profile shows characteristic oscillations near the surface and that the oscillations die out as one moves away from the surface into the bulk system. It was claimed that: "the layer thickness and the domain sizes both in directions parallel and perpendicular to the surface grow as a power law in time with an asymptotic growth exponent of 1/3. The magnitudes of the domain sizes in these two directions are found to be different. The average domain size is larger in the direction parallel to the surface" [191]. They also tested a dynamical scaling hypothesis for the density profile function and the pair-correlation functions and demonstrated by numerical simulations that the scaling hypothesis works reasonably well at late times for the quenches

considered in their study [191]. Surfaces have a great impact on the structure and associated properties of multiphase polymeric materials, including polymer blends [197]. Especially, phase transitions in the bulk in the form of unmixing or microphase separation may be accompanied by surface-induced transitions by creation of wetting layers, surface-directed spinodal decomposition and surface-induced arrangement.

Binder [197] provided a short overview on the phenomenological theories of such phenomena, highlighting the easiest method based on Flory-Huggins-de Gennes free energy approach coupled with Monte Carlo simulations. It was shown that a model, where the Flory-Huggins free energy was modified by gradient terms and suitable boundary conditions at walls, could deliver a qualitative explanation of different phenomena. Extensions of this method could also explain surface-induced ordering in block copolymers, surface-induced spinodal decomposition, etc. “Surface enrichment and wetting of one species of a mixture is expected to occur at a hard wall of a container or solid substrate onto which a polymer film is brought, as well as the surface of the blend open to the air or at an interface formed with another (immiscible) fluid” [197].

In another study by Puri and Frisch [198], they critically reviewed the modeling of surface-directed SD, specifically, the phase separation dynamics of a critical or near-critical binary mixture in a surface with a favored attraction for one component of the mixture. Effective models of surface-directed SD are usually made of a bulk equation, which explains phase separation using CHC equation with two boundary conditions that model the wall. It is possible to simulate SD in a polymer film geometry using a pair of proper boundary conditions at each wall of the film. If the surface applies a long-ranged force on the favored

component, the bulk CHC equation should explicitly include this expression. In their study, the surface field was only established in the boundary conditions. The competition between the surface field and the order parameter gradient made the first boundary condition quickly maintain the order parameter at the surface to its equilibrium value. The second boundary condition was the no-flux condition maintaining the order parameter [198].

Focusing on the off-critical condition, the quench depth dependence of surface-directed phase separation in the polymer binary mixture was numerically investigated by Yan and Xie [200] through combination of the CHC theory and the Flory–Huggins–de Gennes (FHdG) theory. They discussed two distinct situations, i.e., for the wetting, the minority component is preferred by the surface and the majority component is preferred by the surface. The simulated results (Figure 2.9) showed that: "both the quench depth and the off-critical extent affected the formation mechanism of the wetting layer. Moreover, a diagram, illustrating the formation mechanisms of the wetting layer with various quench depths and compositions, was obtained on the basis of the simulated results. They found that, when the minority component is preferred by the surface, the growth of the wetting layer can exhibit pure diffusion limited growth law, logarithmic growth law, and Lifshitz-Slyozov (LS) growth law and the wetting-layer thickness at a certain time increases with increasing quench depth, compared to the reduction of that when the minority component is preferred by the surface. The opposite variation trends are due to the difference between the chemical potential in the bulk and that near the wetting layer" [200].

Figure 2.9 shows the development of the polymer morphology with initial average concentration of component A; $\phi_0 = 0.65$. "The droplets are of almost similar sizes, resulting

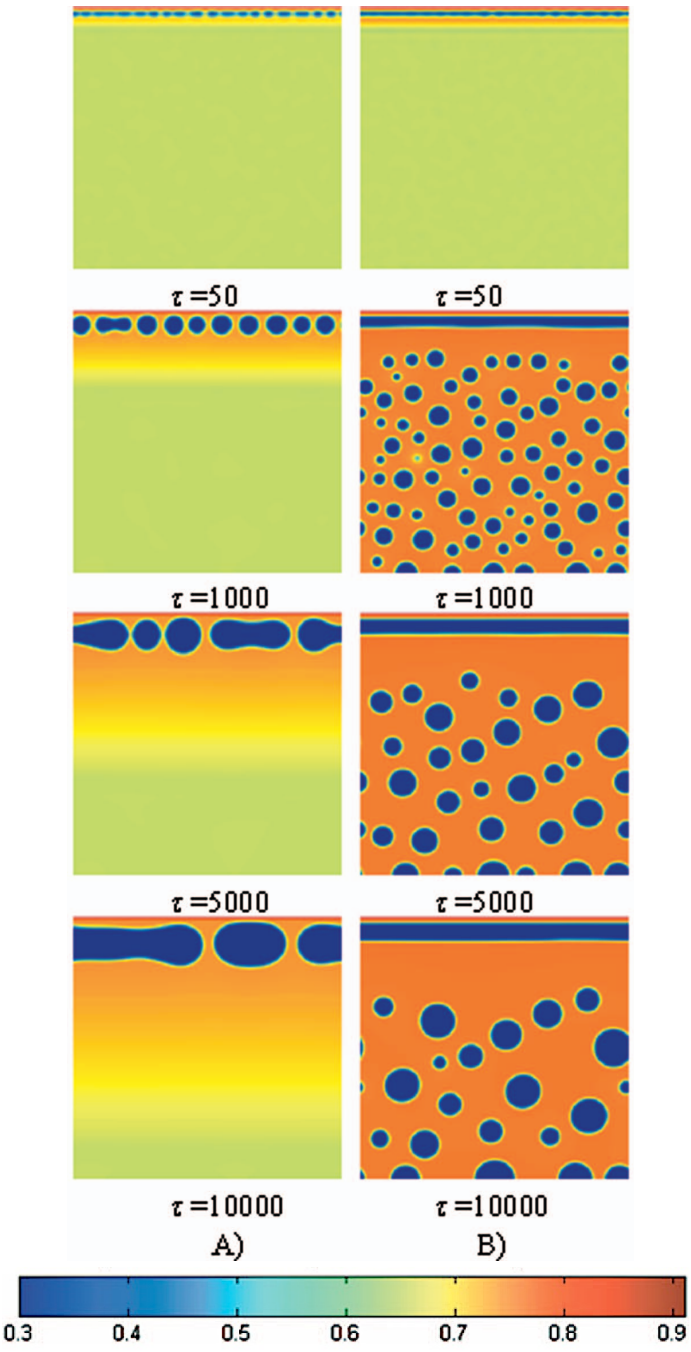

Figure 2.9: Development of the polymer morphology with initial dimensionless average concentration of component A: $\phi_0 = 0.65$ and dimensionless quench depth $\varepsilon = 0.1$ for (A) and 0.12 for (B), when the majority component is preferred by the surface. τ is representing dimensionless time [200].

from the well-defined structure of the metastable depletion layer organized by the surface. Then, the droplets grow up with the mutual coalescence, till the formation of a new depletion layer. Moreover, it can be found that the majority component gradually gathers below the droplets or the depletion layer with a gradient distribution. In other words, the minority component is removed from the large region below the droplet layer. However, when the majority component is preferred by the surface, the wetting layer always grows logarithmically, regardless of the quench depth and the off-critical extent" [200]. Their simulated results demonstrated that: "the surface-induced nucleation only occurs below a certain value of the quench depth, and a detailed range about it is calculated and indicated in the formation mechanism diagram of the wetting layer. Furthermore, the formation mechanisms of the wetting layer were theoretically analyzed in depth by the chemical potential gradient" [200].

Yan *et al*. [201] numerically investigated the phase separation of polymer blend films on the stripe-patterned surface through pairing up the FHdG equation with the CHC equation, which better fits the polymer blend. "The phase morphologies and its evolution of polymer films near patterned surfaces were considered in both real space and reciprocal space" [201] (Figure 2.10). Their main purposes were to exhibit a more complete and detailed kinetic pathways of SDPS in binary polymer mixture and to gain insight into the kinetic mechanisms. They realized that the great variation of the chemical potential at the edges of stripes caused the formation of the branch structure. Their model also showed that: "the phase inversion, happening not only in the polymer/air interface but also in the bulk, could greatly influence the isotropic phase separation and the periodic structure relationship" [201].

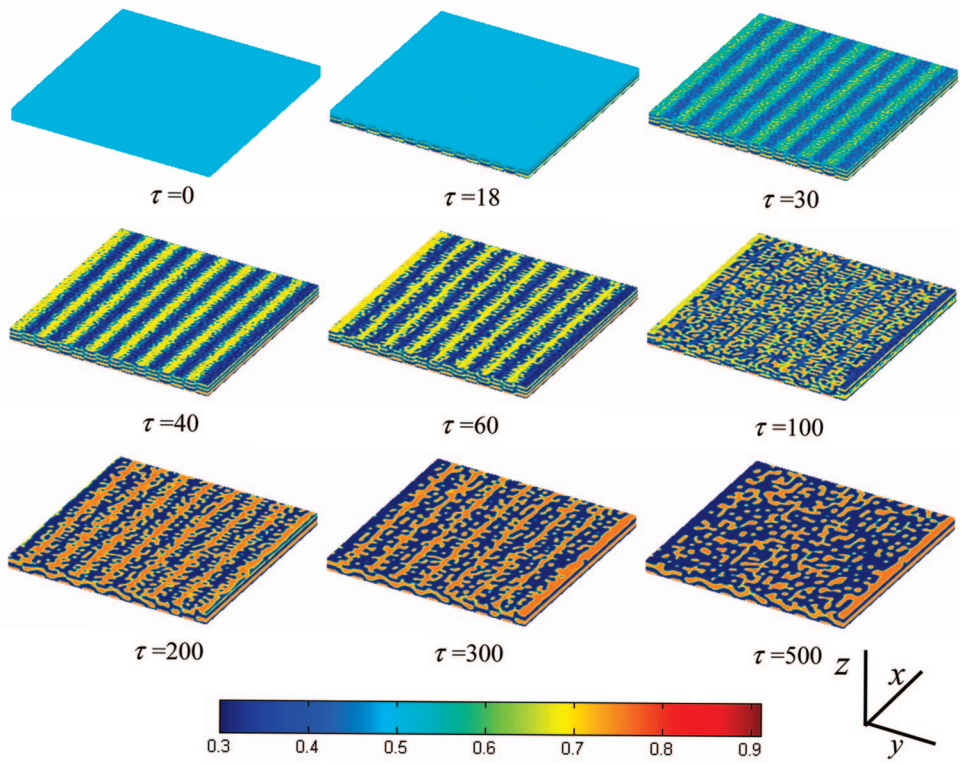

Figure 2.10: 3D patterns showing the development of the polymer morphologies following surface-induced phase separation. The bar indicates the concentration of the wetting component for the substrate. τ is representing dimensionless time [201].

Basically, the phase inversion in SDPS system is "due to the interplay between the surface potential and the bulk chemical potential" [201]. The study also presented that the development of the phase morphologies in the polymer/air interface followed power law for a thick film. Figure 2.10 illustrates the concentration of component A marked with the color bar. There are two interfaces, i.e., surface/polymer and polymer/air, in the SDPS system. It can be seen that "the fluctuation wave caused by the stripe pattern gradually penetrates into the bulk. In the lateral side, a checkerboard-like structure is created. However, with the

increasing time, the structure coarsens" [201]. As shown in Figure 2.10, "no phase-separated structure can be recognized in the polymer/air interface at the initial time. With the increasing time, the stripe structure occurs in this interface and becomes clear, and the phase structure displays the typical in-phase state where the component in each strip corresponds to the chemical potential in the patterned surface. Some branch structures then form at the edges of strips. These branches grow up and the original in-phase order structures break up gradually. However, the branches can enrich again in the next strip in this interface. At about $\tau = 200$, a clear out-of-phase pattern, where the component in each strip does not correspond to the surface pattern, is visible in the polymer/air interface. Evidently, a phase inversion at the stripes occurs during this stage and in this interface. The edges of these new stripes can be destroyed as the images after $\tau = 200$, and the stripes tend to break up again. Finally, the stripe patterns in the polymer/ air interface are replaced by arrays of fairly uniformly spaced droplets" [201].

In another study, Yan *et al*. [202] proposed and numerically investigated in 3D space a novel strategy to produce large-scale lamellar structure in polymer mixture films. The 3D space model presented a more convincing proof that the lamellar structure could be made when the system was in the equilibration state with very shallow quench inside the unstable region of the phase diagram (Figure 2.11). They also showed that the lamellar structure could also be formed in the polymer blends with the off-critical condition. Yet, because of the chemical potential variety, the phase growth procedures of the favored component of the surface being the majority or the minority component are not the same. Their model confirmed that the creation of the lamellar structure could demonstrate two fundamental processes and followed logarithmic growth law at the early and intermediate stages.

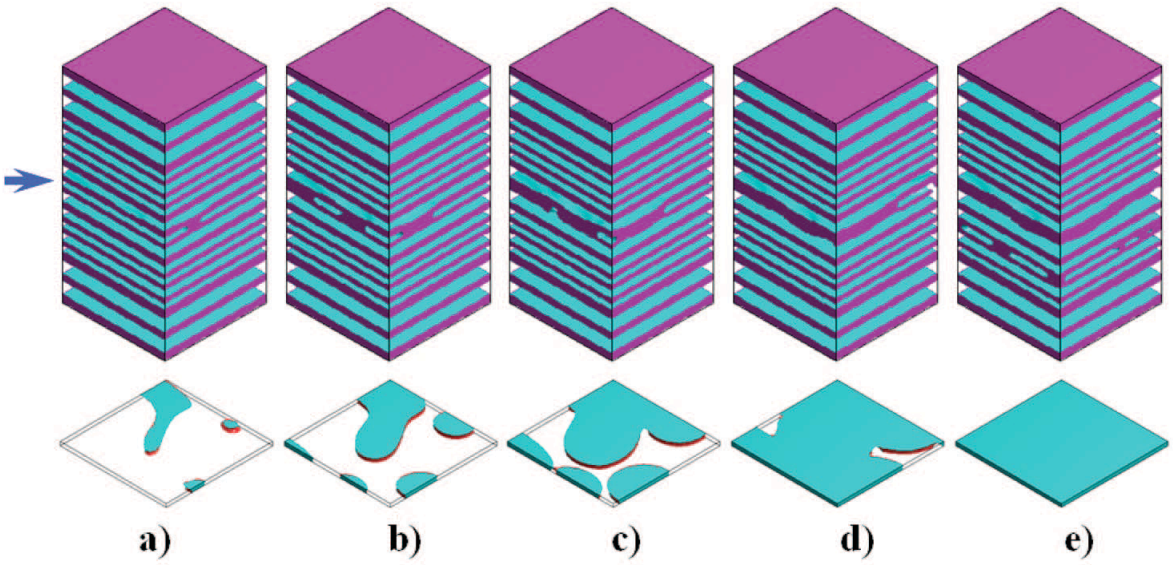

Figure 2.11: A 3D phase morphology of lamellar growth following two-step surface-directed spinodal decomposition following the second quench depth at time τ_2 = 150 where initial average concentration ϕ_0 = 0.5 and dimensionless quench depths ε_1 = 0.001, and ε_2 =0.08. (a) τ_2 = 450, (b) τ_2 = 600, (c) τ_2 = 750, (d) τ_2 = 900 and (e) τ_2 = 1200. The space between the two lamellae shown by arrow is fully filled by the preferential component and a new and thicker lamella comes into being. [202].

In this situation, the development of the wetting layer displayed the pure diffusion-limited growth law during the quench process. Figure 2.11 depicts a detailed dynamic process of lamellar growth following surface-directed spinodal decomposition (SDSP) on the formation process of the lamellar structure induced by thermal quench depth. It can be seen as denoted by the arrow, "two neighboring lamellae are selected. Some connecting points forms between the two lamellae at the original time. With increasing time, these points grow up gradually. Finally, the space between these two lamellae is fully filled by the preferential

component and a new and thicker lamella comes into being. In this case, a lamella confined between two lamellae gradually disappears and the thicknesses of the other two lamellae grow correspondingly" [202]. It exhibits again that: "there is a competitive relation between two dynamic processes, i.e., bulk phase separation and wetting layer growth in SDPS, which dominates the final phase morphology" [202,203].

In a different study by Shang *et al*. [204], the spinodal decomposition of an immiscible binary polymer blend system was examined with mathematical simulations in two- and three-dimensional. They studied mechanism of the evolution of the phase separation. When the phase separation was governed by a heterogeneously functionalized substrate, the characteristic length increase was divided into two stages by a critical time. In this situation, the development of the wetting layer did not follow any rule through the second quench depth, although it displayed the pure diffusion-limited growth law during the first quench process. Figure 2.12 shows the spinodal decomposition with the heterogeneously functionalized pattern. "In the case without the consideration of the elastic energy (a), the patterns evolve rapidly in the early stage of the phase separation. The gradient in the interface of two phases increases very quickly. The situation with the consideration of isotropic elastic energy initiates at a slower pace. The slower rate of evolution is due to the elastic energy term increases when the local composition differs from the average value of the whole domain. The checkerboard structure in the lateral direction decays faster in the case without the elastic energy. The impact of the substrate functionalization cannot spread into the depth of the polymer blends. Since the attraction force only applies on the substrate surface, the checkerboard structure in the domain is replaced by the bi-continuous structure" [204].

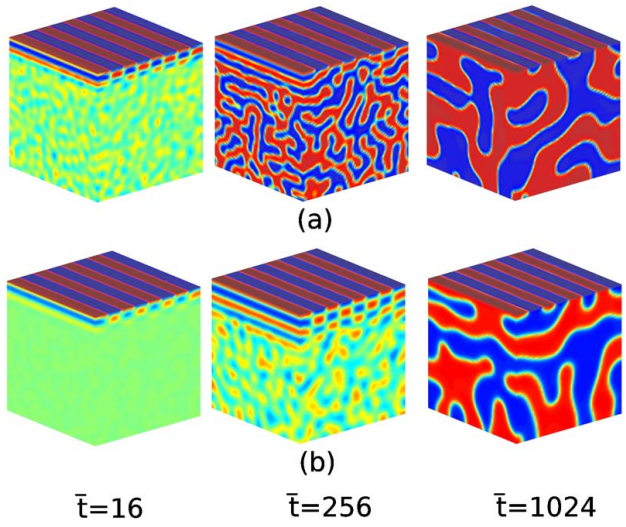

Figure 2.12: Effect of the heterogeneously functionalized pattern on the phase decomposition, (a) without elastic energy; (b) with isotropic elastic energy. $\bar{t}$ is representing dimensionless characteristic time [204].

Yan *et al*. [205] as well, investigated surface-directed phase separation through a quench process in asymmetry polymer mixtures mathematically by pairing the FHdG equation with the CHC equation. Two different conditions, when the minority and majority component was each favored by the surface, were discussed. They analyzed morphology and growth dynamics of the phase structure, particularly the domain structure. The wetting layer development mechanisms within the quench process were also studied. It was demonstrated that various domain arrangements in could be formed by shallow and deep quench depths, which could be used to tailor phase morphology. It was also found that, as quench is in process, the evolution of the wetting layer thickness could cross over to a faster growth when the preferential component was the minority component. At the initial time, the polymer mixture exhibited the usual droplet morphology based on the formation mechanism of

nucleation and growth in the off-critical phase separation [206,207]. With the increasing time, the coalescence of the droplets occurs.

Yan *et al*. [208], in another study, examined numerically the phase dynamics and mechanisms of wetting layer formation thorough pattern-directed phase separation in binary polymer blend films under the off-critical condition. The results showed that the polymer blends on the strip-patterned surface could demonstrate different phase morphologies in the bulk strips for various compositions that can modify the microscopic structures of films (Figures 2.13 and 2.14). "The developments of these phase structures in the bulk strips followed approximately the same power law with an exponent of 1/3, confirming the Lifshitz–Slyozov growth law for the films with different off-critical degrees. It was found that initially, the wetting layer width close to the patterned surface grew logarithmically, the same as the wetting layer formation mechanism of the polymer mixture close to the surface. This showed that patterning the surface potential may not merely change the wetting layer growth law. Their modeled outcomes also indicated that the diffusion of the component in the parallel direction to the surface originated from the edge of the strips. Figure 2.13 shows the phase morphologies in the polymer/air interface. The patterns with compositions $\phi =$ 0.35, 0.4, 0.45 and 0.5 are listed from top to bottom (a to d), and the time (τ) from left to right are 30, 70, 220 and 1000, respectively" [208]. Phase inversion, where A-rich phases will transform to B-rich ones, occurs during the phase evolution except that the mixture with $\phi =$ 0.35 does not undergo phase separation due to the high off-critical degree [209–212]. The branch structures at the boundary between two close stripes demonstrate that the inversion of the phase morphology from in-phase to out-of-phase originates from the edges of the strips [201,213].

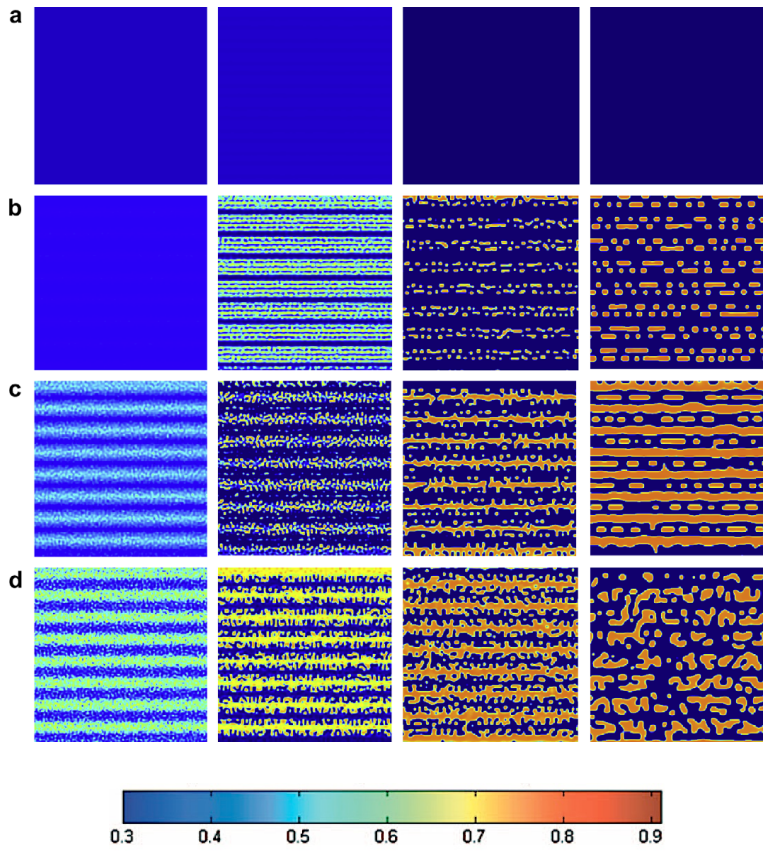

Figure 2.13: 2D morphologies in polymer/air interface with compositions ϕ: (a) 0.35, (b) 0.4, (c) 0.45 and (d) 0.5 from top to bottom and characteristic time from left to right: $\tau = 30$, 70, 220 and 1000 [208].

The mixture with $\phi = 0.4$ is selected as an example to gain detailed insight into this inversion especially near the patterned surface. Figure 2.14 plots the averaged concentration, ϕ_{av}, along y-axis, which indicates the concentration fluctuation during the phase evolution [201]. "At the initial stage ($\tau = 2$), the concentrations of component A in the A-preferring strips (y = 0–8, 16–24, 32–40,...) are lower than the average concentration, i.e., $\phi = 0.4$, which is due to the z-direction diffusion of component A towards the wetting layer due to the attraction from the surface" [208].

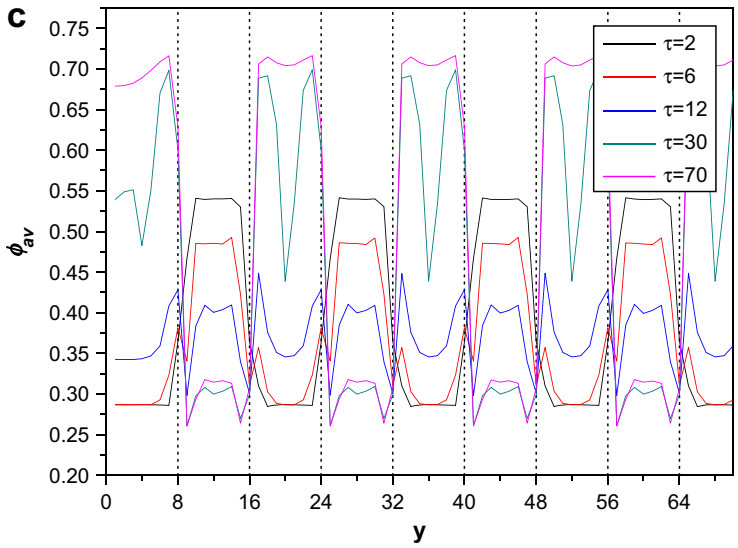

Figure 2.14: Plots of the averaged concentration profiles along *y*-axis with increasing time [208].

This mechanism is similar to that of general SDPS [155,198,209,211,212,214–216]. "However, at the edge of each stripe, the situation differs. The concentration in the edge extremely increases, leading to a strong fluctuation. Basically, the concentration fluctuation is induced by the difference of the potentials of the close strips. Then, the component accumulating in the fluctuation waves near the edges diffuses to the middle of the close trips until the concentration at the edges between two close strips is uniform ($\tau = 70$). Thus, the diffusion of the component parallel to the surface originates from the edge of the strips" [208].

2.3.2 Experimental Studies

The first experimental observation of surface-directed spinodal decomposition (SDPS) was reported by Jones *et al*. [155] thereafter, the effect was studied in a variety of different

experiments [218–222]. Nevertheless, this fact is still mostly unknown, because of the variety of the experimental structures reviewed up to now and also numerous varieties of results revealed in the different time scales that have been recognized in the analysis of bulk phase separation.

Krausch *et al*. [217] reviewed the development of the wetting layer created at the surfaces of symmetric (Figure 2.17) and non-symmetric blends of poly(ethylenepropylene) (PEP) and deuterated poly(ethylenepropylene) (dPEP) throughout SD mechanism. The rate of growth was highly based on the bulk composition of the mixtures for off-critical quenches. If the minority phase would wet the surface, the wetting layer developed slower than in the reverse situation, where the majority phase would wet the surface. It is claimed that in the latter case, the wetting layer growth rate was increased by hydrodynamic effects. For off-critical compositions as compared to critical ones, the surface spinodal waves were shallower. Yet, all surface composition profiles showed scaling behavior in the near-surface region free of bulk composition. Figure 2.15 shows the bulk compositions chosen for their study; all falling within the spinodal region of the phase diagram at 294 K and 321 K. It was found that: "distinct differences occur in the vicinity of the surface depending on whether the wetting phase is the minority or the majority component in the mixture. While the minority phase tends to build up to a surface layer somewhat slower than for critical mixtures, the majority phase was found to wet the surface in a distinctly faster process. Independent of the initial bulk composition, however, all mixtures studied exhibited dynamic scaling behavior" [217]. Their conclusions were supported by simulation results of a coarsening mixture adjacent to a surface that attracted one of the phases.

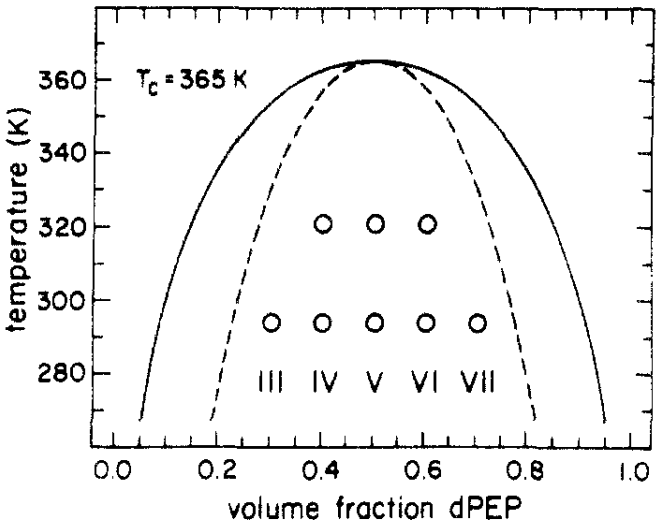

Figure 2.15: dPEP/PEP phase diagram as calculated by Flory-Huggins mean field theory. The different bulk compositions and quench locations are referred to as blends III, IV, V, VI, and VII, relating to dPEP volume fractions of 0.31, 0.40, 0.50, 0.60, and 0.72, respectively with both of equal degree of polymerization (N_{PEP}= N_{dPEP} = 2286). Critical temperature T_c = 365 K and the annealing temperatures of 294 K and 321 K were chosen corresponding to reduced quench depths of 0.81 T_c and 0.85 T_c, respectively [217].

No significant acceleration of the surface layer growth was observed in simulations where the wetting phase was the majority phase, suggesting that the acceleration observed experimentally is due to fluid flow. The numerical simulations confirmed surface-induced nucleation where the majority phase was attracted by the substrate. The nucleation barrier close to the substrate could be lowered by the expulsion of minority phase leading to the nucleation of more droplets compared to the bulk [217].

Geoghegan *et al*. [212,223,392] reviewed the surface and interface impact on the phase

separation of a blend of deuterated polystyrene and poly(α-methylstyrene) applying ^{3}He nuclear reaction analysis. Surface directed spinodal decomposition was detected in the unstable region of the phase diagram. For the deepest quenches, the surface layer grew with a $t^{0.33}$ coarsening behavior. For shallower quenches, the transition occurred at the crossover of logarithmic growth from $t^{0.47}$ to $t^{0.13}$. For the shallowest quench, a critical blend exhibited a $t^{1/2}$ behavior [212,392].

Karim *et al*. [224] studied phase separation in symmetrically separating thin polymer blend film of deuterated polystyrene/poly(vinyl methyl) (dPEP/PEP) using atomic force microscopy (AFM), neutron reflection (NR) and secondary ion mass spectroscopy (SIMS). Phase separation in the sufficiently thin film led to surface-directed spinodal decomposition waves of the liquid-air boundary (Figure 2.16). At a very late stage, the formed droplets became flattened. Interfacial free energy minimization argument was used to justify the aspect ratio of these droplets. The sample had a UCST type phase separation. Figure 2.16 shows isolated droplets that are arranged in an array-like pattern. This result is expected to be due to the large quench depth (ΔT = 151°C), which led to faster kinetics. Thus, they concluded that the phenomenon of phase-separation-induced surface pattern formation is common to symmetrically surface segregating thin polymer blend films. External surfaces can significantly alter the phase decomposition of polymer blends in thin films [155]. The break of the symmetry of polymer blend and preferential attraction of one of the blend components lead to a surface-oriented mode of phase decomposition [155–157,214] or the formation of wetting layers [225–227].

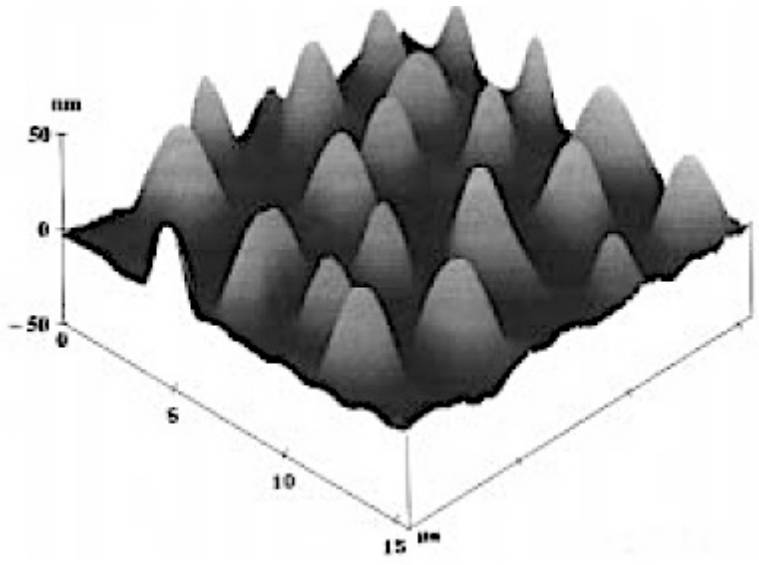

Figure 2.16: AFM image of a phase-separated film of deuterated polystyrene/poly(vinyl methyl) (dPEP/PEP) with composition of $\phi = 0.5$. The sample with a UCST type phase separation was quenched into the two-phase region at 90 °C for 48 h [224].

Cyganik *et al*. [228] studied phase separation phenomenon for poly(vinylpyridine) (PVP) and deuterated (dPS)- or brominated (PBrS)-polystyrene blends. Self-assembled monolayers (SAM) stripes of $HS(CH_2)_{15}CH_3$ (CH_3-SAM) on Au substrate were used. Transfer of the pattern from the substrate to the film interior and to the film surface was examined with secondary ion mass spectroscopy (SIMS) and atomic force microscopy (AFM) combined with selective dissolution of blend components. "Fourier transform analysis (FTA) of topographic (AFM) and compositional (SIMS) maps was performed. FTA confirmed that the pattern-directed composition variations coincide with the surface undulations driven by the modulation of surface tension (temperature quench)" [213,228,229].

Thus, spinodal decomposition was advocated for the sample and effective surface-polymer interactions, leading to anisotropic composition waves, were of short-range character due to surface-directed phase separation (Figure 2.17). For blends with higher concentrations, weaker effective surface interactions result in surface layers with more fragmented phase domains and reduced amplitudes of the surface-directed composition waves [228].

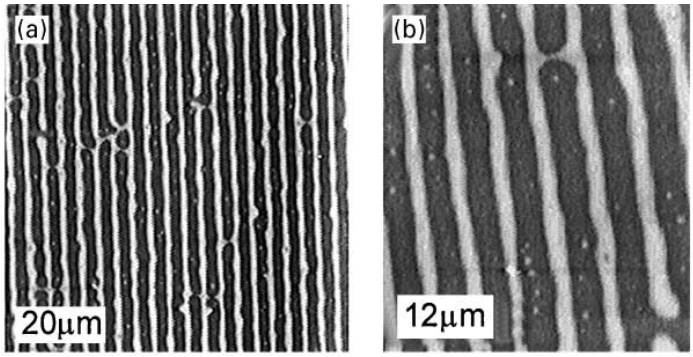

Figure 2.17: AFM images of the phase domain morphology and surface topography of thin polymer blend films (PVP/PBrS) undergoing phase decomposition during spin coating on the Au/CH_3-SAM substrate as cast. The pattern replications are different due to the change in the length scale of phase domain morphology and the variation of substrate/polymer interactions [228].

"Phase separation occurs in polymer blends when molecular mobility is promoted by a temperature above the glass transition but inside the two-phase region (temperature quench)" [213,229–231]. "This phenomenon can be altered by a homogeneous surface or pre-patterned substrate, resulting, in self-stratification or pattern replication, respectively" [232]. Such self-

organization processes ordering polymer phases were observed by Budkowski et al. [232] for: “model polymer blends (deuterated/hydrogenated polystyrene, dPS/hPS, and deuterated/partially brominated PS, dPS/PBrS, both with hPS-polyisoprene diblocks added; dPS/poly(vinylpyridine) and PBrS/PVP with high-resolution ion beam techniques (Nuclear Reaction Analysis, profiling and mapping mode of dynamic Secondary Ion Mass Spectrometry) and Atomic Force Microscopy” [232]. AFM images (Figure 2.18) show relatively good ordering of surface undulations, resembling the substrate pattern. Narrow and elevated strips alternate with wider regions located lower.

This structural feature is confirmed by the AFM image (Figure 2.18), which was taken after selective dissolution of the PVP-rich phase domains. “Protruded linear PVP domains are located on Au stripes, while the PBrS-rich phase is displaced onto CH_3-SAM substrate regions with no preferential attraction” [228]. It has been claimed that preferential attraction of one component to one substrate region is the key driving force of pattern creation in many experiments [213,228–233]. In contrast, it is usually assumed in numerical studies that both blend components differently separate to alternating stripes of the heterogeneous substrate [232,234,235]. “The self-stratification process was strongly affected by both the range as well as the strength of the surface-polymer interactions. This was illustrated for the temperature-quenched blends with surface-active copolymer additives tuning the interactions exerted by both external surfaces” [228].

Figure 2.19 depicts the AFM images of the blend PVP/dPS cast on the Au/CH_3-SAM stripes indicating drastic changes accompanying the modification of the phase domain scale, which was obtained by changing the total polymer concentration.

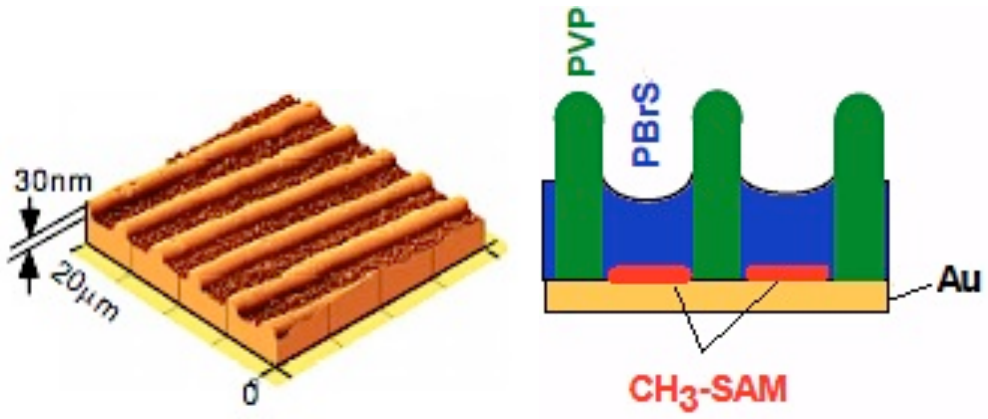

Figure 2.18: AFM image of overall phase domain morphology for the PVP/PBrS blend films cast at identical conditions on the substrate patterned with alternating stripes of Au and CH_3-SAM. Narrow and elevated strips alternate with wider regions located lower [232].

Apparently too large phase domains (Figure 2.19 b) developing during the quench are not very susceptible to periodic variations of substrate interactions.

Budkowski *et al*. [232] carefully adjusted substrate/polymer interactions by exchanging one of two polymer blend components (non-polar dPS for slightly polar PBrS, Figures 2.19 a and c) as well as one of two alternating stripes forming the patterned substrate (Au for polar COOHSAM, Figures 2.19 a and d). The first substitution worsened the quality of the created patterns. Well separated linear protrusions for PVP/dPS (Figure 2.19 a), are intermittently connected for PVP/PBrS (Figure 2.19 c). The polymer exchange hardly affected the compatibility of blend components (solubility parameters of dPS and PBrS are very similar [228]). Therefore they attributed the change in pattern replication to the reduced difference in surface tension between blend components positioned on Au stripes.

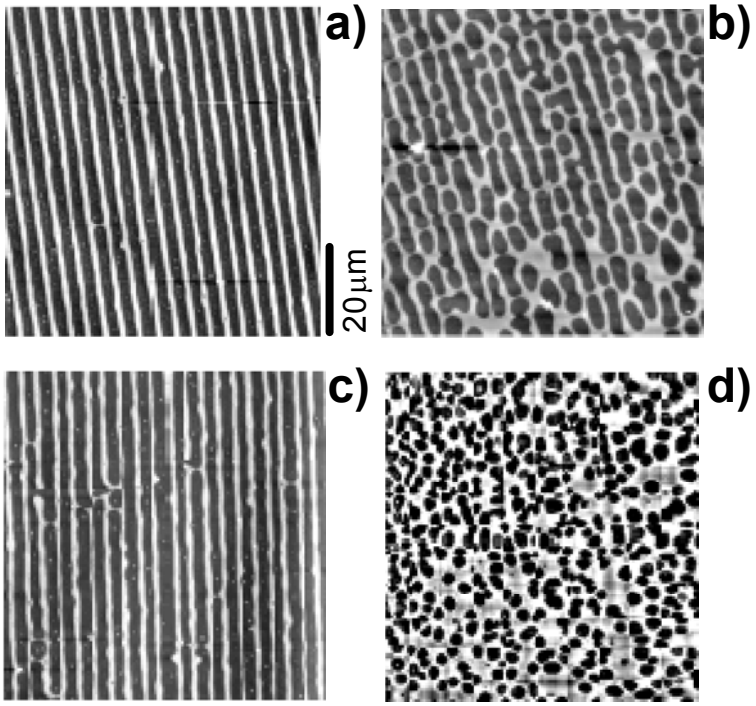

Figure 2.19: AFM images of the blend films PVP/dPS and PVP/PBrS cast on the substrate stripes: Au/CH_3-SAM (a–c) and COOH-SAM/CH_3-SAM (d). The image indicates drastic changes accompanying the increase of the phase domain scale from a to d which was obtained by varying the total polymer concentration [232].

The exchange of the striped regions of Au for polar COOH-SAM resulted in a larger surface energy difference with respect to the other stripes composed of non-polar CH_3-SAM. "Surprisingly this step did not improve but rather worsened the situation for the PVP/dPS blend films. Most probably the interactions (driving the lateral order in the film) between polar PVP and a dipole moment induced in the Au surface were more favorable than those between PVP and the COOH-terminated SAM layer" [228,232].

Han *et al*. [152] used "the patterned substrate with alternating SiO_2 and

octadecyltrichlorosilane (OTS)-SAM to induce phase separation of PS (polystyrene) and PVP (poly2-vinylpyridine) binary polymer blend films by altering the presence of patterned substrate with lateral pattern of surface energy. The PS and PVP phase were situated on the OTS and SiO_2 domains, respectively" [152]. They concluded that: "even though the characteristic length scales of phase separation were different from the periods of pre-patterned substrates, if the surface interaction between each component and substrate was strong enough, the lateral growth of phase separation domains would be significantly constrained and the domains would replicate the surface patterns" [152].

Figure 2.20 shows the film topographies after PS/PVP (w/w=1:3.4) spun-cast onto the patterned substrates from tetradrofurane (THF) solution. The thickness of the film is about 85 nm. The patterned substrates featured alternating stripes and lattices, respectively. The width of stripes is 5μm (Figure 2.20 a) and 10μm (Figure 2.20 b). It can be seen from the cross sections, "the width of the bump parts and the groove parts are nearly equal to that of patterns on the substrates. For thicker blends films, bulk-like phase separation will occur, which leads to the formation of an isotropic, disordered phase morphology with a characteristic length scale. But for thin blend films (usual thickness is less than 100 nm), since the surface-area-to-volume ratio is relatively large, both air/polymer and polymer/substrate interfaces play an important role in determining the morphology of phase separation due to the presence of wetting-dewetting behavior of each polymer component to the air or substrate. Multilayer films will emerge originating from the surface-directed phase separation when each phase strongly wet the substrate" [152,155].

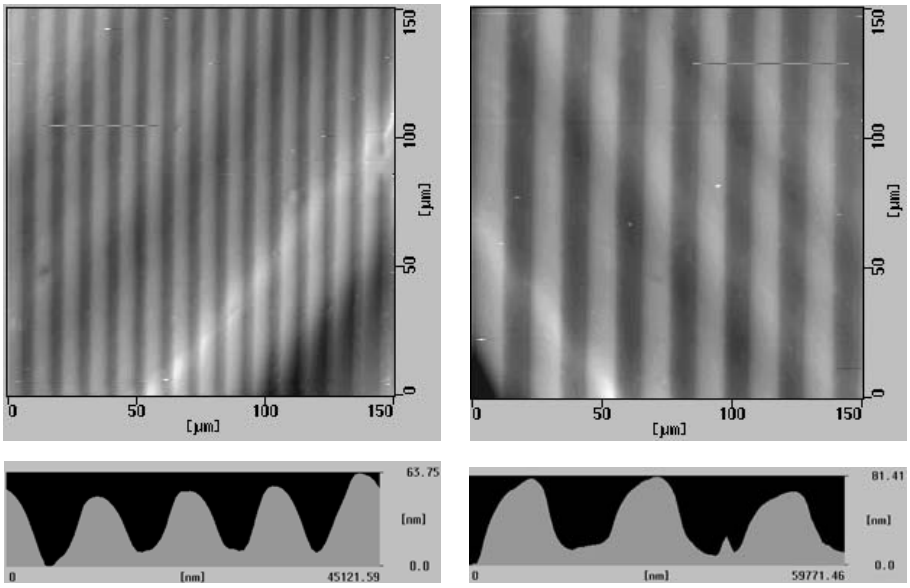

(a) (b)

Figure 2.20: "AFM images of PS/PVP blend (1:3.4 w/w) spin-cast from a tetradrofurane (THF) solution (1 wt%) onto the patterned silicon wafers, which featured with stripes and lattices of SiO_2 and OTS SAMs. (a) The width of the stripes is 5µm. (b) The width of the stripes is 10µm. The cross sections taken along the lines in the images were shown below the figures" [152].

Strategies for the utilization of phase separation to generate ordered pattern in polymer films were reviewed again by Han *et al*. [236]. They discussed the fundamental theory and factors influencing phase separation in polymer films as well as the development of ordered patterns caused by phase separation in polymer films under the effect of a chemical heterogeneous substrate or convection. The morphology caused by phase separation were then reviewed to demonstrate that multi-component patterns might be formed by adjusting the conditions or subjecting the model to different situations with more complicated

structures. “Most polymer blends of high molecular weight polymers are basically immiscible, and therefore phase separate under appropriate conditions because of the vanishing entropy of mixing. Phase separation occurs when the undiluted mixture is held above the glass transition temperature of the system. Phase separation of polymer blends can lead to different morphologies, such as bicontinuous structure, islands, or holes when altering the system characteristics such as the composition, molecular weight and structure, film thickness, solvent, or changes in the exterior environment, including the substrate, pressure, temperature, and external fields. This offers a means to pattern polymeric materials by controlling the phase separation morphologies in thin polymer blend films. Numerical simulation is playing an increasingly important role in illuminating the undergoing mechanism that can be used to guide the experiments for ideal templating. The phase separation during the spin coating is so complicated that most simulations focus on the phase separation of a thin polymer blend film on strip-patterned substrate under thermal annealing, which will shed some light on how the substrate pattern influences the phase separation” [236].

2.4 Temperature Gradient in TIPS Method

Effect of temperature gradient on morphology of polymer blends has been studied in literature both experimentally and numerically and has lot of industrial application such as fabrication of membranes with an anisotropic porous morphology [152,159,173,174,197,199,202,204,218,224,228,232,236–242]. Typically, phase separation happens when a polymer blend is quenched in temperature from the one-phase region of the

phase diagram into a point inside the spinodal curve of the two-phase region (Figure 2.21 a) [227,243,244]. Thermally induced composition fluctuations may be presented as composition waves with growing amplitude and wavelength (Figure 2.21 b). These composition waves have random directions and phases in the bulk of the blend (Figure 2.21 c). The surface disturbs this phenomenon by breaking the symmetry of the system and preferentially attracting one of the blend components. As a result, composition waves with a fixed phase develop normally to the surface (Figure 2.21 d). In the late stage of this process the domains of coexisting phases are formed, and the growth of phase domain morphology is characterized by a single time-dependent length scale (Figure 2.21 e). Morphology coarsening is driven in all its diffusive regimes [245] by interfacial tension between coexisting phases. This coarsening is ordered by surface/polymer interactions, specified by the difference of surface tension between coexisting phases [232].

Caneba and Soong [6] studied the fabrication of a PMMA membrane. Thermal-inversion technique was used in membrane fabrication where one side of the polymer solution was cooled while the other side was attached to an insulator and kept in the one-phase region. A time dependent temperature gradient was then produced. The results for early stage of spinodal decomposition showed that the cooler portion of the polymer solution consisted of smaller pores and the hotter portion had larger ones.

Hashimoto *et al*. [246] performed phase separation by applying small temperature gradients above the coexistence temperature in polystyrene-polybutadiene-dioctylphthalate blend. Before the start of convection, spinodal-like patterns developed proportionally with time and continued for hours.

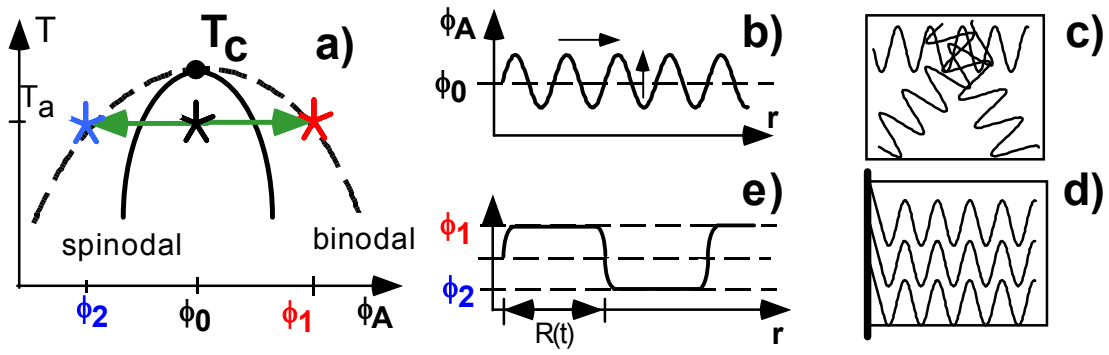

Figure 2.21: Bulk (c) and surface-directed (d) spinodal decomposition (a, b, e) of a binary mixture. Coexisting compositions are ϕ_1 and ϕ_2, while the initial concentration is ϕ_0 [232].

Despite temperatures within the mixture exceeded the thermodynamic coexistence temperature; large thermally driven concentration gradients perpendicular to the surface had caused phase separation parallel to the surface. It was shown that phase separation of polymer blends could be achieved in the homogeneous one-phase region of the phase diagram under the influence of a temperature gradient in which an interconnected structure was obtained [246].

Polymerization-induced phase separation (PIPS) through spinodal decomposition (SD) under a temperature gradient for the case of a monomer polymerizing in the presence of a non-reactive polymer was studied by Oh and Rey [247] using high performance computational methods. An initial polymer (A)-monomer (B) one-phase mixture, which had an upper critical solution temperature (UCST) and was maintained under a temperature gradient, phase-separated and evolved to form spatially inhomogeneous microstructures. The space-dependence of the phase-separated structures under the temperature gradient field was

determined and characterized using quantitative visualization methods. They found that a droplet-type phase-separated structure was formed in the high-temperature region, corresponding to the intermediate stage of SD. On the other hand, lamella or interconnected cylinder type of phase-separated structure was observed in the low-temperature region, corresponding to the early stage of SD structure, in the large or small temperature gradient field, respectively. The kinetics of the morphological evolution was dependent on the magnitude of the temperature gradient field. The non-uniform morphology induced by the temperature gradient was characterized using novel morphological techniques, such as the intensity and scale of segregation. It was found that significant non-uniform structures were formed in a temperature gradient in contrast to the uniform morphology formed under constant temperature [247].

Chan *et al*. [138,146,163,249] studied the influence of linear spatial temperature gradients on the morphological development during the fabrication of anisotropic binary polymer solution undergoing thermally induced phase separation using mathematical modeling and computer simulation. Their one-dimensional mathematical model [163] describing this phenomenon incorporated "the nonlinear Cahn-Hilliard theory for spinodal decomposition (SD), the Flory-Huggins theory for polymer solution thermodynamics, and the slow-mode theory and Rouse law for polymer diffusion. The resulting governing equation and auxiliary conditions were solved using the Galerkin finite element method. The temporal evolution of the spatial concentration profile from the computer simulation showed that an anisotropic morphology resulted when a temperature gradient was maintained along the polymer solution sample. The final anisotropic morphology depended on the overall phase separation time. If phase separation was terminated at very early stages, smaller

(larger) droplets were formed in the lower (higher) temperature regions due to the deep (shallow) quench effect. On the other hand, if phase separation was allowed to proceed for a long period of time, then larger droplets were formed in the low-temperature regions, whereas smaller droplets were developed at higher temperatures. This was due to the fact that the low-temperature regions had entered the late stage of SD, while the high temperature regions were still in the early stage of SD. The presence of a temperature gradient during thermally induced phase separation introduced spatial variations in the change of chemical potential, which was the driving force for phase separation. These numerical results provided a better understanding of the control and optimization during the fabrication of anisotropic polymeric materials using the thermally induced phase separation technique" [163]. The 2D mathematical outcomes [138] (Figure 2.22) presented that: "an anisotropic morphology was formed when a temperature gradient was applied along the polymer solution sample. The droplet size and density decreased as temperature increased through the intermediate stage of SD" [138]. The spatial temperature gradient, yet, had insignificant effect on the droplet shape.

Bin *et al*. [248] studied: "crystallization and phase separation of polyethylene blend under a controlled temperature gradient condition. Branched low molecular weight polyethylene (B-LMWPE) and ultrahigh molecular weight polyethylene (UHMWPE) blend films were made by forming the blend solutions on the temperature gradient stage" [248] followed by evaporation of the solvent. The morphological development of blend films was examined fully. The blend films presented a constant gradients surface. The degrees of crystallization of B-LMWPE and UHMWPE reduced in the blend films after the temperature was increased.

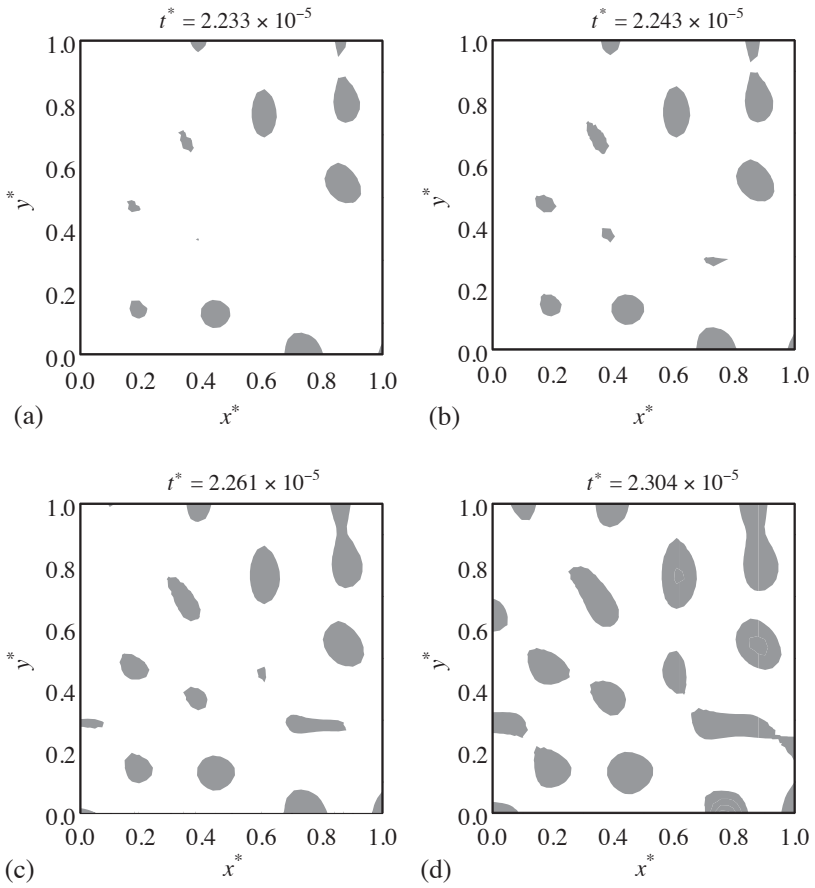

Figure 2.22: Time evolution of droplet formation for the uniform quench case. The gray areas represent solvent-rich phase while the white area denote the polymer-rich phase. The asterisks are representing the dimensionless values [138].

The results showed that phase separation behavior of B-LMWPE and UHMWPE blend with composition 10/1 or 5/1 happened in both of solution and gel, and the phase separation occurred before crystallization. It is proposed that phase separation must have encouraged molecular ordering and crystallization in the B-LMWPE/UHMWPE blend in the early stage, and the phase separation and crystallization compete with each other in the later period. Moreover, high viscosity of blend solution played a more significant role in phase separation

rather than in crystallization [248].

Chan *et al.* [250] investigated thermally induced phase separation in liquid crystalline polymer (LCP)/polycarbonate (PC) blends (Figure 2.23). The applied LCP was a main-chain form of copolyester containing p-hydroxybenoic and 6-hydroxy-2-naphthoic acids prepared by melt blending for microscopic observation. The specimens were heated to preselected temperatures of 265, 290, and 300^{o}C, held for isothermal phase separation. The LCP contents of 10, 20, and 50 wt % were used corresponding to various places on the phase diagram of the blends. The phase-separated morphology growth in the blends was observed in real time and space. They observed an early fast phase separation then the coarsening of the dispersed domains. The blends grew into different kinds of phase-separated morphology, based on the concentration and temperature at which phase separation happened.

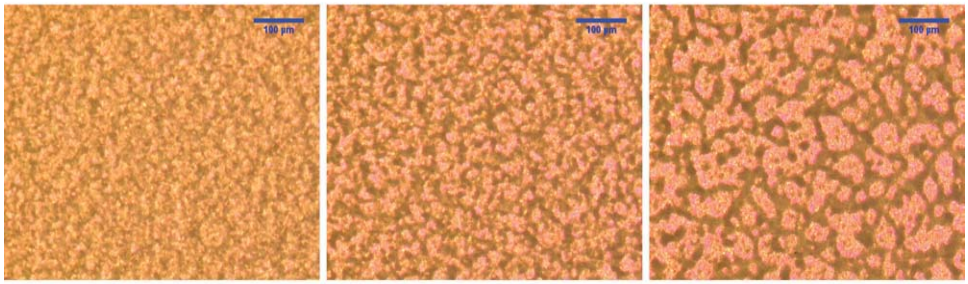

Figure 2.23: Phase-separated structure development in 20 wt.% LCP/PC blends in the early stage at 300 ^{o}C. Scale bar on images represents 100 μm [250].

The coarsening procedure of the phase-separated domains were observed in the late stages of the phase separation in these blends as follows: (i) diffusion and merging of the

LCP-rich droplets; (ii) disappearance of the PC-rich domains after the evaporation-condensation mechanism; and (iii) rupture and size reduction of the LCP-rich domains [250].

Xie *et al.* [5] experimentally investigated the gradient morphology and surface properties of the ethylene-vinyl acetate and polypropylene blends under the influence of increasing temperature. They observed a distribution of increasing droplet size from the center to the material surface.

Chapter 3

3. Theoretical Background

This chapter introduces the basic phase separation method and theories of spinodal decomposition and nucleation and growth. A novel mechanism is described to form binary polymer blends due to temperature variations. Phase diagram for polymer blends are presented in detail. The experimental techniques to obtain these thermodynamic phase diagrams are introduced as well. Polymer blends are differentiated according to Gibbs free energy of mixing ΔG_M . The majority of polymer blends are immiscible. These heterogeneous polymer blends have a positive ΔG_M value. In some cases, they are soluble. However, they tend towards phase separation to form multiphase at some temperature and molecular weight.

In many applications, miscibility of the phases is not desired or required. Therefore, phase separation methods have been one of the practical methods to obtain multi-component polymer blends. For example, the desired morphology of the blends can be obtained by controlling the polymer concentration and processing conditions such as temperature and shear rate. In order to obtain the heterogeneous mixtures and control their phase morphology, it is fundamentally important to understand the phase separation method. In addition, phase separation is an important field of polymer formation, modification and processing.

3.1 Phase Separation Thermodynamics

Thermodynamics is a fundamental factor in determining polymer blends miscibility [251–254]. Phase separation occurs when a homogenous single-phase polymer blend transforms into inhomogeneous state. For a binary polymer blend, the phase separated system consist of polymer A rich and polymer B rich phases. The factors that will affect polymer-polymer miscibility are [255,256]:

- Entropy of mixing: the most important parameter for miscibility of small molecules but less important for high-molecular-weight polymers.
- Dispersion forces: Possibly the attractive force between nonpolar molecules or induced dipole force.
- Specific interactions: like Lewis acid-base or electrostatic interactions or hydrogen bonding that is in favor of mixing of two polymers.
- Free-volume differences between polymers: leads to negative volume of mixing, so demising is favorable.

Based on the second law of thermodynamics, the mixture is completely miscible only if the Gibbs free energy is released upon mixing; i.e. $\Delta G_M < 0$ [257]. In addition, at temperatures above critical solution temperature (T_c) the mixture is completely miscible because for all mole fractions the second partial derivative of free energy with respect to concentration is positive; i.e. $[\partial^2 \Delta G_M / \partial c^2] > 0$ where c_i is the volume fraction of the i th component. The Gibbs free energy of mixing is expressed as:

$$\Delta G_M = \Delta H_M - T\Delta S_M \tag{3.1}$$

where ΔH_M and ΔS_M represent enthalpy and entropy of mixing, respectively. T is the temperature. Generally, the distinctive property of polymers is their large molecular weight that can be used to control the miscibility of a multi-component mixture. Entropy of mixing is typically positive, thus whether the Gibbs energy of mixing is negative (miscibility) or positive (non-miscibility) depends on the value of the enthalpy of mixing. The mixing entropy ΔS_M of a large molecular weight polymer almost equals zero. On the other hand, the enthalpy of mixing ΔH_M is positive in most polymers, at least for non-polar polymer systems. Therefore, the Gibbs free energy of mixing is seldom negative which means that phase separation always occurs in polymer blends. In the case of binary polymer blend systems, the Gibbs free energy of mixing ΔG_M versus volume fraction of a polymer diagram can be constructed as a function of temperature. Figure 3.1 shows a schematic diagram of Gibbs energy of mixing and temperature as a function of mole fraction of polymer in the blend. Points with temperature T_2 represent lower Gibbs energy of the mixture than points with T_3 temperature, so a mixture with overall composition of c at temperature T_2 or T_3 splits into two polymer phases.

As shown in Figure 3.1, the shape of the free energy of mixing curve and the beginning of phase separation varies by changing the temperature values from T_1 to T_3 $\left(T_1 > T_2 > T_3\right)$. Critical point is also shown in the figure where the spinodal and binodal curve meet each other. In phase separation mechanism, the miscible polymer blend at an initial temperature T_1 goes down into the lower temperatures, eventually becomes a totally

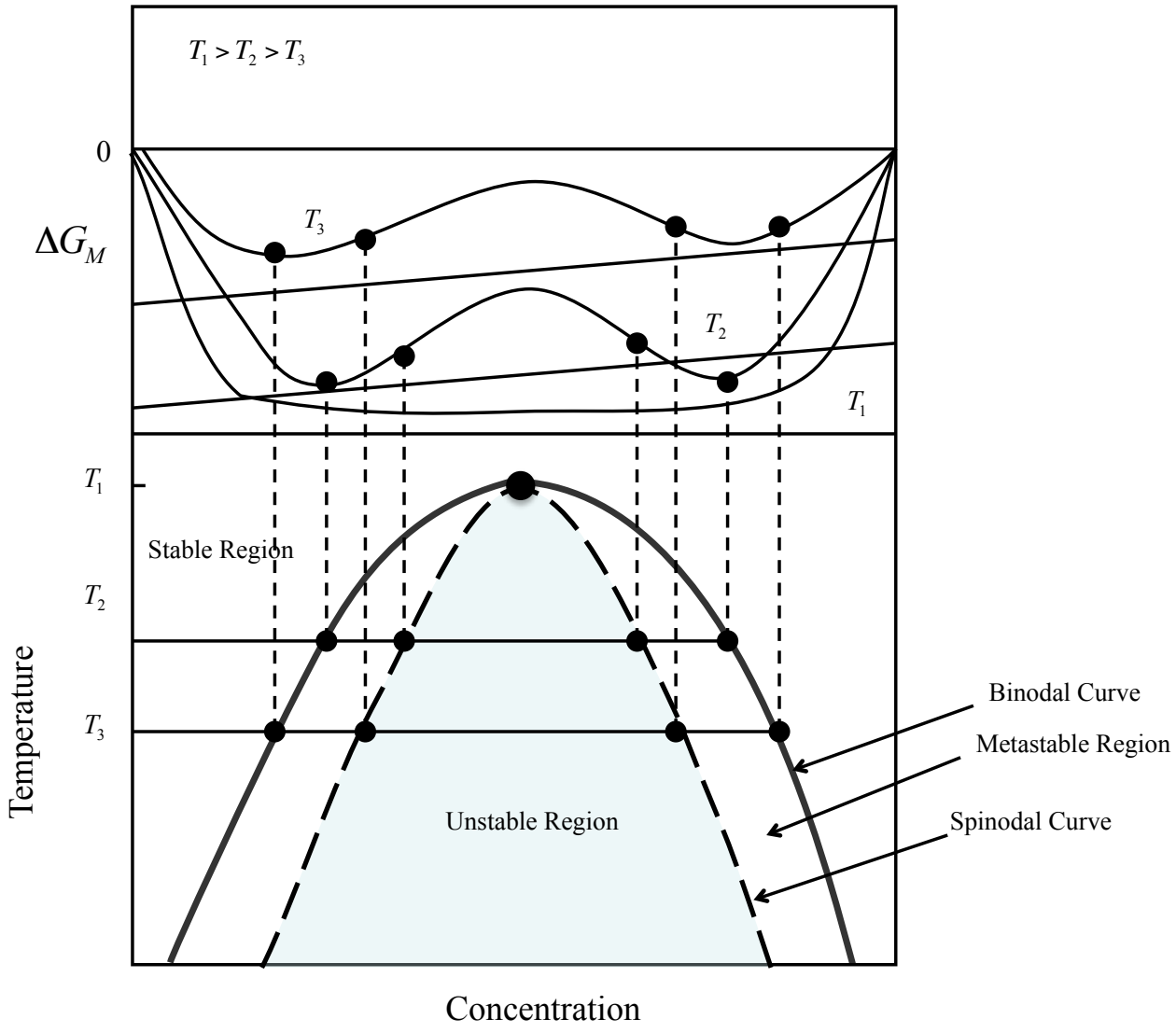

Figure 3.1: Schematic diagram of Gibbs free energy (top half) and temperature of a polymer blend (bottom half) as a function of polymer concentration showing the stable, metastable and unstable spinodal (shaded area) regions. T_1 is the critical solution temperature [253].

immiscible system. In the upper part of the diagram, the binodal (cloud-point) curve is formed by projecting minimum points and the spinodal curve is obtained by the projection of the inflection points as shown in Figure 3.1.

The straight lines are the common tangential lines for the free energy curve. For a polymer blend, the Gibbs free energy of mixing ΔG_M must be negative in order to form a homogenous mixture. In Figure 3.1 at T_1 (critical temperature), ΔG_M shows only one minimum over the polymer concentration range. Therefore, the system is completely miscible over the whole range of polymer concentration as shown in the phase diagram. At T_2 and T_3, even though ΔG_M is lower than zero for the whole range of polymer concentration, the system is only partially miscible. Since ΔG_M shows two local minima, in order to have the free energy ΔG_M of the system at the overall minimum, the system will separate into two phases with the concentrations of the two phases determined by the tangent points on the ΔG_M curve [148] where:

$$\left[\frac{\partial \Delta G_M}{\partial c}\right]_1^{First\ phase} = \left[\frac{\partial \Delta G_M}{\partial c}\right]_2^{Second\ phase} \tag{3.2}$$

where c_1 and c_2 are representing the concentrations of components 1 and 2 of the polymer blend in the two equilibrium phases. These two points are called binodal points, and the curve joining these points at different temperatures is named the binodal curve. The binodal curve is the boundary between the one phase region and the two-phase region. The inflection points of $\Delta G_M - c$ curve corresponding to $[\partial^2 \Delta G_M / \partial c^2] = 0$ are the spinodal points, and the curve connecting these points is called the spinodal curve. The spinodal and binodal curves meet at the critical point [148]. The critical temperature (T_1) which is the intersection point of the binodal and spinodal curves, is an important quantity for binary polymer blend phase diagrams since:

$$[\partial \Delta G_M / \partial c] = [\partial^2 \Delta G_M / \partial c^2] = [\partial^3 \Delta G_M / \partial c^3] = 0 \quad (3.3)$$

In the phase diagram, the region above the binodal curve is the stable region where a homogenous mixture can be formed. The region inside the spinodal curve is the unstable region corresponding to $[\partial^2 \Delta G_M / \partial c^2] < 0$ where the system spontaneously phase-separates into two co-continuous phases. Between the binodal and spinodal curves, the system may be one phase but not stable which is called the metastable region, where $[\partial^2 \Delta G_M / \partial c^2] > 0$.

The phase behavior shown in the lower part of Figure 3.1 is the typical behavior of systems showing an upper critical solution temperature (UCST), where the system enters the two-phase region upon decreasing temperature [258]. If increasing the temperature brings the system from miscible to immiscible region, it is referred to a lower critical solution temperature (LCST) type of phase behavior, which is caused by special interactions between the two polymer components such as strong polar interactions or hydrogen bonds. Figure 3.2 shows different combinations of these two types of behaviors. In addition to only UCST (B) and LCST (C), a system can display both types of phase behaviors. This is illustrated by diagram D and E which shows an island of immiscibility. The UCST and LCST branches in diagram D can merge to form an hourglass shape phase diagram (diagram F). This type of transition has been observed experimentally in polystyrene blends in acetone [180] where two branches at higher pressures move to each other and merge at lower pressures [148].

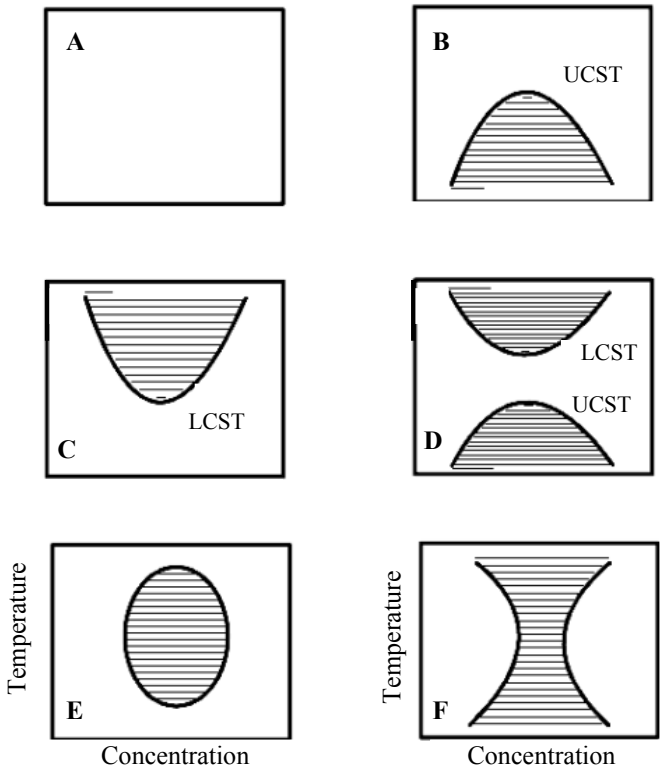

Figure 3.2: Schematic of phase behavior in polymer blends. Shaded areas represent the two-phase regions and the un-shaded areas represent one-phase regions [180].

3.2 Flory-Huggins Theory

In this section, the derivation of the thermodynamics of polymer blends is reviewed. Flory-Huggins (FH) theory was formulated independently by P. J. Flory [259] and M. L. Huggin [253] in the middle of the last century. The entropy and enthalpy of mixing of two polymers were derived and phase diagrams of polymer pairs were explained on the basis of enthalpy interactions. Several researchers have extended this theory to explain the phase diagrams presented in the literature.

This model is based on the two-dimensional statistical lattice model. This lattice model is used to characterize the possible arrangements of the components' segments in the polymer mixtures. Polymer solutions are considered as the irregular non-ideal solutions, where both ΔH_M and ΔS_M deviate from their ideal values. Following assumptions have been made in this theory:

1. The components of the mixture are placed in "lattice".

2. Volume is unchanged during mixing.

3. Mixing entropy is strongly influenced by the chain connectivity of the polymer component.

4. Mixing enthalpy for polymer-small molecule mixtures is similar to that for regular solutions.

5. Each repeating unit of the polymer ("segment") occupies one position.

If we assume that we have two polymers with N_1 and N_2 number of monomers in their chains and if there is no volume change on mixing in the square two dimensional lattice model based on Boltzmann's law of entropy:

$$\Delta S_M = k_B \ln \Omega \tag{3.4}$$

where k_B is the Boltzmann's constant and Ω is the number of possible random arrangements in the lattice space. Using the constant density approximation yields a correlation between mole fraction and volume fraction in a straightforward manner and by substituting the resultant equation in Equation (3.4) yields an expression for the entropy of

mixing for a polymer blend [253]:

$$\Delta S_M = -k_B\left[\frac{c}{N_1}\ln c + \frac{(1-c)}{N_2}\ln(1-c)\right] \tag{3.5}$$

where c is the volume fraction of component 1:

$$c = \frac{N_1}{N_1 + N_2} \tag{3.6}$$

and $(1-c)$ is volume fraction of component 2. If we assume between two component segments there is a repulsive or attractive interactions, this energy could change the Helmholtz free energy of mixing.

The energy of mixing can be either negative (promoting mixing) or positive (demixing). Applying the regular solution theory, it is assumed that change in energy arises from the formation of new solvent-polymer interactions on mixing, which several of the solvent-solvent and polymer-polymer interactions in the pure solvent and pure polymer separately, become substituted by these contacts. Enthalpy part of free energy of mixing could be calculated as [253,261]:

$$\Delta H_M = k_B T \chi c(1-c) \tag{3.7}$$

where, T is the temperature, and χ is the Flory-Huggins interaction parameter. Combining Equations (3.5) and (3.7) into Equation (3.1) free energy of mixing could be obtained:

$$f(c)=\frac{k_B T}{\upsilon}\left[\frac{c}{N_1}\ln c+\frac{(1-c)}{N_2}\ln(1-c)+\chi(1-c)\right] \tag{3.8}$$

It is known that χ is temperature dependent; it could be express as following:

$$\chi=\frac{1}{2}-\psi\left(1-\frac{\theta}{T}\right) \tag{3.9}$$

where, ψ is the dimensionless entropy of dilution parameter, and θ is the theta temperature at which the polymer solution behaves like an ideal solution [253,259–261]. This is due to the equal attraction and repulsion intermolecular forces between two monomers within the polymer chain in which the forces cancel out each other resembling an ideal-type solution. At θ temperature the polymer coil is in an unperturbed condition. Above the theta temperature, expansion of the polymer coil takes place, because of interactions with solvent, and below θ, the polymer segments attract one another, coils tend to collapse, and phase separation occurs [253]. The lattice model often can describe the main characteristics of liquid mixtures containing non-polar molecules differing in size and shape. In particular change of volume upon mixing are beyond the scope of such theory so even for mixtures of n-alkanes, the excess thermodynamic properties cannot described satisfactorily by lattice theory. The major deficiency of the lattice theory is its inability to account for the additional properties of the pure components beyond those that reflect molecular size and potential energy.

3.2.1 Entropy of Mixing of Polymer Blends

The phase stability of a binary polymer mixture system can be well understood based on the Flory-Huggins lattice theory. Thus, the Flory-Huggins free energy Equations (3.4) and

(3.8) are the most widely and successfully used theories in phase equilibrium studies [250]. A polymer chain molecule in itself is a large and complicated structure of repeat units and can assume a high number of configurations by itself. Entropy is defined as the degree of randomness of a system. Thus, a polymer chain molecule has higher entropy than an ordinary small molecule. Consequently, a polymer blend is not affected significantly by mixing, as the increase in entropy due to mixing is minor. The determination of the entropy of mixing for a polymer blend is important for the strictness of the theory and is defined analogous to simple liquids.

3.2.2 Enthalpy of Mixing of Polymer Blends

According to Flory's approach [259], the enthalpy of mixing (ΔH_M) for a polymer blend consisting of two monomers can be calculated by taking the difference between the enthalpy of the mixture ($H_{1,2}$) and the enthalpy of the pure components ($H_{1,1}$ and $H_{2,2}$) to yield the relation:

$$\Delta H_M = H_{1,2} - (H_{1,1} + H_{2,2}) \tag{3.10}$$

$H_{1,1}$, $H_{2,2}$, and $H_{1,2}$ are defined using an interaction energy that exists between every two segments. Hence, the total enthalpy of mixing for a polymer blend would be derived as Equation (3.7). For the case of a polymer blend, a variety of effects would have to be taken into account, such as incomplete filling of the lattice sites, chain connectivity, branching and more. It is for this reason that the Flory-Huggins interaction parameter is not generally

calculated by this expression. An empirical relationship is used to define the parameter that has a reciprocal dependence on absolute temperature as described by the theory and whose constants can be derived and fitted to the experimental phase diagrams to account for the deviations in both the entropy and enthalpy of mixing in real polymer blends [253,261,262]:

$$\chi = \alpha + \frac{\beta}{T} \tag{3.11}$$

where α and β constants are determined experimentally and represent the entropic and enthalpic contribution, respectively [262,278]. The entropic contribution accounts for the segment-segment interactions between the polymers within the mixture. The enthalpic term accounts for the change in energy upon mixing of the polymers as a result of the interactions between segments. The χ parameter measures the solubility of polymer blends. Due to the small entropy of mixing, miscibility can only be achieved if χ is very small or negative [262–271,275–277]. This explains why most polymer blends are immiscible or partially miscible [262,277]. Many experimental and numerical works [263–272,277,279–281] have reported various values of χ for different nonionic polymers ranging from –7.37 [281] to 7.5 [272]. Larger values of χ have been found in ionomers, where single ionic units cause phase separation within super strong segregation regime [272]. The positive and larger values of χ are indication of repulsion forces between the polymers segments [275,276]. The Flory-Huggins interaction parameter of polymer blends would be positive in the lack of a specific interaction, resulting in a blend being immiscible [278].

3.3 Determination of Phase Diagram

The free energy density of mixing, $f(c)$, can be represented as a sum of the configurational entropy and enthalpy of mixing by the Flory-Huggins treatment [250]. The Gibbs free energy of mixing, ΔG_M, is the initial point of the model, given by Equation (3.1). The incompressibility assumption, $c_1 + c_2 = 1$, leads to the reduction of the free energy ΔG_M in a single independent thermodynamic variable $c_1 = c$ and $c_2 = 1 - c$. Gibbs derived an essential condition for the stability of a fluid phase that the chemical potential of a component must rise with increasing the density of that component.

In the situation of a two-component system this yields the relation, $[\partial^2 \Delta G_M / \partial c^2] > 0$. If this condition is not satisfied, then the mixture becomes unstable with respect to any infinitely small composition fluctuations. Also, the total free energy of mixing should be negative for the process to be thermodynamically favorable, i.e. $\Delta G_M < 0$. According to a basic thermodynamics principle, materials always progress toward a minimum free energy state in order to reach equilibrium [282]. This concept is expressed mathematically utilizing the Gibbs free energy of isotropic mixing. Consistent with the F-H theory, entropy of mixing is given by Equation (3.8) and enthalpy of mixing can be expressed as Equation (3.4). Equation (3.5) introduces the temperature dependence into the F-H equation, thus providing a direct temperature-concentration relationship. where υ is the volume of a cell or segment. Depending on phase equilibrium condition that each component's chemical potential is unchanged within all phases at a specified temperature and pressure, the two binodal points are measured through solving a pair of nonlinear algebraic equations [250]. The chemical

potentials of each components, μ_1 and μ_2 are obtained by taking the first order partial derivative of ΔG_M with respect to N_1 and N_2 [283]:

$$\Delta\mu_1 = k_B T\left[\ln c + \left(1-\frac{N_1}{N_2}\right)(1-c) + \chi N_1 (1-c)^2\right] \tag{3.12}$$

$$\Delta\mu_2 = k_B T\left[\ln(1-c) + \left(1-\frac{N_2}{N_1}\right)c + \chi N_2 c^2\right] \tag{3.13}$$

The conditions for equilibrium between two phases in polymer blends are expressed by specifying equality of the chemical potentials in the two phases:

$$\mu_p\left(c^\alpha\right) = \mu_p\left(c^\beta\right) \tag{3.14}$$

$$\mu_s\left(c^\alpha\right) = \mu_s\left(c^\beta\right) \tag{3.15}$$

where the superscripts α and β designate two equilibrium phases. The binodal points at a given temperature can be determined by solving Equations (3.14) and (3.15) simultaneously. Under the same equilibrium condition, the two spinodal points at the same temperature can also be obtained by solving the second order partial derivative of the free energy of mixing with respect to concentration (Figure 3.3):

$$\left[\frac{\partial^2 \Delta G_M}{\partial c^2}\right] = \frac{1}{N_1 c} - \frac{1}{N_2(1-c)} - 2\chi \tag{3.16}$$

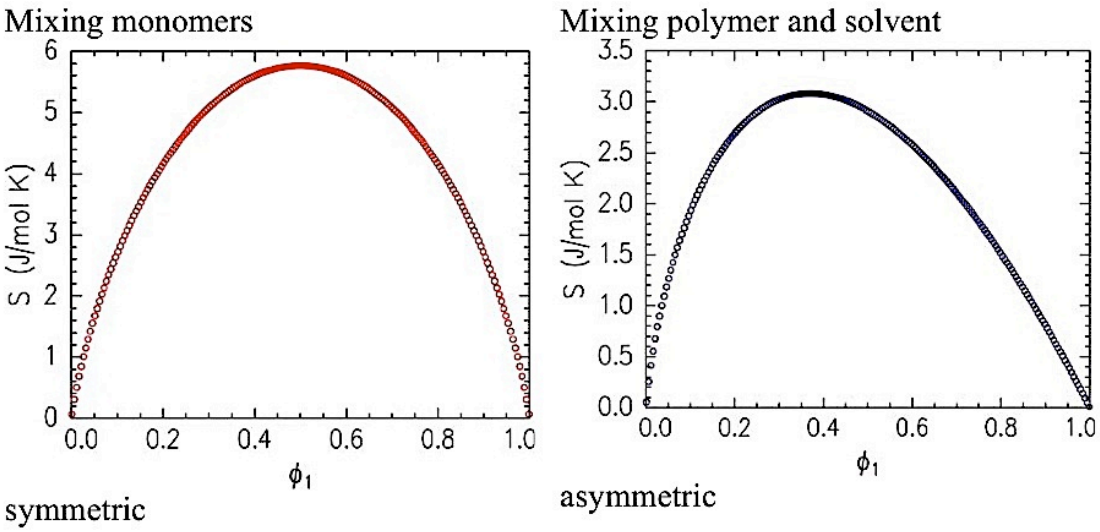

Figure 3.3: Phase diagram of entropy of mixing versus polymer composition for a polymer blend (left) and a polymer solution (right). Solid curves are computed using the Flory-Huggins mixing theory [284].

Figure 3.1 schematically illustrates a free energy curve, its derivative and a hypothetical phase diagram demonstrating the thermodynamic conditions for polymer mixtures. The regime enclosed by the spinodal curve is called the unstable phase, which originates from spinodal decomposition (SD). Metastable phase due to nucleation and growth (NG) belongs to the regime between the spinodal curve and the binodal curve. The critical point can be obtained from the condition for the criticality. By solving Equation (3.3), the critical concentration c_c and the critical interaction parameter χ_c can be determined.

3.4 Reptation Theory and Self-Diffusion Coefficient

In polymer blends with big number of monomers in their chain, the chains entangle to each other and decrease the freedom of the polymer chain to move. The only motion that

exists is due to sliding or a creeping effect along the contours of the polymer length, this worm like movement called by de Gennes as reptation motion and it is shown in Figure 3.4 [285].

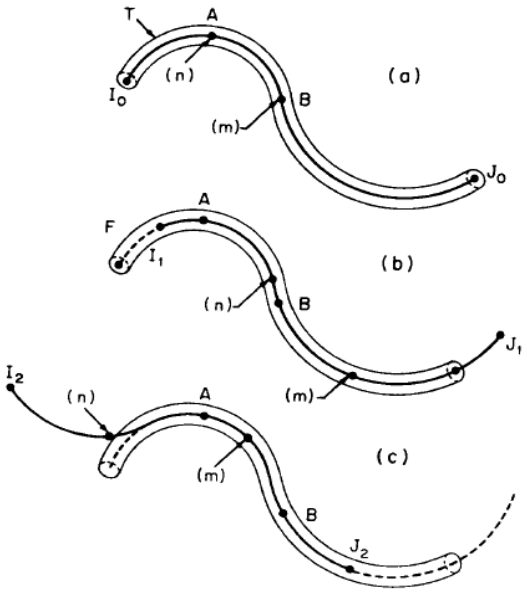

Figure 3.4: Movement of a single polymer chain due to its reputation motion in an entangled blend [285].

Diffusion of a single chain polymer in the blend could be expressed as:

$$D_{reptation} = \frac{k_B T a^2}{3N^2 \xi b^2} \tag{3.17}$$

where a is the step length of primitive chain that represents the diameter of confining tube of polymer chain where the reptation occurs. b is the effective bond length between two monomers within the polymer chain. Relation between a and b in Equation 3.17 is: $a^2 = \frac{4N_e b^2}{5}$ where N_e is the number of monomers between two entaglemnet points of the polymer chain. Therefore, final expression for diffusion of each component is:

$$D_i = \frac{4k_BT}{15\xi_i}\left(\frac{N_{e,i}}{N_i^2}\right) \tag{3.18}$$

Reptation behavior of polymer mixture occurs when $N > N_c$ where N_c is the minimum number of monomers required for the entanglement of the polymer chains in the blend. N_c should be define experimentally for each polymer but it is approximately 300 monomer units [286,287].

3.5 Spinodal Decomposition Theory

It is of great importance to understand the dynamic aspects of the phase separation as well as the thermodynamic features. Hence, in this section, the basic theories on the phase separation kinetics will be briefly reviewed. Starting from the stable region, the polymer blend can be quenched to the metastable region or unstable region. Depending on the location where the system is brought to, the system will undergo phase separation via two different mechanisms [148]: (Figure 2.6-route1) nucleation and growth, or (Figure 2.6-routes 2, 3 and 4) spinodal decomposition. Furthermore, SD-type phase separation is grouped into bi-continuous (interconnected) and droplet SD which was already discussed in Chapter 2.

When a polymer blend is quenched critically (passing through critical point of its phase diagram) into the unstable region (Figure 2.6-route 3) the mechanism of phase separation is proceeded by spinodal decomposition and the resulting morphology would be interconnected or bicontinuous structure (Figure 2.7-c). Figures 2.7 b and d (a) schematically illustrate the growth of the concentration fluctuation of one component during phase separation according

to SD (NG). In the early stages of SD (Figure 3.5), periodic concentration fluctuations with wavelength λ are built up throughout the sample space and amplitude of concentration fluctuation increases with time, while λ remains essentially constant. The wavelength is influenced by the thermodynamic conditions of the mixture characterized by the quench depth while the amplitude of the fluctuation is determined by the kinetics and the time of phase separation. Spinodal decomposition refers to the phase separation, which takes place under the condition that the energy barrier is negligible and the compositional fluctuation is even small. It is a kinetic process of generating a spontaneous and continuous phase within the unstable region.

The time evolution of domain structure in polymer blends through spinodal decomposition will be categorized into the subsequent main steps: (i) early stage, (ii) intermediate stage, and (iii) late stage [150,180] as illustrated in Figures 3.5 (same as Figure 2.2). In the first SD stage, the fluctuations development is weakly nonlinear. This growth can be well estimated by the linearized Cahn's theory's predictions [288] and may define the orientation of sinusoidal concentartion variations of a constant wavelength with random amplitude, positioning and phase. In this stage of SD, the concentration fluctuations are small at t_i and as time increases to t_1, the amplitude of the concentration increases but the wavelength remains constant. This region is usually the most difficult to visualize since it happens at such a fast rate. For this reason, the C-H equation can be approximated by a linear function [289,290]. This has proven to be a very useful estimation for the initial stage of SD.

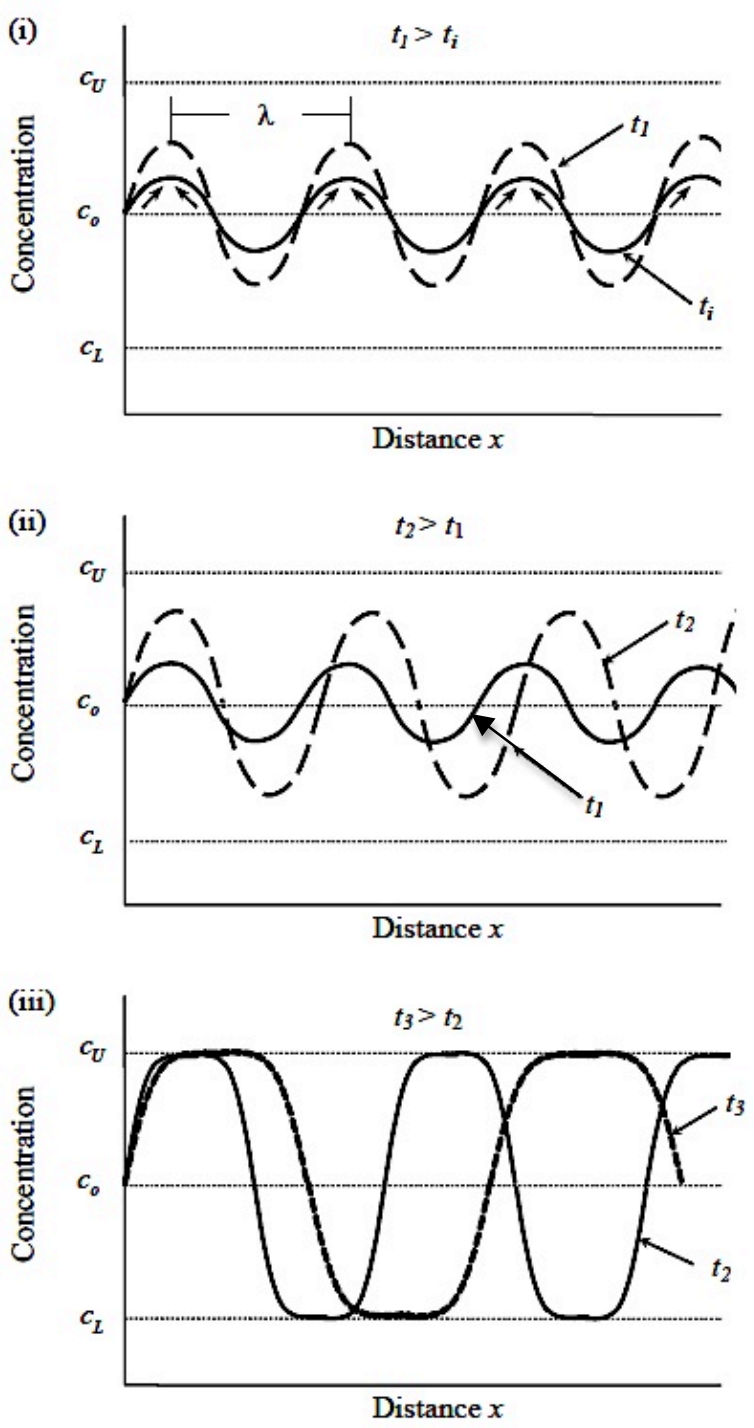

Figure 3.5: The three stages of SD plotted as concentration vs. distance, (i) early stage, (ii) intermediate stage and (iii) late stage. c_0 is the average concentration of the polymer [164].

In the early stage, droplet formation occurs (Figure 3.5 i). The reduction of one polymer from another in polymer blends, migrating towards the droplet, forms the dispersion of droplets within a continuous phase of the polymer. Figure 3.5 (i) also shows the depletion and migration of one polymer with arrows moving from low concentration to high concentration known as uphill diffusion [179]. In the intermediate stage (Figure 3.5 ii) the concentration fluctuations are still increasing with time from t_1 to t_2 showing an increase in amplitude. However, there is an increase in the wavelength of the concentration fluctuation spatially. This effect requires the use of the non-linear C-H equation [289,291,292]. Finally, in the late stage of SD (Figure 3.5 iii), the concentration fluctuations increase until they reach their respective equilibrium concentrations with constant amplitude, labeled c_u (higher concentration) and c_l (lower concentration). The wavelength increases with time as the droplets join together to form larger droplets.

3.6 Cahn-Hilliard Theory

Fick's law states that the flux of a diffusing species is proportional to its concentration gradient:

$$J_A = -D\nabla c_A \tag{3.19}$$

where c_A the concentration (volume fraction) of component A and D is its diffusion coefficient. Fickian diffusion does not support a multiphase system because even at equilibrium there are concentration differences between the phases with no net diffusion

[293]. Thus, we can change Equation 3.19 based on chemical potential rather than concentration:

$$J_A = -Dc_A \nabla \mu_A \tag{3.20}$$

where μ_A is the chemical potential of component A. Nonlinear diffusion in polymer/solvent and polymer/polymer systems is significant since the equal molar counter-diffusion assumption can be totally wrong [293]. While Becker and Doring [294] in 1935 and Lifshitz and Slyozov [295] in 1961 worked on nucleation theories, the primary effort to discuss spinodal decomposition was in 1958 through the phenomenological Cahn-Hilliard equation [296]. Cahn and Hilliard were the first to discuss the spontaneous phase separation of mixtures via spinodal decomposition in binary alloys of metals. This particular process of phase separation does not require activation energy unlike NG mechanism, but proceeds spontaneously in the presence of minimal concentration fluctuations or thermal noise. As already mentioned, SD can be classified by three stages according to time: early, intermediate, and late. The early stage can be characterized by a linearized diffusion equation, which has been solved analytically. There is, however, no analytical mixture to the intermediate and late stages of SD. The diffusion driving force was presumed by Cahn and Hilliard to be a gradient in $\mu_A - \mu_B$ rather than just μ_A [293]. They similarly applied the mobility, *M*, rather than the molecular diffusion coefficient, *D*, and omitted the pre-gradient mole fraction in the flux equation so continuity equation becomes as:

$$J = -M\nabla\left(\mu_2 - \mu_1\right) = -M\nabla\frac{\delta F}{\delta c} \tag{3.21}$$

These assumptions are frequently used in the physics literature, however, it is mostly accepted today that M has to be concentration-dependent even for an ideal solution. On the other hand, the diffusion coefficient can be constant, at least for binary diffusion. Total free energy of mixing can be given by following expression:

$$F = \int \left[f(c) + \kappa \nabla c^2 \right] dV \tag{3.22}$$

Cahn-Hilliard equation is formed on the hypothesis that the total free energy of an inhomogeneous, binary mixture is sum of two features [160,278]: the first term $f(c)$ in Equation (3.22) represents the homogeneous free energy, and the second term $\kappa \nabla c^2$ considers any increases in free energy arising from concentration gradients [160,288]. Taylor series expansion of a free energy density is responsible for these two terms [160,290]. In order to describe phase separation in polymer blends, the model equation can be derived from a continuum model. Considering only diffusional flux J, continuity equation can be written as:

$$\frac{\partial c}{\partial t} = -\nabla \cdot J \tag{3.23}$$

If pure diffusion is only considered, the net flux J, might be expressed as the product of concentration dependent mobility M and the gradient of the chemical potential μ of each component:

$$J = -M \nabla (\mu_2 - \mu_1) \tag{3.24}$$

Here M is the mobility, which is treated as a constant in the linear theory. The chemical potential is the derivative of the free energy function:

$$\mu_2 - \mu_1 = \frac{\delta F}{\delta c} = \frac{\partial f(c)}{\partial c} - 2\kappa\nabla^2 c \tag{3.25}$$

Combining Equations (3.24), (3.25) and (3.26) results in the nonlinear Cahn-Hilliard equation:

$$\frac{\partial c}{\partial t} = -\nabla \cdot \left[M\nabla\left(\frac{\partial f(c)}{\partial c} - 2\kappa\nabla^2 c \right) \right] \tag{3.26}$$

where c is the volume fraction. In this thesis, c is defined as the component A volume fraction in the binary mixture. κ is a positive gradient energy parameter related to the interfacial constant, and $f(c)$ is the free energy of a homogeneous mixture. This non-linear Cahn-Hilliard equation is valid for all stages of phase separation. Cahn linearized this non-linear equation about the average concentration c_0. For very short times following the quench, one would expect this linearization to be valid since the concentration fluctuations should be small. Therefore, the linear C-H equation would be:

$$\frac{\partial c}{\partial t} = M\left(\frac{\partial^2 f(c)}{\partial c^2}\Big|_{c_0} \nabla^2 c - 2\kappa\nabla^4 c \right) \tag{3.27}$$

M and κ are assumed constant. The diffusion equation with a spatially changeable diffusion constant would be:

$$D = M\left(\frac{\partial^2 f(c)}{\partial c^2}\right) \tag{3.28}$$

Equation (3.28) is known as a collective diffusion coefficient [288,297]. This diffusion constant is negative inside the spinodal region. For this reason, Cahn termed the initial stage of spinodal decomposition uphill diffusion. Taking the Fourier transform of Equation (3.27) [291]:

$$c(\mathbf{r},t) - c_{\circ} = \sum_{k} A(\mathbf{k},t)e^{i\mathbf{k}.\mathbf{r}} \tag{3.29}$$

where $A(\mathbf{k},t)$, the magnitude of the Fourier transform of the concentration fluctuations in the system is:

$$A(\mathbf{k},t)e^{i\mathbf{k}.\mathbf{r}} = A(\mathbf{k},0)e^{R(k)t} \tag{3.30}$$

and the growth rate (amplification factor), $R(k)$ is given as:

$$R(k) = -Mk^2\left(\frac{\partial^2 f(c)}{\partial c^2}\Big|_{c_0} + 2\kappa k^2\right) \tag{3.31}$$

where $k_i = \dfrac{2\pi}{\lambda_i}$ and λ_i is the wavelength for fluctuation *i*. For concentration fluctuations to occur $R(k)$ has to be positive and $\left|\dfrac{\partial^2 f(c)}{\partial c^2}\Big|_{c_0}\right| > \left|2\kappa k^2\right|$. Thus inside the classical spinodal region where $(\partial^2 f / \partial c^2) < 0$, $R(k)$ is positive for $k < k_c$ in the unstable region. $R(k)$ changes sign at the critical wave number:

$$k_c = \left[\left(-\frac{1}{2\kappa}\right)\left(\frac{\partial^2 f(c)}{\partial c^2}\Big|_{c_0}\right)\right]^{1/2} \tag{3.32}$$

and has a sharp maximum at:

$$k_m = \frac{1}{\sqrt{2}} k_c \tag{3.33}$$

In Equation (3.32) the exponent contains the amplification factor, therefore, the concentration fluctuations that grows the fastest is k_m. The above derivation shows that the linear C-H equation predicts phase separation as a superposition of periodic concentration fluctuations of fixed wavelengths with random amplitude, orientation and phase [291]. This model has been used in the prediction of morphology for TIPS and polymerization induced phase separation (PIPS) [298]. In scattering experiments, however, $c(r,t)$ is not measured but instead, the structure factor which is proportional to scattering intensity is measured by [301]:

$$I(k,t) = I(k,0)e^{2R(k)t} \tag{3.34}$$

where $I(k,0)$ is the initial intensity. Thus according to the linear theory the initial stages of SD should produce an exponential growth in intensity for $k < k_c$, with a peak at time dependent wavenumber k_m. Cahn [288] interpreted this k_m as the wavenumber, which characterizes the fine uniformly dispersed precipitate seen in SD studies. Quantitative information can be obtained from the time-resolved light scattering intensity profile $I(q,t)$ where q is the scattering wave number. The numerical equivalence of this profile is the

structure factor $S(k,t)$, i.e. $I(q,t) \propto S(k,t) = \left\| A(k,t)^2 \right\|$ for $q = k$ [54,56,57,59,73]. Consequently, the light intensity $I(q,t)$ contains information on the concentration fluctuation time and length scales.

Figure 3.6 shows the development of scattering wave number first at an approximate value of 5 μm^{-1}, which seems static for a short time denoting early stage of phase separation through SD, and then rapidly moves to lower scattering wave number values in the intermediate to the late stage SD. The change in the intensity as time changes indicates the changes in the coarsening of the phase separating structure for the intermediate and late stages of SD. The relation is shown in Equations (3.35) and (3.36) for $q = k$. Equation 3.35 is the scattering intensity, which is now defined as [288,335]:

$$I(q,t) = I(q,0)e^{2R(q)t} \tag{3.35}$$

$I(q,t)$ is the scattering intensity, q is the scattering wave number, R an amplification factor and t is time. The scattering wave number q, is a function of the wavelength λ, and the scattering angle θ, expressed as [335]:

$$q = \left(\frac{4\pi}{\lambda}\right)\sin\left(\frac{\theta}{2}\right) \tag{3.36}$$

The wavelength λ is expressed as [291]:

$$\lambda = 2\sqrt{2}\pi\left[\left(-\frac{1}{2\kappa}\right)\left(\frac{\partial^2 f(c)}{\partial c^2}\Big|_{c_0}\right)\right]^{1/2} \tag{3.37}$$

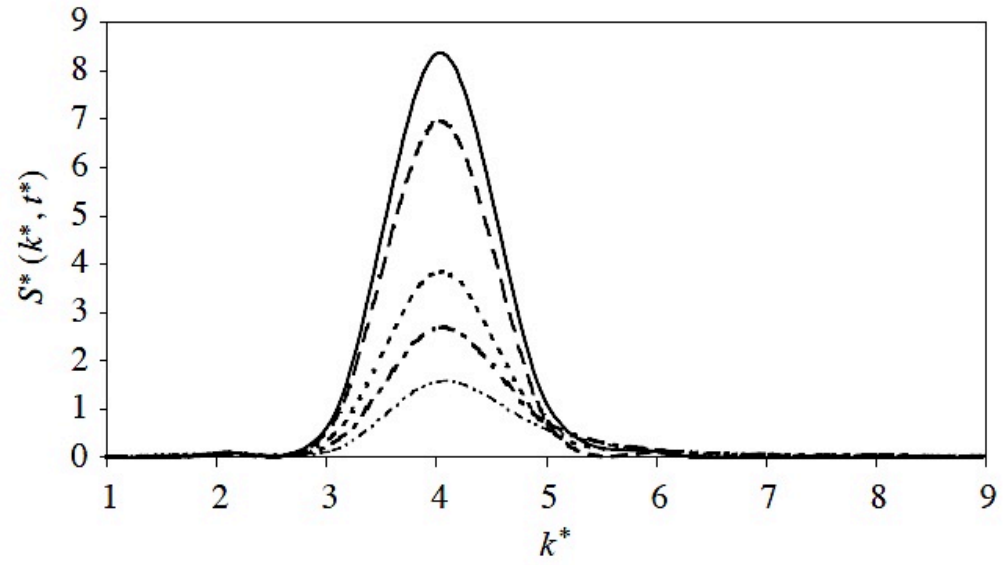

Figure 3.6: Typical early to the intermediate stage evolution of the dimensionless structure factor for a single critical quench into the unstable spinodal region of the phase diagram of a polymer blend at different dimensionless times [145].

The morphological features study, such as the phase structure type and droplet size distribution, is the most important aspect of the TIPS process. Two various kinds of morphology are formed based on the primary average concentration: the interconnected structure and the droplet-type morphology [250,278]. Therefore, Equation (3.27) is a key methodology to predict the morphological features of polymer blends in critical (interconnected structure) and off critical (droplet structure) TIPS.

3.7 Concentration Dependent Mobility and Mutual Diffusion

The kinetics of phase separation by SD can best be described by the Cahn-Hillard equation (C-H) [289,290]. The C-H equation describes the fluctuations in concentration in

terms of wavelengths for the three stages of SD. The early stage of SD can be described by the linear C-H equation. The intermediate and later stages require the non-linear C-H equation. The difficulty in modeling polymer blends is determining the constants in C-H equation such as mobility, F-H interaction parameter and the constant related to the interfacial constant. However, there have been several techniques used to determine these parameters for polymer blends [262–271,275–281]. The mobility in the C-H equation is assumed constant but has been shown to be dependent on concentration and temperature [303,305]. Concentration dependent mobility can be expressed by mutual diffusion coefficient that measures the rate of dispersion of a component in the mixture as:

$$M(c) = \frac{D(c)}{\frac{\partial^2 f(c)}{\partial c^2}} \tag{3.38}$$

where D is the mutual diffusion coefficient. The mobility, M *is* dependent on both the polymer molecular chain length and local concentration. Many numerical studies, however, have been performed assuming M and κ (interfacial parameter) constant with an attempt to simplify the problems [199,306–310] and only a few studies have been performed with a molecular weight and concentration dependent mobility [301,311–315]. Similar to M, that is very sensitive to concentration fluctuations [316], the interfacial parameter κ is concentration dependent (explained in 3.8). The molecular chain lengths and local concentration dependence of the mobility can be captured from its relation with the self-diffusion coefficient by Equation (3.38). Two theories that describe the mobility in polymer mixtures are: the slow mode theory and the fast mode theory [134,317,318]. According to the

slow mode theory, the slower component limits mutual diffusion of the polymer blend while fast mode theory predicts that the faster one limits the diffusion rate.

The concentration dependent mobility for a polymer mixture was introduced by de Gennes [285,319]. The mutual diffusion coefficient Λ, for a binary system, is generally given by:

$$\Lambda = \frac{\Lambda_1 \Lambda_2}{\Lambda_1 + \Lambda_2} \tag{3.39}$$

where $\Lambda = \frac{D_i N_i}{c}$ is Onsagar coefficient of the individual component describing the diffusion in a polymer system and has following relation with mobility:

$$\Lambda_i = k_B T M_i \tag{3.40}$$

where k_B is the Boltzmann's constant and T is an absolute temperature. Replacing Equation (3.40) in (3.39), considering a binary mixture would result in [318]:

$$\frac{1}{M} = \frac{1}{M_1} + \frac{1}{M_2} \tag{3.41}$$

where M is the total mobility and M_1 and M_2 are the individual mobility of two components. Using Equation (3.41) and Flory free energy gives the following expressions:

$$M(c) = \frac{\left[N_1 D_1 c\right]\left[N_2 D_2 (1-c)\right]}{\frac{k_B T}{\upsilon}\left[N_1 D_1 c + N_2 D_2 (1-c)\right]} \qquad \text{Slow mode} \tag{3.42}$$

$$M(c) = \frac{N_1 D_1 c(1-c)\upsilon + N_2 D_2 c\upsilon(1-c)}{k_B T} \qquad \text{Fast mode} \qquad (3.43)$$

Polymer blends could be explained better with slow mode theory [319–321]. The total mobility M can be also expressed as:

$$M = \frac{4\upsilon N_e}{15\xi}\left[c(1-c)\right] \qquad (3.44)$$

where c is the average concentration of the mixture, υ is the volume of a cell or segment and ξ is monomer friction coefficient. The self-diffusion coefficient equation of Rouse model is also defined as [322]:

$$D_i = \frac{k_B T}{N_i \xi_i} \qquad (3.45)$$

where N_i is the degree of polymerization for each component.

3.8 Concentration-Dependent Gradient Energy

The energy gradient in non-linear C-H (Equation 3.26) is for concentration fluctuation effect on free energy and it is resulted from formation of interfaces between the two polymers. De Gennes [285] proposed κ has enthalpic and entropic parts; a term about the efficient series of the interactions $a^2\chi$ and a term whose basis is the configurational entropy of the Gaussian coils:

$$\kappa(c) = \kappa_{entropic} + \kappa_{enthalpic} = \frac{a^2}{36c(1-c)} + a^2\chi \tag{3.46}$$

The entropic effect is due to connectivity of monomer unites so is only for polymer mixtures and takes into account energy changes due to spatial variation in the concentration while phase separation happens. But in polymer blends $\kappa_{entropic} >> \kappa_{enthalpic}$ and second term could be neglected [197]:

$$\kappa(c) \cong \frac{a^2}{36c(1-c)} \tag{3.47}$$

This term could be used in C-H equation to predict phase separation of polymer blends more accurately.

3.9 Noise Term

Cook [323] made an important contribution to the theoretical development of the linear theory by observing that it is necessary to add a noise term η, to C-H Equation (3.26) in order to have a correct statistical description of the dynamics. Cook's observation was that, in addition to a flux produced by the gradient of a local chemical potential, there is additional flux arising from random thermal motion of the atoms:

$$\frac{\partial c}{\partial t} = -\nabla \cdot J + \eta \tag{3.48}$$

where η is the random force term taken to be a Gaussian distribution. Its mean value is zero and the correlation satisfies the fluctuation-dissipation relation [324], i.e.: $\langle \eta \rangle = 0$. Cook's noise term, however, is disregarded in the present study due to its little impact on the domain growth in critical and off-critical quench conditions [325]. It is often omitted for numerical studies, which cover the areas far from critical point. Novick [296] in her numerical work verified the behavior of the nonlinear Cahn-Hilliard equation for asymmetric systems within the unstable spinodal region. She managed to obtain the same features of SD and NG which are accessible through the nonlinear Cahn-Hilliard equation without using any noise term and demonstrated that the Cahn-Hilliard theory equation, regardless of all the information included in a full noise driven model, is considerably richer than what would be predicted from linear theory only.

Oono and Puri [326] computationally modeled space-time phase ordering dynamics of unstable SD region. The two dimensional lattice of 100 × 100 was used for the simulation. There, they supported the idea that the effect of noise is unimportant for the late stages of phase separation kinetics. In another simulation performed by Oono and Puri [327], "the long-time behavior of two-dimensional systems undergoing spinodal decomposition was studied numerically with the aid of a cell-dynamical approach both without and with noise." [327] In both cases, the representative length scale of the pattern behaved the same where the crossover time increased with an increase in amplitude of the noise. They demonstrated that the effect of noise appears to be unimportant. They also performed simulations in which noise had a Gaussian distribution and this made no difference to their results. Furthermore, they also studied the evolution patterns in the case where they started off with zero (non-zero) amplitude of noise and switched on (off) the noise after a certain number of iterations.

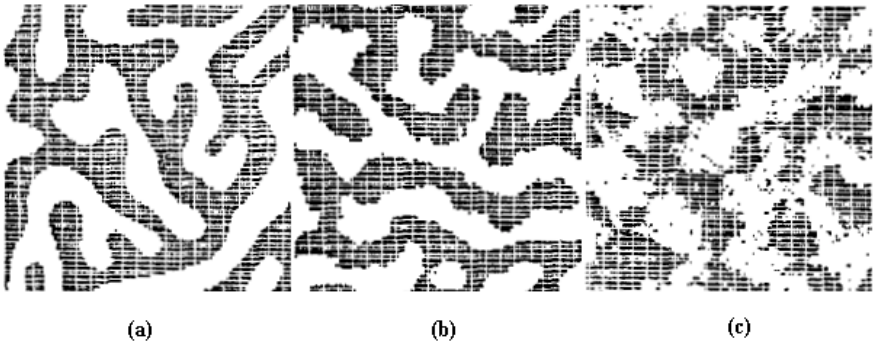

Figure 3.7: Typical pattern for the (a) noiseless (b) noisy and (c) strongly noisy cases [327].

The patterns rapidly (within about 10 iterations) went to the noisy (noiseless) forms. This indicated that there is no cumulative effect of noise. In the usual interpretation of the deterministic C-H-C equation they even simply discarded the noise while retaining the usual kinetic coefficients. Figure 3.7 shows the patterns obtained from the same initial conditions for the noiseless and noisy cases. "For the noiseless case (a) the boundary walls are smooth and regular. In the noisy (b) case the pattern size at comparable times is of the same order as in the noiseless case, but the boundary walls are ragged. In case (c) a typical pattern for the strongly noisy case with the same initial conditions as before" [327] is shown.

"This pattern is more ragged than the pattern for the case (b) and is similar to previously published patterns [326] from Monte Carlo simulations" [327]. They, as well, plotted the scaled scattering function $S(k,t)(\langle k\rangle(t))^2$ as a function of $k/\langle k\rangle(t)$ for different times. In the scaling regime a universal curve was expected. Figure 3.8 shows data from different times "for the noiseless case (denoted by circles). They can be seen to lie on a smooth master curve. The points marked by tiny crosses in Figure 3.8 correspond to the noisy case" [327].

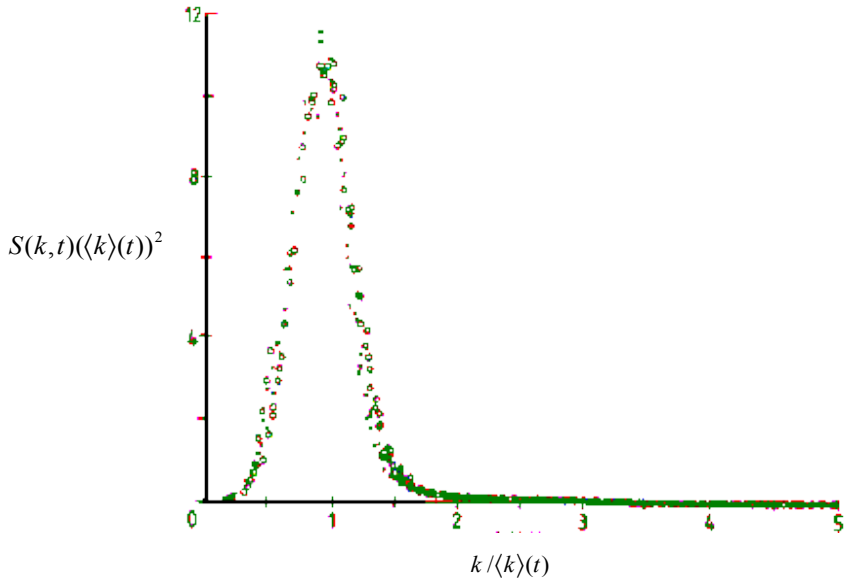

Figure 3.8: Scaled scattering function $S(k,t)(\langle k\rangle(t))^2$ as a function of $k/\langle k\rangle(t)$ for the noiseless and noisy cases. The circles (tiny crosses) are data from the noiseless (noisy) case at different times [327].

"Both the noiseless and noisy cases have the same master curve for moderate values of $k/\langle k\rangle(t)$. However, the tails of the curves, which correspond to relatively (compared to pattern size) short wavelength fluctuations, are quite different though this difference is not evident on the scale of the figure" [327]. For the noiseless case, the tail of the curve drops off faster than x^{-3}, where $x = k/\langle k\rangle(t)$. The same model as Oono and Puris' [326,327], without noise, was studied extensively by Chakrabarti and Gunton [328] later.

In a study performed by Yeung [329] over the dynamics governed by the time-dependent Ginzburg-Landau and Cahn-Hilliard equation, the results were consistent with numerical simulations, which confirmed that the scaling function is independent of the

magnitude of the noise. Brown and Chakrabarti [330,331] demonstrated in contrary to the Ginzberg-Landau model that suggests the noise effects are irrelevant for the late time growth laws and scaling behavior in small molecule systems when noise effects are included, the thermally induced fluctuations in the local concentration are important in late time domain growth for the polymer blends but however, both off critical and critical mixtures behave similarly for deep quenches (which is a benefit to our assumption of ignoring the noise term in the simulation).

Zhu *et al*. [332] implemented semi-implicit Fourier spectral method is: "to solve the Cahn-Hilliard equation with a variable mobility. The method is more efficient than the conventional forward Euler finite-difference method, thus allowing them to simulate large systems for longer times" [332]. They studied "the coarsening kinetics of interconnected two-phase mixtures using a Cahn-Hilliard equation with its mobility depending on local compositions" [332]. To simplify the problem, they did not include the noise term in their study because it usually took a lot of CPU time for generating the Gaussian noise. "The noise term has no significant effect on the time to get scaling results or the stability of the numerical algorithm, they believed. For bulk-diffusion-controlled dynamics, it is usually accepted that the noise term does not affect some important features of the late stages of evolution such as the growth law for the characteristic domain size and the scaling functions for spinodal decomposition" [332].

Clarke [333] independently investigated and simulated a process to gain controlled morphologies in polymer blends by allowing particles of one polymer to dissolve in a different polymer matrix. The blend was quenched into the two-phase region, before the

dissolution was completed, to make phase separation happen. The noise term in his simulation has also been neglected. The addition of the noise term significantly increased the computation time but did not impact the overall behavior.

Fialkowski and Holyst [334] analyzed a two-step process of phase separation in binary mixtures. The system was first brought into the thermodynamically instable region where phase separation occurred via SD process. Next, they heated up the system to make a temperature jump back to the curing temperature above the spinodal. There, they assumed a fully deterministic dynamic without the thermal noise in the system.

In this thesis however, we have ignored the noise term for simplicity of the simulated model and decreasing the computational time based on the experimental and numerical studies that have been so far performed on its effects.

Chapter 4

4. Short Range Surface Potential

This section explains the model development for the TIPS method of surface directed phase separation of a binary polymer blend, involving the surface potential field and thermal diffusion phenomena under the externally imposed spatial temperature gradient. This model is developed based on nonlinear Cahn-Hilliard theory and Flory-Huggins-de Gennes free energy, which explains well TIPS phase separation method for binary blends with a surface attraction on *one side* of the domain. Then, the results are presented and discussed in detail in the form of morphology formation and surface enrichment growth rate. Effects of diffusion coefficient, quench depth, temperature gradient and surface potential are as well investigated over surface enrichment.

4.1 Model Development

The nonlinear Cahn-Hilliard theory incorporating the Flory-Huggins-de Gennes free energy theory is used to study the thermal-induced phase separation (TIPS) phenomenon in binary polymer blends with competing surface and temperature gradient effects. Phase separation could be expressed by the following equation:

$$\frac{\partial c}{\partial t} = -\nabla \cdot J \tag{4.1}$$

where c is the concentration of solvent in terms of its volume fraction, and J is the mass flux caused by combined phenomena of non-Fickian diffusion and thermal diffusion under an externally imposed spatial temperature gradient. Mass flux J can be expressed with the following expression [288]:

$$J = \left[-M(c)\nabla(\mu_2 - \mu_1)\right] - \nabla \cdot \left[D_T c(1-c)\nabla T\right] \tag{4.2}$$

where, M is the concentration dependent mobility, and chemical potential for each component is μ_1 and μ_2 of the component; D_T is the thermal diffusion coefficient. Chan *et al.* [336] showed that effect of noise term on morphology of polymer mixture via the spinodal decomposition mechanism and under linear temperature gradient is negligible thus the thermal flux term is not considered in the model:

$$J = -M(c)\nabla(\mu_2 - \mu_1) \tag{4.3}$$

Change in the chemical potential is equal to the change of free energy for each component in the system:

$$(\mu_2 - \mu_1) = \frac{\delta F}{\delta c} \tag{4.4}$$

By substituting Equations 4.3 and 4.4 into Equation 4.1 and discarding noise term:

$$\frac{\partial c}{\partial t} = -\nabla \cdot \left[M\nabla\left(\frac{\delta F}{\delta c}\right)\right] \tag{4.5}$$

Free energy that considers all aspects of UCST-type polymer blends including chain entanglement is based on the Flory-Huggins-de Gennes theory, which is based on lattice model, and is expressed as:

$$\frac{F}{k_B T} = \frac{c}{N_1}\ln c + \frac{1-c}{N_2}\ln(1-c) + \chi c(1-c) + \kappa(\nabla c)^2 \tag{4.6}$$

where N_1 and N_2 are the degrees of polymerization of the two components and κ is the interfacial energy parameter, k_B , is Boltzmann's constant, T is the temperature, χ is Flory's interaction parameter, and c is the volume fraction of the component. De Gennes [319] proposed that κ is the sum of enthalpic term relating to the effective range of the interactions $\left(a^2\chi\right)$ and entropic parts; a term whose origin is the configurational entropy of the Gaussian coils [197]:

$$\kappa(c) = \kappa_{entropic} + \kappa_{enthalpic} = \frac{a^2}{36c(1-c)} + a^2\chi \tag{4.7}$$

The entropic effect is due to connectivity of monomer units. Hence it is only for polymer mixtures and takes into account energy changes due to spatial variation in the concentration while phase separation happens. In polymer blends: $\kappa_{entropic} >> \kappa_{enthalpic}$ and Equation (4.7) becomes:

$$\kappa(c) \cong \frac{a^2}{36c(1-c)} \tag{4.8}$$

Equation (4.8) can be used in Cahn-Hilliard equation to predict phase separation of polymer blends more accurately. Diffusion of a single polymer chain in the blend can be expressed, using the reptation theory:

$$D_{reptation} = \frac{k_B T a^2}{3N^2 \xi b^2} \tag{4.9}$$

where a is the step length of primitive chain that represents the diameter of confining tube of polymer chain where the reptation occurs. b is the effective bond length between two monomers within the polymer chain. N is the number of monomers in the chain, k_B is Boltzmann's constant, ξ is the frictional coefficient per polymer chain and T is the temperature. The reptation theory indicates that D is related to N^{-2}. Since lengths a and b are related by:

$$a^2 = \frac{4N_e b^2}{5} \tag{4.10}$$

The reptation model can be expressed for each component i as:

$$D_i = \frac{4k_B T}{15\xi_i}\left(\frac{N_{e,i}}{N_i^2}\right) \tag{4.11}$$

where N_e is average number of monomers existing between each two entanglement points of the polymer chains. Reptation behavior of polymer mixture occurs when $N > N_c$ where N_c is the minimum number of monomers required for the entanglement of the polymer chains in the blend also known as the critical degree of polymerization and is defined experimentally.

Approximate value of N_c is 300 monomer units [286,287]. The diffusion coefficient could be expressed as:

$$D = M\left(\frac{\partial^2 f(c)}{\partial c^2}\right) \tag{4.12}$$

If mutual diffusion of the binary polymer blend is controlled by the slower moving component, the slow mode theory by de Gennes [285,319] may be used to determine the mobility [318]:

$$\frac{1}{M} = \frac{1}{M_1} + \frac{1}{M_2} \tag{4.13}$$

where M_1 and M_2 are the mobility of polymer 1 and 2, respectively. Combining Equations (4.11) and (4.13) and considering that $N_{e1} = N_{e2} = N_e$ and $\xi_1 = \xi_2 = \xi$ the following expression for the mobility in a binary polymer blend is obtained:

$$M = \frac{4\upsilon N_e c(1-c)}{15\xi\left[N_2 c + N_1(1-c)\right]} \tag{4.14}$$

The linear temperature gradient used in this study is expressed as [138,336]:

$$T(x) = \left(\frac{T_2 - T_1}{x_2 - x_1}\right)(x - x_1) + T_1 \qquad \text{for} \quad x_1 < x_2 \tag{4.15}$$

where T_1 and T_2 are temperatures at x_1 and x_2, respectively. By substituting Equations (4.6), (4.8), (4.14), (4.15) into Equation (4.5) and using the following dimensionless variables:

Dimensionless time: $$t^* = \left(\frac{4\upsilon k_B N_e T_c a^2}{15\xi L^4} \right) t \tag{4.16}$$

Dimensionless diffusion coefficient: $$D^* = \frac{k_B T_c L^2}{\upsilon \left(\frac{k_B T_c}{\upsilon} \right) a^2} \tag{4.17}$$

Dimensionless concentration: $$c^* = c \tag{4.18}$$

Dimensionless temperature: $$T^* = \frac{T}{T_c} \tag{4.19}$$

Dimensionless horizontal length: $$x^* = \frac{x}{L} \tag{4.20}$$

Dimensionless vertical length: $$y^* = \frac{y}{L} \tag{4.21}$$

The following form of dimensionless Flory-Huggins interaction parameter is used in the model:

$$\chi^* = \alpha + \frac{\beta}{T^*} \tag{4.22}$$

where α and β constants are determined experimentally and represent the entropic and enthalpic contribution, respectively. The expected value of the parameter α for a binary polymer blend without any specific intermolecular interactions is between –1 to 1 and parameter β has the order of magnitude of 10^{-1}. An example of low noise binary polymer mixture is perdeuterated polybutadiene (DPB) and protonated ploybutadiene (HPB) blend; an UCST-type system. For this mixture, α and β (after normalization) have values of -5.34×10^{-4} and 8.44×10^{-4}, respectively [317,337]. These values of α and β are fitted to the expected linear dependence on T^{-1} used in the model simulations.

The reason for using only the temperature dependent interaction parameter and exclusion of concentration dependent term in the parameter is due to the fact that for polymer blends, interaction parameter is very weakly dependent on concentration values. For this reason, numerous theoretical [244,262,337,340,342–344] and experimental [338,339,341] works have placed more weight on the temperature dependency of interaction parameter rather than its weakly dependent concentration term. Londono and Wignall [338] doubled the molecular weight of the polystyrene/poly(*p*-methylstyrene) blend component and observed no change in χ parameter. Kumar *et al*. [342], Gujrati [343], and Crist *et al*. [344] tracked the experimental treatment of scattering data and verified their separate results using three different models: Sanchez-Lacombe, the Bethe lattice approach and optimized cluster theory, respectively. It is concluded that the composition dependence of the interaction parameter is not as strong as temperature reliance.

Using Equations 4.6 and 4.14 through 4.22 then substituting them into the dimensionless form of Equation 4.5, the following governing equation for the short-range surface potential will be obtained for concentration change over time $\left(\frac{\partial c^*}{\partial t^*}\right)$:

$$\frac{\partial c^*}{\partial t^*} = D\left[\left\{\left\{\frac{1}{N_1}-\frac{1}{N_2}+\frac{\ln c^*}{N_1}-\frac{\ln\left(1-c^*\right)}{N_2}+\alpha\left(1-2c^*\right)\right\}\left[\frac{\left(N_1-N_2\right)c^*+N_1\left(1-2c^*\right)}{\left(N_2c^*+N_1\left(1-c^*\right)\right)^2}\right]\right.\right.$$

$$\left.\left.-4\alpha\left[\frac{c^*\left(1-c^*\right)}{\left(N_2c^*+N_1\left(1-c^*\right)\right)}\right]\right\}\nabla T^*\nabla c^*\right.$$

$$+\left\{\left[\frac{\left(N_1-N_2\right)c^{*2}+N_1\left(1-2c^*\right)}{\left(N_2c^*+N_1\left(1-c^*\right)\right)^2}\right]\left\{\frac{1}{N_1c^*}+\frac{1}{N_2\left(1-c^*\right)}-2\chi^*\right\}T^*\right.$$

$$\left.+\left[\frac{c^*\left(1-c^*\right)}{\left(N_2c^*+N_1\left(1-c^*\right)\right)}\right]\left\{-\frac{1}{N_1c^{*2}}+\frac{1}{N_2\left(1-c^*\right)^2}\right\}T^*\right\}\left(\nabla c^*\right)^2$$

$$+\left[\frac{c^*\left(1-c^*\right)}{\left(N_2c^*+N_1\left(1-c^*\right)\right)}\right]\left[\frac{1}{N_1c^{*2}}+\frac{1}{N_2\left(1-c^*\right)^2}-2\chi^*\right]T^*\nabla^2c^*\Bigg]$$

$$+\left[\frac{4kN_ea^2}{15\xi}\right]\left[\left\{\left[\left[\frac{\left(N_1-N_2\right)c^{*2}+N_1\left(1-2c^*\right)}{\left(N_2c^*+N_1\left(1-c^*\right)\right)^2}\right]\frac{-1}{18\left(1-c^*\right)c^*}\nabla T^*\right.\right.\right. \tag{4.23}$$

$$\left.\left.\left.+\left[\frac{c^*\left(1-c^*\right)}{\left(N_2c^*+N_1\left(1-c^*\right)\right)}\right]\left(\frac{\left(1-2c^*\right)}{9\left(1-c^*\right)^2c^{*2}}\nabla T^*\right)\right\}\nabla c^*\nabla^2c^*\right.$$

$$+\left\{\left[\frac{\left(N_1-N_2\right)c^{*2}+N_1\left(1-2c^*\right)}{\left(N_2c^*+N_1\left(1-c^*\right)\right)^2}\right]\left(\frac{\left(1-2c^*\right)}{18\left(1-c^*\right)^2c^{*2}}\right)\right.$$

$$\left.-\frac{\left(3c^{*2}-3c^*+1\right)}{9\left(1-c^*\right)^3c^{*3}}\right\}T^*\left(\nabla c^*\right)^2\nabla^2c^*$$

$$+\left\{\left[\frac{c^*\left(1-c^*\right)}{\left(N_2c^*+N_1\left(1-c^*\right)\right)}\right]\left(\frac{\left(1-2c^*\right)}{18\left(1-c^*\right)^2c^{*2}}\right)T^*\right\}\nabla^2c^*\nabla^2c^*$$

$$+\left\{\left[\frac{\left(N_1-N_2\right)c^{*2}+N_1\left(1-2c^*\right)}{\left(N_2c^*+N_1\left(1-c^*\right)\right)^2}\right]\left(\frac{-1}{18\left(1-c^*\right)c^*}\right)\right.$$

$$+\left(\frac{-1}{9\left(1-c^*\right)c^*}\right)\left[\frac{c^*\left(1-c^*\right)}{\left(N_2c^*+N_1\left(1-c^*\right)\right)}\right]\nabla T^*\nabla^3c^*$$

$$\left.-\left[\frac{c^*\left(1-c^*\right)}{\left(N_2c^*+N_1\left(1-c^*\right)\right)}\right]\left(\frac{-1}{18\left(1-c^*\right)c^*}\right)T^*\nabla^4c^*\right.$$

4.1.1 Initial Conditions

The infinitesimal concentration fluctuations are always present in the polymer blend initially even in the single-phase region. These infinitesimal concentration fluctuations are sufficient to drive the process of phase separation by the spinodal decomposition mechanism. Therefore, the expression of the initial concentration can be shown as:

$$c^*\left(t^*=0\right)=c_0^*+\delta c^*\left(t^*=0\right) \tag{4.24}$$

where, c_0^* is the dimensionless initial concentration, and $\delta c^*\left(t^*=0\right)$ represents any deviation from the average initial concentration c_0^* or the infinitesimally small concentration fluctuations which may be present in the blend.

4.1.2 Boundary Conditions

In the short range surface potential case the model domain is composed of four surfaces where *only one* of them has a surface attraction. Each surface will have two boundary conditions. Assuming an external surface potential in the system for the domain side with surface attraction, the first boundary condition (suggested by Schmidt and Binder [345]) would become:

$$-h-gc_1^*+\gamma\left.\frac{\partial c^*}{\partial x^*}\right|_{x^*=0}=0 \tag{4.25}$$

whereas *h* represents the surface potential with preference to one of the components, *g* shows the change interactions near the surface in the underlying lattice model and γ has relation to the bulk correlation length. Furthermore, the second boundary condition shows that no penetration of material is possible through the boundary surface. In other words, at this surface, the concentration flux is zero and there is a no-flux boundary condition [135,136,346]:

$$J\big|_{x^*=0} = 0 \tag{4.26}$$

or

$$\nabla^3 c^* = 0 \tag{4.27}$$

Therefore, for $x^* = 0$, the following boundary conditions are obtained:

$$\left.\frac{\partial c^*}{\partial x^*}\right|_{x^*=0} = \frac{h + gc^*}{\gamma} \tag{4.28}$$

$$\frac{\partial^3 c^*}{\partial x^{*3}} + \frac{\partial^3 c^*}{\partial x^* \partial y^{*2}} = 0 \tag{4.29}$$

At the surfaces without any preferential attraction to one of the polymers in the blend, there are two boundary conditions applied: i) no-flux boundary condition which is represented Equation (4.26), which refers to a system in which no mass will be exchanged through its boundary with the surrounding, ii) natural boundary conditions obtained from the variational analysis [135,136,292], and is expressed in generalized form as:

$$\left(\nabla c^*\right) \cdot \mathbf{n} = 0 \tag{4.30}$$

where **n** is the outward unit normal to a bounding surface. Therefore for the sides with no surface attraction, the following boundary conditions are developed:

for $x^* = 1$:

$$\frac{\partial c^*}{\partial x^*} = 0 \tag{4.31}$$

$$\frac{\partial^3 c^*}{\partial x^{*3}} + \frac{\partial^3 c^*}{\partial x^* \partial y^{*2}} = 0 \tag{4.32}$$

and for $y^* = 0,\ 1$:

$$\frac{\partial c^*}{\partial y^*} = 0 \tag{4.33}$$

$$\frac{\partial^3 c^*}{\partial y^{*3}} + \frac{\partial^3 c^*}{\partial y^* \partial x^{*2}} = 0 \tag{4.34}$$

Equation 4.23 can be expanded using the following formulas in terms of spatial derivation:

$$\nabla c^* = \frac{\partial c^*}{\partial x^*}\hat{i} + \frac{\partial c^*}{\partial y^*}\hat{j}$$

$$\left(\nabla c^*\right)^2 = \left(\frac{\partial c^*}{\partial x^*}\right)^2 + \left(\frac{\partial c^*}{\partial y^*}\right)^2$$

$$\nabla^2 c^* = \frac{\partial^2 c^*}{\partial x^{*2}}\hat{i} + \frac{\partial^2 c^*}{\partial y^{*2}}\hat{j}$$

$$\left(\nabla^2 c^*\right)^2 = \left(\frac{\partial^2 c^*}{\partial x^{*2}} + \frac{\partial^2 c^*}{\partial y^{*2}}\right)^2$$

$$\nabla^3 c^* = \frac{\partial^3 c^*}{\partial x^{*3}}\hat{i} + \frac{\partial^3 c^*}{\partial x^* \partial y^{*2}}\hat{i} + \frac{\partial^3 c^*}{\partial x^{*2} \partial y^*}\hat{j} + \frac{\partial^3 c^*}{\partial y^{*3}}\hat{j}$$

$$\nabla c^* \cdot \nabla^3 c^* = \frac{\partial^3 c^*}{\partial x^{*3}} \frac{\partial c^*}{\partial x^*} + \frac{\partial^3 c^*}{\partial x^* \partial y^{*2}} \frac{\partial c^*}{\partial x^*} + \frac{\partial^3 c^*}{\partial x^{*2} \partial y^*} \frac{\partial c^*}{\partial y^*} + \frac{\partial^3 c^*}{\partial y^{*3}} \frac{\partial c^*}{\partial y^*}$$

$$\nabla^4 c^* = \frac{\partial^4 c^*}{\partial x^{*4}} + 2\frac{\partial^4 c^*}{\partial x^{*2} \partial y^{*2}} + \frac{\partial^4 c^*}{\partial y^{*4}}$$

$$\nabla T^* = \frac{\partial T^*}{\partial x^*} \hat{i} + \underbrace{\frac{\partial T^*}{\partial y^*}}_{0} \hat{j}$$

$$\nabla T^* \cdot \nabla c^* = \frac{\partial T^*}{\partial x^*} \frac{\partial c^*}{\partial x^*} + \frac{\partial T^*}{\partial y^*} \frac{\partial c^*}{\partial y^*}$$

$$\nabla T^* \cdot \nabla^3 c^* = \frac{\partial T^*}{\partial x^*} \frac{\partial^3 c^*}{\partial x^{*3}} + \frac{\partial T^*}{\partial x^*} \frac{\partial^3 c^*}{\partial x^* \partial y^{*2}} + \frac{\partial T^*}{\partial y^*} \frac{\partial^3 c^*}{\partial x^{*2} \partial y^*} + \frac{\partial T^*}{\partial y^*} \frac{\partial^3 c^*}{\partial y^{*3}}$$

4.2 Numerical Methods of Solution

4.2.1 Method of Lines

The method of lines was applied to solve the partial differential equation (Equation 4.23) computationally, where the spatial related derivatives were discretized by finite difference method and only the time dependent concentration derivative remains continuous.

The method of lines (MOL) is: “a general procedure for the solution of time dependent partial differential equations (PDEs). The basic idea of MOL is to replace the spatial (boundary value) derivatives in the PDE with algebraic approximations. Once this is done, the spatial derivatives are no longer stated explicitly in terms of the spatial independent variables. Thus, in effect only the initial value variable, typically time in a physical problem,

remains. In other words, with only one remaining independent variable, we have a system of ODEs that approximate the original PDE. The challenge, then, is to formulate the approximating system of ODEs. Once this is done, any integration algorithm for initial value ODEs can be applied to compute an approximate numerical solution to the PDE. Therefore, one of the significant features of the MOL is the use of existing, and generally well-established, numerical methods for ODEs" [347]. If the original ODE system approximating the PDE is nonlinear, a system of nonlinear algebraic equations needs to be solved by a Jacobian matrix. Due to the large number of spatial grid points in the MOL approximation of the PDE, especially when solving two dimensional (2D) and three dimensional (3D) PDEs, the Jacobian matrix of the nonlinear algebraic system can become very large and sparse as the number of spatial grid points increases [347].

The MOL is regarded as a special finite difference method but more effective with respect to accuracy and computational time than the regular finite difference method [348]. "MOL has the advantages of both the finite difference method and analytical method; it does not generate spurious modes nor have the problem of relative convergence. Besides, the MOL has the following properties that justify its use:

(i) Computational efficiency: the semi-analytical character of the formulation leads to a simple and compact algorithm, which yields accurate results with less computational effort than other techniques.

(ii) Numerical stability: by separating discretization of space and time, it is easy to establish stability and convergence for a wide range of problems.

(iii) Reduced programming effort: by making use of the state-of-the-art well documented and reliable ordinary differential equations (ODE) solvers, programming effort can be substantially reduced.

(iv) Reduced computational time: since only a small amount of discretization lines are necessary in the computation, there is no need to solve a large system of equations; hence computing time is small" [348].

4.2.2 Discretization in Space

The model domain has been spatially discretized by a $N \times N$ (256 × 256) mesh (Figure 4.1).

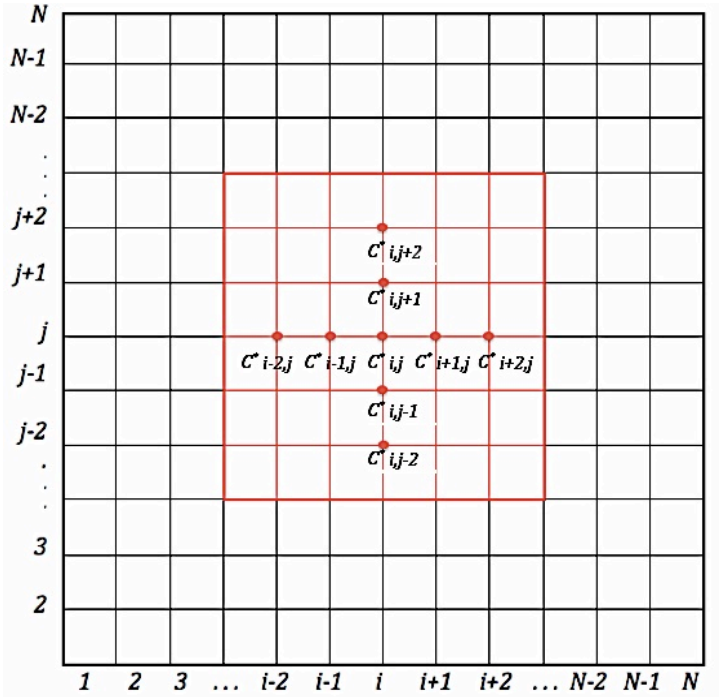

Figure 4.1: Schematic diagram of spatial discretization of model domain.

As mentioned before, central difference scheme method has been used for spatial discretization using point-value solution. Using FDM approach, the following finite difference formulas for several derivatives in two-dimensional (2D) will be obtained:

$$\left(\frac{\partial c^*}{\partial x^*}\right)_{i,j} = \frac{c^*_{i+1,j} - c^*_{i-1,j}}{2\Delta x^*}$$

$$\left(\frac{\partial c^*}{\partial y^*}\right)_{i,j} = \frac{c^*_{i,j+1} - c^*_{i,j-1}}{2\Delta y^*}$$

$$\left(\frac{\partial^2 c^*}{\partial x^{*2}}\right)_{i,j} = \frac{c^*_{i+1,j} - 2c^*_{i,j} + c^*_{i-1,j}}{2\Delta x^{*2}}$$

$$\left(\frac{\partial^2 c^*}{\partial y^{*2}}\right)_{i,j} = \frac{c^*_{i,j+1} - 2c^*_{i,j} + c^*_{i,j-1}}{2\Delta y^{*2}}$$

$$\left(\frac{\partial^3 c^*}{\partial x^{*3}}\right)_{i,j} = \frac{c^*_{i+2,j} - 2c^*_{i+1,j} + 2c^*_{i-1,j} - c^*_{i-2,j}}{2\Delta x^{*3}}$$

$$\left(\frac{\partial^3 c^*}{\partial y^{*3}}\right)_{i,j} = \frac{c^*_{i,j+2} - 2c^*_{i,j+1} + 2c^*_{i,j-1} - c^*_{i,j-2}}{2\Delta y^{*3}}$$

$$\left(\frac{\partial^4 c^*}{\partial x^{*4}}\right)_{i,j} = \frac{c^*_{i+2,j} - 4c^*_{i+1,j} + 6c^*_{i,j} - 4c^*_{i-1,j} + c^*_{i-2,j}}{\Delta x^{*4}}$$

$$\left(\frac{\partial^4 c^*}{\partial y^{*4}}\right)_{i,j} = \frac{c^*_{i,j+2} - 4c^*_{i,j+1} + 6c^*_{i,j} - 4c^*_{i,j-1} + c^*_{i,j-2}}{\Delta y^{*4}}$$

Mixed derivatives:

$$\left(\frac{\partial^3 c^*}{\partial x^* \partial y^{*2}}\right)_{i,j} = \frac{c^*_{i+1,j+1} - 2c^*_{i+1,j} + c^*_{i+1,j-1} - c^*_{i-1,j+1} + 2c^*_{i-1,j} - c^*_{i-1,j-1}}{2\Delta x^* \Delta y^{*2}}$$

$$\left(\frac{\partial^3 c^*}{\partial x^{*2} \partial y^*}\right)_{i,j} = \frac{c^*_{i+1,j+1} - 2c^*_{i,j+1} + c^*_{i-1,j+1} - c^*_{i+1,j-1} + 2c^*_{i,j-1} - c^*_{i-1,j-1}}{2\Delta x^{*2} \Delta y^*}$$

$$\left(\frac{\partial^4 c^*}{\partial x^{*2} \partial y^{*2}}\right)_{i,j} = \frac{c^*_{i+1,j+1} - 2c^*_{i,j+1} + c^*_{i-1,j+1} - 2c^*_{i+1,j} + 4c^*_{i,j} - 2c^*_{i-1,j} + c^*_{i+1,j-1} - 2c^*_{i,j-1} + c^*_{i-1,j-1}}{2\Delta x^{*2} \Delta y^{*2}}$$

All boundary conditions can be spatially discretized according to the following formulas. For the side with the surface attraction ($i = 1$):

$$\left(\frac{\partial c^*}{\partial x^*}\right)_{i,j} = \frac{h + gc^*_{i,j}}{\gamma} \Rightarrow c^*_{0,j} = c^*_{2,j} - \frac{2\Delta x^*}{\gamma}\left(h + gc^*_{1,j}\right)$$

and

$$\frac{\partial^3 c^*}{\partial x^{*3}} + \frac{\partial^3 c^*}{\partial x^* \partial y^{*2}} = 0 \Rightarrow \frac{c^*_{3,j} - 2c^*_{2,j} + 2c^*_{0,j} - c^*_{-1,j}}{\Delta x^{*3}} + \frac{c^*_{2,j+1} - 2c^*_{2,j} + c^*_{2,j-1} - c^*_{0,j+1} + 2c^*_{0,j} - c^*_{0,j-1}}{2\Delta x^* \Delta y^{*2}} = 0$$

$$if\, \Delta x^* = \Delta y^* \Rightarrow\ c^*_{-1,j} = c^*_{3,j} - 4c^*_{2,j} + 4c^*_{0,j} + c^*_{2,j+1} + c^*_{2,j-1} - c^*_{0,j+1} - c^*_{0,j-1}$$

The boundary for the sides with no surface attraction are discretized and simplified as follows:

$i = N$:

$$\left(\frac{\partial c^*}{\partial x^*}\right)_{N,j} = 0 \Rightarrow c^*_{N+1,j} = c^*_{N-1,j} \tag{4.35}$$

$$\frac{\partial^3 c^*}{\partial x^{*3}} + \frac{\partial^3 c^*}{\partial x^* \partial y^{*2}} = 0 \Rightarrow c^*_{N+2,j} = c^*_{N-2,j} \tag{4.36}$$

$j = 1$:

$$\frac{\partial c^*}{\partial y^*} = 0 \Rightarrow c^*_{i,2} = c^*_{i,0} \tag{4.37}$$

$$\frac{\partial^3 c^*}{\partial y^{*3}} + \frac{\partial^3 c^*}{\partial y^* \partial x^{*2}} = 0 \Rightarrow c^*_{i,3} = c^*_{i,-1} \tag{4.38}$$

$j = N$:

$$\frac{\partial c^*}{\partial y^*} = 0 \Rightarrow c^*_{i,N+1} = c^*_{i,N-1} \tag{4.39}$$

$$\frac{\partial^3 c^*}{\partial y^{*3}} + \frac{\partial^3 c^*}{\partial y^* \partial x^{*2}} = 0 \Rightarrow c^*_{i,N+2} = c^*_{i,N-2} \tag{4.40}$$

The above boundary conditions will be incorporated in the governing Equation (4.23) to be reduced to a system of ODEs where only time derivatives will be remained.

4.2.3 CVODE Solver

The system of ODEs can be solved by generic solvers. The stiff ODE solver namely CVODE, based on the Generalized Minimal Residual Iteration (GMRES) method incorporated with the Backward Differentiation Formulas (BDF) method, was used to solve the proposed model for different time steps.

"SUNDIALS is a widely used suite of advanced computational codes for solving large-scale problems that can be modeled as a system of nonlinear algebraic equations, or as initial-value problems in ordinary differential or differential-algebraic equations" [351–354]. "The basic versions of these codes are called KINSOL, CVODE, and IDA, respectively. The codes are written in ANSI standard C and are suitable for either serial or parallel machine environments. Common and notable features of these codes include Inexact Newton-Krylov methods for solving large-scale nonlinear systems; linear multistep methods for time-dependent problems; a highly modular structure to allow incorporation of different preconditioning and/or linear solver methods; and clear interfaces allowing for users to provide their own data structures underneath the solvers" [351–354]. To meet this need, Lawrence Livermore National Laboratory (LLNL) has developed open-source software for

solving ODEs [351,355,356]. CVODE solves stiff ODE initial value problems in real *N*-space written as:

$$\frac{\partial y}{\partial t} = f\left(t, y\right) \tag{4.41}$$

with an initial value of: $y\left(t_0\right) = y_0 \qquad y \in R^N$

"The user first selects one of two variable-order, variable-step linear multistep method families, implicit Adams methods (orders 1 to 12) or methods based on BDFs (orders 1 to 5). Then the user specifies either functional or Newton iteration for the treatment of the implicit nonlinear equations. For non-stiff systems, Adams method with functional iteration is sufficient. For stiff systems, characterized by at least one rapid decay mode (with time constant much smaller than the solution time scale), one must choose Newton iteration and a linear system solver that is appropriate to the problem" [357]. "The user may also require that CVODE find, and stop at the roots of a set of given functions during the integration of the ODEs. In the Newton case, CVODE must solve linear systems of dimension $N \times N$ of the form $\left(I - \gamma J\right)x = b$ that arise at each time step. Here γ is a scalar and J is the Jacobian $\partial f / \partial y$. The user specifies one of six algorithms to solve these systems" [359,363]. For the model of study, GMRES, a Krylov iterative method, was used due to its powerful tool in solving large, sparse, unsymmetrical, semi-positive definite linear systems [363].

For stiff problems, CVODE includes the BDFs in so-called fixed-leading coefficient form. BDFs are formulas that give an approximation to a derivative of a variable at a time t_n in terms of its function values $y(t)$ at t_n and earlier times (backward). For the Newton

approach, CVODE provides a choice of four methods where Scaled Preconditioned GMRES is selected for this model [358]. For large stiff systems, where direct methods are not feasible, the combination of a BDF integrator with the GMRES algorithm yields a powerful tool since it combines established methods for stiff integration, nonlinear iteration, and Krylov (linear) iteration. For stiff systems, the value of BDF methods lie in their superior stability properties which allow them to take much larger step sizes than would be possible with explicit methods. "The Jacobian matrix can be either supplied by the user or internally approximated by difference quotients. In the direct cases, the nonlinear iteration at each time step is Modified Newton, and the approximate Jacobian used is only updated when necessary to achieve convergence, rather than every step. The GMRES is matrix-free [359,363]. This means that, for the solution of a system $Ax = b$, each iteration requires only the value of a matrix-vector product Av, and that product is (on default) obtained by a difference quotient not requiring the matrix A explicitly" [361].

"CVODE chooses its step sizes and method orders automatically and dynamically, so as to keep estimated integration errors within given tolerances. Both relative and absolute tolerance parameters are required inputs from the user. Optionally, the user can specify that the selection of method order be augmented by an algorithm that attempts to detect when step sizes are limited by the BDF stability region boundary at order 3 or more" [359,360]. A critical part of CVODE, making it an ODE solver rather than just an ODE method, is its control of local error. At every step, the local error is estimated and required to satisfy tolerance conditions, and the step is redone with reduced step size whenever that error test fails [359]. The fixed-leading-coefficient form of BDF was also applied to increase the accuracy of derivatives approximations for each time steps based on their values at previous

times. For all simulations, the absolute tolerance was set to 10^{-10} and relative tolerance was equal to 10^{-8}. The number of nodes was kept at 256 × 256 in a lattice, and each simulation on average took 2 weeks on a computer with Intel i7 CPU core, due to high nonlinearity and stiffness of the model.

4.3 Results and Discussion

In this section numerical results and discussion will be presented for short-range surface potential. The focus is on the formation and evolution of the phase separated-structures and the different factors that control the morphology to fabricate functional polymeric material. Hence, only the early and intermediate stages of phase separation were emphasized in this study. In the late stage of spinodal decomposition, the morphology coarsens thus destroying the functionality of the composite material. In all simulations, the dimensionless interaction parameter variables, α and β were selected from a typical polymer blend (DPB/HPB) and were kept constant with the values of -5.34×10^{-4} and 8.44×10^{-4}, respectively [317,337].

The degree of the polymerization for the blend was $N_1 = N_2 = N = 1000$ which is well above $N_c = 300$ for the reptation theory to be applicable due to entanglement of polymer chains [286,287]. Values of dimensionless diffusion coefficient, D, is in order of 10^5 which is consistent with literature for polymer blends [145,317]. The change of interactions near the surface (g) is considered to be – 0.5 (g/γ) since this value incorporates different wetting behaviors including partial and complete wetting as surface potential (h/γ) changes [397].

Both g and h represent the g/γ and h/γ values, respectively and the g parameter can be positive or negative [345]. However, simple bond-counting arguments consistent with the nearest-neighbor interaction assumed in the Flory-Huggins model suggest that g should be negative [396]. The temperature at the surface with favorable attraction to one of the component is T_1^* while the temperature on the other side of the domain with no surface attraction is T_2^*. Figure 4.2 shows the dimensionless temperature versus dimensionless concentration UCST-type phase diagram for the symmetric polymer blend used in this study. The concentration shown in the phase diagram represents the volume fraction of polymer component 1. The solid curve represents the binodal (equilibrium curve) and the dotted curve is the spinodal curve.

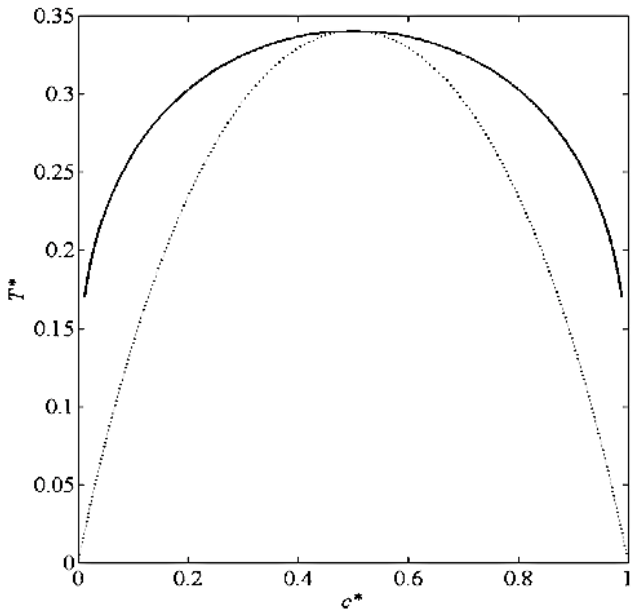

Figure 4.2: Dimensionless temperature versus dimensionless concentration phase diagram for a symmetric polymer blend with polymer degree of polymerization $N_1 = N_2 = 1000$. The solid (dot) line represents the binodal (spinodal) line.

4.3.1 Effect of Quench Depth on Surface Enrichment

The morphology formation of the polymer binary blend under different temperature gradients, surface attraction to one polymer, concentrations, quench depths and diffusion coefficients has been studied for short-range surface potential cases. For cases that the attracting surface was completely wetted by a component, the rate of the growth of the wetting layer is compared with literature values. It is well known that morphology formation and its evolution rate following the thermal induced spinodal decomposition process depends on the temperature that blends are quenched to, the diffusion coefficient, the molecular weight of each component (the degree of polymerization), and the miscibility of the two components. Furthermore, for the surface directed phase separation, the amount of surface attraction to the favorable component could affect the nature of the surface wetting (complete or partial wetting), and also the rate of the enrichment of the surface (attraction of polymer to the surface) by favorable polymer. To study the effect of the above parameters on the formation of the morphology, one parameter was changed at a time. Quench depth value ε can be obtained through the following equation:

$$\varepsilon = \frac{\chi - \chi_s}{\chi_s} \tag{4.42}$$

where χ is the Flory-Huggins interaction parameter and χ_s is the value of χ at spinodal temperature [335]. According to Equation 4.22, χ is inversely proportional to temperature (T), therefore, lower values of T represent deeper quench depths. Phase separation induced by short-range surface attraction potential is initiated in the layer close to the surface and

proceeds to include and engage the whole domain due to the intermolecular attraction forces between like polymers within the domain.

Figure 4.3 depicts a schematic diagram of the domain bulk geometry under temperature gradient for short-range surface potential case. As mentioned previously, the temperature at the surface with favorable attraction to one of the component is T_1^* while the temperature on the other side of the domain with no surface attraction is T_2^*. It should be noted that there are two types of phase separation mechanisms studied through all cases (short-range, multiple-surface and long-range) of surface potential leading to different morphologies: i) phase separation at the surface with preferential attraction to one of the polymers and ii) phase separation within the bulk.

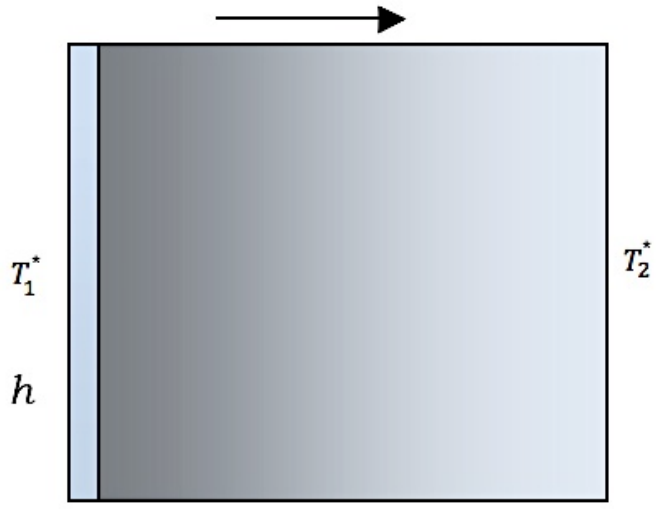

Figure 4.3: Schematic representation of the dimensionless temperature gradient and positioning of the side with surface potential (h) at T_1^* for a short-range surface attraction case. The direction of arrow depicts the temperature gradient form T_1^* to T_2^*.

Phase separation within the bulk is mainly governed by spinodal decomposition while the phase separation at the surface is induced by both; the attraction of one polymer that is preferred by that surface in addition to spinodal decomposition mechanism. The impact of change in each parameter (temperature gradient, surface attraction to one polymer, concentration, quench depth and diffusion coefficient), individually or coupled with each other, have been studied through different models. It has been noticed that there is a competition between the mechanisms of phase separation at the surface and within the bulk. The morphologies obtained in each case are found to be controlled mostly by the mechanism that is more dominant through phase separation. Although, at early stages, the surface is *always* prominent in initiating the phase separation prior to any bulk intervention (partial to complete wetting), however, during intermediate stages, the bulk, may govern the spinodal phase separation. This can be tracked when the morphology is reversed from complete wetting to partial wetting during phase separation. According to the results of this work, domination of bulk comes more into effect over time mostly for deep quench cases.

Figure 4.4 shows a typical phase separation for the short-range surface potential case for different off-critical quenching depths from a one-phase region into the two-phase region with dimensionless concentration of $c_0^* = 0.3$. In this case, the dimensionless parameter values are: $D = 4 \times 10^5$, $h = 0.5$, $g = -0.5$ and $T_2^* = 0.20$. The temperature gradient is created by setting T_1^* to (a) 0.22, (b) 0.24 and (c) 0.26. It can be observed that phase separation is initiated in the form of partial wetting earlier in (a) deeper quench depth of $\varepsilon = 0.4147$ at the surface and reaches complete wetting earlier than shallow quench depths (b and c) of $\varepsilon = 0.2793$ for (b) and $\varepsilon = 0.1647$ for (c).

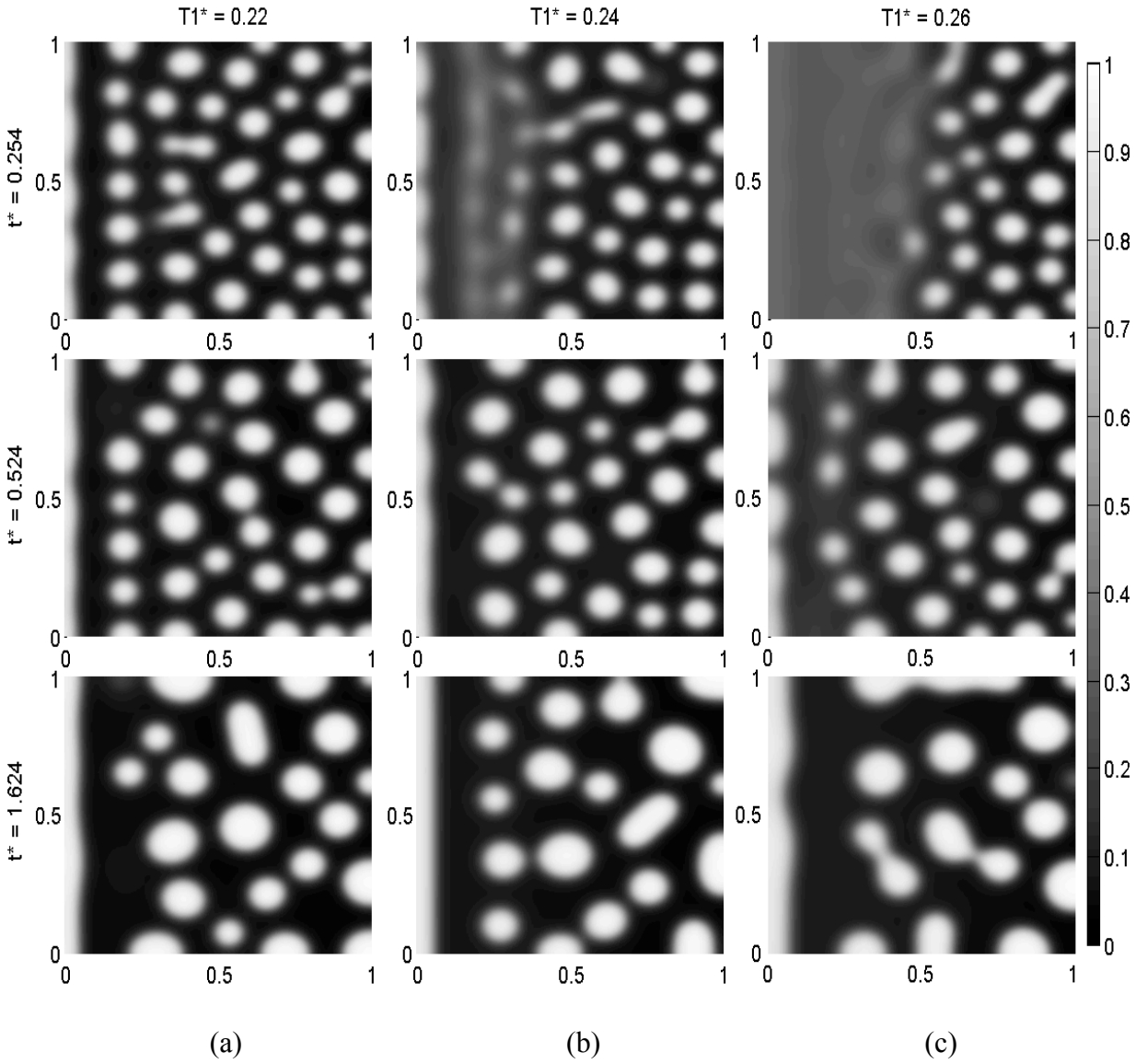

Figure 4.4: Typical morphology changes to reach complete wetting resulted from various off-critical ($c_0^* = 0.3$) quenching depths from a one-phase region into the two-phase region in a short-range surface potential case. In this case, the dimensionless parameter values are: $D = 4 \times 10^5$, $h = 0.5$, $g = -0.5$ and $T_2^* = 0.20$. The dimensionless temperature, T_1^*, varies from 0.22 with a quench depth of $\varepsilon = 0.4147$, for a deep quench to 0.24 and 0.26 with quench depths of $\varepsilon = 0.2793$ and 0.1647, respectively for a shallow quench. Droplet morphology confirms the off-critical quenching conditions.

In Figure 4.4 (a), complete wetting is obtained at dimensionless time t^* = 0.254, (b) at t^* = 0.524 and (c) at t^* = 1.624. The morphology emphasizes that increasing the quench depth will accelerate the transition from early stage to intermediate stage. The phase separation mechanism is primarily triggered at early stage by the surface. During intermediate stage, the surface still controls the phase separation in its vicinity due to the fact that there is no sign of morphology shift from complete wetting to partial wetting during the intermediate stage. This is an indication of studied quench depths being unable to make the bulk win the competition with the surface attraction force in governing the phase separation mechanism. The morphology also reveals that for a shallow quench, more polymer growth occurs on the surface (surface enrichment) [212].

As typical of off-critical quenching conditions within spinodal region, droplets are formed during surface directed phase separation. The obtained morphology is consistent with the numerical [162,173,200,205,303,336,364,369] and experimental work [228,298,365–368].

4.3.2 Structure Factor Growth

The dimensionless structure factor, $S^*\left(k^*,t^*\right)$, is a significant parameter to characterize the development of phase separated domains by spinodal decomposition mechanism in polymer blends [301]. Structure factor makes connections between the numerical results and experimental studies performed on the phase separation mechanism in polymer blends. Consequently, the time evolution of the two-phase structures, such as ones produced during

the phase separation process in the polymer blend systems studied in this work can also be measured using the dimensionless structure factor. The dimensionless structure factor $S^*\left(k^*,t^*\right)$ is calculated using Fourier transform of concentration fluctuations, $A^*\left(q^*,t^*\right)$, in the system. Accordingly, from Equation (4.43) [145,299,302–304]:

$$S^*\left(k^*,t^*\right)=\left\|A^*\left(q^*,t^*\right)\right\|^2 \qquad \text{for} \qquad k^*=q^* \tag{4.43}$$

where q^*, is the dimensionless scattering wave number [300], S^* is the structure factor and k^* is the dimensionless wave number in Fourier space. In the early stages of phase separation by spinodal decomposition, the dimensionless structure factor (S^*) grows exponentially and the scattering wave number, q^*, is independent of time. The growth of the concentration fluctuations is weakly nonlinear. In intermediate stages of phase separation, the structure factor continues to increase but at a slower rate than in early stages of phase separation by spinodal decomposition. Scattering wave number (q) decreases and wavelength $\left(\lambda\right)$ increases accordingly. The relation between q and λ is defined as [335]:

$$q=\left(\frac{4\pi}{\lambda}\right)\sin\left(\frac{\theta}{2}\right) \tag{4.44}$$

where θ is the scattering angle. The dimensionless structure factor S^* can be obtained by taking the squares of the magnitude of the Fourier transform of the concentration fluctuations, $A^*\left(k^*,t^*\right)$. Accordingly, from Equation (4.43), the structure factor can be expressed as:

$$S^*\left(k^*,t^*\right)=\left\|A^*\left(k^*,t^*\right)\right\|^2=\left\|\sum_{m=0}^{N=1}\sum_{n=0}^{N=1}\left[c^*\left(r^*,t^*\right)-c_0^*\right]e^{\left[\frac{2\pi i}{n}\left(mk_1^*+nk_2^*\right)\right]}\right\|^2 \tag{4.45}$$

where, $c^*(r^*,\ t^*)$ is the solvent concentration at node (m, n), c_0^*, is the mean solvent concentration, and k^* is the two-dimensional position vector, (k_1^*, k_2^*) in Fourier space. The dimensionless structure factor was calculated at different dimensionless times to guarantee that the numerical work in this study is in agreement with the known evolution of scattering profiles as related to the structure factor. To determine the Fast Fourier Transform of the model results at a specific time, a small algorithm was developed in MATLAB and by squaring the magnitude of the Fast Fourier Transform results the values of the structure factors can be determined for each time.

Figure 4.5 presents the typical evolution of the dimensionless structure factor for off-critical quench from a one-phase region into the two-phase region at different dimensionless times in a short-range surface potential phase separation model under temperature gradient. It shows for polymer blend bulks undergoing deep quench spinodal decomposition, dimensionless structure factor appears stationary for a short time (at t^* = 0.206) indicating early stages of spinodal decomposition, then rapidly grows exponentially with time in the intermediate stages of phase separation and displays a maximum that grows with time. The wave number remains constant during the phase separation process in the early to the beginning of the intermediate stages, which is a normal trend during the early stage of the phase separation. “This indicates that the phase separation results are in the early stage and beginning of the intermediate stage of spinodal decomposition” [135]. The obtained evolution of the dimensionless structure factor diagram is in good agreement with numerous

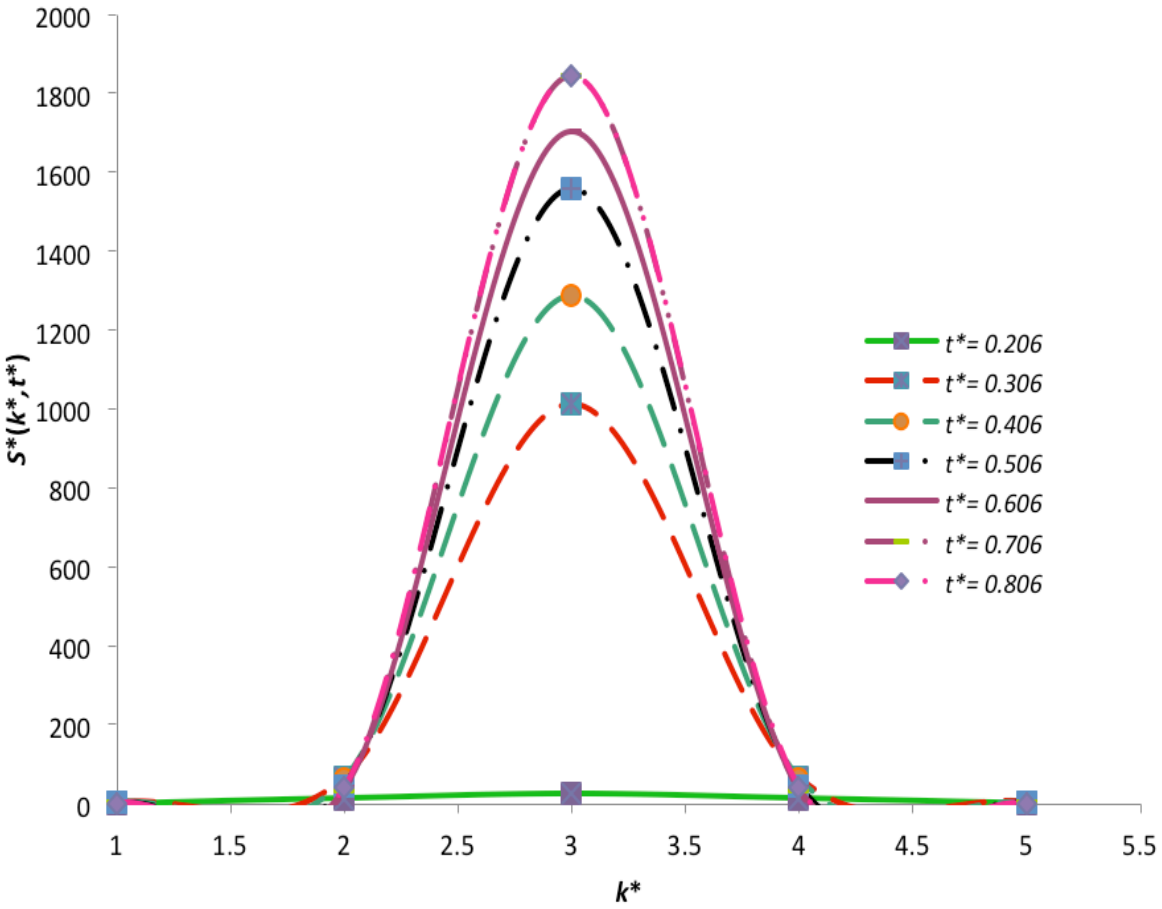

Figure 4.5: Typical evolution of the dimensionless structure factor for off-critical quench from a one-phase region into the two-phase region at different dimensionless times (the legend) in a short-range surface potential phase separation model (Figure 4.4) under temperature gradient where $c_0^* = 0.3$, $g = -0.5$, $D = 4 \times 10^5$, $T_1^* = 0.24$ (shallow quench), $\varepsilon = 0.2793$, $T_2^* = 0.20$ and $h = 0.5$.

numerical [145,184,201,208,317,370,373–375,] and experimental [164,303,304,371,372] results. To further investigate the transition time, which corresponds to the transition from the early stages to the beginning of the intermediate stages of phase separation, 1D (one dimension) dimensionless structure factors were developed in the vertical sections of the bulk

domain. This is due to the existence of temperature gradient within the horizontal direction (x^*) of the bulk. In order to better examine the effect of surface attraction over the bulk, the impact of temperature gradient was eliminated by considering a vertical section of the domain where the surface structure could clearly present the surface influence over the bulk.

Figure 4.6 is a logarithmic plot of the structure factor $S^*(k^*_m, t^*)$ as a function of dimensionless time t^* corresponding to the case shown in Figure 4.4. $S^*(k^*_m, t^*)$ is the structure factor $S^*(k^*, t^*)$ evaluated at the dimensionless wavenumber k^*_m, which is where the maximum of $S^*(k^*, t^*)$ is located at time t^*. It is noticed that $S^*(k^*_m, t^*)$, increases exponentially in the early stage but it slows down as the phase separation enters the intermediate stage. This trend in the evolution of $S^*(k^*_m, t^*)$ has already been observed experimentally in polymer blends. As well, Figure 4.6 shows the transition time from the early to intermediate stages of SD mechanism within the bulk occurs at a later time for shallower quenches at dimensionless temperatures 0.23, 0.2357 and 0.2525 and earlier time for deeper quenches at dimensionless temperatures 0.2075 and 0.2225. The obtained diagram is consistent with previous experimental [298,376–379] and numerical [135,136,145,160,317] results.

Figure 4.7 depicts a typical diagram selected from Figure 4.6 ($T_1^* = 0.2525$) of the logarithmic structure factor $S^*(k^*_m, t^*)$ as a function of dimensionless time corresponding to the case presented in Figure 4.4 to illustrate the transition time using the tangent lines drawn over early stage and intermediate stage crossover region ($t^* = 0.5480$). The intersection of tangent lines represents the transition time between the early and intermediate stages of spinodal decomposition.

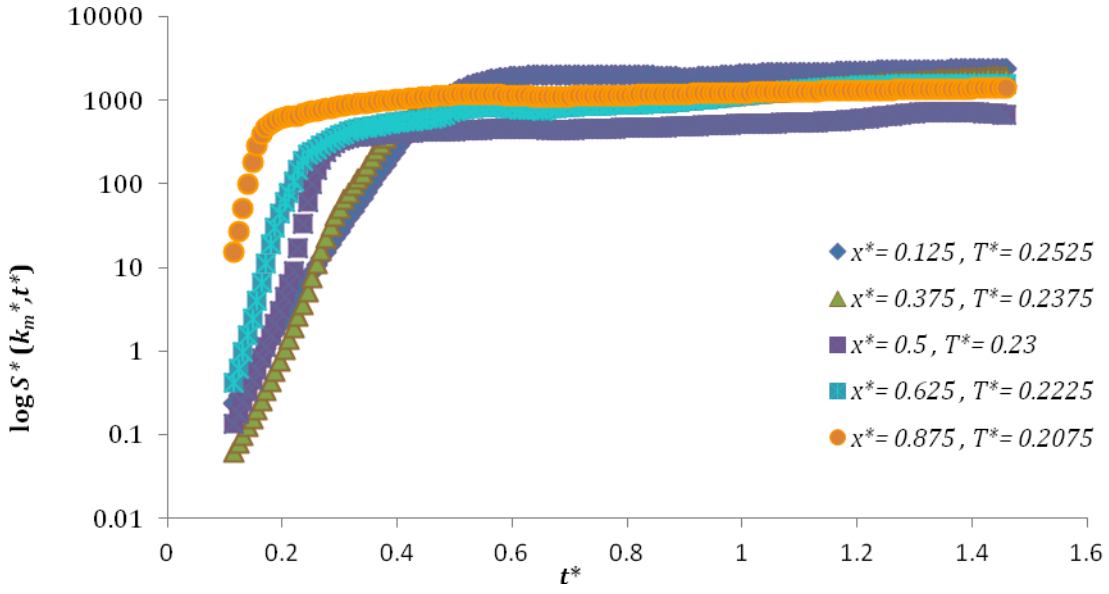

Figure 4.6: Maximum structure factor $S^*(k^*_m, t^*)$ as a function of dimensionless time t^* for the simulation shown in Figure 4.4. This curve is typical of spinodal decomposition, since there is an exponential growth at first but then it slows down. The transition time from the early to intermediate stages of SD mechanism occurs in a later time for shallower quenches at dimensionless temperatures 0.23, 0.2357 and 0.2525.

Typically $S^*\left(k^*,t^*\right)$ has power-law dependence on time as [380–383]:

$$S^*\left(k^*,t^*\right) \approx t^{*\alpha} \tag{4.46}$$

where α is the growth exponent. The amount of α is based on the order parameter conservation, system and order-parameter dimensions [384]. Here, of course, we are dealing with phase separation where the order-parameter is conserved and for this particular problem, is a scalar quantity. Equation 4.46 is referred to as the Lifshitz-Sloyozov (LS) law [295].

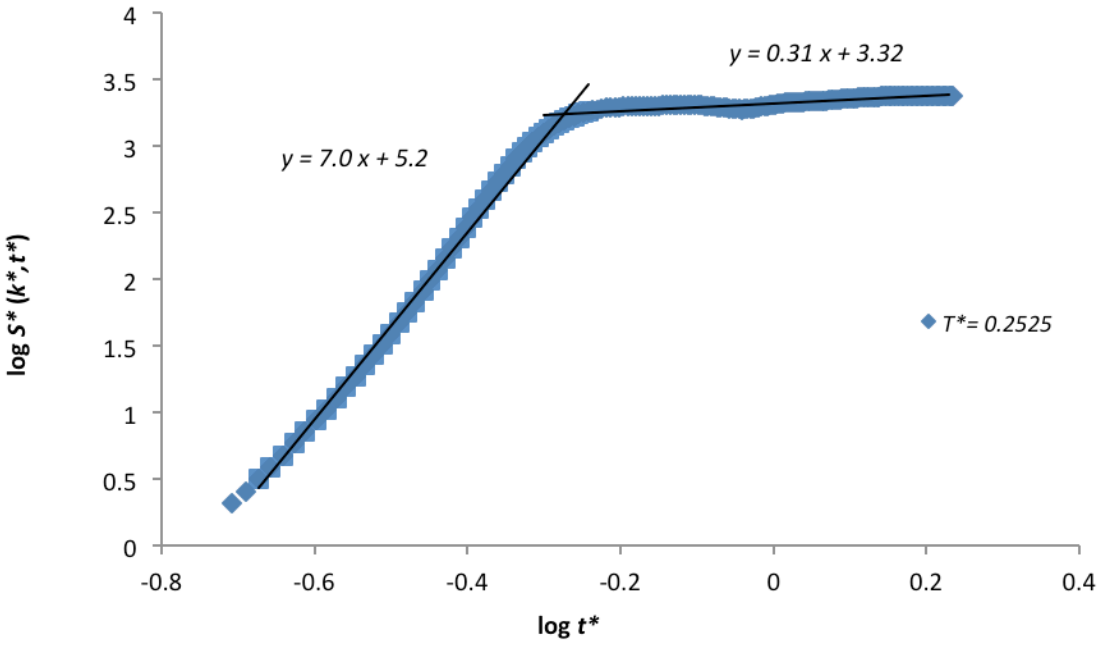

Figure 4.7: Typical diagram selected from Figure 4.6 (T_1^* = 0.2525) of the logarithmic structure factor $S^*(k^*_m, t^*)$ as a function of dimensionless time corresponding to the case presented in Figure 4.4. The intersection of tangent lines drawn over early stage and intermediate stage of SD represents the transition time (t^* = 0.5480). The slope of the tangent line for the intermediate stage is calculated to be 0.31 consistent with the Lifshitz-Sloyozov (LS) law.

The LS behavior is the only growth law anticipated for the phase separation of polymer systems when there is dominant bulk diffusion. Logarithmic plot of structure factor versus dimensionless time (Figure 4.7) reveals a growth exponent of 0.31 (slope of tangent line) for intermediate stage of SD phase separation in the model bulk. The result is consistent with previous numerical [173,184,191,199,209,215,217,385,387–389] and experimental [198,212,221,386,390,391] work, though, dominant interface diffusion at very low temperature can give rise to different values of the exponent [384].

To calculate the thickness layer of the polymer that wetted the surface, two considerations were taken into account. Firstly, only the cases in which the polymer completely wetted the surface were considered in the process. For this selection the following procedure was applied. Initially, the concentration of component 1 on the hypothetical line (the line adjacent to the surface that was parallel and close to the wetting surface) was calculated for each node. It was observed that for complete wetting the difference between the highest and the lowest concentration along this line was less than 15%. Therefore this criterion was used to define the enrichment of the surface as a complete wetting along the hypothetical line. Secondly, to calculate the thickness of the wetting layer at each time step for each point along the surface, the distance between the wetting surface and the first point in the domain in the direction perpendicular to the surface that had the closest value to c_{limit} was measured and then the average of these values was calculated [215]. For calculating the c_{limit}, Equation (4.47) was used based on the difference between the concentration of component 1 at the surface, which represents the highest value of concentration for the spinodal wave, and its concentration at the first minima of the spinodal wave:

$$c_{limit} = \frac{c_{\max} + c_{\min}}{2} \tag{4.47}$$

Average of these thickness layers in 128 points along the surface represented the thickness of wetting layer at that specific time labeled as:

$$z\left(t^*\right) \approx t^{*m} \tag{4.48}$$

where z and m represent thickness of the wetting layer and the growth rate, respectively.

Growth rate (m) can be then obtained as a slope of $\log z\left(t^*\right)$ versus $\log t^*$. Figure 4.8 shows how surface enrichment layer growth typically changes with time within early and intermediate stage of SD phase separation at the surface for a shallow quench case. It is observed that in the early stage of SD phase separation, the growth rate of surface enrichment layer will increase rapidly (m = 0.5). As the system is merging into the intermediate stage, the growth rate decreases (m = 0.13). This can be explained by the fact that during phase separation at the surface for a shallow quench, due to the lack of competition between the surface and the bulk, the initially formed droplets adjacent to the surface will grow faster in the absence of bulk phase separation commencement. The favored polymer would then be attracted to the surface till the phase separation is initiated in the bulk. During intermediate stage, because of the bulk phase separation, the surface enrichment layer growth becomes slower and tends to break up (partial wetting). This behavior has been observed experimentally [212,218,392,393,406,407] through a transition from the complete wetting to partial wetting of the polymer at the surface for a shallow quench.

Enrichment of the surface will continue during intermediate stage. Figure 4.8 shows that the rate of growth of the wetting layer on the surface for a typical shallow quench, with parameters: $c_0^* = 0.5$, $g = -0.5$, $h = 0.5$, $D = 4 \times 10^5$, $T_1^* = 0.30$ (shallow quench) with quench depth $\varepsilon = 0.8768$ and $T_2^* = 0.20$ ($\varepsilon = 0.8768$). The growth rate of the surface wetting layer follows the trend as in previously published experimental results [212,392,393] where at first, the growth rate of $t^{*0.5}$ is reduced to $t^{*0.13}$ at later times.

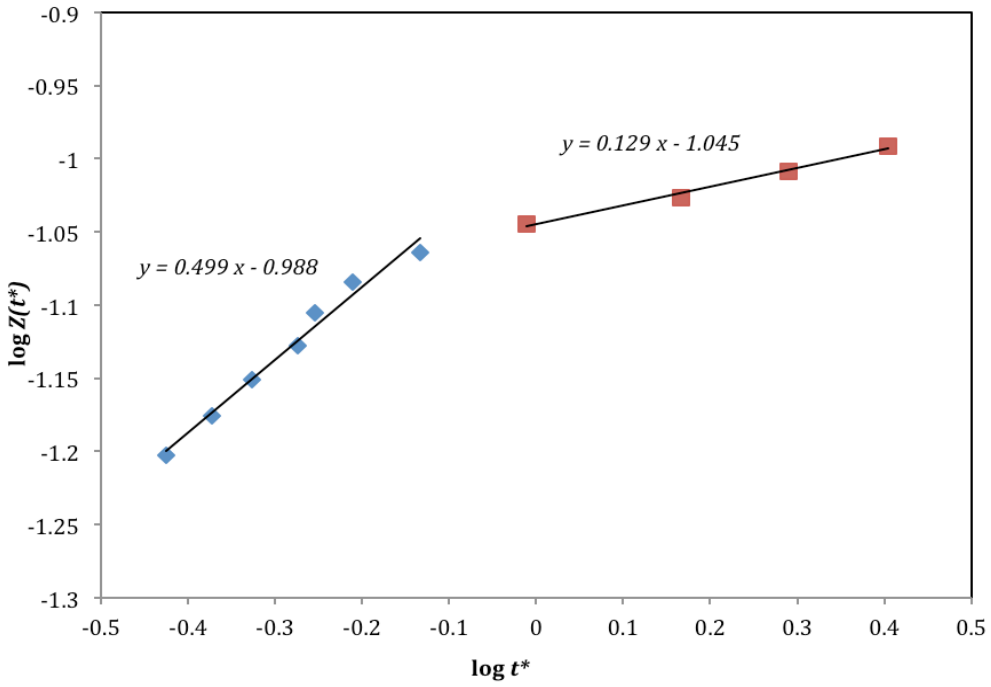

Figure 4.8: Typical change of growth rate at early (m = 0.5) and intermediate (m = 0.13) stages of the phase separation for a shallow quench in a short-range surface potential case with the following parameter values: $c_0^* = 0.5$, $D = 8 \times 10^5$, $h = 0.5$, $g = -0.5$, $T_1^* = 0.30$ (ε = 0.1679) and $T_2^* = 0.20$ ($\varepsilon = 0.8768$).

The results are typical for short-range surface potential cases with different parameters corresponding to systems undergoing SD phase separation induced by a shallow quench.

In order to better observe the morphology formation of complete wetting transition to partial wetting, Figures 4.9 was developed. It shows the morphological changes over time from complete wetting to partial wetting for variations from shallow quenches to deep quenches of a polymer blend where the phase separation mechanism is governed by off-critical quenching conditions. This trend has been observed for different values of polymer concentration, g, and h parameters [210,394,395].

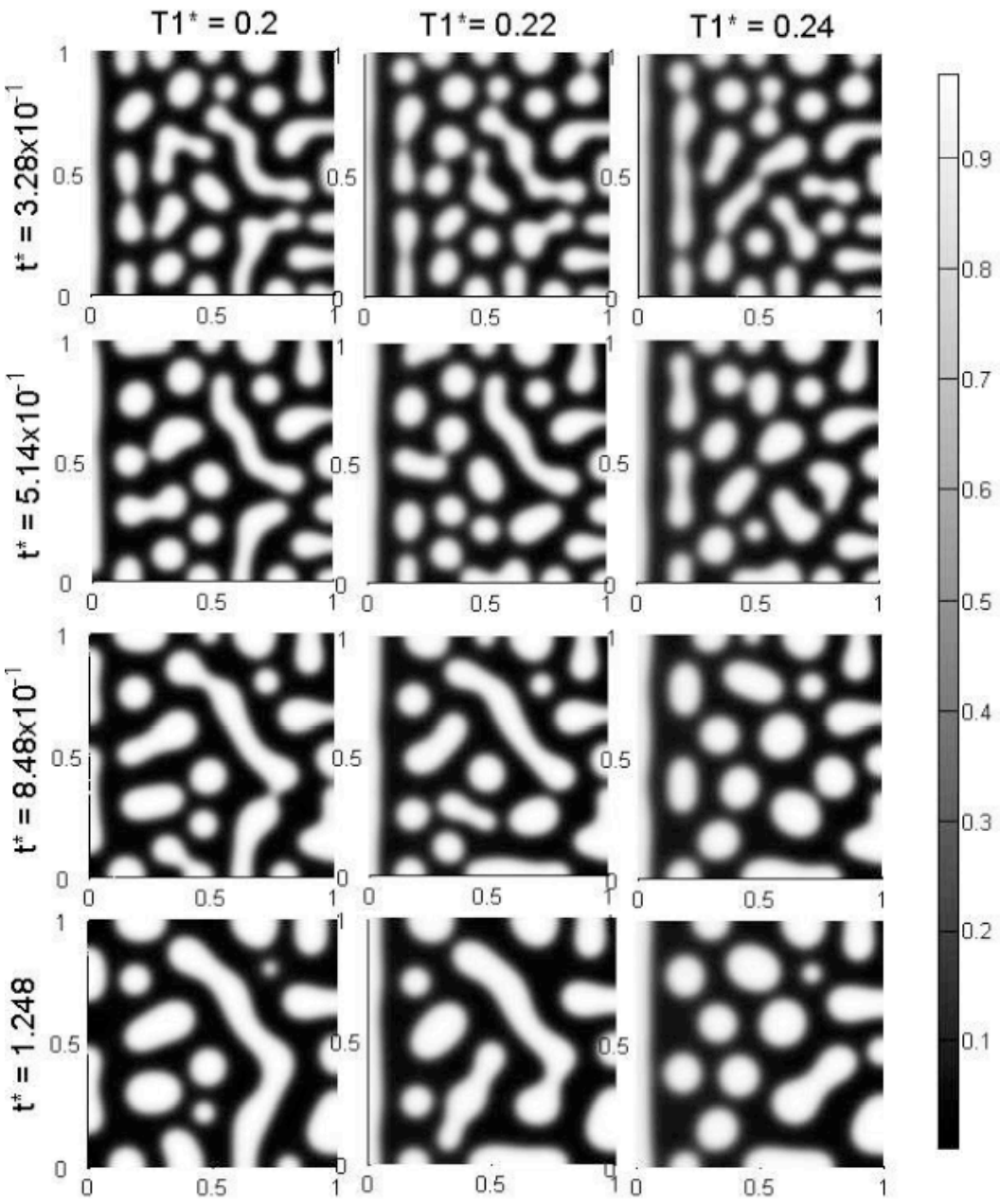

(a) (b) (c)

Figure 4.9: Morphology changes from complete wetting to partial wetting for various off-critical quenching depths in a short-range surface potential case. In this case, the parameter values are: $c_0^* = 0.4$, $D = 4 \times 10^5$, $h = 0.5$, $g = -0.5$, $T_2^* = 0.20$. The temperature T_1^* varies from (a) 0.20, $\varepsilon = 0.8023$, for a deep quench to (c) 0.24, $\varepsilon = 0.4619$, for a shallow quench.

Figure 4.9 (a) shows partial wetting of the layer attached to the surface at $t^* = 8.48 \times 10^{-1}$ earlier than (b) and (c) due to its deeper quench temperature. Higher values of temperature (shallower quench) have lower quench depth amount (ε). This transition from the complete wetted surface to the partial one will happen at earlier time if the quench depth is increased due to the acceleration of the phase separation in deeper quenches. As a result, the deeper the quench is, the quicker the partial wetting will appear at the surface. Figure 4.10 shows this phenomenon for a typical off-critical quench, where only the quench depth at the surface was varied. It can be seen from this figure that the transition time decreases as quench depth increases.

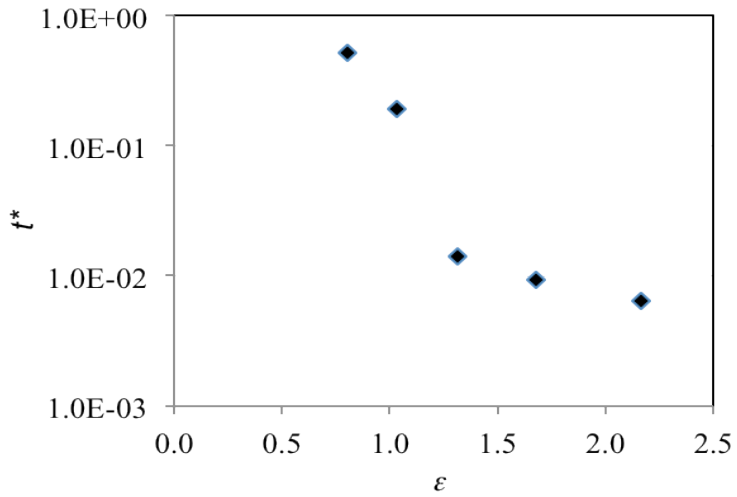

Figure 4.10: Typical transition time from complete wetting to partial wetting for different deep quench depths at the surface in a short-range surface potential case. The parameter values are $c_0^* = 0.4$, $D = 4 \times 10^5$, $h = 0.5$, $g = -0.5$ and $T_2^* = 0.20$. The temperature T_1^* varies from 0.20, $\varepsilon = 0.8514$, for a deep quench to 0.12, $\varepsilon = 2.2500$, for the deepest quench performed.

This trend of faster transition time for deeper quenches happens regardless of the surface attraction strength, the diffusion coefficient or value of the temperature gradient in the system.

4.3.3 Effect of Different Diffusion Coefficients

Figure 4.11 presents the morphology formation for three dimensionless diffusion coefficient values, $D = 3 \times 10^5, 5 \times 10^5$ and 6×10^5. Temperature gradient remained constant at $T_1^* = 0.25$ and $T_2^* = 0.20$. The initial concentration is $c_0^* = 0.4$ for this case but in general, all different initial concentrations follow the same pattern. It can be observed that as expected, the lower diffusion value, $D = 3 \times 10^5$, has less driving force to perform phase separation, hence it needed more time to reach to the final stages of the phase separation process compared to the higher value of the diffusion coefficient, $D = 6 \times 10^5$. It is also shown that at $t^* = 9.75 \times 10^{-3}$ when $D = 6 \times 10^5$, the phase separation is already in the intermediate stage of spinodal decomposition whereas for the lower dimensionless diffusion coefficient of $D = 5 \times 10^5$, the process is just starting to enter the intermediate stage and for $D = 3 \times 10^5$, the phase separation has not started yet. Consequently, as D increases, so does the driving force for the phase separation. It is observed in the morphology that as diffusion coefficient increases, the surface enrichment rate decreases as well. This is due to the high rate of phase separation through the bulk, which leads to the starvation of surface in attracting favorable component. In Figures 4.12 and 4.13, the higher amount of diffusion coefficient leads to higher rate of phase separation within the bulk and creates finer morphology structures in both off-critical (Figure 4.12) and critical (Figure 4.13) cases.

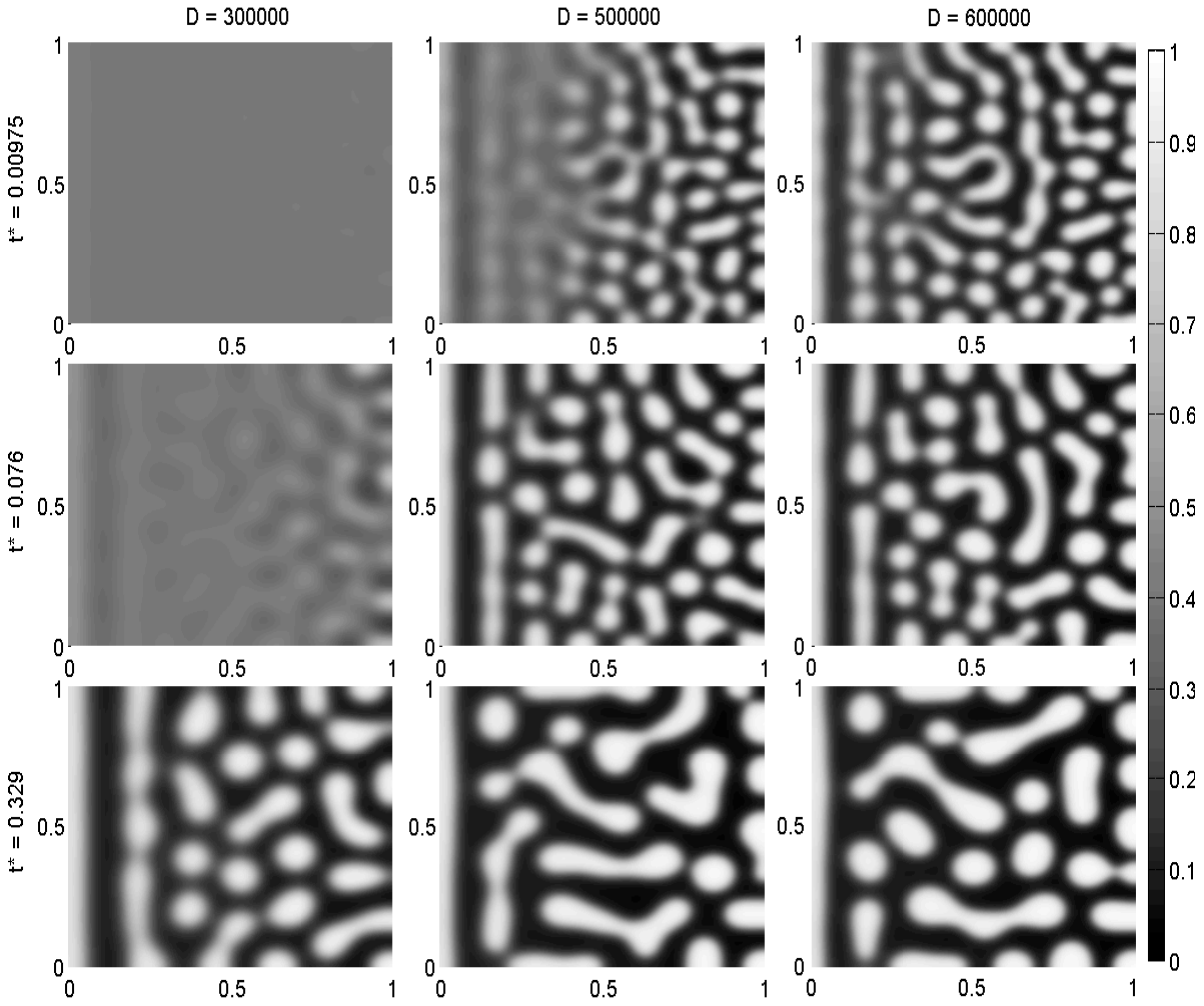

Figure 4.11: Morphology formation for three dimensionless diffusion coefficient values in a short-range surface potential case where (a) $D = 3 \times 10^5$, (b) 5×10^5 and (c) 6×10^5. Temperature gradient remained constant at $T_1^* = 0.25$ and $T_2^* = 0.20$. $c_0^* = 0.4$ (off-critical quench), $h = 1$ and $g = -0.5$. As D increases, so does the driving force for SD phase separation.

Figure 4.13 also confirms the effect of diffusion coefficient on the growth rate of surface-wetting layer in spite of changing parameters h and c_0^* to different values.

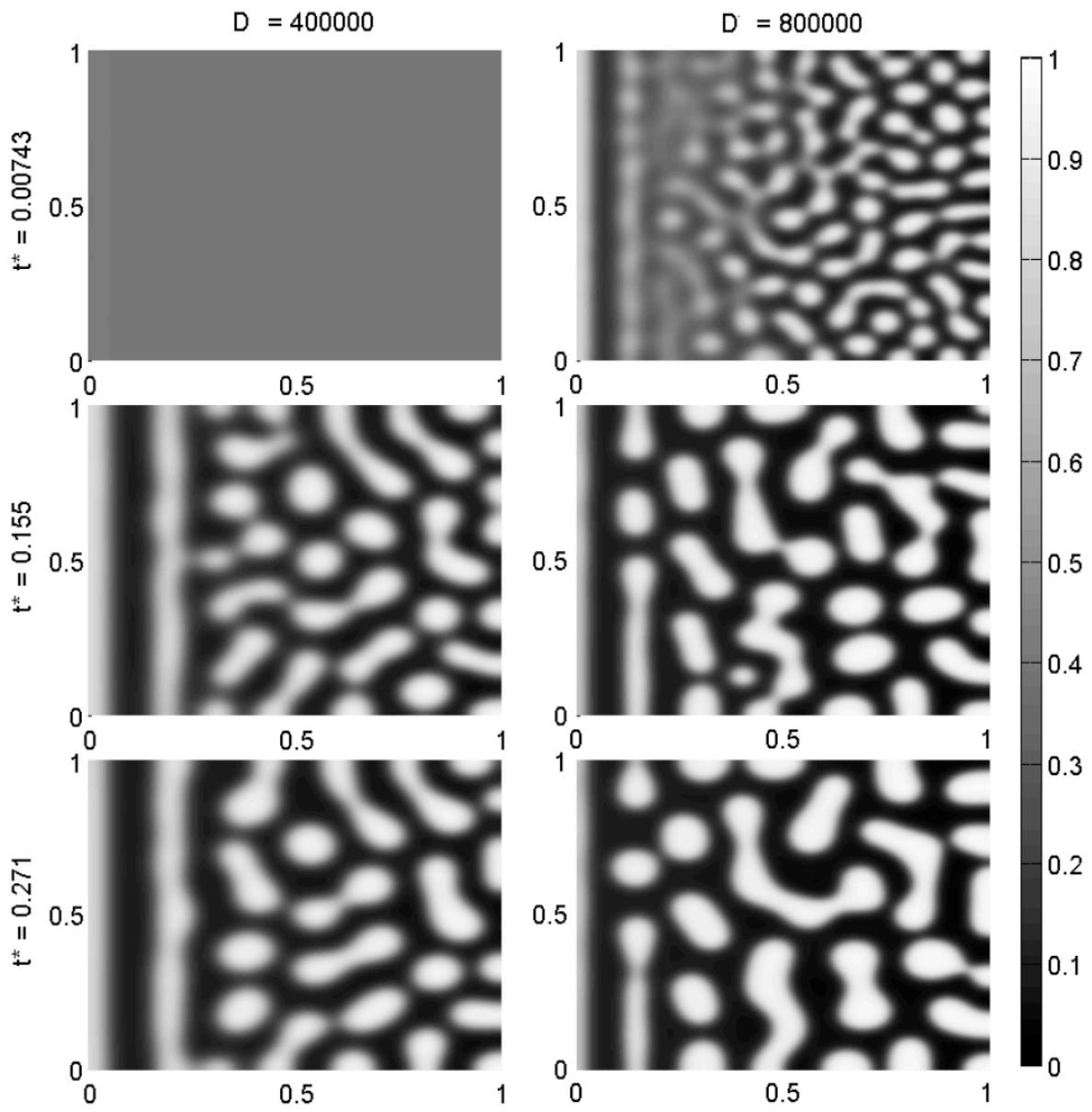

(a) (b)

Figure 4.12: Typical effect of diffusion coefficient value on growth rate of wetting layer on the surface in a short-range surface potential case for (a) $D = 4 \times 10^5$, (b) 8×10^5, $T_1^* = 0.25$, $T_2^* = 0.20$, $c_0^* = 0.4$, $h = 2$ and $g = -0.5$. As D increases, the surface enrichment decreases.

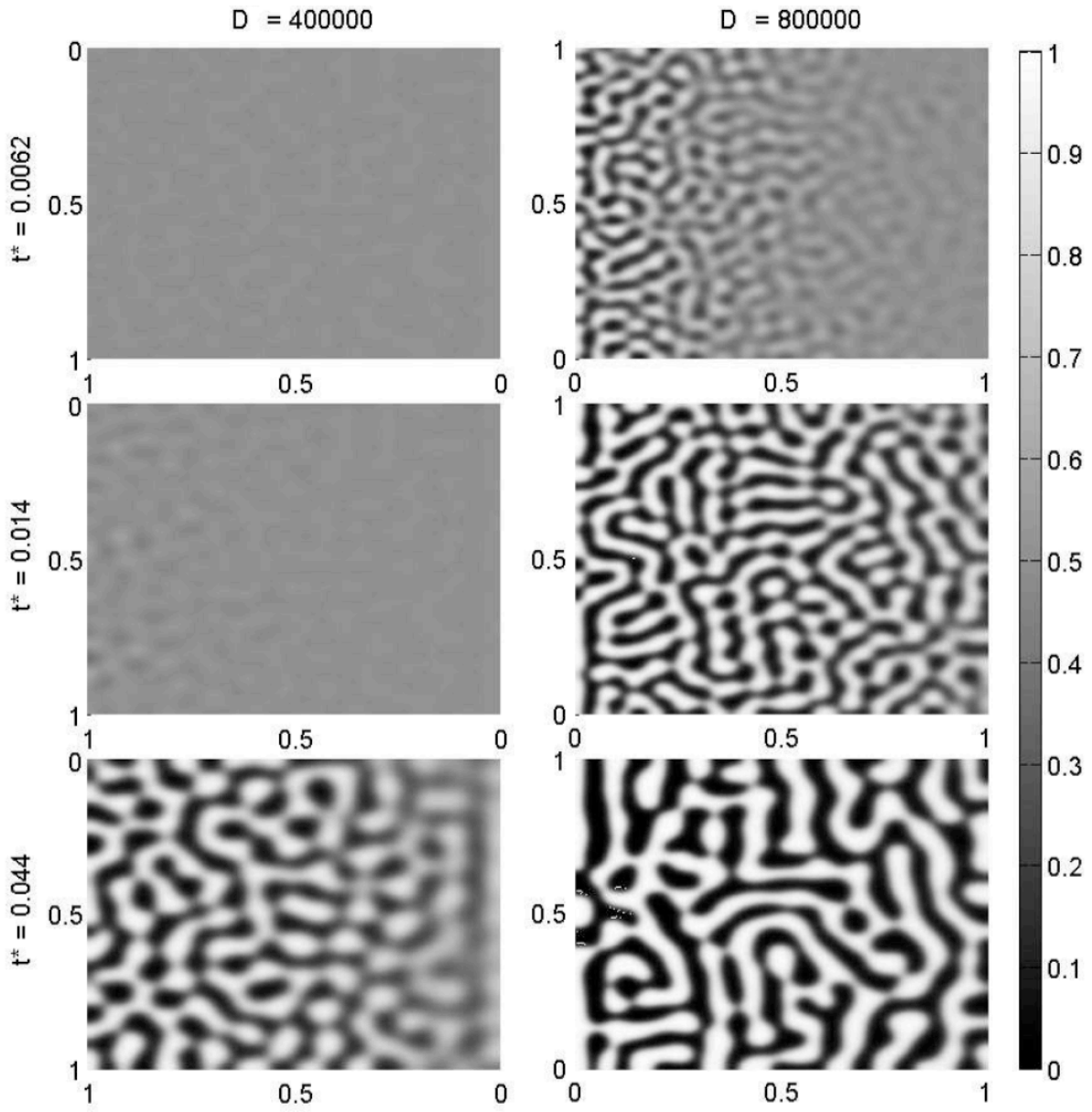

(a) (b)

Figure 4.13: Morphology formation for two dimensionless diffusion coefficient values, (a) $D = 4 \times 10^5$ and (b) 8×10^5 for a critical quench in a short-range surface potential case. $T_1^* = 0.25$, $T_2^* = 0.20$, $c_0^* = 0.5$, $h = 1$ and $g = -0.5$.

The formation of interconnected structure is visible as the result of phase separation in a critical condition ($c_0^* = 0.5$). Figure 4.13 also shows the dependency of the rate of surface enrichment as a function of diffusion coefficient. Thus, the higher values of diffusion coefficient (4.13 b) will cause more separation of phases in addition to increasing the rate of surface enrichment. As time passes, the size of the morphology structure grows to its typical coarsening amount. Thus, the dimensionless diffusion coefficient *D* controls the rate of phase separation. This coefficient, however, does not affect the type of morphology formed; i.e., an interconnected structure (droplet-type morphology) forms after a critical (off-critical) quench into the unstable region of the binary phase diagram. The results are in agreement with extensive numerical work of Chan *et al*. [135,136,138,145,160–163,249,302,317,336,398].

4.3.4 Effect of Temperature Gradient on Surface Enrichment

In this section, the effect of the temperature gradient on the morphology formation is studied. Figure 4.14 shows typical morphology evolution for an off-critical quench where the parameter values are $c_0^* = 0.4$, $D = 4 \times 10^5$, $h = 0.5$, $g = -0.5$ and $T_1^* = 0.25$. The dimensionless temperature T_2^* was then varied from 0.10 to 0.20. It is important to note that phase separation through TIPS method is always induced by temperature quench whether with or without temperature gradient within the bulk. It was observed the influence of the surface potential was not as strong as the role of the temperature in SD phase separation mechanism. In Figure 4.14, the deepest quench, $T_2^* = 0.10$, allowed more polymer component to be attracted to the surface at any specific time.

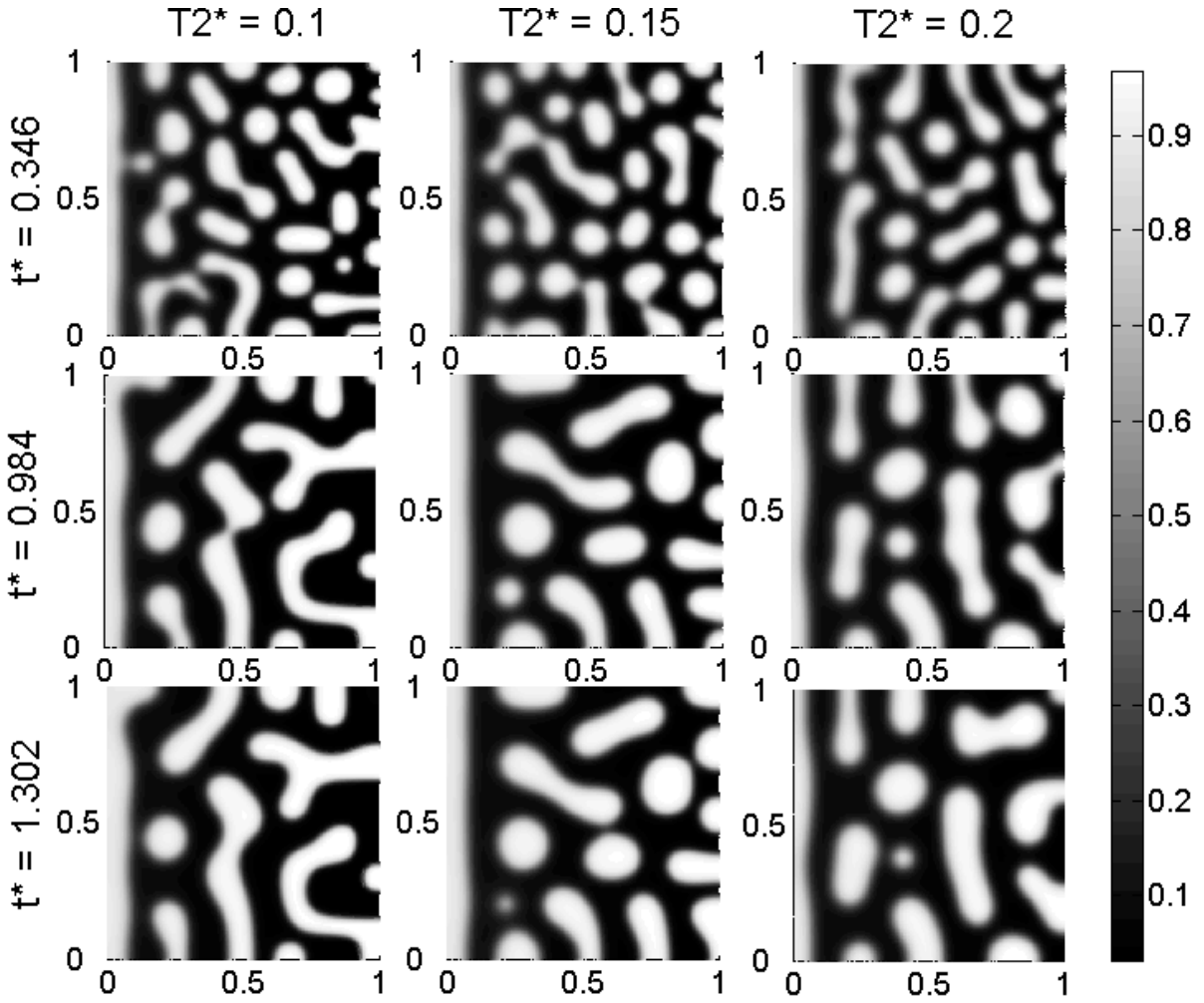

(a) (b) (c)

Figure 4.14: Effect of temperature gradient on surface enrichment growth rate where phase separation is governed by an off critical quenching condition in a short-range surface potential case. The parameter values are $c_0^* = 0.4$, $D = 4 \times 10^5$, $h = 0.5$, $g = -0.5$ and $T_1^* = 0.25$, T_2^* = (a) 0.1, (b) 0.15 and (c) 0.2.

The thickness of the wetting layer for deeper quench (higher temperature gradient with lower temperature at T_2^* side) is bigger than that of the shallower quench depth. This behavior was observed for different values of g, h and D, considering the fact that in competition to

attract favorable polymer to the surface, part of the domain that has a deeper quench is at more advanced stage of the SD phase separation and should attract more material to the region; therefore the surface which favors one of the components will face lack of the material to enrich itself in a higher rate. On the other hand, the initiation of the phase separation on the other side of the domain can boost the phase separation process for the whole domain and make the morphology formation process start at earlier time even for the area with shallower quench depth, T_1^*, which will lead to the higher attraction of the polymer component to the surface as T_2^* decreases; this increases the rate of surface enrichment. To the best of our knowledge, the effect of temperature gradient on surface enrichment when T_1^* is constant and T_2^* is decreasing (non-uniform quench), has been analyzed for the first time in this thesis.

4.3.5 Effect of Surface Potential on Surface Enrichment

Figure 4.15, shows the effect of the surface potential on the surface formation where phase separation is governed by an off-critical quenching condition in a short-range surface potential case. T_1^* and T_2^* are 0.20 and 0.18, respectively and the value of h changes from (a) 0.5 to (b) 2.0 and (c) 6. The higher values of h result in delaying transition time from complete wetting to partial wetting. When the surface potential is high, more favored polymer would be attracted to the surface during early stages of phase separation leading to the faster formation of surface complete wetting. As the system approaches intermediate stages, where phase separation is governed mostly through the bulk, the partial wetting mechanism of the completely wetted layer would be delayed due to the higher surface

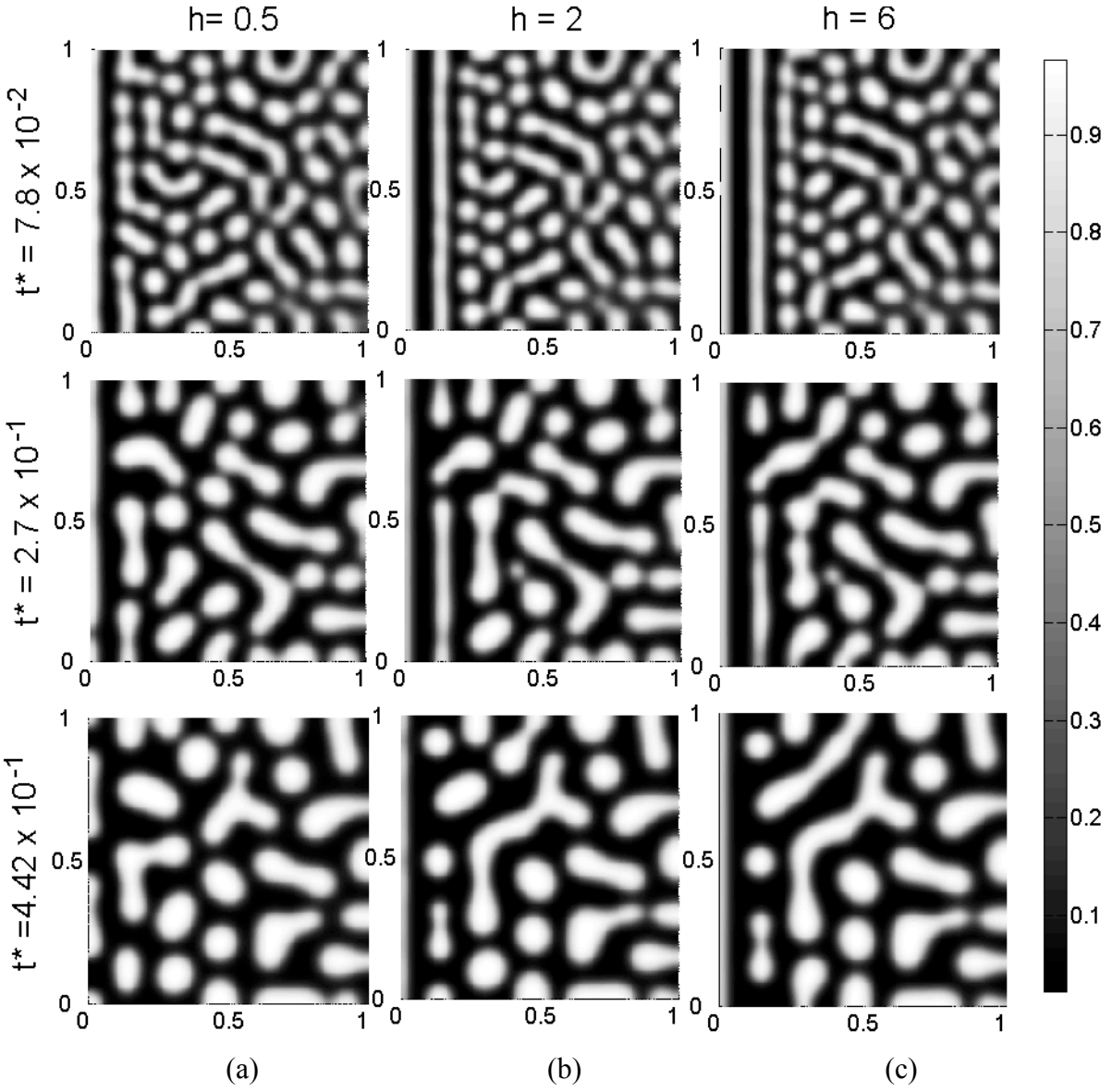

Figure 4.15: Typical effect of the surface potential on the surface formation where phase separation is governed by an off critical quenching condition in a short-range surface potential case. In this case $c_0^* = 0.4$, $g = -0.5$, $D = 4 \times 10^5$, T_1^* and T_2^* are 0.20 and 0.18, respectively and the value of h changes from (a) 0.5 to (b) 2.0 and (c) 6. Higher h values delays the transition from complete wetting to partial wetting.

attraction (h). In Figure 4.15 (a), the bulk domain has initiated the surface partial wetting at $t^* = 2.7 \times 10^{-1}$ earlier than domains of (b) and (c). The domain in Figure 4.15 (b) is about to start its partial wetting at $t^* = 4.42 \times 10^{-1}$ while in (c) there is no sign of partial wetting yet. This complies well with the fact that higher values of surface attraction potential resist against partial wetting and tends to enrich more of the preferred component to the surface. This causes full wetting of the layer close to the surface. The elongated domain morphology is the result of the system concentration being close to its critical value; where the droplets tend to form interconnected structure [218,403,406,407].

The white strip in Figures 4.15 (b) and (c) at $t^* = 7.8 \times 10^{-2}$ show a spinodal decomposition wave directly proportional to the higher values of surface potential h. As time passes, the phase separation in the bulk overcomes the phase separation initiated by the surface leading to rupture of the spinodal decomposition wave [155,222].

Figure 4.16 presents the typical logarithmic structure factor $S^*(k^*_m, t^*)$ as a function of dimensionless time corresponding to the $x^* = 0.125$ case of Figure 4.15 morphologies which shows the effect of the surface potential on the surface vicinity within the bulk where phase separation is governed by an off-critical quenching condition in a short-range surface potential case. Higher values of surface potential resulted in faster transition time from early stage to intermediate stage within the bulk [204]. This is due to the higher attraction of favored polymer to the surface. Referring to Figure 4.15 morphology, Figure 4.17 displays the transition time at $x^* = 0.5$ from the surface (deeper in the bulk), for all surface potential values are equal; an evidence of short-range surface potential case. This result complies well with the previous experimental [401] and numerical [204,395,402] work.

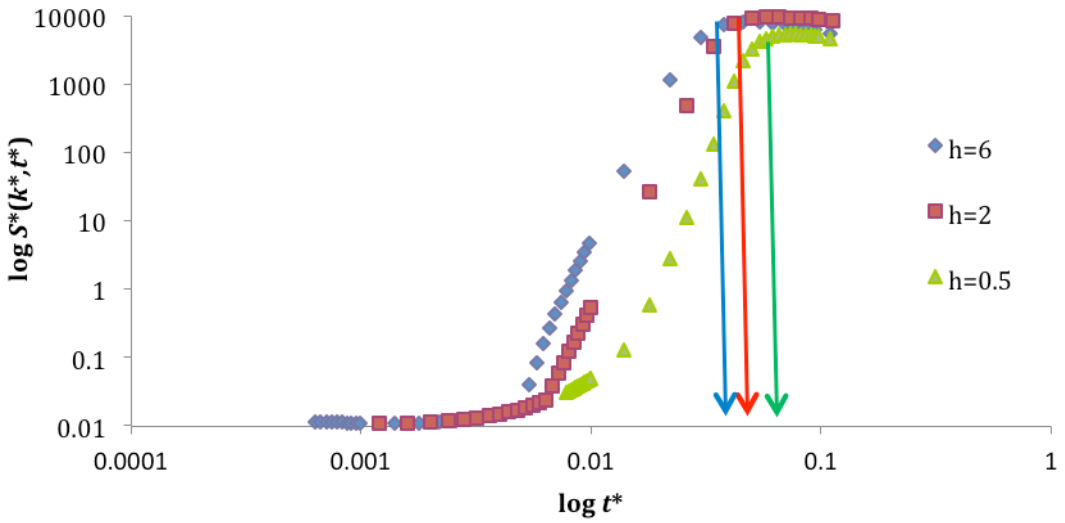

Figure 4.16: Typical logarithmic structure factor $S^*(k^*_m, t^*)$ as a function of dimensionless time corresponding to the case presented in Figure 4.15 in the vicinity of the surface ($x^* = 0.125$) presenting the effect of the surface potential on the surface formation where phase separation is governed by an off-critical quench in a short-range surface potential case. In this case $c_0^* = 0.4$, $g = -0.5$, $D = 4 \times 10^5$, and the value of h changes from (a) 0.5 to (b) 2.0 and (c) 6. Higher h values resulted in faster transition time from earlier stage to intermediate stage within the bulk.

Figure 4.18 shows the typical logarithmic structure factor $S^*(k^*_m, t^*)$ as a function of dimensionless time at the early stages of phase separation, where the slope of tangent lines are measured for different dimensionless horizontal distances from the surface (x^*). For critical quenches, as shown in Figure 4.18 where $c_0^* = 0.5$, the morphology development also occurs faster near the vicinity of the surface wall like in the off-critical quench cases above. Thus, morphology development occurs fastest near the surface wall regardless of initial

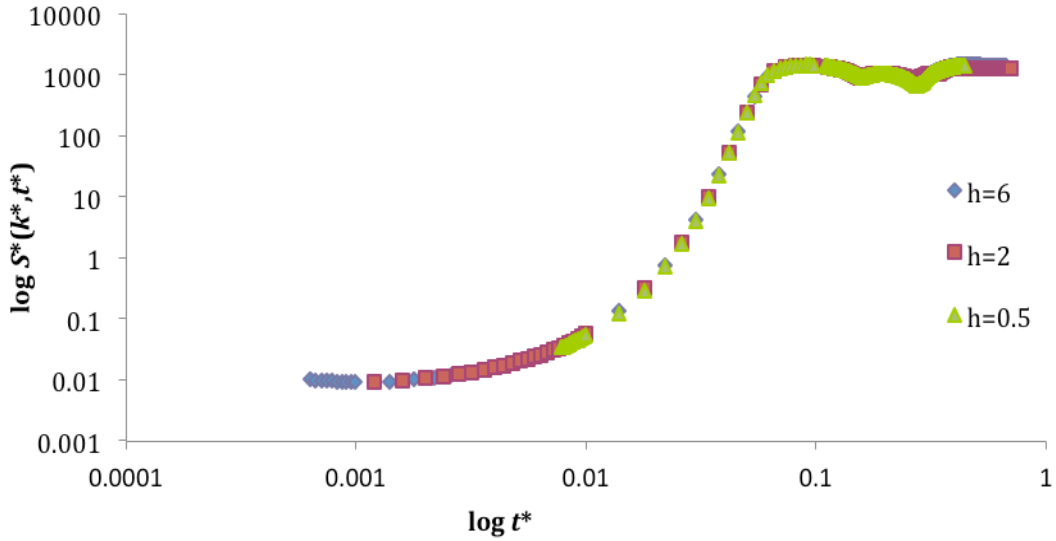

Figure 4.17: Typical logarithmic structure factor $S^*(k^*_m, t^*)$ as a function of dimensionless time corresponding to the case presented in Figure 4.15, where $x^* = 0.5$ presenting the effect of the surface potential on the surface formation where phase separation is governed by an off-critical quench in a short-range surface potential case. In this case $c_0^* = 0.4$, $g = -0.5$, $D = 4 \times 10^5$, and the value of h changes from (a) 0.5 to (b) 2.0 and (c) 6. Different h values have no impact on the transition time from earlier to intermediate stage within the bulk for distances farther away from the surface; an evidence of a short-range surface potential case.

concentration. For $x^* = 0.125$, the slope of the tangent line is the largest, indicating the higher rate of growth in the vicinity of the surface within the bulk as well as faster approach to the transition time of early stage to intermediate stage of SD phase separation within the bulk [173,184,191,198,200]. Figures 4.19 and 4.20 show the typical effect of the surface potential strength to control the evolution and formation of the wetting layer on the surface for critical and off-critical quenching conditions, respectively.

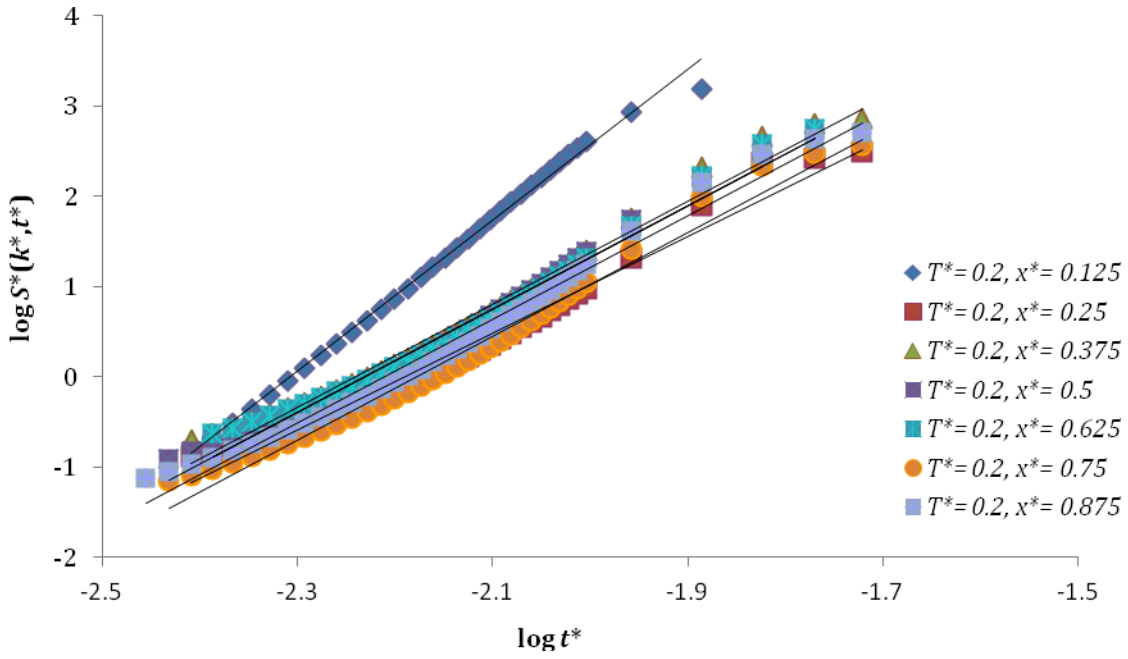

Figure 4.18: Typical logarithmic structure factor $S^*(k^*_m, t^*)$ as a function of dimensionless time, presenting the effect of the surface potential on the transition time approach where phase separation is governed by a critical quench in a short-range surface potential case. In this case $c_0^* = 0.5$, $g = -0.5$, $D = 8 \times 10^5$, $h = 2.0$, and $T_1^* = T_2^* = 0.2$. Slope of the line corresponding to $x^* = 0.125$ is the highest indicating faster morphology development near the surface wall vicinity.

It is shown that for higher h values there is a higher attraction of the favorable component to the surface [395,401,402]. Consequently, after the increase of h from 1 to 2.5, more attraction to the surface was occurred enforcing more complete wetting and delaying the partial wetting. This is due to the fact that complete wetting of the surface has lower system energy, which leads to the full wetting of the surface. Further increase of h to 6.0 resulted to the higher rate of surface enrichment (Figure 4.15). The interconnected structure

presented in Figure 4.20 is obtained as a result of critical quenches, which has been widely explored numerically by Chan *et al*. [135,136,138,145,160–163,249,302,317,336,398] and experimentally by other groups [218,367,368,406,407].

Figures 4.15, 4.19 and 4.20 illustrate the fact that the higher the surface potential is, the more polymer attachment to the surface occurs. As well, in shallow quenches complete wetting proceeds as opposed to deep quenches where partial wetting is favorable. The obtained results are in good agreement with numerical [395,402] and experimental work [212,218,401,406,407] previously performed. Table 4.1 shows how increase of the surface potential value will increase the transition time from complete wetting to the partial wetting on the surface. This trend was expected, as having higher surface potential would help attract the favorable component more aggressively to the surface in competition to the phase separation within the bulk. As a result, in lower surface values partial wetting occurs earlier.

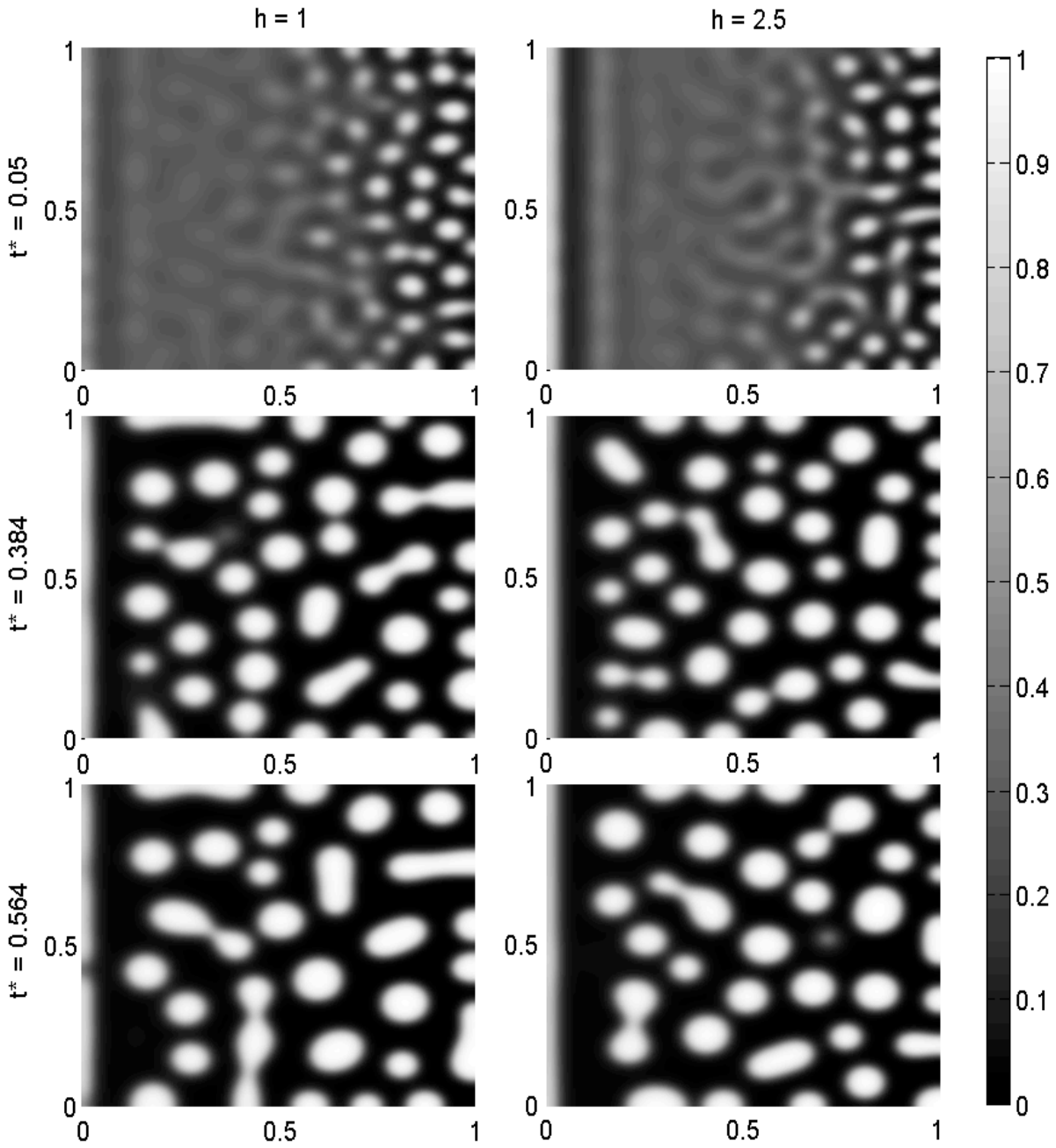

Figure 4.19: Effect of the surface potential on the surface formation where phase separation is governed by an off critical quenching condition in a short-range surface potential case. In this case $c_0^* = 0.3$, $g = -0.5$, $D = 4 \times 10^5$, T_1^* and T_2^* are 0.20 and 0.15, respectively and the value of h changes from (a) 1 to (b) 2.5.

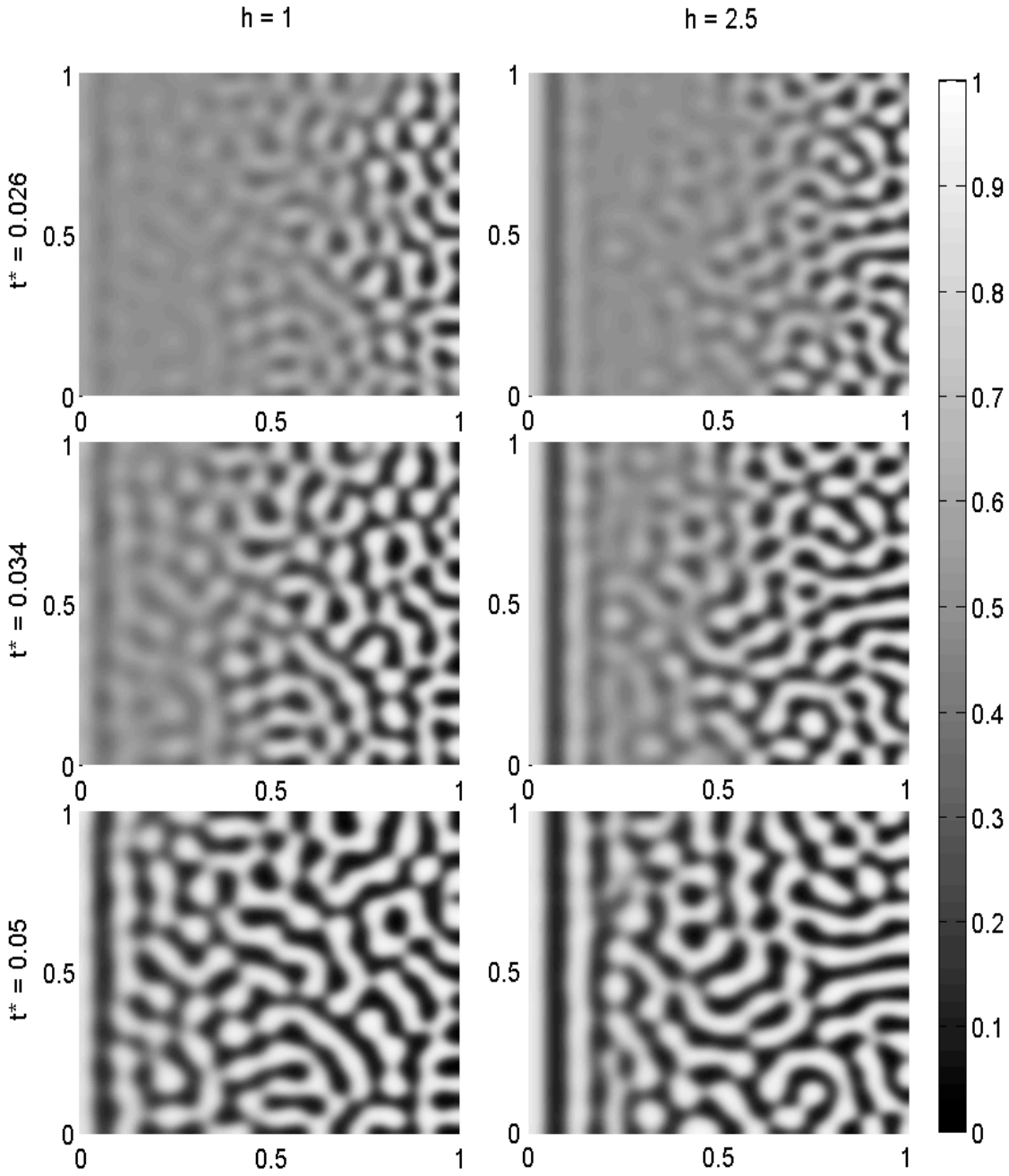

Figure 4.20: Effect of the surface potential on the surface formation where phase separation is governed by a critical quenching condition in a short-range surface potential case. In this case $c_0^* = 0.5$, $g = -0.5$, $D = 4 \times 10^5$, T_1^* and T_2^* are 0.20 and 0.15, respectively and the value of h changes from (a) 1 to (b) 2.5.

Table 4.1: Change of partial wetting to complete wetting transition by increasing the h value, for $c_0^* = 0.4$, diffusion coefficient, $D = 4 \times 10^5$, surface coefficients, $g = -0.5$, T_1^* and T_2^* are 0.20 and 0.15, respectively. PW (CW) stands for partial (complete) wetting.

c_0^*	D	T_1^*	T_2^*	g	h	Wetting	Time PW Observed
0.4	400000	0.20	0.15	– 0.1	0.1	PW	0.0034
0.4	400000	0.20	0.15	– 0.1	0.5	PW	0.356
0.4	400000	0.20	0.15	– 0.1	1	PW	0.371
0.4	400000	0.20	0.15	– 0.1	2	CW	N/A
0.4	400000	0.20	0.15	– 0.1	3	CW	N/A

4.4 Summary & Conclusions

In this chapter, the nonlinear Cahn-Hilliard theory and the Flory-Huggins theory were used to study numerically the phase separation phenomena of a model binary polymer blend quenched into the unstable region of its binary symmetric phase diagram. Short-range surface potential within a simple geometry, where one side of the domain is exposed to a surface with preferential attraction to one component of a binary polymer blend under temperature gradient in x direction, was integrated in the model. The initial conditions reflected the infinitesimal thermal concentration fluctuations in the blend. In order to solve the governing equation in a two-dimensional domain, according to the method of line, the equation was spatially discretized using finite difference method. The resulting set of ODE's was then solved by CVODE solver. The numerical solutions and calculated morphologies replicate frequently reported experimental observations and numerical work.

The impacts of different quench depths, diffusion coefficients, surface potentials, temperature gradients, and concentrations were studied numerically. The results have been presented in the form of morphology plots, and validated by logarithmic graphs in which they replicated comparable experimental and numerical work performed by other groups.

The structure factor analysis showed a faster exponential growth at the early stage of phase separation and a slower growth rate at the intermediate stage with a slope of 0.31 through the bulk; consistent with Lifshitz-Sloyozov (LS) law. The investigation of surface enrichment rate at the surface wall demonstrated faster growth rate at the early stage with the slope of 0.5. This rate of growth became slower at the intermediate stage with a slope of 0.13 near the surface; consistent with experimental observations. To examine the role of quench depths in the phase separation morphology, the following results were obtained: deeper quenches led to the i) faster transition time from complete wetting to partial wetting of the surface, ii) higher rate of morphology development within the bulk that contributed to faster transition time from early to intermediate stage, iii) lower surface enrichment due to losing the competition to the bulk in attracting favorable polymer to the surface, and iv) smaller droplets and finer morphology formation.

Higher diffusion coefficients led to the increase of phase separation driving force and consequently the faster morphology development. For critical quenches ($c_0^* = 0.5$), the interconnected morphology, near critical ($c_0^* = 0.4$), elongated structure, and for off-critical quenches ($c_0^* = 0.3$), droplet-like morphology was obtained in agreement with experimental and numerical work.

The influence of various temperature gradient values on the surface enrichment rate with the constant temperature T_1^* at the surface and different temperature T_2^* for the opposite surface was studied for the first time. The results showed that the thickness of the wetting layer increased by rise of ΔT^* value where the side with T_2^* temperature goes under deep quench. This feature is due to the phase separation starting at earlier stage at the wetting surface region since the other part of the sample that is in more advanced stage could stimulate the initiation of phase separation earlier in all domains.

The development of structure factor analysis over the surface potential effect on the phase separation within the bulk close to the surface showed earlier transition time for higher values of h. However, there was no difference observed for transition time within the bulk at distances farther away from the surface. As surface potential increased, spinodal wave became more visible in the bulk and the transition time from complete wetting to partial wetting occurred at a later time on the surface.

Chapter 5

5. Multiple Range Surface Potential

In this section, a model, composed of the nonlinear Cahn-Hilliard and Flory Huggins-de Gennes theories, is developed to numerically simulate the surface directed phase separation and pattern formation phenomena of a representative binary polymer blend with a surface attraction on *all sides* of the domain when it is quenched into the unstable region of its binary phase diagram. The model incorporates the surface potential field and thermal diffusion phenomena under the externally imposed spatial temperature gradient. The results are presented and discussed in detail in the form of morphology formation and surface enrichment growth rate. Effects of quench depth; diffusion coefficient, surface potential and temperature gradient are as well investigated over surface enrichment.

5.1 Model Development

The model development steps and equations for multiple-surface attraction case including initial condition, method of lines, discretization in space and using CVODE solver are all exactly the same as short-range surface potential case discussed in detail in Chapter 4. The nonlinear Cahn-Hilliard [149] theory (Equation 4.1) incorporating the Flory-Huggins-de Gennes [82,259] (Equation 4.2) free energy theory is used to study TIPS phenomenon in binary polymer blends with competing surface and temperature gradient effects. The

governing equation obtained for the multiple-range potential case is also the same as Equation 4.22. The only difference appeared in boundary conditions since all surfaces of the domain take part in the wetting process.

5.1.1 Boundary Conditions

In the multiple-range surface potential case the model domain is composed of four surfaces where *all* of them have surface potential attraction. Each surface will have two boundary conditions. Assuming an external surface potential in the system for all domain sides with surface attraction, the first boundary condition (suggested by Schmidt and Binder [345]) would become:

Surface 1 ($x^* = 0$):

$$-h_1 - gc_1^* + \gamma \left. \frac{\partial c^*}{\partial x^*} \right|_{x^*=0} = 0 \tag{5.1}$$

Surface 2 ($x^* = 1$):

$$-h_2 - gc_1^* + \gamma \left. \frac{\partial c^*}{\partial x^*} \right|_{x^*=1} = 0 \tag{5.2}$$

Surface 3 ($y^* = 0$):

$$-h_3 - gc_1^* + \gamma \left. \frac{\partial c^*}{\partial y^*} \right|_{y^*=0} = 0 \tag{5.3}$$

Surface 4 ($y^* = 1$):

$$-h_4 - gc_1^* + \gamma \left. \frac{\partial c^*}{\partial y^*} \right|_{y^*=1} = 0 \tag{5.4}$$

whereas h_1 to h_4 represent the surface potential of each surface with preference to one of the components, g shows the change interaction near the surfaces in the underlying lattice model and γ is related the bulk correlation length. The second boundary condition confirms that no penetration of material is possible through the boundary surfaces and no mass will be exchanged with the surrounding. In other words, at each surface, the concentration flux is zero and there is a no-flux boundary condition [135,136,346]:

$$J\big|_{x^*=0} = 0 \tag{5.5}$$

or

$$\nabla^3 c^* = 0 \tag{5.6}$$

Therefore, for $x^* = 0$, the following boundary conditions are obtained:

$$\left. \frac{\partial c^*}{\partial x^*} \right|_{x^*=0} = \frac{h_1 + gc^*}{\gamma} \tag{5.7}$$

$$\frac{\partial^3 c^*}{\partial x^{*3}} + \frac{\partial^3 c^*}{\partial x^* \partial y^{*2}} = 0 \tag{5.8}$$

and for $y^* = 0$:

$$\left. \frac{\partial c^*}{\partial y^*} \right|_{y^*=0} = \frac{h_2 + gc^*}{\gamma} \tag{5.9}$$

$$\frac{\partial^3 c^*}{\partial y^{*3}} + \frac{\partial^3 c^*}{\partial y^* \partial x^{*2}} = 0 \tag{5.10}$$

and for $x^* = 1$:

$$\left.\frac{\partial c^*}{\partial x^*}\right|_{x^*=1} = \frac{h_3 + gc^*}{\gamma} \tag{5.11}$$

$$\frac{\partial^3 c^*}{\partial x^{*3}} + \frac{\partial^3 c^*}{\partial x^* \partial y^{*2}} = 0 \tag{5.12}$$

and for $y^* = 1$:

$$\left.\frac{\partial c^*}{\partial y^*}\right|_{y^*=1} = \frac{h_4 + gc^*}{\gamma} \tag{5.13}$$

$$\frac{\partial^3 c^*}{\partial y^{*3}} + \frac{\partial^3 c^*}{\partial y^* \partial x^{*2}} = 0 \tag{5.14}$$

5.2 Results and Discussion

In this section numerical results and discussion will be presented for multiple-range surface potential. The focus is on the formation and evolution of the phase separated-structures and the different factors that control the morphology to fabricate functional polymeric material. Similar to short-range surface attraction model, only the early and intermediate stages of phase separation were emphasized in this study. The temperature on surface h_1 is T_1^* and on the opposite side h_3 is T_2^* (Figure 5.1). Figure 5.1 is a schematic diagram of the bulk geometry with different h values and temperature gradient for the multiple-surface attraction case.

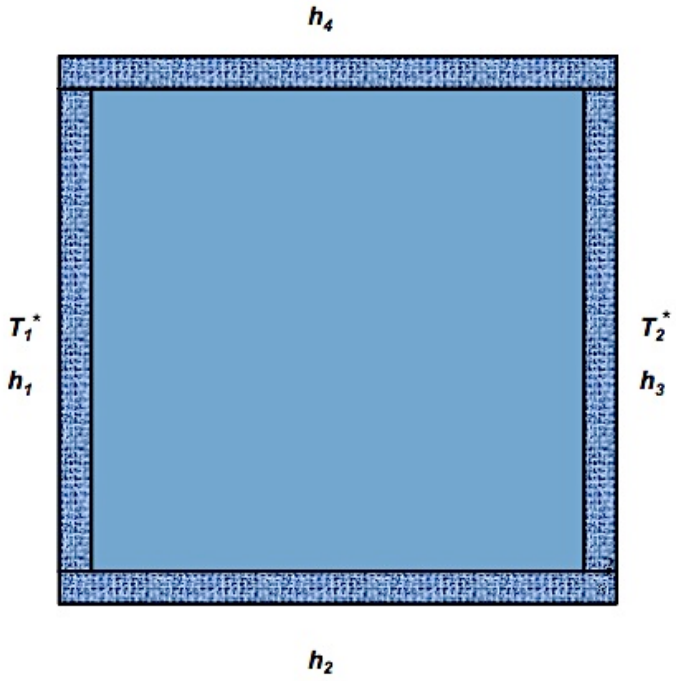

Figure 5.1: Schematic representation of the temperature gradient and positioning of different surface potential values for a multiple-surface attraction case. The temperature difference between sides with surface potentials h_1 and h_3 will induce the linear temperature gradient.

While all surfaces will favor attraction to one component, the linear temperature gradient is only caused by the temperature difference between sides with surface attractions h_1 and h_3. Sides with surface potentials h_2 and h_4 will have linear temperature gradient as well affected by the temperature difference between sides with h_1 and h_3. The linear temperature gradient is considered since temperature distribution occurs within a short range of distance [399,400].

5.2.1 Morphology Formation and Surface Enrichment

In multiple-surface potential cases, the morphology formation of the polymer binary blend under temperature gradient as well as each surface attraction to one of the polymers have been studied. The rate of the growth of the wetting layer for cases that the attracting surfaces were wetted by one polymer is compared with literature values. As mentioned before, morphology formation and its evolution rate after the thermal induced spinodal decomposition process depends on the temperature that blends are quenched to (known as quench depth), diffusion coefficient, the molecular weight of each component (the degree of polymerization) and the miscibility of the two components.

In multiple-surface cases, for the surface directed phase separation, the amount of each surface attraction to the favorable component could influence the nature of complete or partial wetting, as well as the rate of the enrichment of each surface. It is the same mechanism as for the short-range surface potential case with the difference of having all four surfaces engaged in attracting favored polymer. For this reason, each surface would act like a short-range surface potential case contributing to the phase separation of the whole domain. The effect of the above parameters on the formation of the morphology has been studied as well.

5.2.2 Effect of Different Diffusion Coefficients

The morphology formation for three dimensionless diffusion coefficient values, $D = 2 \times 10^5$, 4×10^5 and 8×10^5 is presented in Figure 5.2. Temperature gradient was imposed from

T_1^* = 0.15 to T_2^* = 0.25 in a multiple-surface attraction potential case where all surface potential values are the same ($h_1 = h_2 = h_3 = h_4 = 0.5$). The constant concentration is c_0^* = 0.5 for this case. As observed before in short-range surface attraction case, the lower diffusion value, $D = 2 \times 10^5$, has less driving force to induce phase separation within the bulk in multiple-surface attraction case. Thus it needed more time to reach to the final stages of the phase separation process compared to the higher value of the diffusion coefficient, $D = 8 \times 10^5$.

The morphology confirms that as the diffusion coefficient increases, similar to the short-range cases, rate of phase separation will increase in all four surfaces correspondingly. It is also shown that when $D = 8 \times 10^5$, the phase separation is in the termination of its intermediate stage of spinodal decomposition at $t^* = 0.0318$, whereas for the lower dimensionless diffusion coefficient of $D = 2 \times 10^5$, the separation is not started yet. The formation of interconnected structure is visible as the result of phase separation in a critical quenching condition ($c_0^* = 0.5$). The figure shows that phase separation starts first from the side that undergoes a deeper quench depth ($T_1^* = 0.15$). Figure 5.2 (a, b and c) also confirms the effect of diffusion coefficient on the growth rate of surface-wetting layer. Rate of surface enrichment will decrease as the diffusion coefficient increases. By increasing the diffusion coefficient, the phase separation through the bulk will undergo a faster rate and thus there is less favored component for the surfaces to attract for their enrichment.

To study the effect of diffusion coefficient better on the rate of phase separation through the bulk, a typical evolution of the dimensionless structure factor for critical quench

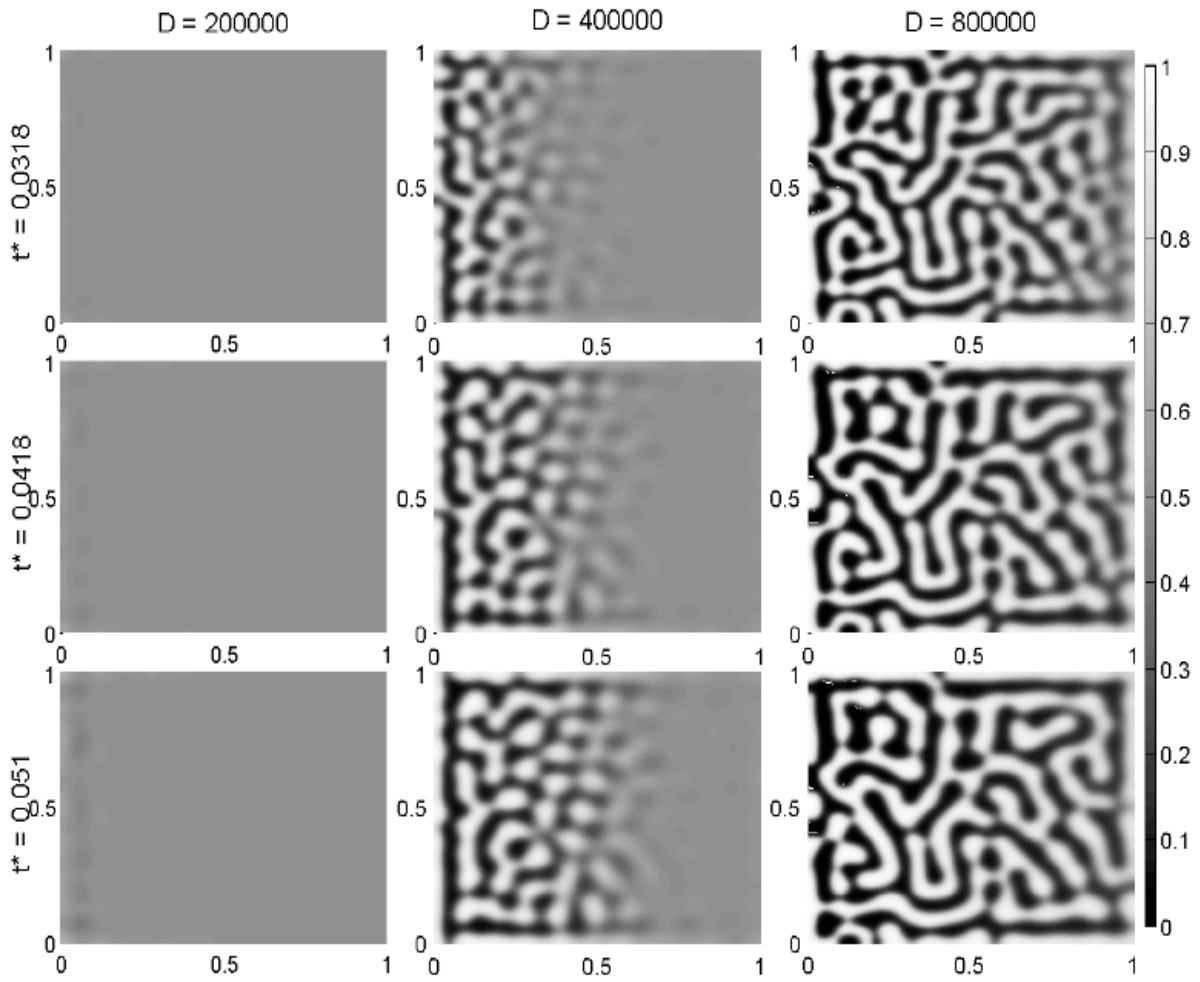

(a) (b) (c)

Figure 5.2: Typical morphology formation for three dimensionless diffusion coefficient values (a) $D = 2 \times 10^5$ (b) $D = 4 \times 10^5$ and (c) $D = 8 \times 10^5$ in a multiple-surface attraction case where phase separation is governed by a critical quenching condition. Temperature gradient remained constant at $T_1^* = 0.15$ and $T_2^* = 0.25$, $c_0^* = 0.5$, $h_1 = h_2 = h_3 = h_4 = 0.5$, $N = 1000$ and $g = -0.5$.

at different dimensionless times in a multiple-surface potential phase separation model is developed (Figure 5.3).

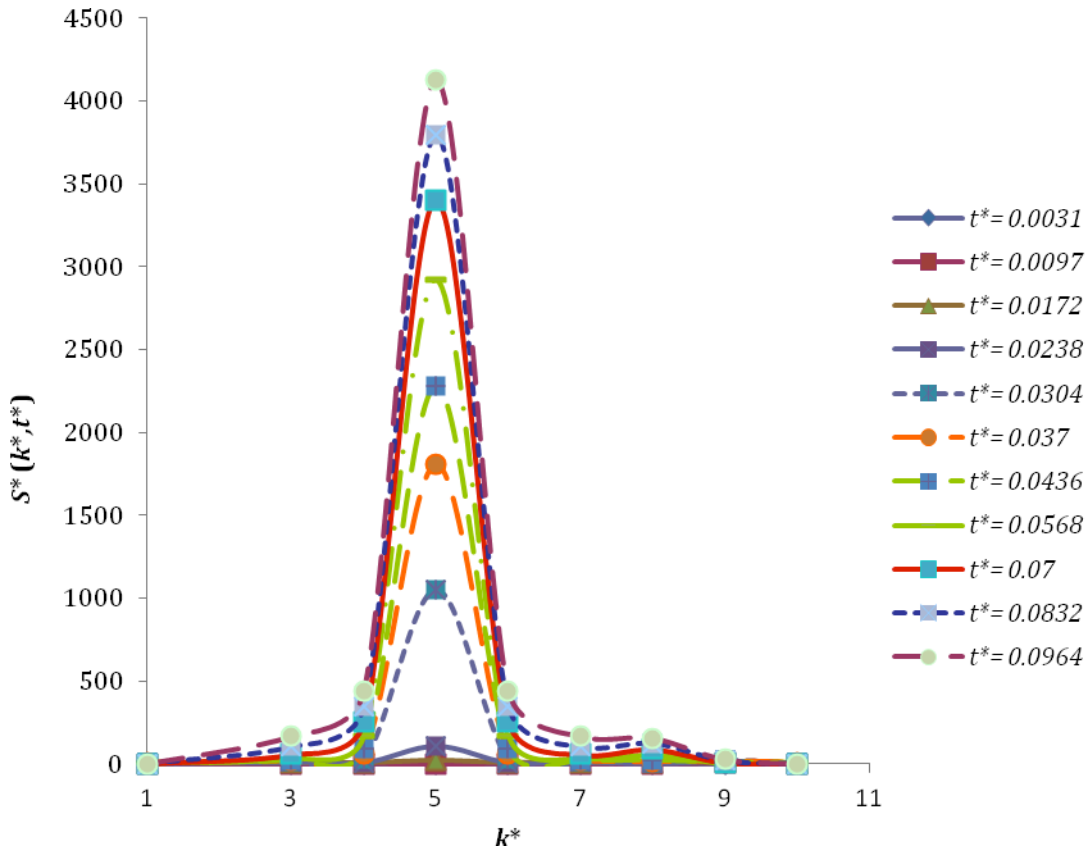

Figure 5.3: Typical evolution of the dimensionless structure factor for critical quench from a one-phase region into the two-phase region at different dimensionless times in a short-range surface potential phase separation model (Figure 5.2 b) under temperature gradient where $D = 4 \times 10^5$, $c_0^* = 0.5$, $h_1 = h_2 = h_3 = h_4 = 0.5$, $N = 1000$ and $g = -0.5$.

It can be observed that the value of the dimensionless structure factor increases exponentially with time in the early stages of phase separation by SD and begins to slow down as it approaches the beginning of the intermediate stages where nonlinear effects come into play. Also, during the early to the beginning of the intermediate stages, the wave number is constant and this is typical of what should be observed [164]. Therefore, the evolution of

the dimensionless structure factor (exponential growth and fixed wave number) for the critical quench case show the same trends that have been reported both in experiment [164,304,355,371] and numerical work [135,136,145,307,317,336,375,400].

Figure 5.4 presents the morphology representation of the numerical modeling resulted from the investigation of the relationship between the diffusion coefficient and different surface potential values for a multiple surface attraction potential case. To verify the impact of the diffusion coefficient on surface enrichment, different values of surface attraction potential (h) were incorporated in the domain. In this case, surface potential values have been selected to be: $h_1 = 0.5$, $h_2 = 1.0$, $h_3 = 2.0$ and $h_4 = 4.0$ [345]. Thus, the higher values of diffusion coefficient have shown to induce more phase separation through the bulk while decreasing the rate of surface enrichment. The results show that regardless of surface attraction magnitude the reduction of surface enrichment growth rate with increasing diffusion coefficient continued.

In Figure 5.4 (a), the phase separation within the bulk occurs with a slower pace as opposed to Figures (b) and (c). In this case, temperature has been considered constant with no gradient. When the model carries different surface potentials, it is observed that there exists a competition between the surfaces in attracting the favored component irrespective of diffusion coefficient values.

In brief, the increase of diffusion coefficient led to an accelerated phase separation through the bulk. The results are in agreement with extensive numerical work of Chan *et al*. [135,160,161,317].

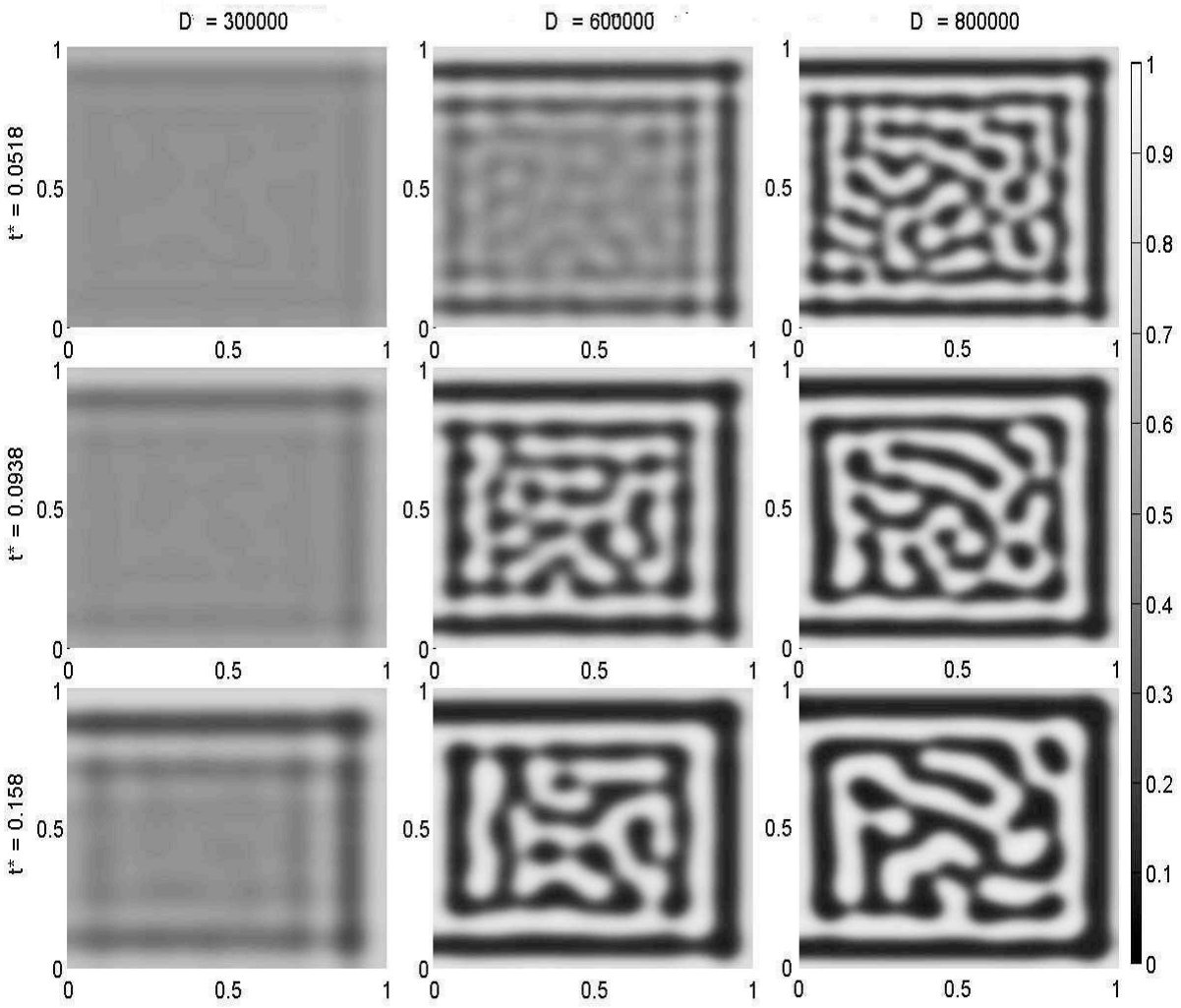

(a) (b) (c)

Figure 5.4: Morphology formation for three dimensionless diffusion coefficient values, (a) $D = 3 \times 10^5$ (b) $D = 6 \times 10^5$ and (c) $D = 8 \times 10^5$ in a multiple-surface attraction case where phase separation is governed by a critical quenching condition with no temperature gradient ($T_1^* = T_2^* = 0.25$), $c_0^* = 0.5$, $h_1 = 0.5$, $h_2 = 1.0$, $h_3 = 2.0$, $h_4 = 4.0$, $N = 1000$ and $g = -0.5$.

5.2.3 Effect of Quench Depth on Surface Enrichment

Figure 5.5 presents the morphology formation of different quench depths with constant surface potentials. Figure 5.5 displays that the deeper the quench temperature is, the faster the rate of phase separation will be. For this reason, the partial wetting is approached earlier by the surfaces. It is noticeable that the formed morphologies have different sizes such that for deeper quenches the size of the interconnected/droplet type structure has smaller sizes compared to shallower quenches [162,173,200,205,224,228,303,336,365,368,369]. Figure 5.5 confirms the fact that deeper quench accelerates the rate of phase separation. The interconnected type morphology is also seen for critical quenching conditions. In Figure 5.5 (a), at $t^* = 0.0932$ for $T_1^* = T_2^* = 0.20$, all surfaces have reached their partial wetting while in shallow quenches (Figure 5.5 b) the surfaces are completely wetted since there is not enough phase separation within the bulk, therefore each surface continues to get enriched by attracting more favored component. Although, if given enough time to the bulk, the transition to partial wetting will take place but it occurs at a very late time [218,406,407].

It is noticeable in Figure 5.5 that in both shallow and deep quenches within the bulk domain, the obtained morphology is symmetric. This is because of the uniform surface attraction applied by all sides of the domain as well as the uniform quench depth within the bulk. Figure 5.6 is a logarithmic dimensionless structure factor versus dimensionless time diagram at different dimensionless horizontal distance of domain (x^*). The figure shows the scale factor of obtained morphology at $x^* = 0.125$ and $x^* = 0.875$ (having the same distance from the domain center) as well as $x^* = 0.25$ and $x^* = 0.75$ are identical over the phase separation time period.

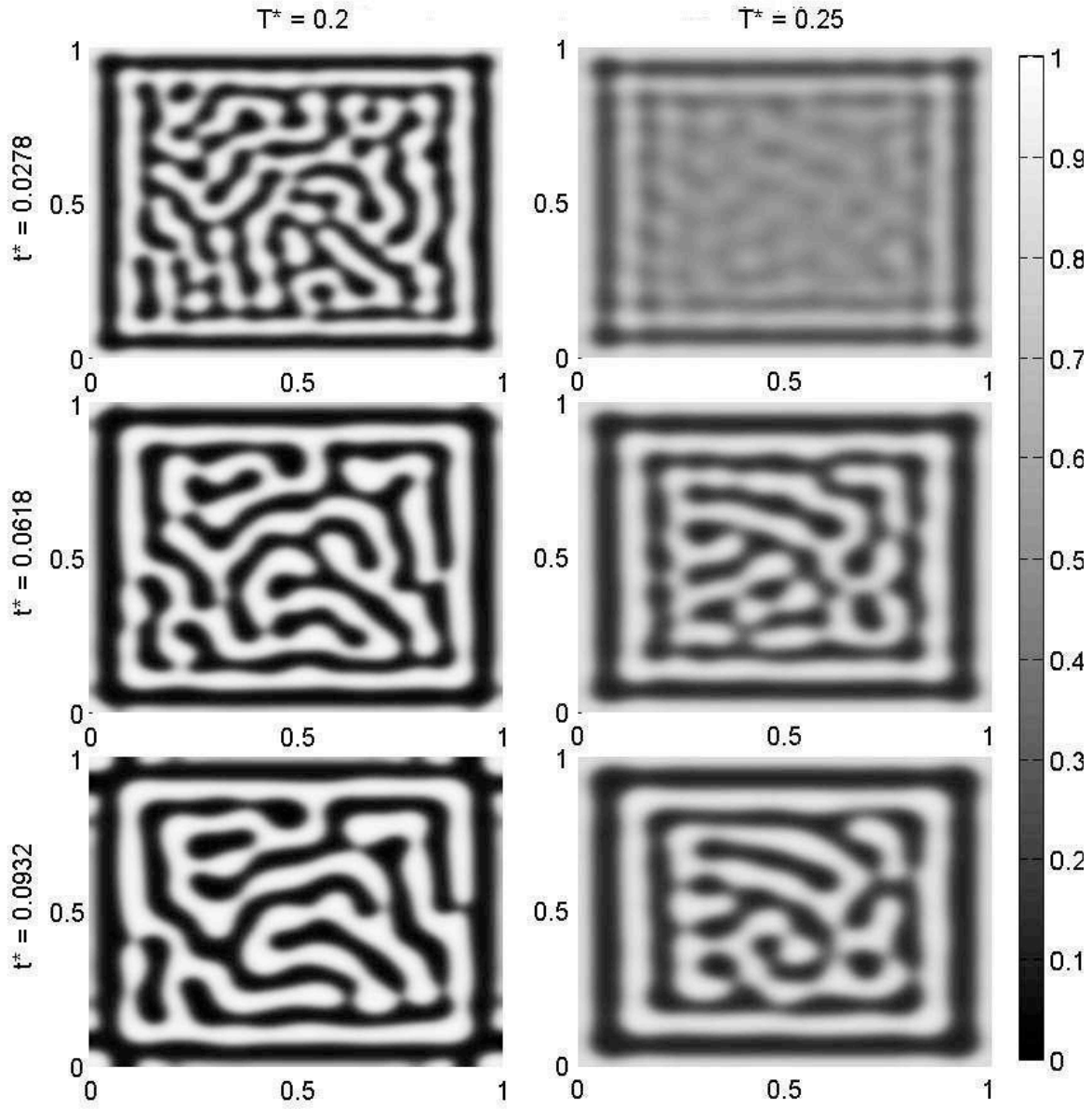

(a) (b)

Figure 5.5: Morphology formation of (a) deep and (b) shallow critical temperature quench in a multiple-surface attraction case where the surface potential is the same for all surfaces. In this case, the parameter values are $c_0^* = 0.5$, $D = 8 \times 10^5$, $h_1 = h_2 = h_3 = h_4 = 2.0$, $N = 1000$, $g = -0.5$. The initial temperature is lowered to (a) $T_1^* = T_2^* = 0.20$, $\varepsilon = 0.8768$, for a deep quench and (b) $T_1^* = T_2^* = 0.25$, $\varepsilon = 0.4514$, for a shallow quench.

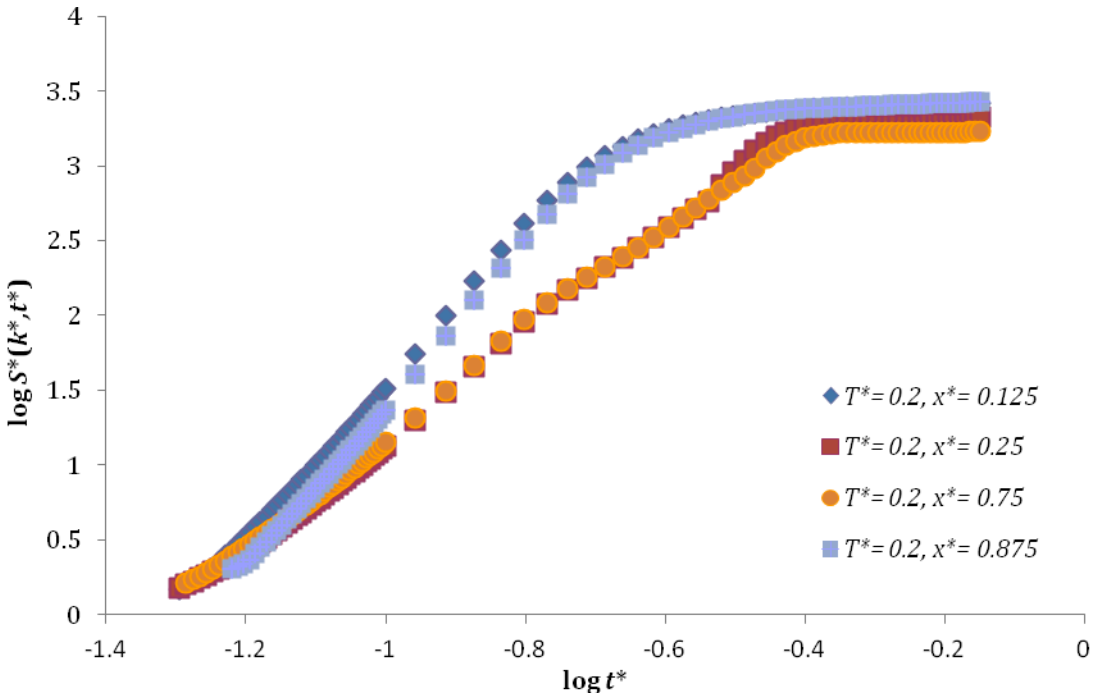

Figure 5.6: Logarithmic dimensionless structure factor versus dimensionless time diagram at different dimensionless horizontal distance of domain (x^*) corresponding to parameter values: $c_0^* = 0.3$, $D = 2 \times 10^5$, $h_1 = h_2 = h_3 = h_4 = 2.0$, $N = 1000$, $g = -0.5$ and $T_1^* = T_2^* = 0.20$.

The resulting trend depicted in Figure 5.6 has been observed in both off-critical and critical concentration values indicting the concentration independence nature of transition time in SD phase separation mechanism within the bulk. To confirm the generality of this trend the concentration has been selected to be off-critical ($c_0^* = 0.3$) for both Figures 5.6 and 5.7.

To further analyze the transition time of SD phase separation mechanism within the bulk, the logarithmic structure factor $S^*(k^*, t^*)$ as a function of dimensionless time is developed in Figure 5.7.

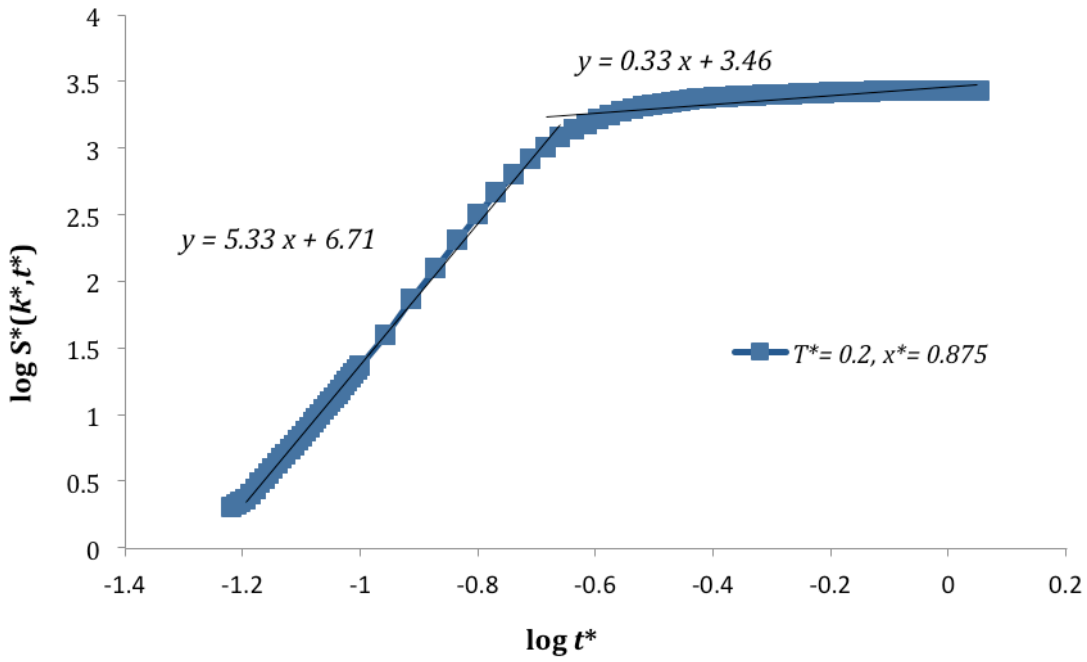

Figure 5.7: Logarithmic dimensionless structure factor versus dimensionless time diagram at different dimensionless horizontal distance of domain (x^*) corresponding to parameter values: $c_0^* = 0.3$, $D = 2 \times 10^5$, $h_1 = h_2 = h_3 = h_4 = 2.0$, $N = 1000$, $g = -0.5$ and $T_1^* = T_2^* = 0.20$.

Using the tangent lines drawn over early stage and intermediate stage crossover region, a growth exponent of 0.33 (slope of tangent line) for intermediate stage of SD phase separation in the model bulk is observed. The result is consistent with previous numerical [173,184,191,199,209,215,217,385,387–389] and experimental [198,212,221,386,390,391] work, though, dominant interface diffusion at very low temperature can give rise to different values of the exponent [384].

Figure 5.8 presents effect of different off-critical quench depths on the morphology of phase separation in a multiple-surface attraction case where the parameter values are $c_0^* = 0.4$, $D = 2 \times 10^5$, $h_1 = 1.0$, $h_2 = 2.0$, $h_3 = 3.0$ and $h_4 = 4.0$.

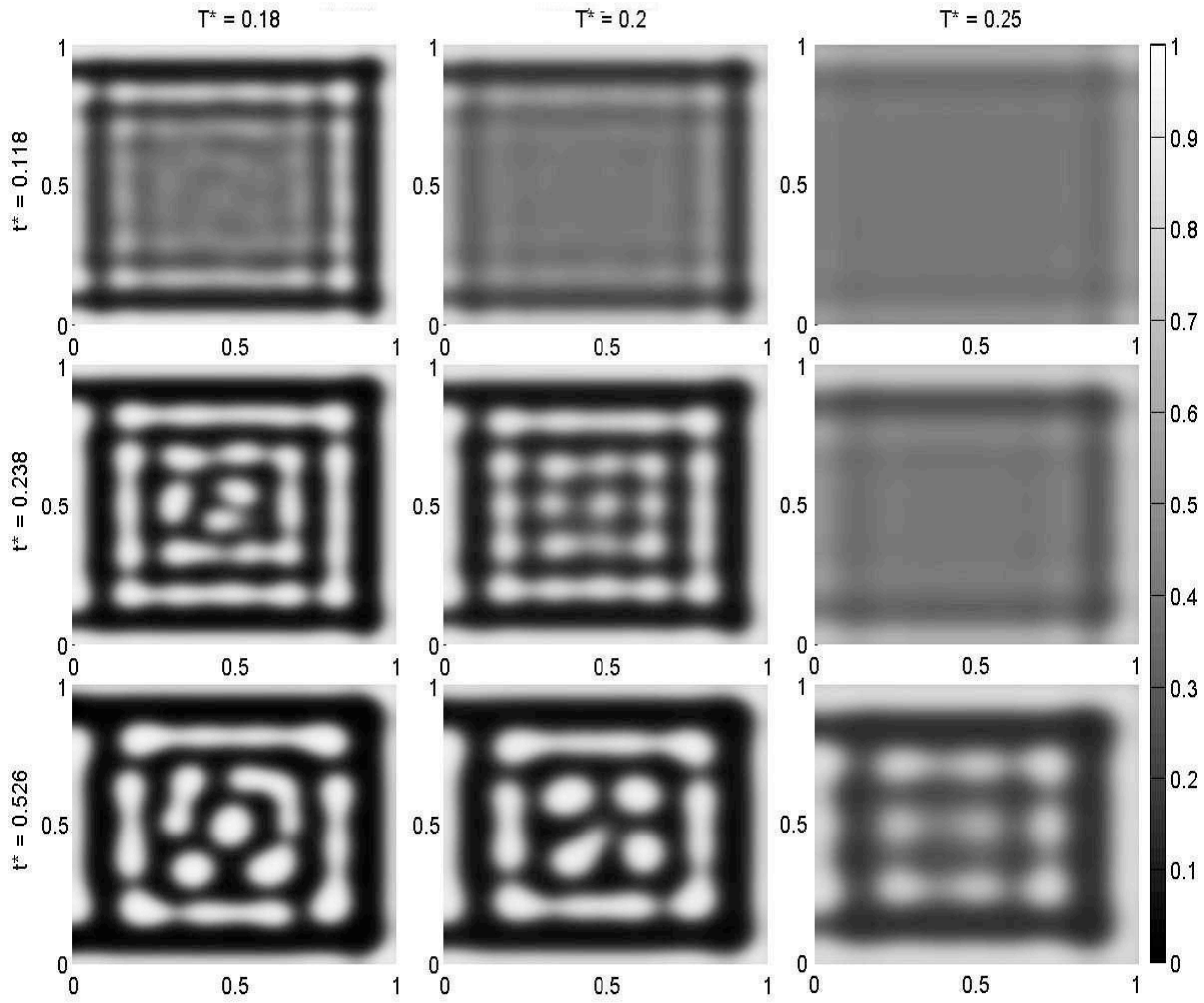

(a) (b) (c)

Figure 5.8: Effect of different off-critical quench depths on the morphology of phase separation in a multiple-surface attraction case. In this case, the parameter values are $c_0^* = 0.4$, $D = 2 \times 10^5$, $h_1 = 1.0$, $h_2 = 2.0$, $h_3 = 3.0$ and $h_4 = 4.0$, $N = 1000$ and $g = -0.5$. The temperature is lowered down to (a) $T_1^* = T_2^* = 0.18$, $\varepsilon = 1.0845$, (b) $T_1^* = T_2^* = 0.20$, $\varepsilon = 0.8514$ and (c) $T_1^* = T_2^* = 0.25$, $\varepsilon = 0.4318$.

It is noticeable in Figure 5.8 (c) that in shallow quenches within a domain where each side has a different surface potential, the phase separation within the bulk slows down in comparison with Figures 5.8 (a) and (b) that experience deeper quenches. As well, the surface with lower surface potential (h_1) is unable to put up with the strength of surface attractions of the adjacent sides (h_2 and h_4). Consequently, h_1 surface experiences its partial wetting from the start of SD phase separation while the other surfaces remain fully wetted. This behavior is typical for all quench depths [212]. The elongated domain morphology is the result of the system concentration being close to its critical value; where the droplets tend to form interconnected structure [403].

5.2.4 Effect of Surface Potential on Surface Enrichment

Although the role of surface potential strength has been verified in previous cases where different diffusion coefficients and quench depths were present, the significance of surface attraction function by itself was studied separately.

Higher values of surface potential would help attract the favorable component more aggressively to the surface in competition to the phase separation in the bulk. Figure 5.9 presents the effect of the surface potential on the surface enrichment of a polymer blend model where SD phase separation is governed by critical quenching condition in a multiple-surface potential case. The morphology shows that at the early stage of SD phase separation, higher surface potential (Figure 5.9 c) attracts more polymer to itself at $t^* = 0.0218$ while in Figure 5.9 (a), at the same time, the initial partial wetting is observed to be merging into complete wetting.

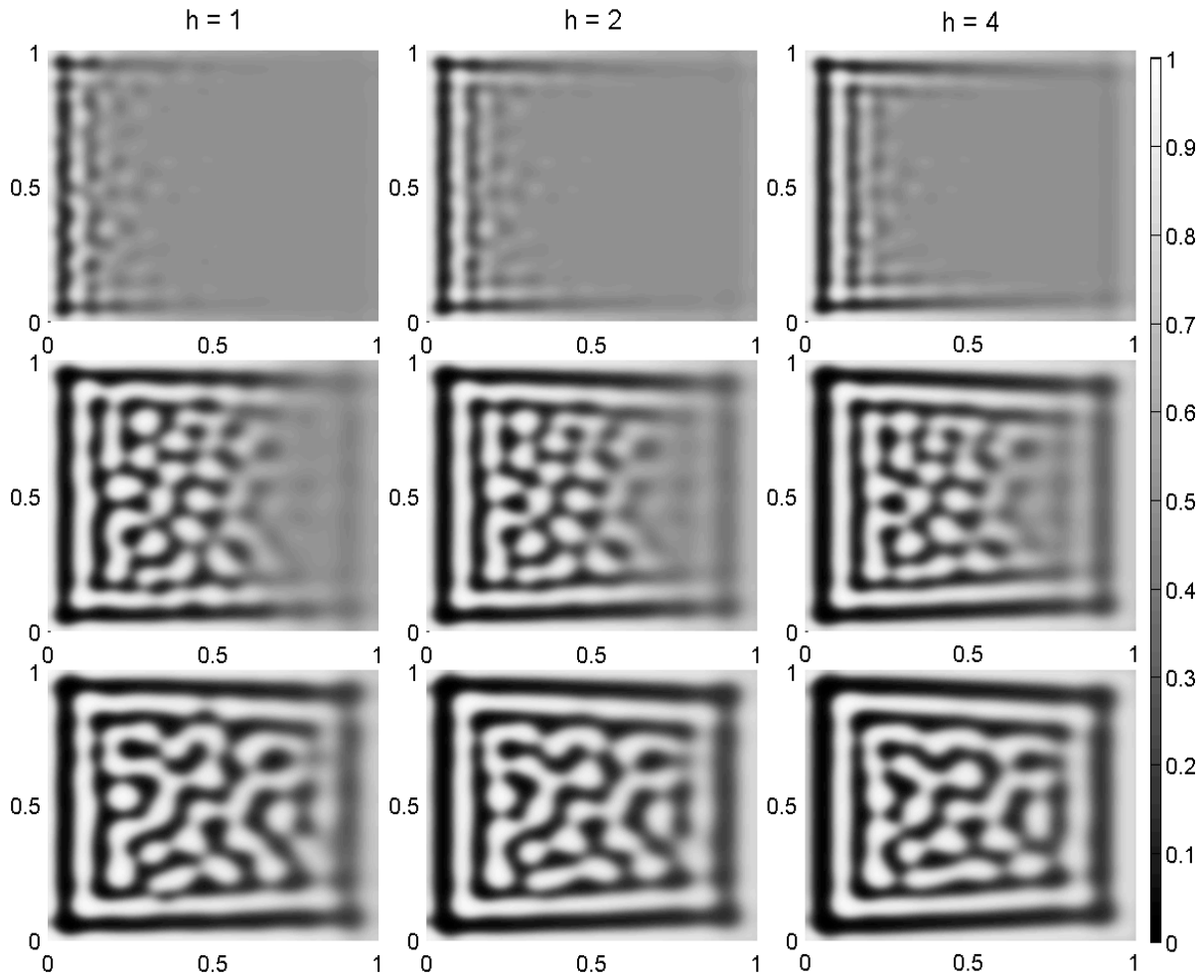

Figure 5.9: Effect of the surface potential on the surface formation where phase separation is governed by critical quenching condition in a multiple surface potential case. In this case c_0^* = 0.5, N = 1000, g = – 0.5, $D = 4 \times 10^5$, T_1^* and T_2^* are 0.15 and 0.25, respectively and the values of $h_1 = h_2 = h_3 = h_4$: (a) 1.0, (b) 2.0 and (c) 4.0.

Figure 5.9 shows that the surface with a lower temperature (deeper quench) has a lower surface enrichment regardless of its surface potential strength. This behavior was also observed in the short-range surface potential case (Figure 4.14) since the bulk wins the

competition against surface to attract more of one polymer to it while surface is unable to enrich itself as much.

Figure 5.10 (a) presents transition time from early stage to intermediate stage at $x^* = 0.125$ for three different surface potential values corresponding to Figure 5.9. At higher values of surface potential the transition time is approached earlier than the lower surface potentials. Figure 5.10 (a) also confirms the fact that the higher surface potential boosts not only the surface enrichment but also the morphology development of SD phase separation through the bulk in the vicinity of each surface. It should be noted that at $x^* = 0.5$ (Figure 5.10 b) the impact of the surface potentials h_1 and h_3 is negligible over the bulk phase separation due to their short-range nature of attraction. Nevertheless, h_2 and h_4 are expected to affect the phase separation across the domain where $x^* = 0.5$ at the vicinity of the interface between the bulk and surface. Hence, this minor effect causes the phase separation at $x^* = 0.5$ to partially advance the transition times from early stage to intermediate stage but not as much as $x^* = 0.125$.

Figure 5.11 presents the morphology formation of multiple surface potential attractions with three surfaces holding the same surface attraction strength ($h_1 = h_2 = h_4 = 2.0$) and one surface with variable surface potential ($h_3 = 1.8$, 3.0 and 4.0). The domain is under the temperature quench from $T_1^* = 0.20$ to $T_2^* = 0.22$. As surface potential of h_3 increases, while the other surface potentials are constant, more favorable polymer is attracted to the surface. This attraction causes more phase separation within the bulk that is located in the vicinity of h_3 surface. It can be noticed that at $t^* = 0.374$, the phase separated morphology pattern is the same for $x^* < 0.5$ and is different for $x^* > 0.5$ in each case.

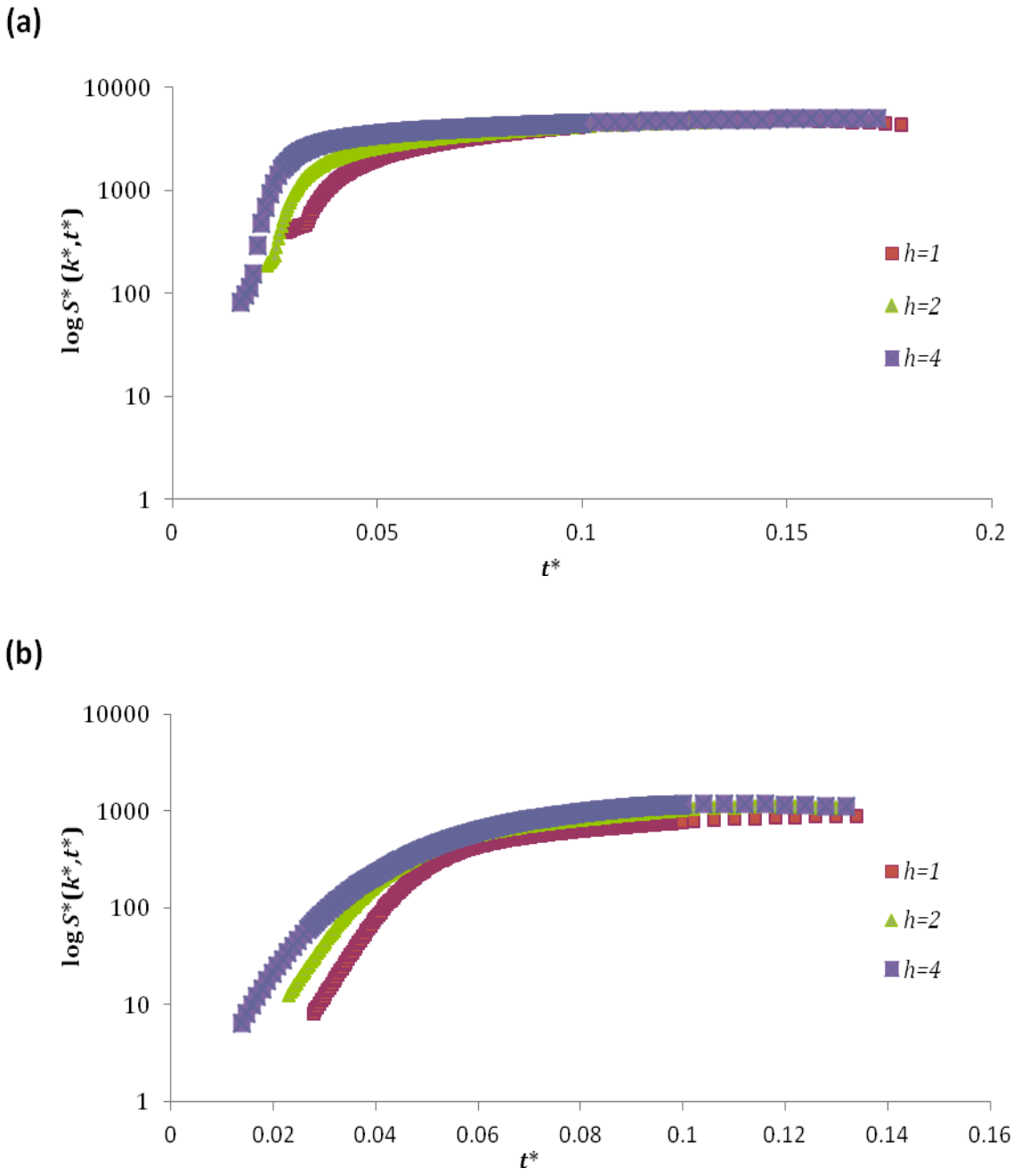

Figure 5.10: Logarithmic dimensionless structure factor versus dimensionless time diagram at dimensionless horizontal distance of domain (a) $x^* = 0.125$ and (b) $x^* = 0.5$ corresponding to Figure 5.9. Parameter values are: $c_0^* = 0.5$, $D = 2 \times 10^5$, $h_1 = h_2 = h_3 = h_4$: 1.0, 2.0 and 4.0., $N = 1000$, $g = -0.5$, $T_1^* = 0.15$ and T_x^* (temperature at x^*) = (a) 0.1625 and (b) 0.2.

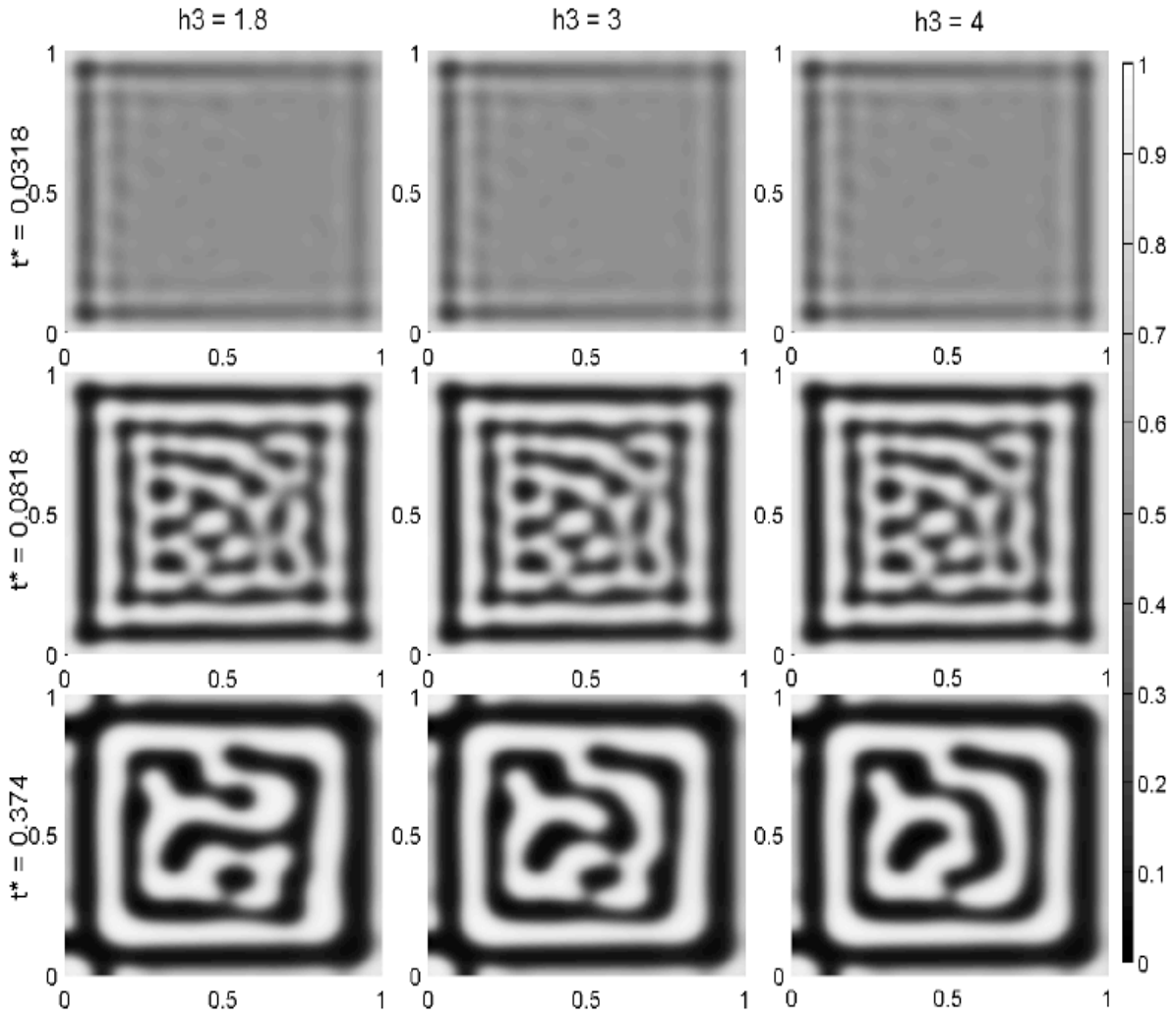

(a) (b) (c)

Figure 5.11: Effect of the surface potential on the surface formation where phase separation is governed by critical quenching condition in a multiple surface potential case where $c_0^* =$ 0.5, $N = 1000$, $g = -0.5$, $D = 4 \times 10^5$, T_1^* and T_2^* are 0.20 and 0.22, respectively. $h_1 = h_2 = h_4$ = 2.0, h_3 = (a) 1.8, (b) 3.0 and (c) 4.0.

As h_3 increases, the morphology of the domain close to h_3 surface is more ordered and the number of spinodal waves increases from one ($h_3 = 1.8$) to two ($h_3 = 3.0$).

This phenomenon is more conspicuous in Figures 5.11 (a) and (c) at $t^* = 0.374$. In Figure 5.11 (a) although the surfaces with surface potential of 2.0 ($h_1 = h_2 = h_4$) have a higher surface potential value than $h_3 = 1.8$, and therefore h_3 surface is supposed to have initiated the partial wetting prior to other surfaces, but only the surface with attraction potential of h_1 has already initiated its partial wetting earlier than other surfaces, which is another proof for the dominance of quench depth effect against surface potential on phase separation [218,406,407]. Then, the magnitude of surface potential comes into effect imposing h_2 and h_4 surface potential to wet partially prior to h_3 surface.

To investigate the effect of surface potential over the bulk phase separation corresponding to Figure 5.11, where one side (h_3) has a different (and increasing) surface attraction, logarithmic dimensionless structure factor versus dimensionless time diagram at horizontal distance of: (a) $x^* = 0.5$ and (b) $x^* = 0.875$ was developed (Figure 5.12). Figure 5.12 (b) displays transition time from early to intermediate stages of SD phase separation near the surface with h_3 surface potential. Increasing h_3 from 1.8 to 3 and 4 has expedited the transition time of the bulk that is close to the h_3 surface ($x^* = 0.875$). Further distance from h_3 ($x^* = 0.5$) has no impact on the transition time of the bulk phase separation, proving the range of surface potential being short.

Figure 5.13 shows the effect of the surface potential strength in controlling the evolution and formation of the wetting layer on the surfaces for critical quenching conditions. The increase of surface potential from 1.0 to 8.0, led to late transition from complete wetting to the partial wetting of surface. This trend was expected according to short-range surface potential case.

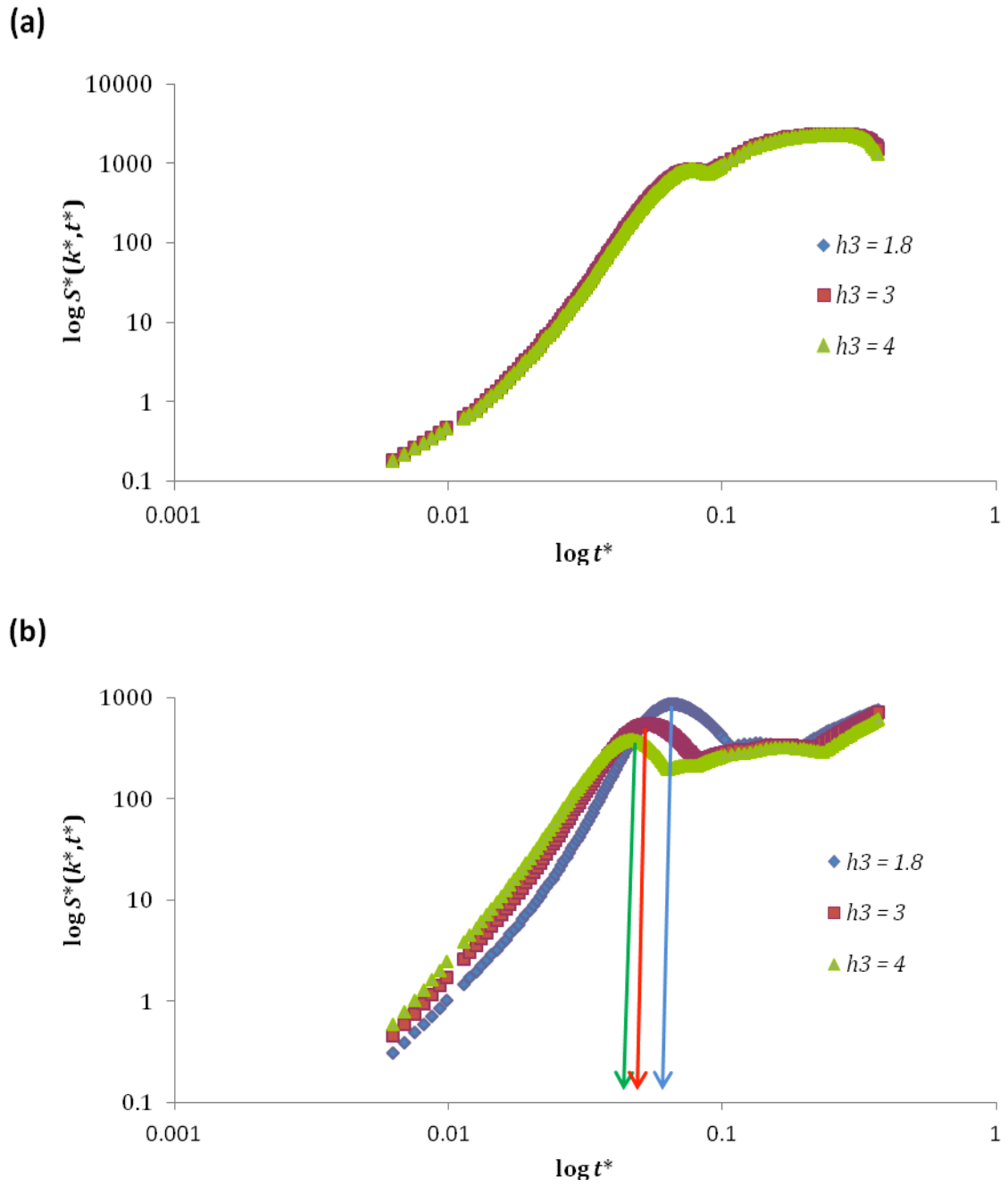

Figure 5.12: Logarithmic dimensionless structure factor versus dimensionless time diagram at horizontal distance of: (a) $x^* = 0.5$ and (b) $x^* = 0.875$ where $c_0^* = 0.5$, $N = 1000$, $g = -0.5$, $D = 4 \times 10^5$, T_1^* and T_2^* are 0.20 and 0.22, respectively. $h_1 = h_2 = h_4 = 2.0$, $h_3 = 1.8$, 3.0 and 4.0.

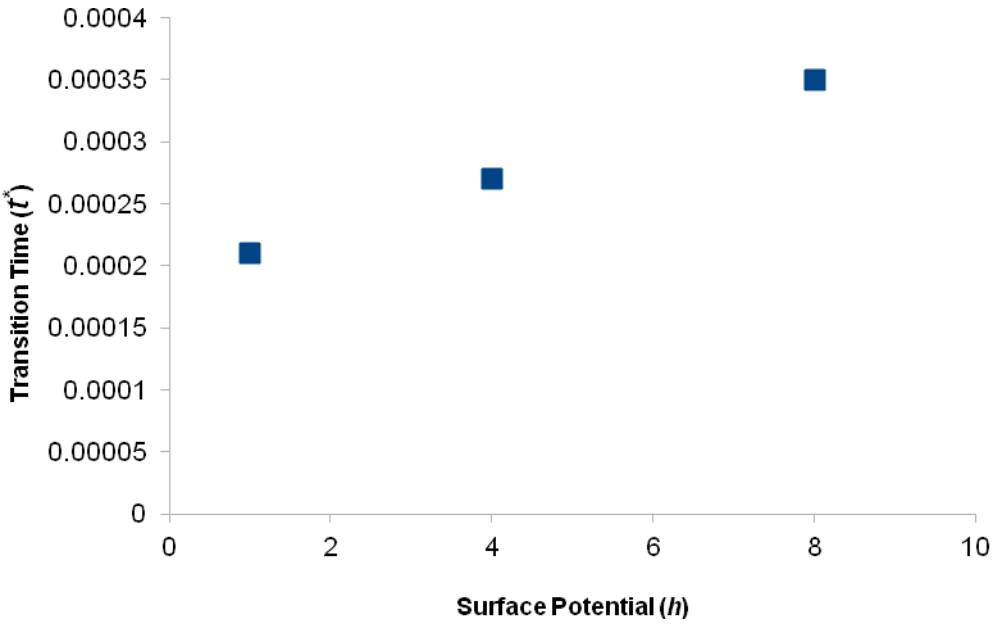

Figure 5.13: Effect of surface potential on the transition time from complete wetting to partial wetting in a multiple surface potential phase separation governed by a critical quenching condition in a multiple surface potential case. In this case $c_0^* = 0.5$, $N = 1000$, $g = -0.5$, $D = 8 \times 10^5$, $h_1 = h_2 = h_3 = h_4 = 1$, 4, and 8, for all surfaces and $T_1^* = T_2^* = 0.05$.

5.2.5 Effect of Concentration on Surface Enrichment

Effect of concentration itself as well as accompanied by a temperature gradient on the morphology of phase separation in polymer blends is a significance task to perform. Since the morphology is highly affected by concentration changes, different models were investigated to identify the mechanism of phase separation in a multiple surface potential case. In Figure 5.14, different concentrations were imposed on the blend in addition to a temperature gradient within the domain, which disturbed the uniformity of the phase

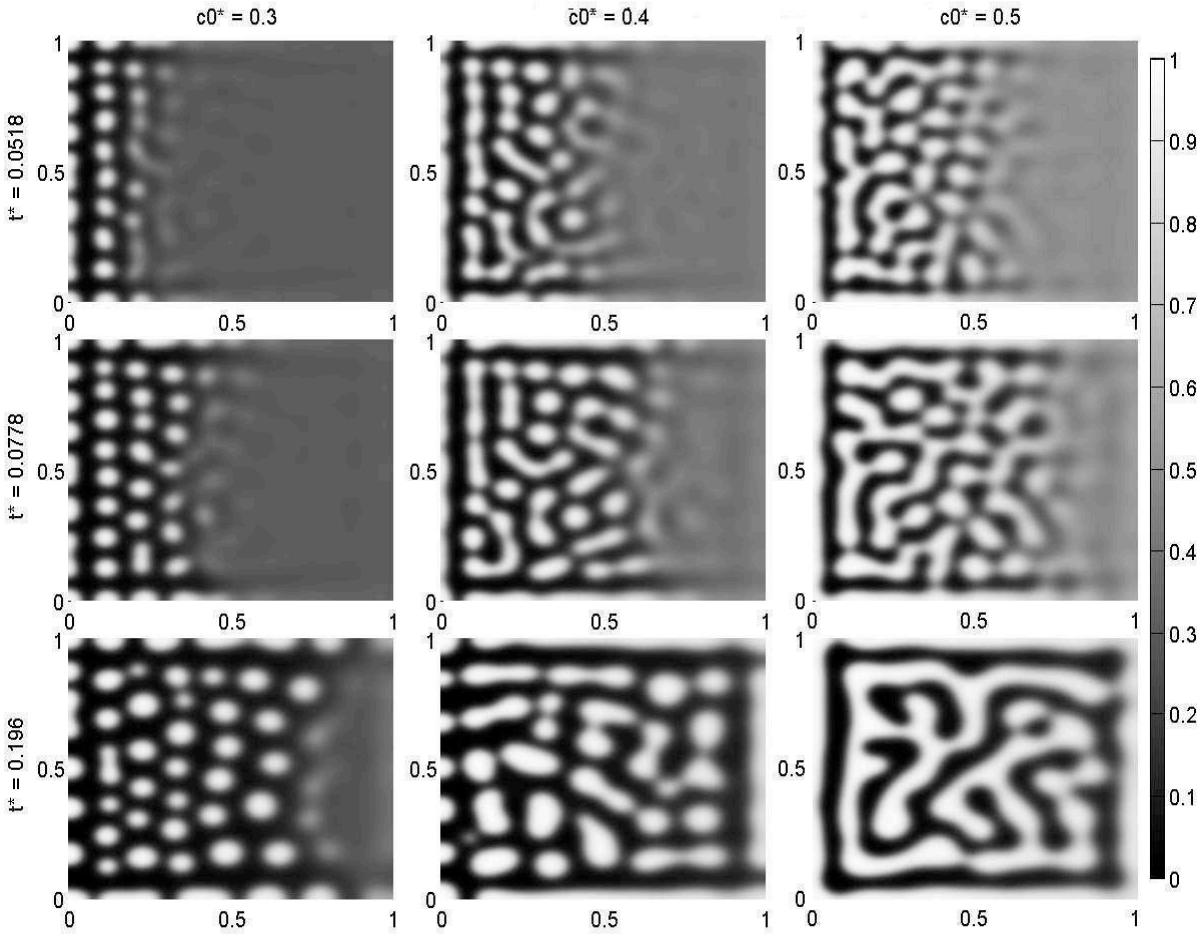

(a) (b) (c)

Figure 5.14: Effect of the concentration on the surface formation where phase separation is governed by off critical (a and b) and critical (c) quenching conditions in a multiple surface potential case where c_0^* = (a) 0.3, (b) 0.4, (c) 0.5, N = 1000, g = – 0.5, $D = 4 \times 10^5$, $T_1^* =$ 0.15, $T_2^* = 0.25$ and $h_1 = h_2 = h_3 = h_4 = 0.5$.

separation and caused the side with a lower temperature ($T_1^* = 0.15$) to initiate the phase separation earlier than the opposite side ($T_2^* = 0.25$). Figure 5.14 depicts the morphologies obtained for the case where phase separation was triggered by the temperature quench in a

multiple surface potential domain where all surfaces had the same surface attraction strength (h = 0.5). The structure changes from interconnected morphology (c_0^* = 0.5) [135,136,138,162,163,247,250,336,398,403] to droplet type (c_0^* = 0.3) [135,136,138,145,160–163,247,249,317,336,398] and elongated morphology (c_0^* = 0.4) [403].

Figure 5.15 presents two models where in one of them (a) the phase separation is governed by an off-critical concentration quenching condition (c_0^* = 0.3) resulting in droplet type morphology in the domain whereas in (b), due to approaching to the critical concentration, although the quench is still in off-critical range, the domain is undergoing the phase separation mechanism (c_0^* = 0.4) resulting in an elongated morphology [403]. It is important to note that although there is no temperature gradient within the domain itself ($T_1^* = T_2^* = 0.2$), the blend is undergoing a quench, which leads to the phase separation uniformly induced along the domain. Figure 5.15 also shows that the more the quench depth is, the faster the rate of phase separation will become (Figures 5.15 a and b at t^* = 0.0218 [404].

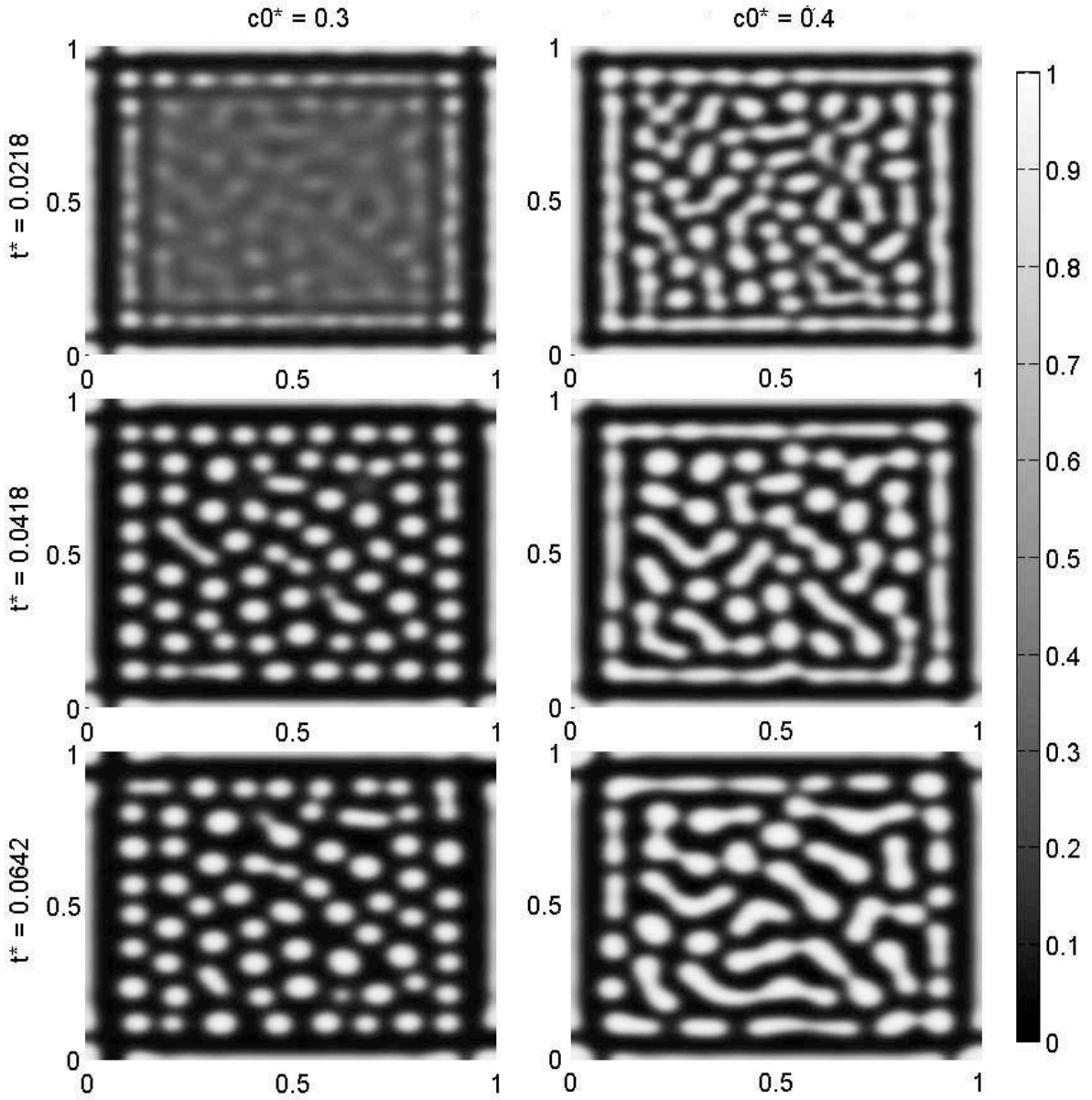

(a) (b)

Figure 5.15: Effect of the concentration on the surface formation where phase separation is governed by (a) off-critical and (b) near critical quenching conditions in a multiple surface potential case where c_0^* = (a) 0.3, (b) 0.4, N = 1000, g = – 0.5, $D = 8 \times 10^5$, $T_1^* = T_2^* = 0.20$ and $h_1 = h_2 = h_3 = h_4 = 2.0$.

5.2.6 Effect of Temperature Gradient on Surface Enrichment

In this section the effect of temperature gradient on the morphology formation has been studied. Attempt was placed on investigating the temperature gradient between the surfaces. Figure 5.16 shows the morphology formation of a multiple surface potential case where T_1^* has been selected to mimic (a) a non-uniform and (b) a uniform phase separation within the medium. For this goal, the T_1^* temperature was set at 0.10 and 0.20 for quenching conditions with and without temperature gradient, respectively while maintaining T_2^* at 0.20. The morphology resulted in a structure quite predictable in advance. As illustrated in Figure 5.16 (b), the uniform quenching condition has resulted in a steady and uniform phase separation among each layer with the same surface potential amount. There is no competition between surface in accelerating the phase separation rate as well as complete and partial wetting timeframe. However, when temperature gradient is imposed within surfaces one (T_1^*) and three (T_2^*), the rate of phase separation changes along the surfaces expediting the complete and its following partial wetting on the side with lower temperature (Figure 5.16 a).

Similar to the single-surface potential case, the deeper quench, $T_1^* = 0.10$, allowed more polymer component to attract to the surface at the beginning and as time passes the thickness of wetting layer became bigger toward the surface with the shallower quench depth. This is because of the fact that for shallower quench the morphology development of the surface and the bulk is slower, but forms bigger size droplets in the domain. This behavior was observed for different values of *g*, *h* and *D*, since in competition to attract favorable polymer to the

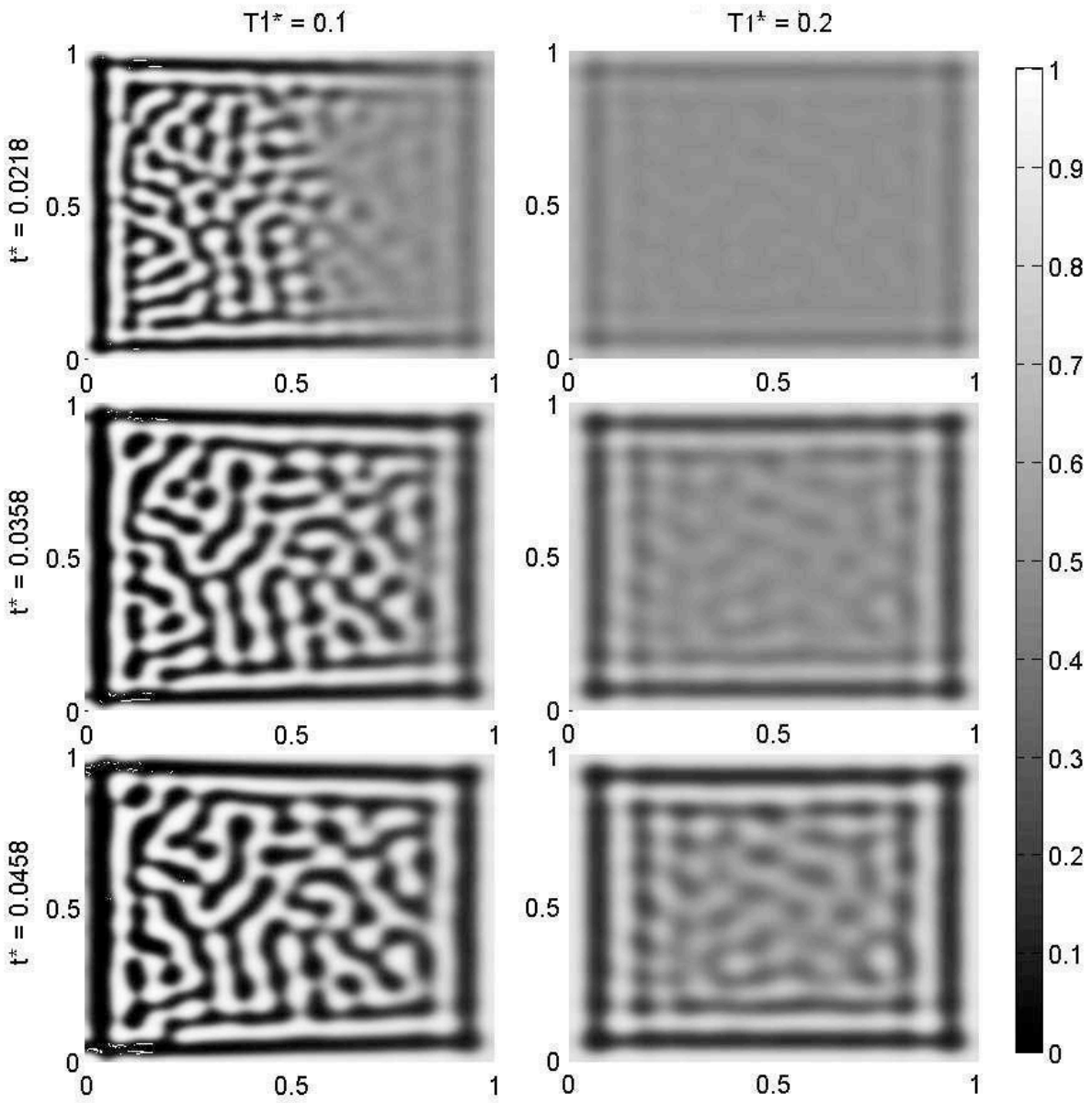

(a) (b)

Figure 5.16: Effect of temperature gradient on the surface enrichment growth rate with (a) non-uniform and (b) uniform quench, where phase separation is governed by a critical quenching condition in a multiple-surface attraction case. The parameter values are $c_0^* = 0.5$, $D = 4 \times 10^5$, $h_1 = h_2 = h_3 = h_4 = 2.0$, $N = 1000$, $g = -0.5$, $T_2^* = 0.20$ and (a) $T_1^* = 0.10$ and (b) $T_1^* = 0.20$.

surface, part of the domain that has a deeper quench is at more advanced stage of the phase separation and is expected to initially attract more material to the region. The induction of the phase separation on one side of the domain, however, can develop the phase separation process for the whole domain resulting in an earlier morphology formation even for the area with shallower quench depth, T_2^*.

The effect of temperature gradient on the surface enrichment growth rate was investigated in which the temperature on one side (T_1^*) was maintained at 0.15 and on the opposite side (T_2^*) was determined to be three different values of 0.10, 0.15 and 0.20 as shown in Figure 5.17 a, b and c, respectively. The phase separation mechanism was governed by an off-critical quenching condition (c_0^* = 0.4) and the surface potential value was the same for the all four surfaces ($h_1 = h_2 = h_3 = h_4 = 0.5$). This is unlike the previous case (Figure 5.16) where T_1^* varied from 0.10 to 0.20 and T_2^* was maintained constant. In Figure 5.17 (a), due to the temperature gradient and in accordance with the former simulation, the phase separation started from the side with a lower temperature (deeper quench) triggering the phase separation within the whole domain. The droplet morphology is in accordance with the off-critical quenching condition. As the temperatures on both sides of the domain (T_1^* and T_2^*) become equal, uniform phase separation morphology is formed reaffirming what had been already observed in the earlier case (Figures 5.5, 5.15 and 5.16 b). As predicted, partial wetting occurred on all surfaces of the domain when the domain underwent a deep quench; considering the weak surface attraction of all domain sides [395,402].

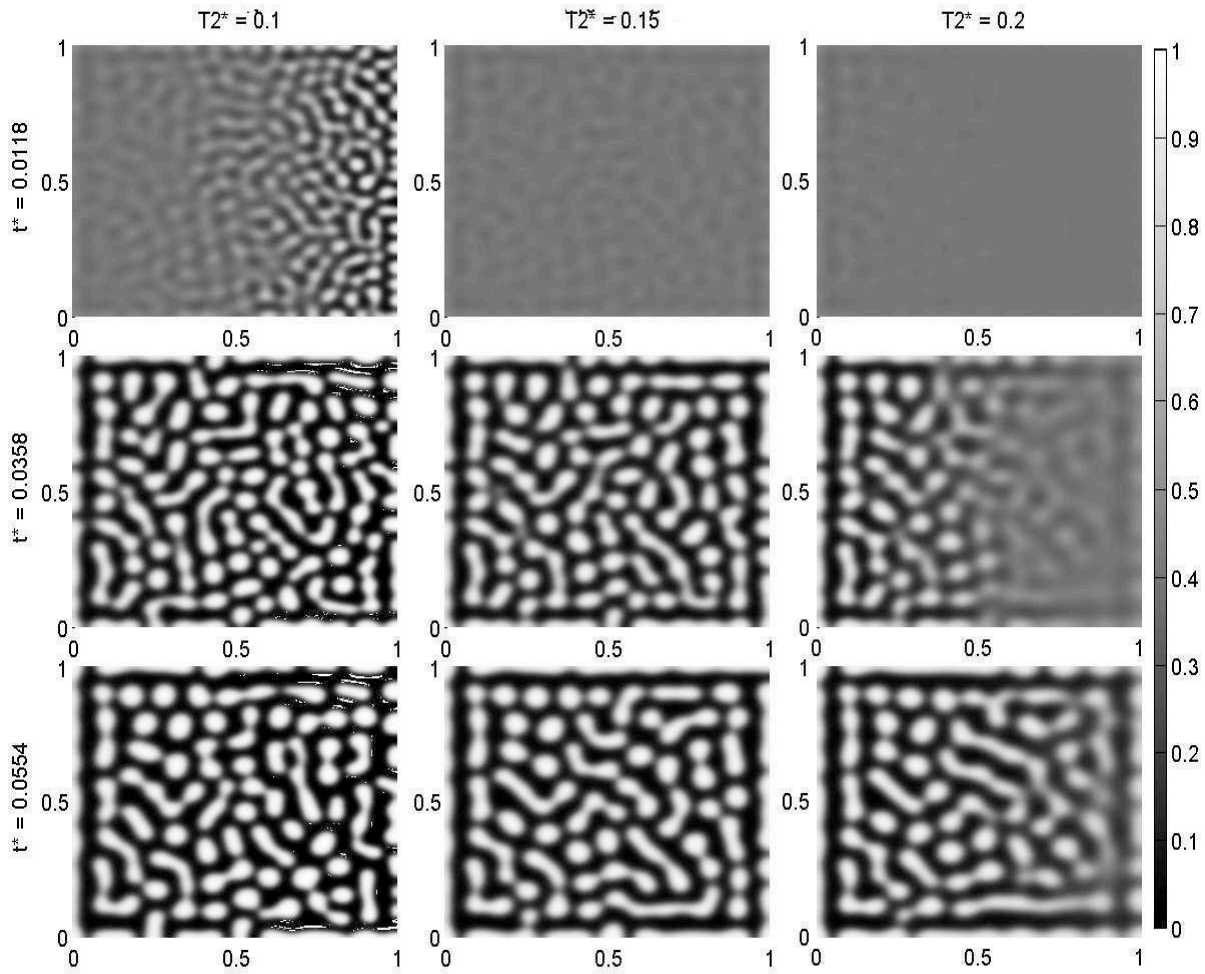

(a) (b) (c)

Figure 5.17: Effect of temperature gradient on the surface enrichment growth rate with T_1^* = 0.15 vs. (a) temperature gradient (T_2^* = 0.10), (b) uniform quench (T_2^* = 0.15) and (c) temperature gradient (T_2^* = 0.20) where phase separation is governed by an off-critical quenching condition in a multiple-surface attraction case. The parameter values are c_0^* = 0.4, $D = 4 \times 10^5$, $h_1 = h_2 = h_3 = h_4 = 0.5$, $N = 1000$, $g = -0.5$.

Figure 5.18 confirms that the deeper quench and higher temperature gradient on the side with T_2^* accelerates the rate of phase separation on the surface with constant temperature T_1^* in the presence of constant-remained values such as diffusion coefficient and surface potential. As shown in Figure 5.18, at temperature $T_2^* = 0.1$ (deeper quench), the transition time from complete wetting to partial wetting [218,406,407] at the other surface with T_1^* occurred at $t^* = 0.011$ while for a shallow quench ($T_2^* = 0.2$) the transition time on the surface took place at $t^* = 0.0114$.

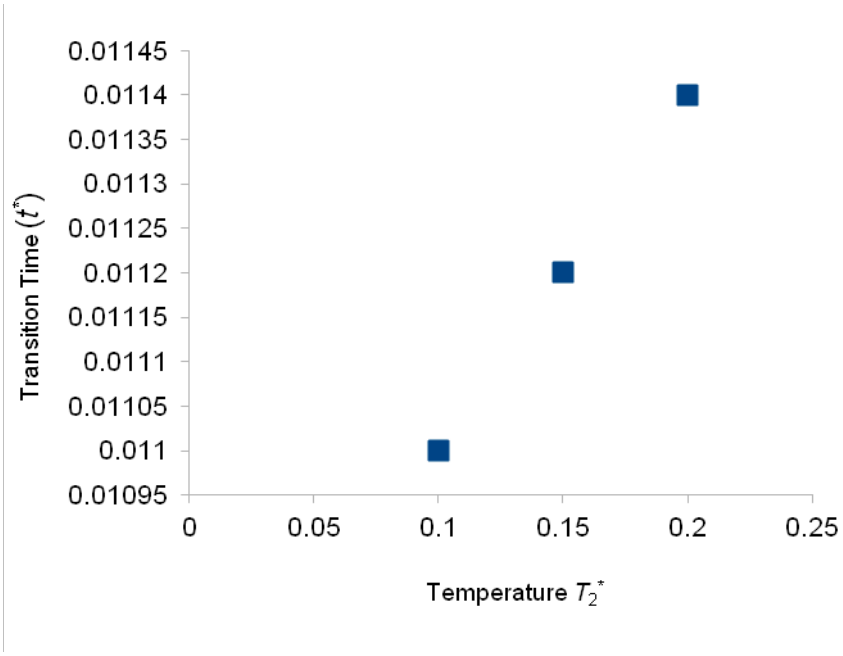

Figure 5.18: Effect of temperature gradient on the transition time from complete wetting to partial wetting in a multiple surface potential phase separation governed by an off-critical quenching condition in a multiple surface potential case. In this case $c_0^* = 0.4$, $N = 1000$, $g = -0.5$, $D = 4 \times 10^5$, $h_1 = h_2 = h_3 = h_4 = 0.5$ for all surfaces and $T_1^* = 0.15$.

This is because of the fact that a deep quench accelerates phase separation of the bulk affecting the phase separation of the whole domain and ultimately expediting the transition of complete wetting to partial wetting.

In a different setting simulation (Figure 5.19), the focus was given on the critical concentration quenching conditions in addition to maintaining T_1^* at 0.20 along with the temperature gradient to the other side of the domain but this time with values very close to T_1^* . The purpose of this type of modeling was to verify whether the phase separation rate and morphology is greatly affected by the small temperature gradient and if small temperature deviances would trigger any noticeable change in morphology formation. Figure 5.19 shows the surface enrichment near T_2^* is more than the other sides because of shallower quench on the surface.

After modeling a multiple-surface potential case with the temperature gradient when each surface has a different surface potential, the following morphologies depicted in Figure 5.20 were obtained for shallow quenching condition. As expected, the surface with a deeper quench undergoes SD phase separation faster in comparison to the other sides. In Figure 5.20 (a), at t^* = 1.407, the surface with a deeper quench is partially wetted while at the same time in Figures 5.20 (b) and (c), the surface has maintained their complete wetting due to their shallower quench condition. The morphology near the sides with shallow quench has higher rate of coarsening reflected in the surface by higher rate of enrichment.

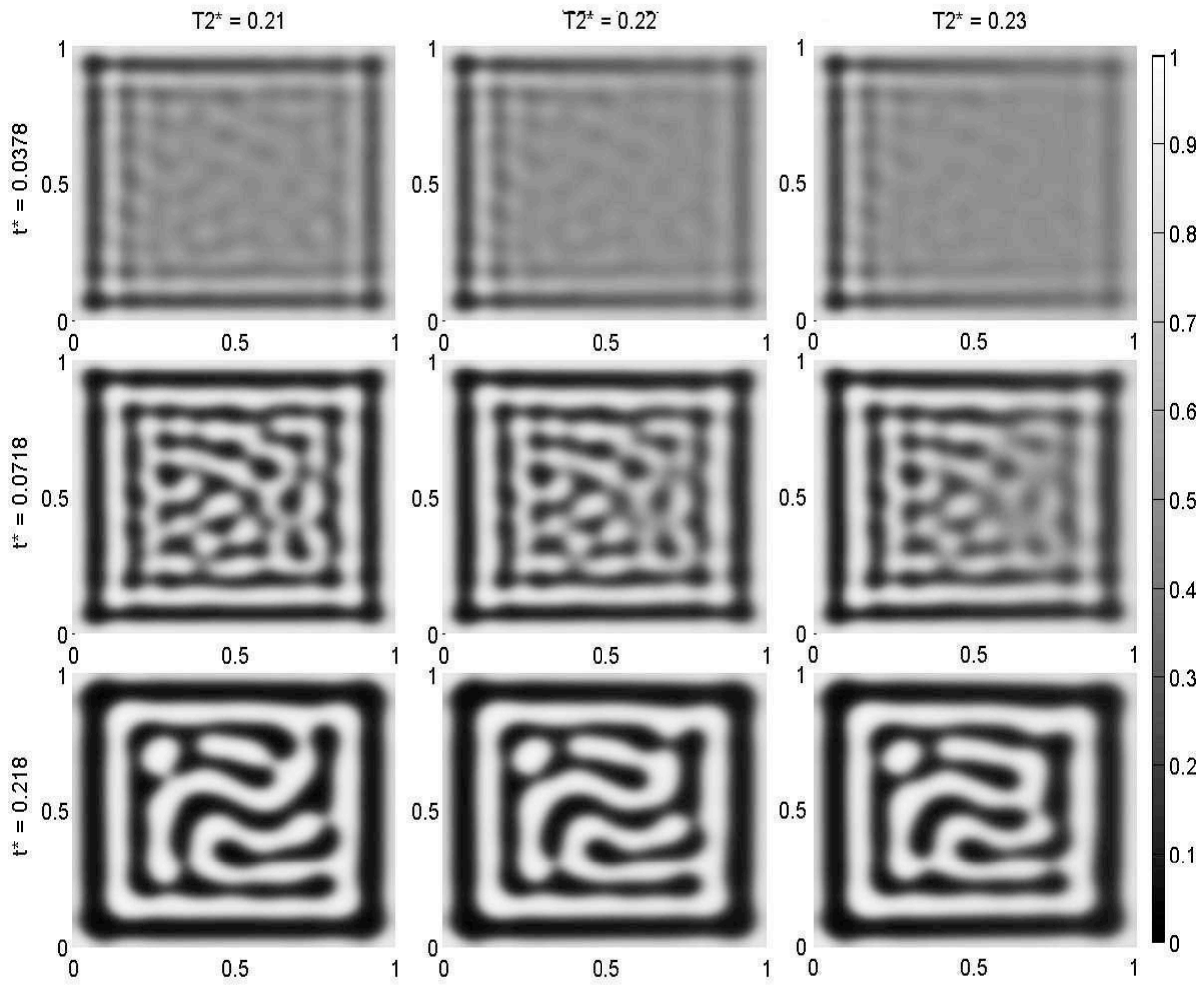

(a) (b) (c)

Figure 5.19: Effect of the small temperature gradient in a multiple surface potential phase separation governed by a critical quenching condition. In this case $c_0^* = 0.5$, $N = 1000$, $g = -0.5$, $D = 4 \times 10^5$, $T_1^* = 0.20$ and $T_2^* = 0.21$ (a), 0.22 (b), 0.23 (c) and $h_1 = h_2 = h_3 = h_4 = 2$.

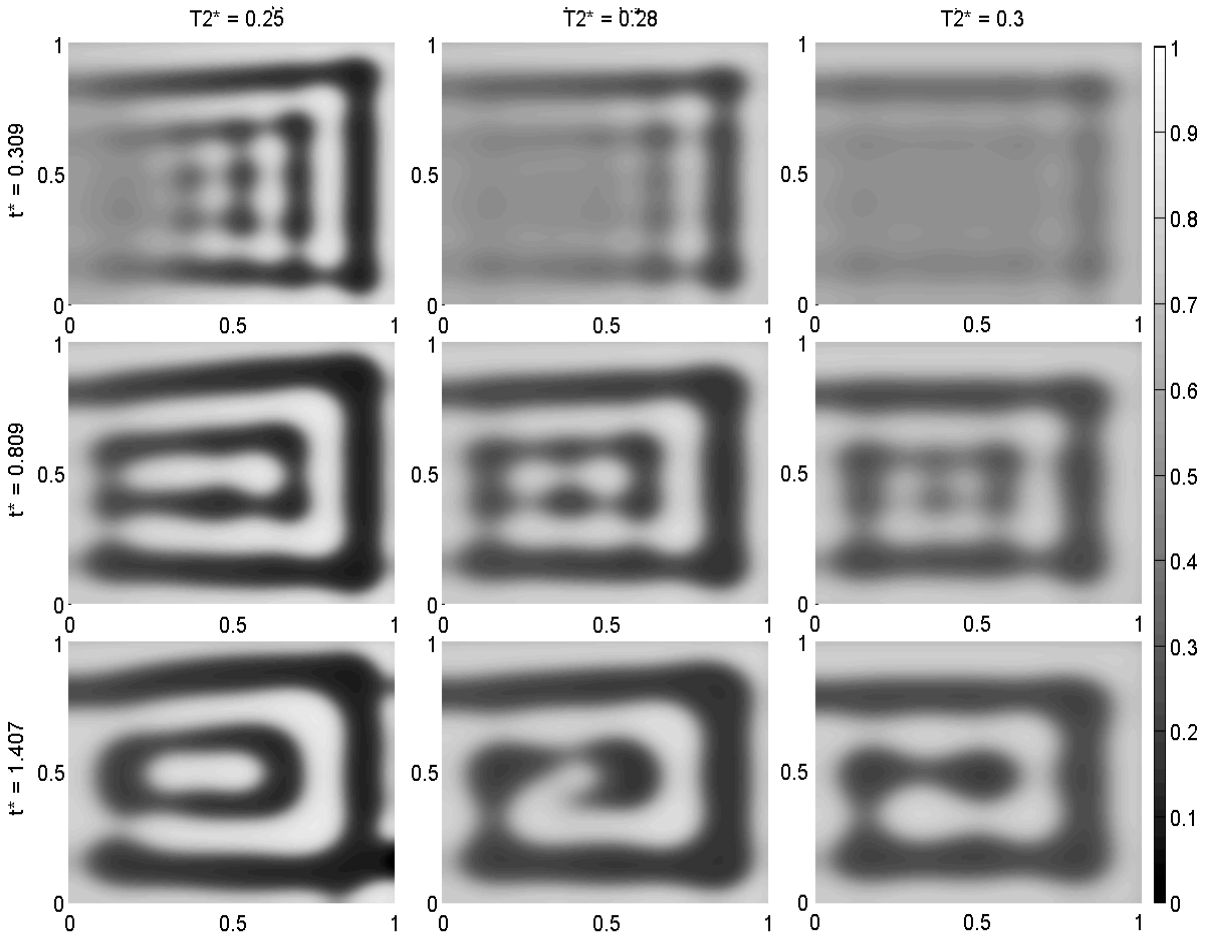

(a) (b) (c)

Figure 5.20: Effect of the temperature gradient in a multiple surface potential phase separation governed by a critical quenching condition in a multiple surface potential case. In this case $c_0^* = 0.5$, $N = 1000$, g = – 0.5, $D = 4 \times 10^5$, $h_1 = 0.5$, $h_2 = 1.0$, $h_3 = 2.0$ and $h_4 = 4.0$, $T_1^* = 0.30$ and $T_2^* = 0.25$, 0.28 and 0.30, respectively.

5.3 Summary & Conclusions

To study numerically the phase separation phenomena of a model binary polymer blend quenched into the unstable region of its binary symmetric phase diagram, the nonlinear Cahn-Hilliard theory along with Flory-Huggins theory were applied. Short-range surface potential within a more complex geometry, where each side of the domain is exposed to a surface with preferential attraction to one component of a binary polymer blend under temperature gradient in x direction, was incorporated in the model. The initial conditions used in the study mimicked the infinitesimal thermal concentration oscillations in the blend. Consistent with the method of line, the equation was spatially discretized by finite difference method to solve the governing equation in a two-dimensional domain. The developed ODE's were then solved by CVODE solver. The numerical solutions and calculated morphologies replicate frequently reported experimental observations and numerical work.

The effects of different quench depths, diffusion coefficients, surface potentials, temperature gradients, and concentrations were studied numerically. The results have been then presented in the form of morphology plots, and validated by logarithmic graphs. The results are in agreement with comparable experimental and numerical work performed by other groups.

The ordered morphology in multiple-surface potential case was found to form when the surface attraction of all sides was the same (same h values) with a uniform quench depth ($T_1^* = T_2^*$). This is because all surfaces are engaged in attracting the preferred polymer simultaneously within the domain. The obtained morphologies in each studied case displayed

the competition between the surfaces. Any side with a higher surface potential would win the competition against the side with a lower surface attraction in case of uniform quench depth.

Higher diffusion coefficients led to the increase of phase separation driving force and consequently the faster morphology development within the bulk. This was due to the competition between the bulk and the surfaces where higher phase separation within the bulk lowers the surface wetting layer enrichment on each side.

The structure factor analysis for the bulk presented a higher growth rate at the early stage of phase separation and a slower growth rate at the intermediate stage with a slope of 0.33 through the bulk; in agreement with Lifshitz-Sloyozov (LS) law. The amount of quench depth also affected the morphology so that smaller droplets and finer morphology were formed under deeper quenches. Deeper quenches also directed the transition time from complete wetting to partial wetting of the surface faster. Higher rate of phase separation within the bulk due to the deeper quench led to the faster transition time from early to intermediate stage in the bulk. In deep quenches, lower surface enrichment was observed since the surface lost the competition to the bulk in attracting favorable polymer.

The development of structure factor analysis over the surface potential effect on the phase separation within the bulk (far from the surfaces) displayed later transition time for higher values of h. As surface potential increased, the transition time from complete wetting to partial wetting occurred at a later time on the surface. In the multiple-surface case, the closer (preferred) polymer to the surface underwent faster transition time from early to intermediate stage of phase separation than the other polymer in the bulk. The transition time

for the polymer within the bulk remained the same in spite of the sides having different values of surface potentials.

The interconnected morphology, for critical quenches ($c_0^* = 0.5$), elongated structure for near critical ($c_0^* = 0.4$), and droplet-like morphology for off-critical quenches ($c_0^* = 0.3$), was obtained replicating comparable experimental and numerical work. The impact of different temperature gradient values on the surface enrichment rate with the constant temperature T_1^* at the surface and different temperature T_2^* for the opposite surface was studied for the first time within a multiple-surface potential setting. The results exhibited that higher values of ΔT^* increased the growth rate of the preferred polymer over the surface adding to the thickness of the wetting layer. The transition time at the side with temperature T_1^* from complete wetting to partial wetting occurred slightly later than the side with a higher temperature of T_2^*.

Chapter 6

6. Long Range Surface Potential

6.1 Model Development

This section presents the model development and the method of solution for the two-dimensional study of phase separation by SD for a long-range surface potential case. The governing equations used in the model development are presented to obtain a general spatial, time dependent, differential equation. From algebraic simplification and rearrangement, the dimensionless equation describing the dynamics of surface directed phase separation by SD is presented. The dynamics of the concentration fluctuations is represented by the continuity equation containing the driving force for phase separation (the chemical potential) within the diffusional flux [288]:

$$\frac{\partial c}{\partial t} = -\nabla \cdot J \tag{6.1}$$

where c is the concentration of one polymer in terms of the volume fraction, and J is the mass flux caused by combined phenomena of non-Fickian diffusion and thermal diffusion under an externally imposed spatial temperature gradient. Mass flux J can be expressed with the following expression [288]:

$$J = \left[-M(c)\nabla(\mu_2 - \mu_1)\right] \tag{6.2}$$

where, M is the concentration dependent mobility, and chemical potential for each component is μ_1 and μ_2 of the component. Free energy that considers all aspects of polymer blends including chain entanglement is based on the Flory-Huggins-de Gennes [319] theory is presented by:

$$F = \frac{k_B T}{\upsilon}\left[\int\left(f(c) + \kappa\left|\nabla c\right|^2\right)dV + \int V(x)\,c\,dx\right] \tag{6.3}$$

where the Flory-Huggins free energy [259] is:

$$f(c) = \frac{k_B T}{\upsilon}\left[\frac{c}{N_1}\ln c + \frac{1-c}{N_2}\ln(1-c) + \chi c(1-c)\right] \tag{6.4}$$

where N_1 and N_2 are the degrees of polymerization of the two components and κ is the interfacial energy parameter. k_B is Boltzmann's constant, T is the temperature, χ is Flory's interaction parameter, and c is the volume fraction of the polymer. For this case, the long-range interaction along with van der Waals forces which decay proportional to x^{-3} [408,409] where x is the horizontal distance from the surface and is expressed as long-range potential on the preferred component of the mixture $V(x)$ [211,385,408–410].

The gradient in chemical potential is defined as the change in the total free energy with respect to composition:

$$(\mu_2 - \mu_1) = \frac{\delta F}{\delta c} \tag{6.5}$$

where functional derivative of Equation 6.3 of free energy:

$$\frac{\delta F}{\delta c} = \frac{k_B T}{\upsilon}\left(\frac{\partial f}{\partial c} + V(x) - 2\kappa\nabla^2 c\right) \tag{6.6}$$

The energy gradient in non-linear C-H (Equation 3.26) is for concentration fluctuation effect on free energy and it is resulted from formation of interfaces between the two polymers. De Gennes [198] proposed κ has enthalpic and entropic parts; a term about the efficient series of the interactions $a^2\chi$ and a term whose basis is the configurational entropy of the Gaussian coils:

$$\kappa(c) = \kappa_{enrtopic} + \kappa_{enthalpic} = \frac{a^2}{36c(1-c)} + a^2\chi \tag{6.7}$$

The entropic effect is due to connectivity of monomer unites so is only for polymer mixtures and takes into account energy changes due to spatial variation in the concentration while phase separation happens. But in polymer blends $\kappa_{entropic} >> \kappa_{enthalpic}$ and second term could be neglected [209]. De Gennes [319] proposed that κ, for polymer blends could be considered as:

$$\kappa(c) \cong \frac{a^2}{36c(1-c)} \tag{6.8}$$

This term could be used in Cahn-Hilliard equation to predict phase separation of polymer blends more accurately. The reptation model can be expressed for each component *i* as:

$$D_i = \frac{4k_B T}{15\xi_i}\left(\frac{N_{e,i}}{N_i^2}\right) \tag{6.9}$$

where N_e is average number of monomers existing between each two entanglement points of the polymer chains. Reptation behavior of polymer blend occurs when $N > N_c$ where N_c is the critical degree of polymerization and is defined experimentally. Approximate value of N_c is 300 monomer units [286,287]. The diffusion coefficient could be expressed as:

$$D = M \frac{\partial^2 f(c)}{\partial c^2} \tag{6.10}$$

Slow mode theory, which takes into account the self-diffusion coefficients of the individual component of the blend, is used. Following expression for the mobility in a binary polymer blend is obtained:

$$M = \frac{4\nu N_e c(1-c)}{15\xi\left[N_2 c + N_1(1-c)\right]} \tag{6.11}$$

The linear temperature gradient used in this study is expressed as [138,336]:

$$T(x) = \left(\frac{T_2 - T_1}{x_2 - x_1}\right)(x - x_1) + T_1 \qquad \text{for} \qquad x_1 < x_2 \tag{6.12}$$

where T_1 and T_2 are temperatures at x_1 and x_2, respectively. Combining Equations (6.1), (6.2), (6.5), (6.6), (6.8), (6.11) and (6.12), it gives non-linear Cahn-Hilliard equation as:

$$\frac{\partial c}{\partial t} = \left[\left(\frac{1}{N_1} - \frac{1}{N_2} + \frac{\ln c}{N_1} - \frac{\ln(1-c)}{N_2} + \alpha(1-2c) + V(x)\right)\frac{\partial M}{\partial c} + 2M\left(\frac{1}{N_1 c} + \frac{1}{N_2 c(1-c)}\right) - 4M\alpha\right]\nabla c \cdot \nabla T$$
$$+\left[\left(\frac{1}{N_1 c} + \frac{1}{N_2 c(1-c)}\right)\frac{\partial M}{\partial c}\cdot T + \left(\frac{-1}{N_1 c^2} + \frac{1}{N_2 c(1-c)^2}\right)MT - 2\alpha T\frac{\partial M}{\partial c} - 2\beta\frac{\partial M}{\partial c}\right](\nabla c)^2$$
$$+\frac{\partial M}{\partial c}T\cdot\nabla V\cdot\nabla c + 2M\cdot\nabla V\cdot\nabla T + MT\cdot\nabla^2 V + \left[\left(\frac{1}{N_1 c} + \frac{1}{N_2 c(1-c)}\right)MT - 2\alpha MT - 2M\beta\right]\nabla^2 c$$
$$+\frac{a^2}{18}\left\{\left[2M\frac{(1-2c)}{(c-c^2)^2} - \frac{1}{(1-c)c}\frac{\partial M}{\partial c}\right]\nabla T\cdot\nabla c\cdot\nabla^2 c + \right.$$
$$\left[\frac{(1-2c)}{(c-c^2)^2}T\frac{\partial M}{\partial c} - 2MT\left(\frac{1}{(c-c^2)^2} + \frac{(1-2c)^2}{(c-c^2)^3}\right)\right]\nabla^2 c\cdot(\nabla c)^2 +$$
$$\left[\frac{(1-2c)}{(c-c^2)^2}MT\right]\nabla^2 c\cdot\nabla^2 c - \left[\frac{2}{c(1-c)}M\right]\nabla T\cdot\nabla^3 c +$$
$$\left[\frac{2(1-2c)}{(c-c^2)^2}MT - \frac{1}{c(1-c)}T\frac{\partial M}{\partial c}\right]\nabla c\cdot\nabla^3 c +$$
$$\left.\left(\frac{-1}{(1-c)c}\right)MT\cdot\nabla^4 c\right\} \tag{6.13}$$

Using the following dimensionless variables:

Dimensionless time:
$$t^* = \left[\frac{4N_e\left(\frac{k_B T_c}{\upsilon}\right)a^2\upsilon}{15\varepsilon L^4}\right]t \tag{6.14}$$

Dimensionless diffusion coefficient:
$$D = \left[\frac{k_B T_c L^2}{\upsilon\left(\frac{k_B T_c}{\upsilon}\right)a^2}\right] \tag{6.15}$$

Dimensionless concentration:
$$c^* = c \tag{6.16}$$

Dimensionless temperature:
$$T^* = \frac{T}{T_c} \tag{6.17}$$

Dimensionless horizontal length: $$x^* = \frac{x}{L} \tag{6.18}$$

Dimensionless vertical length: $$y^* = \frac{y}{L} \tag{6.19}$$

Dimensionless long-range potential: $V(x) = V^*(x^*)$

where:

$$V^*(x) = \begin{cases} h & x^* = 0 \\ \dfrac{h}{(bx^*)^n} & 0 < x^* \le 1 \end{cases} \tag{6.20}$$

b in the Equation 6.20 represents the decay coefficient in order to adjust the decay behavior of the dimensionless long-range potential within the bulk domain [408,410]. The values of b and n in this model are 256 and 3,respectively. The following form of dimensionless Flory-Huggins interaction parameter is used in the model:

$$\chi^* = \alpha + \frac{\beta}{T^*} \tag{6.21}$$

where α and β constants are determined experimentally and represent the entropic and enthalpic contribution, respectively. For this mixture, α and β (after normalization) have values of -5.34×10^{-4} and 8.44×10^{-4}, respectively [317,337]. These values of α and β are fitted to the expected linear dependence on T^{-1} used in the model simulations.

Replacing Equations (6.14–6.21) into Equation (6.13), and assuming $N_1 = N_2 = N$, the following governing equation for the long-range surface potential will be obtained for concentration change over time:

$$\frac{\partial c^*}{\partial t^*} = \frac{D}{N}\left\{\left[\left\{\frac{\ln(c^*)}{N} - \frac{\ln(1-c^*)}{N} + \alpha(1-2c^*) + V^*(x^*)\right\}(1-2c^*) + \frac{2}{N} - 4\alpha.c^*(1-c^*)\right]\nabla c^* \cdot \nabla T^*\right.$$
$$- \left[2\alpha(1-2c^*)T^* + 2\beta^*(1-2c)\right](\nabla c^*)^2 + (1-2c^*)T^* \cdot \nabla V^* \cdot \nabla c^*$$
$$\left. + 2c^*(1-c^*)\nabla V^* \cdot \nabla T^* + c^*(1-c^*)T\nabla^2 V^* + \left[\frac{T^*}{N} - 2\alpha.c^*(1-c^*)T^* - 2c^*(1-c^*)\beta^*\right]\nabla^2 c^*\right\}$$
$$+ \frac{1}{18N}\left\{\left[\frac{(1-2c^*)}{(c^* - c^{*2})}\right]\nabla T^* \cdot \nabla c^* \cdot \nabla^2 c^* - \left[\frac{2T^*}{(c^* - c^{*2})} + \frac{T^*(1-2c^*)^2}{(c^* - c^{*2})^2}\right]\nabla^2 c^* \cdot (\nabla c^*)^2\right.$$
$$+ \left[\frac{(1-2c^*)}{(c^* - c^{*2})}T^*\right]\nabla^2 c^* \cdot \nabla^2 c^* - 2\nabla T^* \cdot \nabla^3 c^* +$$
$$\left.\left[\frac{1-2c^*}{(c^* - c^{*2})} \cdot T^*\right]\nabla c^* \cdot \nabla^3 c^* - T^*\nabla^4 c^*\right\} \tag{6.22}$$

6.1.1 Initial Conditions

There exist infinitesimal derivations from the average concentration called homo-phase thermal fluctuations so that the initial condition is an average concentration plus a very small value, δ:

$$c^*\left(t^* = 0\right) = c_0^* + \delta c^*\left(t^* = 0\right) \tag{6.23}$$

where c_0^* is the dimensionless initial concentration, and $\delta c^*\left(t^* = 0\right)$ represents any deviation from the average initial concentration c_0^* or the infinitesimally small concentration fluctuations which may be present in the blend.

6.1.2 Boundary Conditions

In the long-range surface potential case the model domain is exactly the same as the short-range surface potential model composing of four surfaces where *only one* of them has a surface attraction. Each surface will have two boundary conditions. Assuming an external surface potential in the system for the domain side with surface attraction, the first boundary condition (suggested by Schmidt and Binder [345]) would become:

$$-h - gc_1^* + \gamma \left. \frac{\partial c^*}{\partial x^*} \right|_{x^*=0} = 0 \tag{6.24}$$

where h represents the surface potential with preference to one of the components, g shows the change interactions near the surface in the underlying lattice model and γ has relation to the bulk correlation length. The second boundary condition shows there is no penetration of material through the boundary surface. At this surface, the concentration flux is zero and there is a no-flux boundary condition [135,136,346]:

$$J\big|_{x^*=0} = 0 \tag{6.25}$$

or

$$\nabla^3 c^* = 0 \tag{6.26}$$

Therefore, similar to the short range potential case, for $x^* = 0$, the following boundary conditions are obtained:

$$\left.\frac{\partial c^*}{\partial x^*}\right|_{x^*=0} = \frac{h + gc^*}{\gamma} \tag{6.27}$$

$$\frac{\partial^3 c^*}{\partial x^{*3}} + \frac{\partial^3 c^*}{\partial x^* \partial y^{*2}} = 0 \tag{6.28}$$

The no flux boundary condition refers to a system in which no mass will be exchanged through its boundary with the surrounding. Natural boundary conditions obtained from the variational analysis [135,136,292], and is expressed in generalized form as:

$$\left(\nabla c^*\right) \cdot \mathbf{n} = 0 \tag{6.29}$$

where **n** is the outward unit normal to a bounding surface. At the surfaces without any preferential attraction to one of the polymers in the blend, no-flux and natural boundary conditions represented in Equations (6.26) and (6.29), respectively are applied. Therefore for the sides with no surface attraction, the following boundary conditions are applied similar to the short-range surface potential case:

for $x^* = 1$:

$$\frac{\partial c^*}{\partial x^*} = 0 \tag{6.30}$$

$$\frac{\partial^3 c^*}{\partial x^{*3}} + \frac{\partial^3 c^*}{\partial x^* \partial y^{*2}} = 0 \tag{6.31}$$

and for $y^* = 0,\ 1$:

$$\frac{\partial c^*}{\partial y^*} = 0 \tag{6.32}$$

$$\frac{\partial^3 c^*}{\partial y^{*3}} + \frac{\partial^3 c^*}{\partial y^* \partial x^{*2}} = 0 \tag{6.33}$$

Equation 6.22 can be expanded in terms of spatial derivation as in short-range potential case using the formulas explained in Chapter 4.

6.2 Morphology Formation and Surface Enrichment

The morphology formation of the polymer binary blend under temperature gradient and also surface attraction to one of the polymers have been studied for a long-range surface potential case. Same as the short-range and multiple surface potential case, morphology formation and its evolution rate following the thermal induced spinodal decomposition process depend on the temperature that blends are quenched to (quench depth), diffusion coefficient, the molecular weight of the each component (the degree of polymerization) and the miscibility of the two components. As mentioned before, in surface directed phase separation, the amount of surface attraction to the favorable component could generally influence the surface complete or partial wetting as well as the rate of the enrichment of the surface. In long-range surface potential case, similar to short-range surface potential case, there are two mechanisms of phase separation in competition with each other. First, the *surface* tends to attract the first layer of polymer within the domain, which initiates the phase separation through spinodal waves triggering and contributing to the phase separation of other layers within the bulk domain while each layer itself is also undergoing the phase separation due to the surface attraction force. Second, the SD phase separation is governed through the *bulk* in the domain while the surface maintains its attraction over the farther

layers. Since the surface attraction becomes weaker as the layers are positioned farther away from the surface, the phase separation is controlled by the bulk. In this section one or two parameters were changed at a time to study the effects of the above parameters on the formation of the morphology. In general, through long-range mechanism, each layer will undergo the phase separation when the bulk is quenched into two-phase spinodal region. The surface attachment will also affect the morphology of phase separation.

6.2.1 Effect of Different Diffusion Coefficients

In Figure 6.1, the bulk domain undergoes uniform temperature quench (no temperature gradient) for different diffusion coefficients of (a) 2×10^5, (b) 4×10^5 and (c) 8×10^5. As the morphology shows, there is faster rate of phase separation for the higher values of diffusion coefficient, and due to the lower concentration the droplets are more spherical [135,136,138,145,160–163,247,249,317,336,398].

It also indicates the dependency of the rate of surface enrichment as a function of diffusion coefficient. The rate of surface enrichment will increase as the diffusion coefficient decreases (visible at $t^* = 0.972$). The lower values of diffusion coefficients, similar to the short-range model, has less driving force to induce phase separation within the bulk leading to more of component being left for the surface to attract. In this model, despite the short-range surface potential case, no transition from complete wetting to partial wetting at the surface is observed. This is in agreement with previous numerical work [411]. Long-range surface attraction forces are stronger than short-range surface potential forces [102,113].

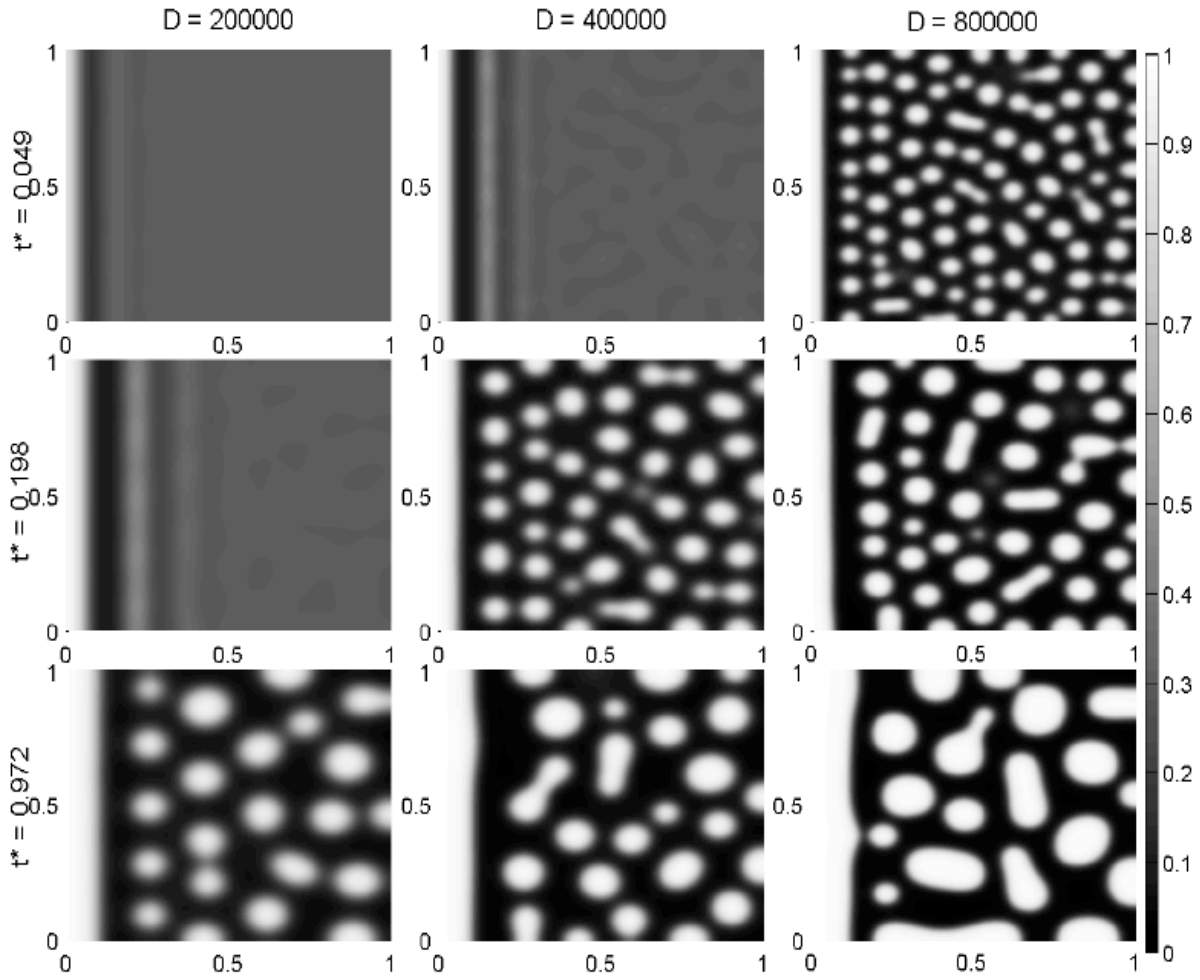

(a) (b) (c)

Figure 6.1: Morphology formation for three dimensionless diffusion coefficient values (a) $D = 2 \times 10^5$, (b) 4×10^5 and (c) 8×10^5 in a long-range surface attraction case where phase separation is governed by an off-critical quenching condition. There is no temperature gradient within the bulk. Initial concentration $c_0^* = 0.3$, $N = 1000$, $g = -0.5$, $h_1 = h_2 = h_3 = h_4 = 0.5$, and $T_1^* = T_2^* = 0.20$.

To study the effect of diffusion coefficient better on the rate of phase separation through the bulk, a typical evolution of the dimensionless structure factor at different

dimensionless times in a long-range surface potential phase separation model is developed (Figure 6.2). Similar to the short-range surface potential, the value of the dimensionless structure factor increases exponentially with time in the early stages of phase separation by SD and begins to slow down as it approaches the beginning of the intermediate stages where nonlinear effects come into play.

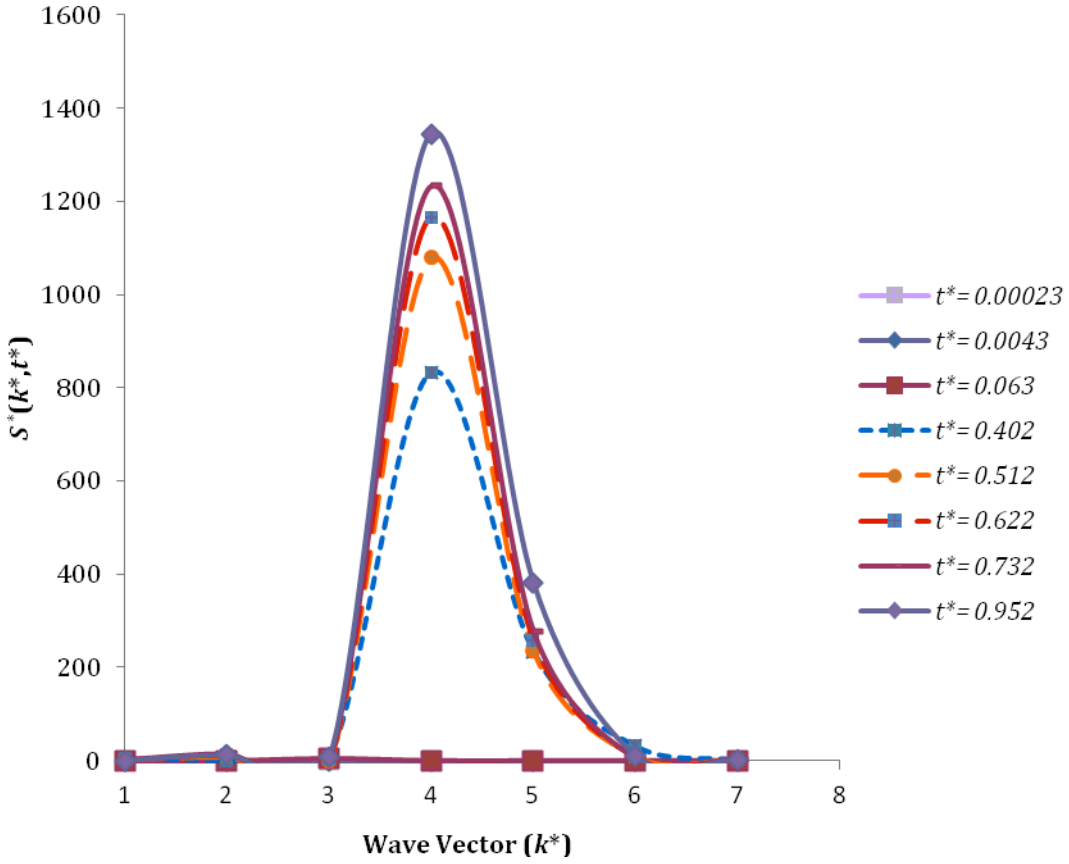

Figure 6.2: Typical evolution of the dimensionless structure factor at different dimensionless times in a long-range surface potential phase separation corresponding to Figure 6.1 (b) where $c_0^* = 0.3$, $h = 0.5$, $N = 1000$, $g = -0.5$, $D = 4 \times 10^5$, and $T_1^* = T_2^* = 0.20$.

The wave number is constant during the early to the beginning of the intermediate stages, and this is typical of spinodal decomposition phase separation mechanism [164]. The evolution of the dimensionless structure factor (exponential growth and fixed wave number) shows the same trends that have been reported both in experimental [164,304,335,371] and numerical work [135,136,145,317,307,336,375,400].

Figure 6.3 is a logarithm plot of the structure factor $S^*(k^*_m, t^*)$ as a function of dimensionless time t^* corresponding to the case shown in Figure 6.1. $S^*(k^*_m, t^*)$ is the structure factor evaluated at the dimensionless wavenumber k^*_m, which is where the

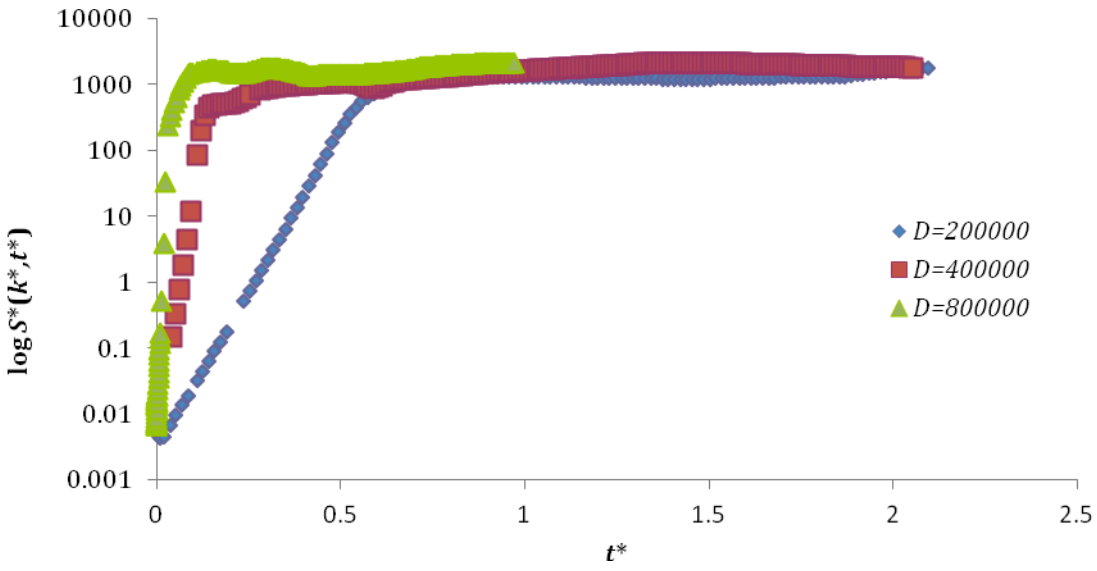

Figure 6.3: Typical maximum structure factor $S^*(k^*_m, t^*)$ as a function of dimensionless time t^* for the simulation shown in Figure 6.1. This curve is typical of spinodal decomposition, since there is an exponential growth at first but then it slows down. $c_0^* = 0.3$, $h = 0.5$, $N = 1000$, $g = -0.5$, $T_1^* = T_2^* = 0.20$, D values: 2×10^5, 4×10^5 and 8×10^5.

maximum of $S^*(k^*, t^*)$ is located at time t^*. It can be observed that $S^*(k^*_m, t^*)$, increases exponentially in the early stage but it slows down as the phase separation enters the intermediate stage. This trend in the evolution of $S^*(k^*_m, t^*)$ has already been observed for short-range surface potential cases. Figure 6.3 shows the transition time from the early to intermediate stages of SD mechanism within the bulk occurs at a later time for lower rates of diffusion coefficient ($D = 2 \times 10^5$) at dimensionless temperature 0.20.

Figure 6.4 depicts a typical diagram selected from Figure 6.3 ($D = 2 \times 10^5$) of the logarithmic structure factor $S^*(k^*_m, t^*)$ as a function of dimensionless time corresponding to the case presented in Figure 6.1 (a) to illustrate the transition time using the tangent lines drawn over early stage and intermediate stage crossover region ($t^* = 0.606$). The intersection of tangent lines represents the transition time between the early and intermediate stages of spinodal decomposition.

Logarithmic plot of structure factor versus dimensionless time (Figure 6.4) reveals a growth exponent of 0.33 (slope of tangent line) for intermediate stage of SD phase separation in the model bulk. The result is consistent with previous numerical [173,184,191,199,209,215,217,385,387,389] and experimental [198,212,221,386,390,391] work, though, dominant interface diffusion at very low temperature can give rise to different values of the exponent [384]. The morphology formation for three dimensionless diffusion coefficient values, $D = 3 \times 10^5$, 4×10^5 and 5×10^5 for long-range surface potential case is shown in Figure 6.5. Temperature gradient was imposed from $T_1^* = 0.15$ to $T_2^* = 0.16$. Since the purpose of this model is to verify the impact of different diffusion coefficients, the

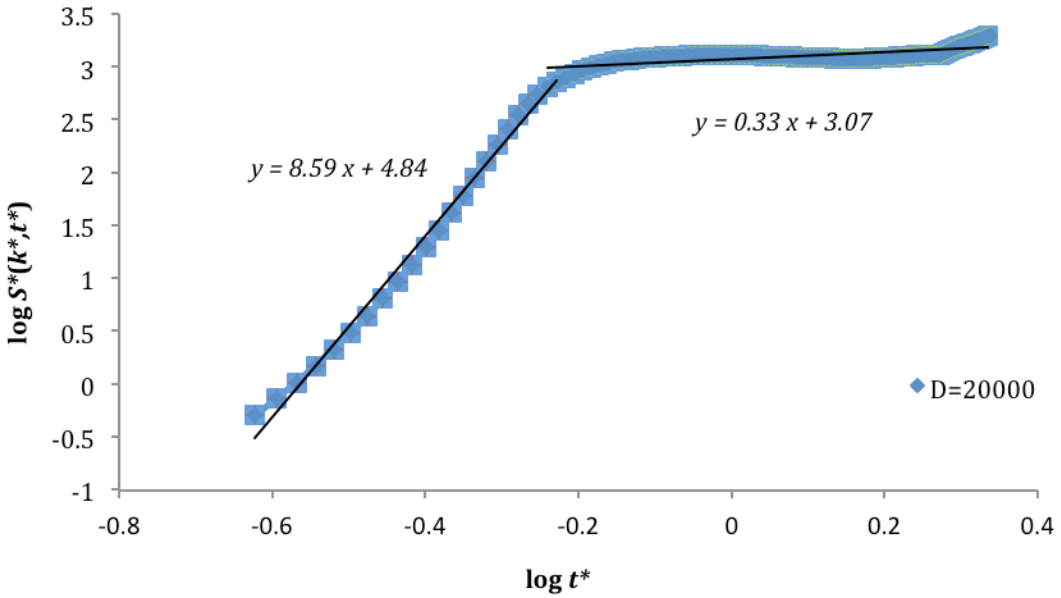

Figure 6.4: Typical diagram selected from Figure 6.3 ($D = 2 \times 10^5$) of the logarithmic structure factor $S^*(k^*_m, t^*)$ as a function of dimensionless time corresponding to the case presented in Figure 6.1 (a). The intersection of tangent lines drawn over early stage and intermediate stage of SD represents the transition time ($t^* = 0.606$). The slope of the tangent line for the intermediate stage is calculated to be 0.33 consistent with the Lifshitz-Sloyozov (LS) law. There is no temperature gradient within the bulk. Initial concentration $c_0^* = 0.3$, $h = 0.5$, $N = 1000$, $g = -0.5$ and $T_1^* = T_2^* = 0.20$.

temperature gradient selected in this study allowed this impact to be visualized and quantified. Phase separation is initiated through a long-range surface potential attraction starting from the surface with h =0.5 that is also accompanied by its lower temperature T_1^* = 0.15. The white solid strip in the layer close to the surface in Figures 6.5 (a), (b) and (c) at t^*

= 0.029 is the representation of spinodal wave through the bulk; consistent with previous experimental work [155,222].

In Figure 6.5 (a) at t^* = 0.029, second spinodal composition wave is also visible. The resulting white strip will rupture inside the bulk over time. The constant concentration is c_0^* = 0.4 for this case mimicking an off-critical quenching mechanism where the elongated droplets are not in spherical form since the concentration is close to the critical value (c_0^* = 0.5) [403]. There is also no transition from complete wetting to partial wetting as expected for long-range surface potential [411]. The morphology is in accordance with the previous results [135,160,161,317] indicating that as the diffusion coefficient increases, rate of phase separation will increase in the bulk domain consistently.

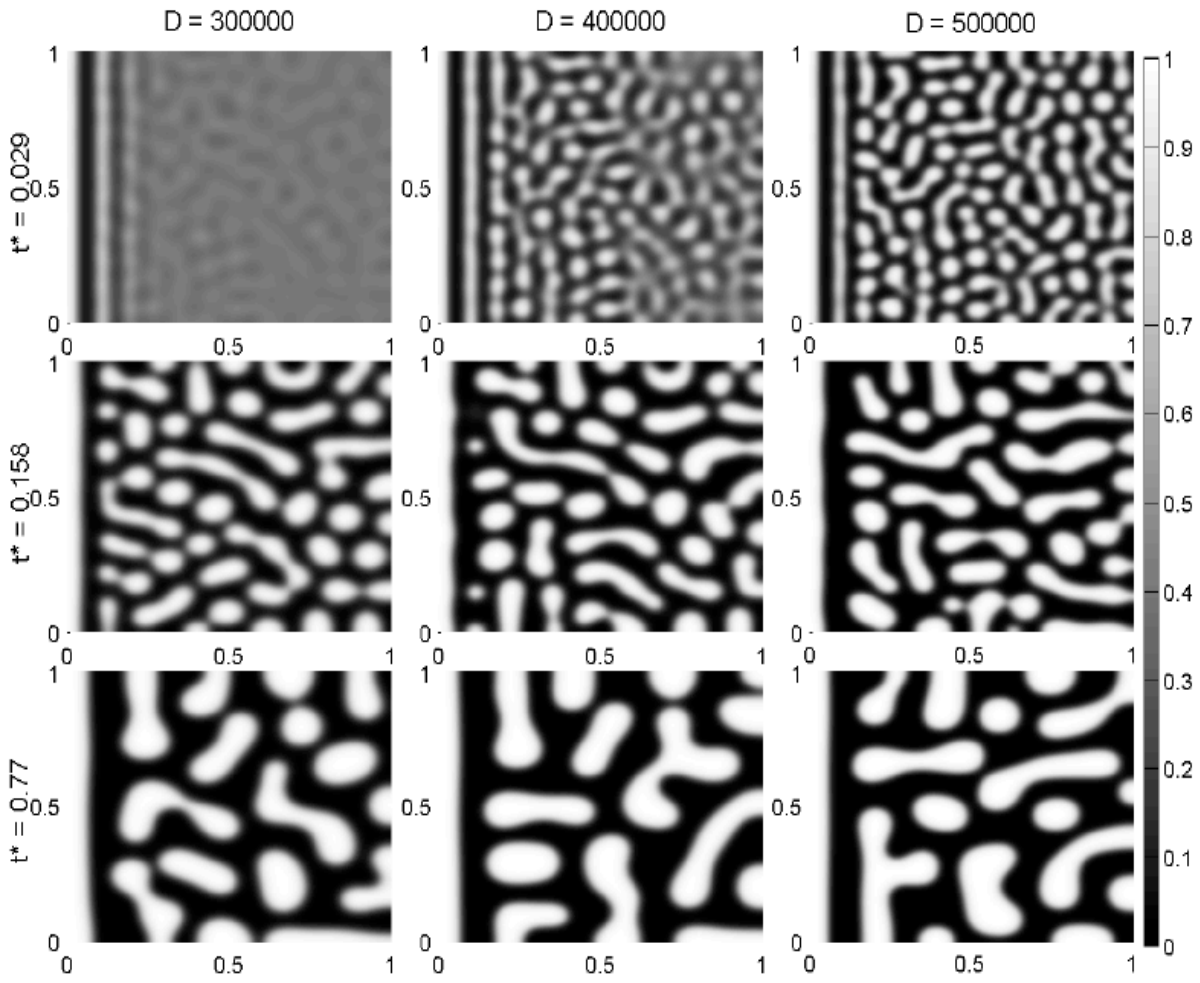

(a) (b) (c)

Figure 6.5: Morphology formation for three dimensionless diffusion coefficient values: D = (a) 3×10^5, (b) 4×10^5 and (c) 5×10^5 in a long-range surface attraction case where phase separation is governed by an off-critical quenching condition. Temperature gradient remained constant at $T_1^* = 0.15$ and $T_2^* = 0.16$. Initial concentration $c_0^* = 0.4$, $h = 0.5$, $N = 1000$, $g = -0.5$.

6.2.2 Effect of Quench Depth on Surface Enrichment

In this section the effect of quench depth on the morphology formation of phase separation in long-range surface potential attraction has been studied. Effort was placed on exploring the impact of quench depth in the surface enrichment as well as the morphology development of the bulk. For shallower quench, similar to short-range surface potential case, the higher rate of surface enrichment was observed. Spinodal decomposition wave [155,222] initiated from the surface is observable for all quench depths, however, for deep quench ($T_1^* = T_2^* = 0.15$), the rupture of the wave took place earlier than shallow quench due to the faster rate of phase separation within the bulk in case of deep quench. This phenomenon is quite conspicuous in Figure 6.6 (a to c) at $t^* = 0.01$. In contrast to the short-range surface potential, the transition from complete wetting to partial wetting is not observed for deep quenches [411]. This is due to the larger strength of long-range surface attraction forces in comparison with the short-range surface potential forces [102,113].

Figure 6.7 presents the effect of different quench depths on the surface enrichment growth rate with temperature gradient (non-uniform quench) in long-range surface potential case. Temperature at the surface T_1^* varies while the temperature T_2^* is constant for all cases. Surface enrichment for shallow quench at surface has a faster rate compared to the deep quench. This typical behavior is visible in Figure 6.7 (a to c) at $t^* = 0.458$. There exists a continuous surface enrichment for all quench depths. There are also two spinodal decomposition waves similar to previous case (Figures 6.5 and 6.6) confirming long-range surface potential of phase separation [155,222]. Hence, the morphology of the polymer blend can be tailored by coupling surface potential and temperature gradient at different stages.

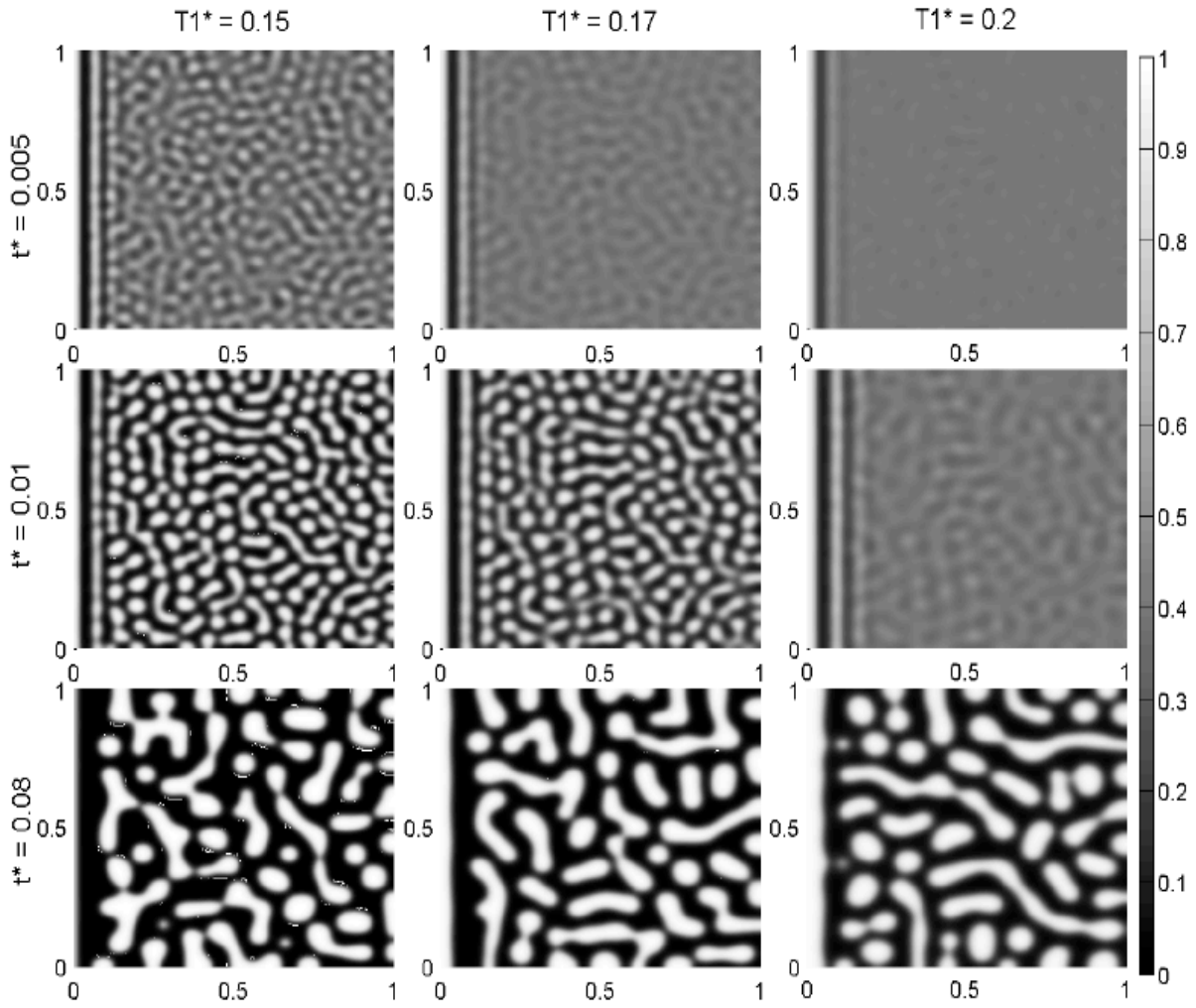

(a) (b) (c)

Figure 6.6: Effect of different quench depths on the surface enrichment with no temperature gradient quench, where phase separation is governed by an off-critical quenching condition in a long-range surface attraction case. The parameter values are $c_0^* = 0.4$, $D = 8 \times 10^5$, $h = 0.5$, $N = 1000$, $g = -0.5$, $T_1^* = T_2^*$ = (a) 0.15, (b) 0.17 and (c) 0.2.

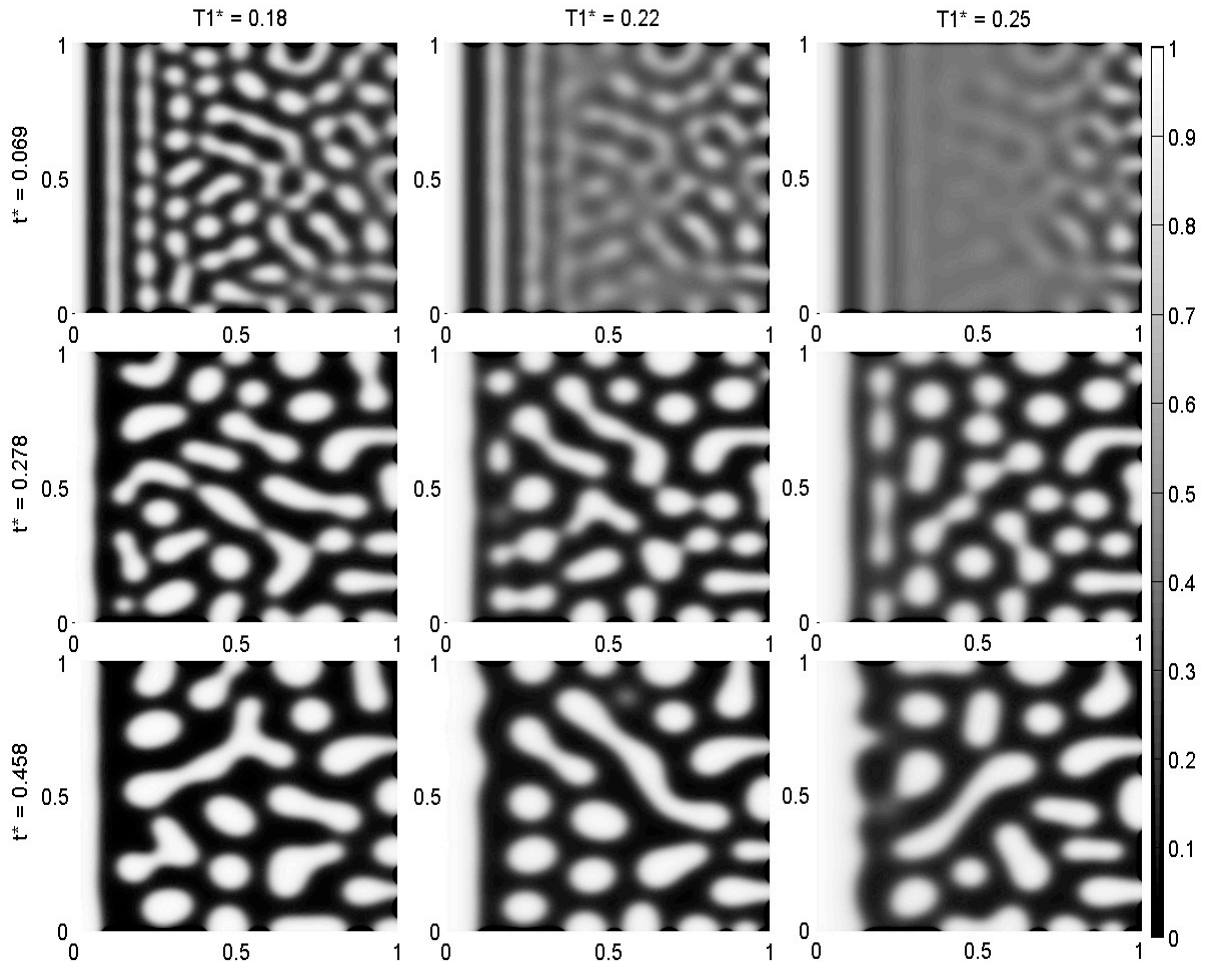

(a) (b) (c)

Figure 6.7: Effect of different quench depths on the surface enrichment growth rate with temperature gradient, where phase separation is governed by an off-critical quenching condition in a long-range surface attraction case. The parameter values are $c_0^* = 0.4$, $D = 4 \times 10^5$, $h = 0.5$, $N = 1000$, $g = -0.5$, and T_1^* = (a) 0.18, (b) 0.22 and (c) 0.25. $T_2^* = 0.2$.

6.2.3 Effect of Temperature Gradient on Surface Enrichment

In this section, the effect of the temperature gradient on the morphology formation is studied. Figure 6.8 shows typical morphology evolution for an off-critical quench where the parameter values are $c_0^* = 0.4$, $D = 4 \times 10^5$, $h = 0.5$, $g = -0.5$ and $T_1^* = 0.15$. The dimensionless temperature T_2^* was then varied from 0.16 to 0.20. As mentioned before, the SD phase separation in TIPS mechanism is always induced by temperature quench. It should be mentioned that the thickness of the wetting layer at the surface with temperature T_1^* for deep quench case ($T_2^* = 0.16$) did not grow significantly higher than the shallow quench depth ($T_2^* = 0.20$), which implies that the effect of temperature gradient over the surface enrichment is less than the short-range surface potential case. To the best of our knowledge, the effect of temperature gradient on surface enrichment in long-range surface attraction, when T_1^* is constant and T_2^* is decreasing, has been investigated for the first time in this thesis.

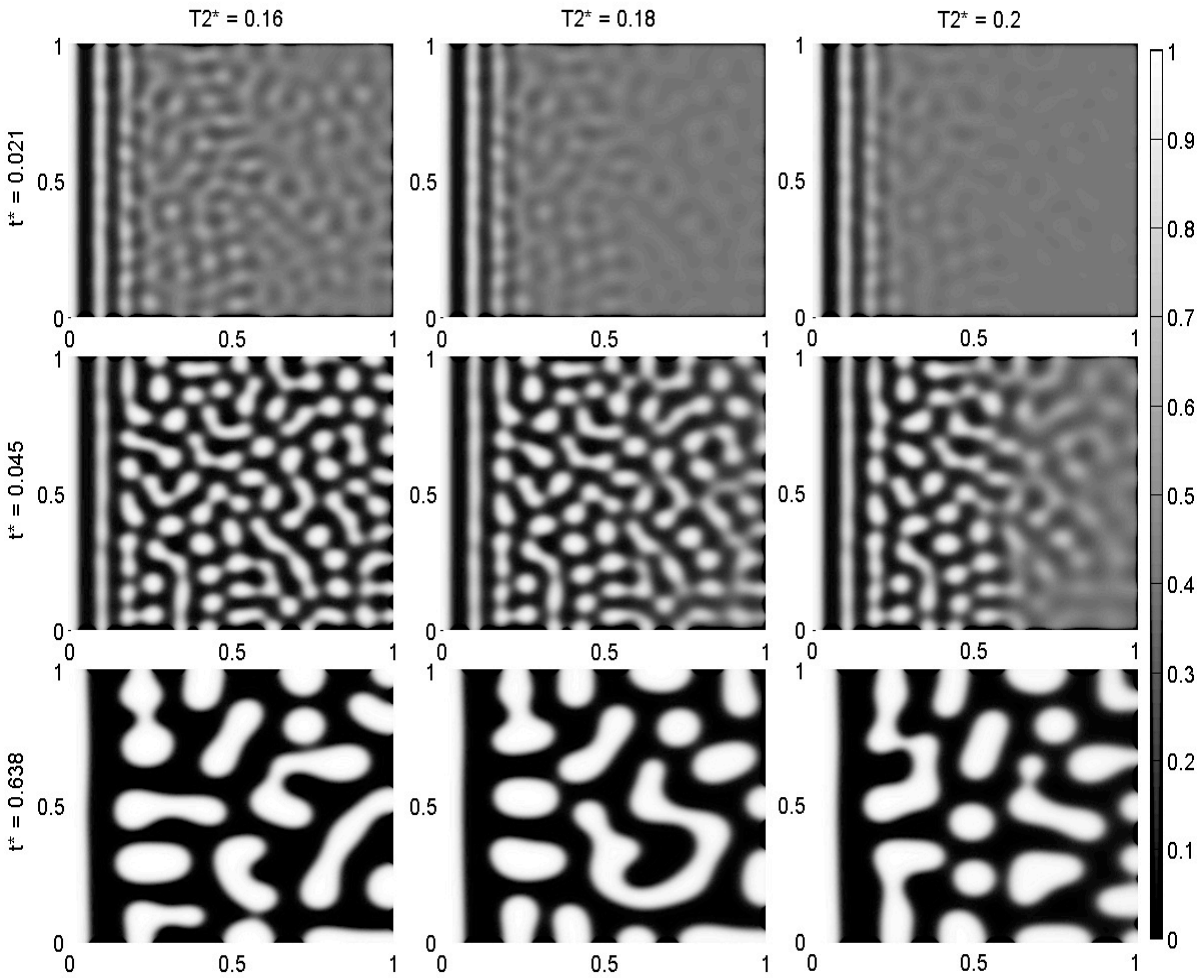

(a) (b) (c)

Figure 6.8: Effect of temperature gradient on surface enrichment growth rate where phase separation is governed by an off critical quenching condition in long-range surface potential case. The parameter values are $c_0^* = 0.4$, $D = 4 \times 10^5$, $h = 0.5$, $g = -0.5$ and $T_1^* = 0.15$, $T_2^* =$ (a) 0.16, (b) 0.18 and (c) 0.20.

6.2.4 Effect of Concentration on Surface Enrichment

Effect of concentration change in long-range surface potential morphology for critical and off-critical quenching conditions are similar to the results obtained in Chapter 4 for short-range surface attraction cases. The interconnected (droplet) morphology is resulted form the quenching conditions in critical (off-critical) concentration. Figure 6.9 presents, two distinct spinodal decomposition waves at the early stage of phase separation for both critical and off-critical quenches. The waves will rupture when the bulk domain undergoes further SD phase separation which leads to (a) droplet type morphology, (b) elongated droplet morphology (c_0^* = 0.4) [403] which is typical for the concentrations close to the critical concentration (c_0^* = 0.5) and (c) interconnected morphology (c_0^* = 0.5).

Figure 6.10 compares the short- and long-range surface potential cases. Two spinodal decomposition waves for the long-range case are quite conspicuous at t^* = 0.026 and they diffuse deep down through the bulk for longer time. While for the short-range case, there is only one spinodal wave that is dissipated at a faster rate within the bulk. For instance, at t^* = 0.062, the spinodal wave is completely ruptured. The surface enrichment for the long-range surface potential case has a higher rate of growth in comparison with the short-range case. Typically, for long-range case there is no transition from complete wetting to partial wetting. This is because of higher attraction of the surface over the favorable polymer and the fact that long-range surface attraction forces are stronger than short-range surface potential forces [102,113].

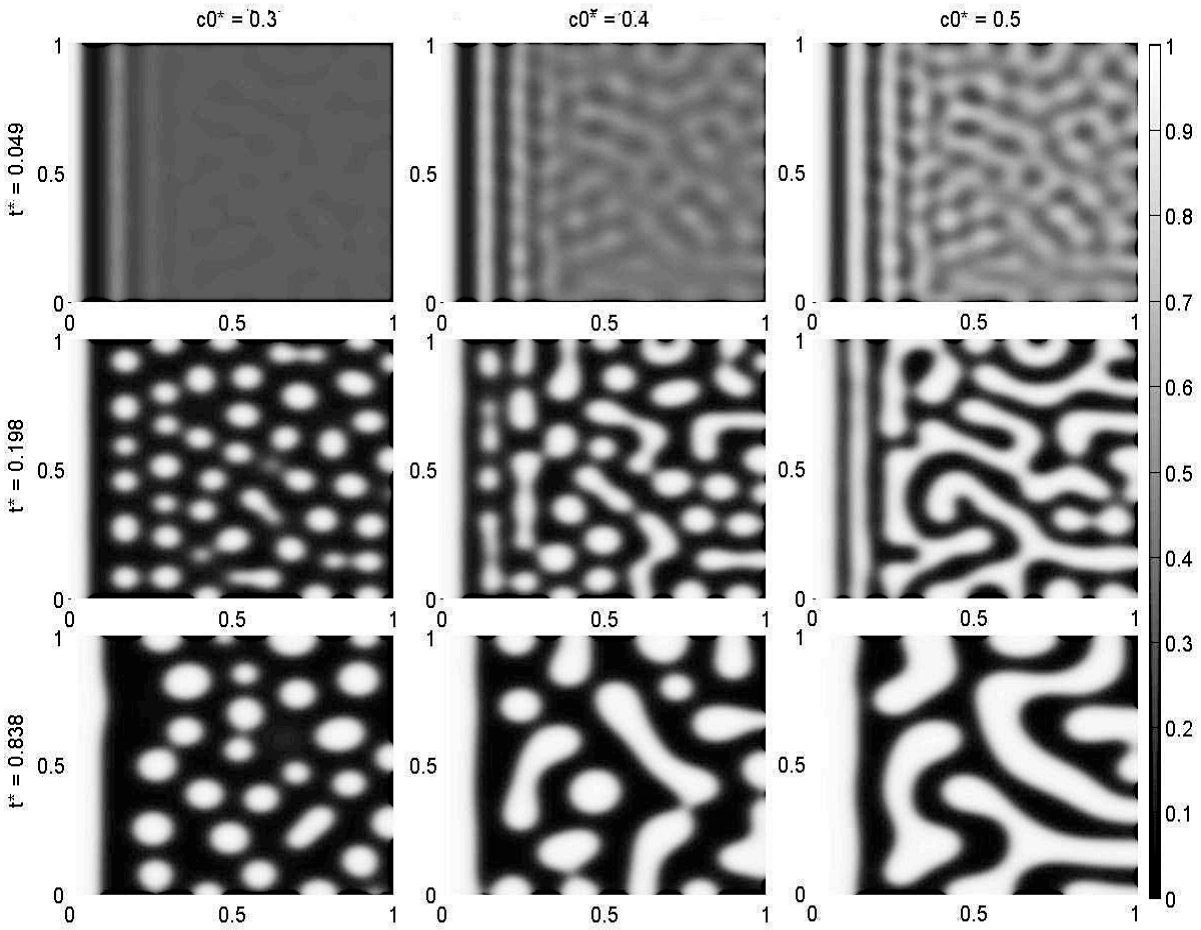

(a) (b) (c)

Figure 6.9: Effect of the concentration on the surface formation where phase separation is governed by (a and b) off-critical and (c) critical quenching conditions in a multiple surface potential case where c_0^* = (a) 0.3, (b) 0.4, (c) 0.5, N = 1000, g = – 0.5, $D = 8 \times 10^5$, $T_1^* = T_2^*$ = 0.20 and h = 0.5.

To further investigate the effect of long-range surface potential over the phase separation in the bulk, the logarithmic dimensionless structure factor is developed according to Figure 6.11 for both short and long-range surface potential cases. At the horizontal distance x^* = 0.25 from the surface, the transition from early stage to intermediate stage

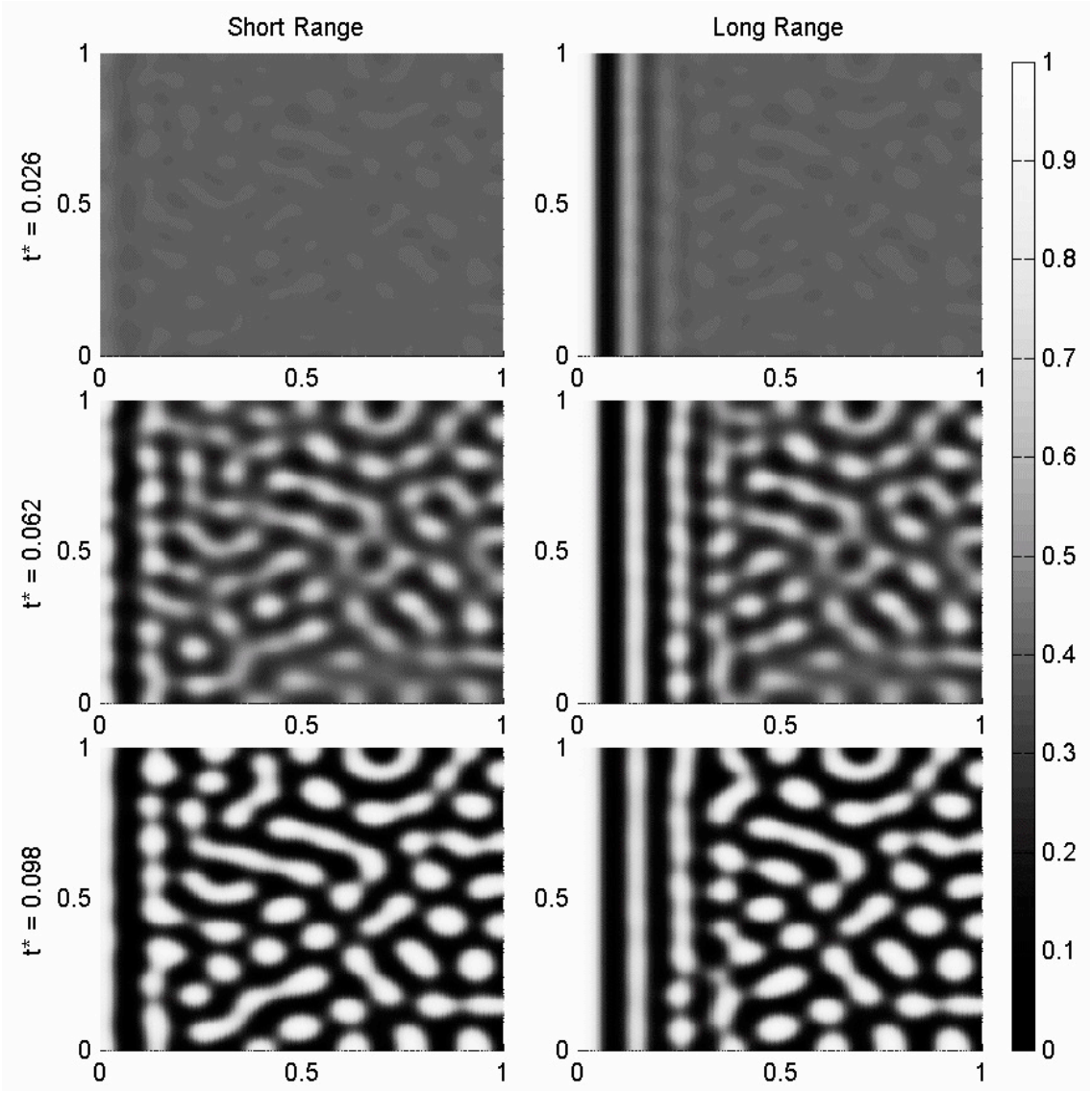

(a) (b)

Figure 6.10: Comparison between short- and long-range surface potential cases for uniform off-critical quench where $c_0^* = 0.4$, $N = 1000$, $g = -0.5$, $D = 4 \times 10^5$, $T_1^* = T_2^* = 0.20$ and $h = 0.5$.

occurred at an earlier time ($t^* = 0.063$) for the long-range case while for the short-range case it occurred at $t^* = 0.086$. This behavior confirms that the long-range surface potential will

(a)

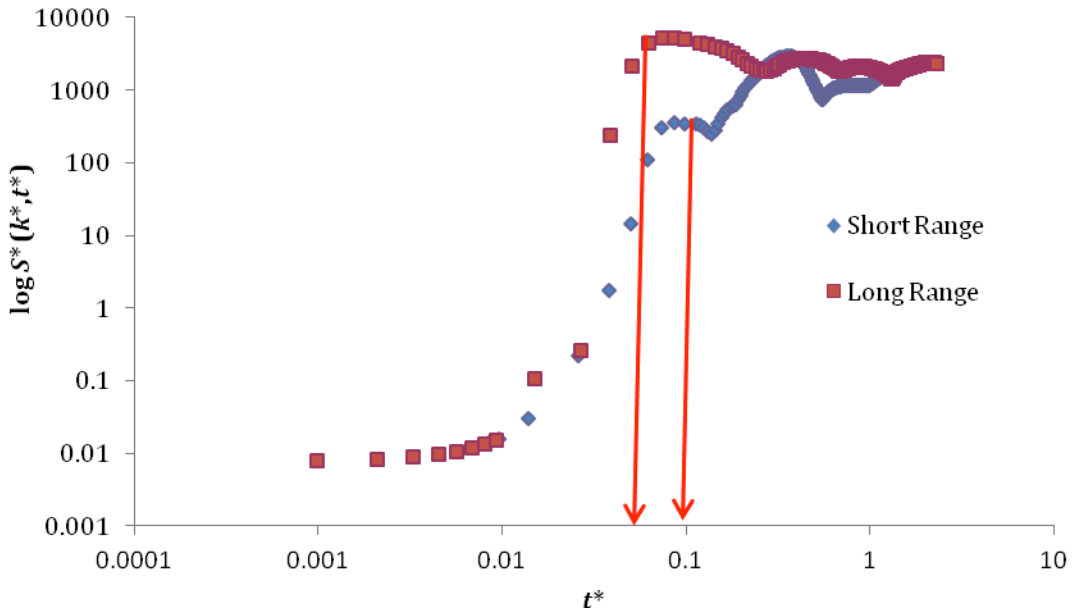

(b)

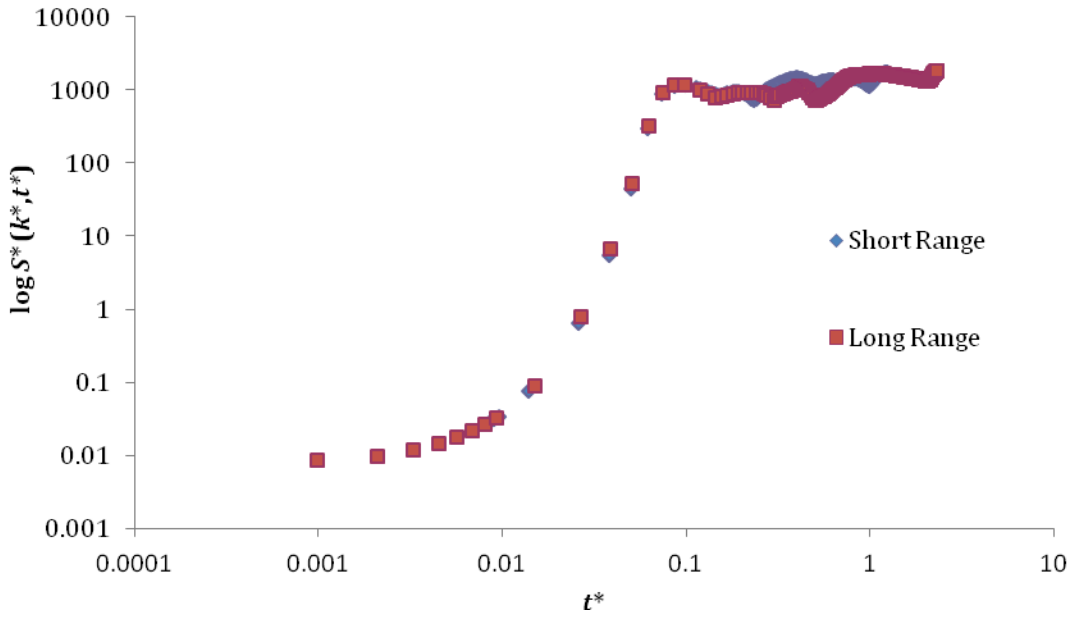

Figure 6.11: Dimensionless logarithmic structure factor of short- and long-range transition time at (a) $x^* = 0.25$ and (b) $x^* = 0.5$ where $c_0^* = 0.4$, $N = 1000$, $g = -0.5$, $D = 4 \times 10^5$, $T_1^* = T_2^* = 0.20$ and $h = 0.5$.

affect the bulk morphology farther through the bulk than short-range surface potential case. It should be noted that the morphology of the bulk, represented by structure factor, as well as the transition time from the early stage to intermediate stage took place identically far from the surface ($x^* > 0.5$) for both short-and long-range cases as presented in Figure 6.11 (b).

6.3 Summary & Conclusions

Phase separation phenomena of a model binary polymer blend quenched into the unstable region of its binary symmetric phase diagram was studied using the nonlinear Cahn-Hilliard theory coupled with the Flory-Huggins theory. Long-range surface potential within a simple geometry, where one side of the domain is exposed to a surface with preferential attraction to one component of a binary polymer blend under temperature gradient in x direction, was incorporated in the model. The initial conditions used in this study reflected the infinitesimal thermal concentration fluctuations in the blend. The equation was spatially discretized by finite difference method to solve the governing equation in a two-dimensional domain using the method of line. CVODE solver was then used to solve the developed ODE's. The numerical solutions and calculated morphologies are in agreement with frequently reported experimental observations and numerical work.

The impacts of different quench depths, diffusion coefficients, surface potentials, temperature gradients, and concentrations were studied numerically. The results were presented in the form of morphology plots, and validated by logarithmic graphs. The results replicate comparable experimental and numerical work performed by other groups.

The spinodal waves observed in models with long-range surface potentials were more vivid and diffused more into the bulk domain than short-range surface potential case. In general, no transition from complete wetting to partial wetting for all quench depths and/or surface potentials was observed. This is because long-range surface attraction forces are stronger than short-range surface potential forces. Though, transition time from early to intermediate stage within the bulk and close to the surface occurred faster than in short-range and multiple-surface potential cases.

The structure factor analysis for the bulk presented an exponential growth rate at the early stage of phase separation, which slowed down at the intermediate stage with a slope of 0.33 through the bulk; in agreement with Lifshitz-Sloyozov (LS) law. As diffusion coefficient increased, the rate of phase separation increased accordingly in the bulk leading to faster transition time from early to intermediate stage within the bulk.

The amount of quench depth also influenced the morphology. In deeper quenches, higher rate of phase separation was observed along with less growth rate on the surface and lower surface enrichment. Deeper quenches also led to the faster rupture of spinodal decomposition waves in the bulk. However, the process of surface enrichment was continuous for all quench depths.

The effect of different temperature gradient values on the surface enrichment rate with the constant temperature T_1^* at the surface and different temperature T_2^* for the opposite side infinitesimal was studied for the first time within a long-range surface potential setting. Unlike the short-range and multiple-surface potential cases, no noticeable changes in surface

enrichment were observed for different temperature gradients in the long-range surface attraction case.

Similar to the short-range and multiple-surface potential cases, the interconnected morphology, for critical quenches ($c_0^* = 0.5$), elongated structure for near critical ($c_0^* = 0.4$), and droplet-like morphology for off-critical quenches ($c_0^* = 0.3$), were obtained replicating comparable experimental and numerical work. However, in long-range surface potential case, morphology development and phase separation are affected in deeper domains within the bulk.

Chapter 7

7. Conclusions

7.1 Conclusions from the Study of SDPS

In this thesis, the morphology development and evolution of the symmetric binary polymer blend during non-uniform thermal-induced phase separation phenomenon via spinodal decomposition in the presence of surface attraction to one of the polymers was studied through modeling and computer simulation. Two-dimensional models based on nonlinear Cahn-Hilliard (C-H) theory incorporating the Flory-Huggins-de Gennes (FHdeG) free energy theory was used to study the thermal-induced phase separation (TIPS) phenomenon in binary blends with competing surface and temperature gradient effects.

Effect of different variables on the morphology formation of following models was investigated:

- Single surface with short-range surface potential
- Multiple surfaces with short-range surface potential
- Single surface with long-range surface potential

The models were able to replicate frequently reported experimental observations in the literature. Overall, through the simulation and modeling of numerous cases discussed in detail in Chapters 4, 5 and 6, it is concluded that the any increase in diffusion coefficient will

speed up the phase separation within the bulk in short- and long-range as well as multiple-surface potential cases resulting in the morphology to form faster, whereas, reduction of diffusion coefficient will increase the enrichment rate of the wetting layer on the surface regardless of the surface potential strength for all cases. Morphology formation and evolution were studied for different quench depths.

Droplet type morphology was observed for off-critical quenches, elongated droplets for near-critical quenches and interconnected morphology were seen for critical quench conditions through phase separation under spinodal decomposition dominance. Moreover, the size of the morphology structure was found to be directly related to the quench depth. Shallower quenches resulted in more coarsened type of morphology while deeper quenches produced smaller structures. The transition from complete wetting to partial wetting for both shallow and deep quenches was demonstrated successfully by short-range models, which were found to be consistent with the experimental as well as numerical results presented in the literature. During morphology analysis, it was observed that deeper quench depths (lower temperatures) would accelerate the transition of complete to partial wetting in short range surface potential cases. However, no transition from complete wetting to partial wetting has been observed for long-rage surface potential case. This is due to the fact that long-range surface attraction forces are stronger than short-range surface potential forces.

Morphology formation and evolution of the polymer blend phase separation in the presence of different surface potentials were also studied. It was found that the higher the surface potential value of a surface is, the stronger the surface becomes in attracting the polymer. It should be noted that transition time from the complete wetting to the partial

wetting of surfaces with short-range surface potential occurred later by higher h values. After h value passes a certain threshold, the surface only shows complete wetting behavior during the early and intermediate stages of the phase separation process.

For shallow quenches in short-range surface potential case, first a growth rate of $t^{0.5}$ was observed and then a decline in the growth rate to $t^{0.13}$ occurred at the surface. On the other hand, for all quenching conditions, in both short- and long range surface potential cases, change of bulk dimensionless structure factor over time demonstrated a slope of 0.31-0.33 in the intermediate stage of phase separation within the bulk, consistent with previous experimental and numerical work.

In case of multiple-surface potential, it was found that surfaces would compete with each other in attracting one polymer to enrich their walls. The surface with higher surface potential would attract the polymer from adjacent surfaces with lower surface potential to enrich its own surface and force the other surfaces to approach their partial wetting faster.

Effect of different temperature gradient values on the growth rate of wetting layer in the condition that T_1^* remained constant but T_2^* had different values was studied for the first time and it showed that the thickness of the wetting layer increases by rise of ΔT^* value (deep quench at T_2^* side). This characteristic could be due to the initiation of phase separation at earlier stage at the wetting surface area since the other part of the sample that is in more advanced stage could act as a driving force to start phase separation earlier in all domains.

Further comparison between short- and long-range surface potential cases shows that proposed model could successfully predict the deeper diffusion of long-range surface

potential through the bulk. Transition time from early to intermediate stage of spinodal decomposition phase separation in the vicinity of surface is studied and proved higher values of diffusion coefficients will accelerate the phase separation in the bulk.

7.2 Original Contributions to Knowledge

The original contributions to knowledge from this thesis are as follow:

1. The development, implementation, solution and validation of a model that describes the phase separation and morphology formation phenomena for the TIPS method in polymer blend systems with short-range potential under temperature gradient. The numerical results and calculated morphologies replicate the frequently reported experimental observations.
2. The development, implementation, solution and validation of a model that describes the phase separation and morphology formation phenomena for the TIPS method in polymer blend systems with multiple-surface potential under temperature gradient in order to represent realistic geometry. The numerical results and calculated morphologies replicate the frequently reported experimental observations.
3. The development, implementation, solution and validation of a model that describes the phase separation and morphology formation phenomena for the TIPS method in polymer blend systems with long-range surface potential under temperature gradient. The numerical results and calculated morphologies replicate the frequently reported experimental observations.

4. The effect of different temperature gradient values on the growth rate of wetting layer was studied for the first time. Understanding and controlling such processes is significant and is necessary in many technological features varying from paper industry and paint formulation to pharmaceutical applications, biophysics, nanocomposite materials, preparation of membrane with anisotropic morphology under temperature gradient, formation of patterned polymer surfaces, and micro-optical devices.
5. One of the recommendation for future work would be to try to incorporate physical properties of polymer blends such as monomer shapes, sizes, hydrogen bonding interactions and polar attraction forces into the mathematical model using more complex geometries.

Appendices

A. Table of Parameter Values for Short-Range Surface Potential Case

Table of Parameter Values (Short-Range)							
Figure No.		c_0*	D	T_1*	T_2*	g	h
Figure 4.4	a	0.3	4×10^5	0.22	0.2	-0.5	0.5
	b	0.3	4×10^5	0.24	0.2	-0.5	0.5
	c	0.3	4×10^5	0.26	0.2	-0.5	0.5
Figure 4.5		0.3	4×10^5	0.24	0.2	-0.5	0.5
Figure 4.6		0.3	4×10^5	0.26	0.2	-0.5	0.5
Figure 4.7		0.3	4×10^5	0.26	0.2	-0.5	0.5
Figure 4.8		0.5	8×10^5	0.3	0.2	-0.5	0.5
Figure 4.9	a	0.4	4×10^5	0.2	0.2	-0.5	0.5
	b	0.4	4×10^5	0.22	0.2	-0.5	0.5
	c	0.4	4×10^5	0.24	0.2	-0.5	0.5
Figure 4.10		0.4	4×10^5	0.12-0.2	0.2	-0.5	0.5
Figure 4.11	a	0.4	3×10^5	0.25	0.2	-0.5	0.5
	b	0.4	5×10^5	0.25	0.2	-0.5	0.5
	c	0.4	6×10^5	0.25	0.2	-0.5	0.5
Figure 4.12	a	0.4	4×10^5	0.25	0.2	-0.5	2
	b	0.4	8×10^5	0.25	0.2	-0.5	2
Figure 4.13	a	0.5	4×10^5	0.25	0.2	-0.5	1
	b	0.5	8×10^5	0.25	0.2	-0.5	1
Figure 4.14	a	0.4	4×10^5	0.25	0.1	-0.5	0.5
	b	0.4	4×10^5	0.25	0.15	-0.5	0.5
	c	0.4	4×10^5	0.25	0.2	-0.5	0.5
Figure 4.15		0.4	4×10^5	0.2	0.18	-0.5	0.5–6
Figure 4.16		0.4	4×10^5	0.2	0.18	-0.5	0.5–6
Figure 4.17		0.4	4×10^5	0.2	0.18	-0.5	0.5–6
Figure 4.18		0.5	8×10^5	0.2	0.2	-0.5	2

Figure 4.19	a	0.3	4×10^5	0.2	0.15	-0.5	1
	b	0.3	4×10^5	0.2	0.15	-0.5	2.5
Figure 4.20	a	0.5	4×10^5	0.2	0.15	-0.5	1
	b	0.5	4×10^5	0.2	0.15	-0.5	2.5

B. Table of Parameter Values for Multiple-Surface Potential Case

Table of Parameter Values (Multiple)										
Figure No.		c_0*	D	T_1*	T_2*	g	h_1	h_2	h_3	h_4
Figure 5.2	a	0.5	2×10^5	0.15	0.25	-0.5	0.5	0.5	0.5	0.5
	b	0.5	4×10^5	0.15	0.25	-0.5	0.5	0.5	0.5	0.5
	c	0.5	8×10^5	0.15	0.25	-0.5	0.5	0.5	0.5	0.5
Figure 5.3		0.5	2×10^5	0.15	0.25	-0.5	0.5	0.5	0.5	0.5
Figure 5.4	a	0.5	3×10^5	0.25	0.25	-0.5	0.5	1	2	4
	b	0.5	6×10^5	0.25	0.25	-0.5	0.5	1	2	4
	c	0.5	8×10^5	0.25	0.25	-0.5	0.5	1	2	4
Figure 5.5	a	0.5	8×10^5	0.2	0.2	-0.5	2	2	2	2
	b	0.5	8×10^5	0.25	0.25	-0.5	2	2	2	2
Figure 5.6		0.3	2×10^5	0.2	0.2	-0.5	2	2	2	2
Figure 5.7		0.3	2×10^5	0.2	0.2	-0.5	2	2	2	2
Figure 5.8	a	0.5	2×10^5	0.18	0.18	-0.5	1	2	3	4
	b	0.5	2×10^5	0.2	0.2	-0.5	1	2	3	4
	c	0.5	2×10^5	0.25	0.25	-0.5	1	2	3	4
Figure 5.9	a	0.5	4×10^5	0.15	0.25	-0.5	1	1	1	1
	b	0.5	4×10^5	0.15	0.25	-0.5	2	2	2	2
	c	0.5	4×10^5	0.15	0.25	-0.5	4	4	4	4
Figure 5.10	a	0.5	4×10^5	0.15	0.25	-0.5	1, 2, 4	1, 2, 4	1, 2, 4	1, 2, 4
	b	0.5	4×10^5	0.15	0.25	-0.5	1, 2, 4	1, 2, 4	1, 2, 4	1, 2, 4
Figure 5.11	a	0.5	4×10^5	0.2	0.22	-0.5	2	2	1.8	2
	b	0.5	4×10^5	0.2	0.22	-0.5	2	2	3	2
	c	0.5	4×10^5	0.2	0.22	-0.5	2	2	4	2
Figure 5.12	a	0.5	4×10^5	0.2	0.22	-0.5	2	2	1.8, 3, 4	2

	b	0.5	4×10^5	0.2	0.22	-0.5	2	2	1.8, 3, 4	2
Figure 5.13		0.5	8×10^5	0.05	0.05	-0.5	1, 4, 8	1, 4, 8	1, 4, 8	1, 4, 8
Figure 5.14	a	0.3	4×10^5	0.15	0.25	-0.5	0.5	0.5	0.5	0.5
	b	0.4	4×10^5	0.15	0.25	-0.5	0.5	0.5	0.5	0.5
	c	0.5	4×10^5	0.15	0.25	-0.5	0.5	0.5	0.5	0.5
Figure 5.15	a	0.3	8×10^5	0.2	0.2	-0.5	2	2	2	2
	b	0.4	8×10^5	0.2	0.2	-0.5	2	2	2	2
Figure 5.16	a	0.5	4×10^5	0.1	0.2	-0.5	2	2	2	2
	b	0.5	4×10^5	0.2	0.2	-0.5	2	2	2	2
Figure 5.17	a	0.4	4×10^5	0.15	0.1	-0.5	0.5	0.5	0.5	0.5
	b	0.4	4×10^5	0.15	0.15	-0.5	0.5	0.5	0.5	0.5
	c	0.4	4×10^5	0.15	0.2	-0.5	0.5	0.5	0.5	0.5
Figure 5.18		0.4	4×10^5	0.15	0.1 – 0.2	-0.5	0.5	0.5	0.5	0.5
Figure 5.19	a	0.5	4×10^5	0.2	0.21	-0.5	2	2	2	2
	b	0.5	4×10^5	0.2	0.22	-0.5	2	2	2	2
	c	0.5	4×10^5	0.2	0.23	-0.5	2	2	2	2
Figure 5.20	a	0.5	4×10^5	0.3	0.25	-0.5	0.5	1	2	4
	b	0.5	4×10^5	0.3	0.28	-0.5	0.5	1	2	4
	c	0.5	4×10^5	0.3	0.3	-0.5	0.5	1	2	4

C. Table of Parameter Values for Long-Range Surface Potential Case

Table of Parameter Values (Long-Range)							
Figure No.		c_0*	D	T_1*	T_2*	g	h
Figure 6.1	a	0.3	2×10^5	0.2	0.2	- 0.5	0.5
	b	0.3	4×10^5	0.2	0.2	- 0.5	0.5
	c	0.3	8×10^5	0.2	0.2	- 0.5	0.5
Figure 6.2		0.3	4×10^5	0.2	0.2	- 0.5	0.5
Figure 6.3		0.3	2×10^5–$8\times1\,0^5$	0.2	0.2	- 0.5	0.5
Figure 6.4		0.3	2×10^5	0.2	0.2	- 0.5	0.5
Figure 6.5	a	0.4	3×10^5	0.15	0.16	- 0.5	0.5

	b	0.4	4×10^5	0.15	0.16	- 0.5	0.5
	c	0.4	5×10^5	0.15	0.16	- 0.5	0.5
Figure 6.6	a	0.4	8×10^5	0.15	0.15	- 0.5	0.5
	b	0.4	8×10^5	0.17	0.17	- 0.5	0.5
	c	0.4	8×10^5	0.2	0.2	- 0.5	0.5
Figure 6.7	a	0.4	4×10^5	0.18	0.2	- 0.5	0.5
	b	0.4	4×10^5	0.22	0.2	- 0.5	0.5
	c	0.4	4×10^5	0.25	0.2	- 0.5	0.5
Figure 6.8	a	0.4	4×10^5	0.15	0.16	- 0.5	0.5
	b	0.4	4×10^5	0.15	0.18	- 0.5	0.5
	c	0.4	4×10^5	0.15	0.2	- 0.5	0.5
Figure 6.9	a	0.3	8×10^5	0.2	0.2	- 0.5	0.5
	b	0.4	8×10^5	0.2	0.2	- 0.5	0.5
	c	0.5	8×10^5	0.2	0.2	- 0.5	0.5
Figure 6.10	a	0.4	4×10^5	0.2	0.2	- 0.5	0.5
	b	0.4	4×10^5	0.2	0.2	- 0.5	0.5
Figure 6.11	a	0.4	4×10^5	0.2	0.2	- 0.5	0.5
	b	0.4	4×10^5	0.2	0.2	- 0.5	0.5

References

[1] White, J. L., & Bumm, S. H. (2011). In I. A. Isayev (Ed.), *Encyclopedia of Polymer Blends Vol. 2* (1–26). Weinheim: Wiley-VCH Verlag GmbH & Co. KGaA.

[2] Hofmann, W. (1963). *Rubber Chem. Technol*., *37*(2), 52–61.

[3] Ramiro, J., Eguiazábal, J. I., & Nazábal, J. (2006). *Macromolecular Materials and Eng., 291*(6), 707–713.

[4] Yave, W., & Quijada, R. (2008). *Desalination, 228*, 150–158.

[5] Xie, X. M., Chen, Y., Zhang, Z. M., Tanioka, A., Matsuoka, M., & Takemura, K. (1999). *Macromolecules, 32*(13), 4424–4429.

[6] Caneba, G. T., & Soong, D. S. (1985). *Macromolecules, 18*(12), 2538–2545.

[7] Caneba, G. T., & Soong, D. S. (1985). *Macromolecules, 18*(12), 2545–2555.

[8] Prime, K. L., & Whitesides, G. M. (1991). *Science, 252*(5009), 1164–1167.

[9] Halls, J. J. M., Walsh, C. A., Greenham, N. C., Marseglia, E. A., Friend, R. H., Moratti, S. C., & Holmes, A. B. (1995). *Nature, 376*(6540), 498–500.

[10] Maxwell, J. C. (1879). *Encyclopedia Britannica* 9th ed. London: Encyclopedia Britannica.

[11] Chappelear, D. C. (1964). *ACS Polym. Papers*, *5*, 363.

[12] Roe, R. J. (1969). *J. Colloid Interface Sci. 31*, 228.

[13] Wu, S. (1970). *J. Phys. Chem. 74*, 632.

[14] Peterson, H. T., Hu, K. H., & Grindstaff, T. H. (1971). *J. Polym. Sci. 34*, 31.

[15] Carriere, C. J., Cohen, A., & Arends, C. B. (1989). *J. Rheol. 33*, 681.

[16] Elemans, P. H. M., Janssen, J. M. H., & Meijer, H. E. H. (1990). *J. Rheol. 34*, 1311.

[17] Chen, C. C., & White, J. L. (1993). *Polym. Eng. Sci. 33*, 923.

[18] Yoon, P. J., & White, J. L. (1994). *J. Appl. Polym. Sci. 51*, 1515.

[19] Barentsen, W., & Heikens, D. (1973). *Polymer, 14*, 579.

[20] Barentsen, W., Heikens, D., & Piet, P. (1974). *Polymer, 15*, 119.

[21] Ide, F., & Hasegawa, A. (1974). *J. Appl. Polym. Sci., 18*, 963.

[22] Heikens, D., Hoen, N., Barentsen, W., Piet, P., & Linden, H. (1978). *J. Polym. Sci. Symp., 62*, 309.

[23] Endo, S., Min, K., White, J. L., & Kyu, T. (1986). *Polym. Eng. Sci., 26*, 45.

[24] Jiang, R., Quirk, R. P., White, J. L., & Min, K. (1991). *Polym. Eng. Sci., 31*, 1545.

[25] Ihm, D., & White, J. L. (1996). *J. Appl. Polym. Sci., 60*, 1.

[26] Min, K., White, J. L., & Fellers, J. F. (1984). *Polym. Eng. Sci., 24*, 1327.

[27] White, J. L., & Min, K. (1984). *Adv. Polym. Technol., 24*, 1327.

[28] Robeson, L. M. (2007). *Polymer Blends: A Comprehensive Review.* Cincinnati, OH: Hanser.

[29] Koleske, J. V., & Lundberg, R. D. (1969). *Polym. Sci., Part A-2, 7*, 795.

[30] Bohn, L. (1968). *Rubber Chem. Technol., 41*, 495.

[31] Buckley, D. J. (1967). *Trans. N.Y. Acad. Sci., 29*, 735.

[32] Olansi, O., Robeson, L. M., & Shaw, M. T. (1979). *Polymer-Polymer Miscibility*. New York: Academic Press.

[33] Krause, S. (1972). *J. Macromol. Sci., Rev. Macromol. Chem., 7*, 251.

[34] McMaster, L. P. (1973). *Macromolecules, 6,* 760.

[35] McMaster, L. P. (1975). *Adv. Chem. Ser., 142*, 43.

[36] Shaw, M. T. (1974). *J. Appl. Polym. Sci., 18*, 449.

[38] Robeson, L. M. (1973). *J. Appl. Polym. Sci., 17*, 3607.

[39] Robeson, L. M., & Joesten, B. L. (1975). Presentation to N.Y. Acad. Sci.

[40] Robeson, L. M. (1982). In K. Solc (Ed.), *Polymer Compatibility and Incompatibility: Principles and Practices* (177). New York: Harwood Academic Pub.

[41] Paul, D. R., & Barlow, J. W. (1980). *J. Macromol. Sci.-Rev. Macromol. Chem., C18*(1), 109 (1980).

[42] Forger, G. R. (1977). *Mater. Eng., 85*, 44.

[43] Wood, A. S. (1979). *Mod. Plast., 56*, 44.

[44] Shaw, M. T. (1982). *Polym. Eng. Sci., 22*, 115.

[45] Corish, P. J., & Powell, B. D. W. (1974). *Rubber Chem. Technol., 47*, 48.

[46] Dunn, J. R. (1976). *Rubber Chem. Technol., 49*, 978.

[47] Corish, P. J. (1967). *Rubber Chem., Technol., 40*, 324.

[48] McDonel, E. T., Baronwal, K. C., & Andries, J. C. (1978). In D. R. Paul & S. Newman (Eds.), *Polymer Blends*, Vol. 2 (263). New York: Academic Press.

[49] Plochocki, A. P. (1978). In D. R. Paul & S. Newman (Eds.), *Polymer Blends*, Vol. 2 (319). New York: Academic Press.

[50] Hammer, C. F. (1978). In D. R. Paul & S. Newman (Eds.), *Polymer blends*, Vol. 2 (219). New York: Academic Press.

[51] Paul, D. R. (1978). In D. R. Paul & S. Newman (Eds.), *Polymer Blends*, Vol. 2 (167). New York: Academic Press.

[52] Kresge, E. N. (1978). In D. R. Paul & S. Newman (Eds.), *Polymer Blends*, Vol. 2 (293). New York: Academic Press.

[53] Kraus, G. (1978). In D. R. Paul & S. Newman (Eds.), *Polymer Blends*, Vol. 2 (243).

New York: Academic Press.

[54] Sperling, L. H. (1981). *Interpenetrating Polymer Networks and Related Materials*, Ch. 8. New York: Plenum Press.

[55] Michaels, A. S. (1965). *Ind. Eng. Chem., 57*, 32.

[56] Lysaght, M. J. (1975). In L. Holliday (Ed.), *Ionic Polymers* (281). New York: Wiley.

[57] Emmett, R. A. (1944). *Ind. Eng. Chem., 36*, 730.

[58] Pittenger, J. E., & Cohan, G. F. (1947). *Mod. Plast., 25*, 81.

[59] MacKnight, W. J., Stoelting, J., & Karasz, F. E. (1971). *Adv. Chem. Ser., 99*, 29.

[60] Georgacopoulos, C. N., & Sardanopoli, A. A. (1982). *Mod. Plast., 59*, 76.

[61] Morris, H. L. (1974). *J. Elast. Plast., 6,* 1.

[62] Fischer, W. K. (1974). *Mod. Plast., 51*, 116.

[63] Dillard, T. R. (1976). Paper presented at 110th Rubber Div. Amer. Chem. Soc. Mtg., San Francisco, Calif.

[64] Bekturov, E. A. & Bimendina, L. A. (1981). *Adv. Polym. Sci., 41*, 99.

[65] Taylor, L. D. (1371). *U.S. Pat.* 3,578,458 (assigned to Polaroid Corp.).

[66] Mishra, K., Hashmi, S. A., & Rai, D. K. (2013). *J. Solid State Electrochem., 17*, 785–793.

[67] Mannan, H. A., Mukhtar, H., Murugesan, T., Nasir, R., Mohshim, D. F., & Mushtaq, A. (2013). *Chem. Eng. Technol., 36*(11), 1838–1846.

[68] Dalmoro, A., Barba, A. A., Lamberti, G., Grassi. M., & d'Amore, M. (2012). *Adv. Polym. Technol., 31*(3), 219–230.

[69] Fleer, G. J., & Lyklema, J. (1983). *Adsorption from Solution at the Solid/Liquid Interface*. New York: Academic Press.

[70] Linse, P., & Kallrot, N. (2010). *Macromolecules, 43*, 2054–2068.

[71] Evans, D. F. & Wennerstrom, H. (1999). *The Colloidal Domain: Where Physics, Chemistry, Biology and Technology Meet*, 2nd ed. New York: Wiley-VCH.

[72] Norde, W. (2003). *Colloids and Interfaces in Life Sciences*. New York: Marcel Dekker Inc.

[73] Gray, J. J. (2004). *Curr. Opin. Struc. Biol., 14*, 110.

[74] Yaseen, M., Salacinski, H. J., Seifalian, A. M., & Lu, J. R. (2008). *Biomed. Mater., 3*, 034123.

[75] Ramanathan, T., Abdala, A. A., Stankovich, S., Dikin, D. A., Herrera-Alonso, M., Piner, R. D., Adamson, D. H., Schniepp, H. C., Chen, X., Ruoff, R. S., et al. (2008). *Nat. Nanotechnol., 3*, 327.

[76] Fleer, G. J., Cohen Stuart, M. A., Scheutjens, J. H. M. H., Cosgrove, T., & Vincent, B. (1993). *Polymers at Interfaces*. London: Chapman & Hall.

[77] Cohen Stuart, M. A., & Fleer, G. J. (1996). *Annu. Rev. Mater. Sci., 26*, 463.

[78] Yethiraj, A. (2002). *Adv. Chem. Phys., 121*, 89.

[79] Cohen Stuart, M. A. (2003). *Surf. Sci. Ser., 110*, 1.

[80] O'Shaughnessy, B., & Vavylonis, D. J. (2005). *Phys.: Condens. Matter, 17*, R63.

[81] Scheutjens, J.M. H. M. & Fleer, G. J. (1980). *J. Phys. Chem., 84*, 178.

[82] De Gennes, P. G. (1981). *Macromolecules, 14*, 1637.

[83] Kramarenko, E. Yu., Winkler, R. G., Khalatur, P. G., Khokhlov, A. R., & Reineker, P. (1996). *J. Chem. Phys., 104*, 4806.

[84] Striolo, A., & Prausnitz, J. M. (2001). *J. Chem. Phys., 114*, 8565.

[85] Sintes, T., Sumithra, K., & Straube, E. (2001). *Macromolecules, 34*, 1352.

[86] Striolo, A., Jayaraman, A., Genzer, J., & Hall, C. K. (2005). *J. Chem. Phys., 123*, 064710.

[87] Hasegawa, R., & Doi, M. (1997). *Macromolecules, 30*, 3086.

[88] Jia, L. C. R., & Lai, P. Y. (1996). *J. Chem. Phys., 105*, 11319.

[89] Zajac, R., & Chakrabarti, A. (1996). *J. Chem. Phys., 104*, 2418.

[90] Takeuchi, H. (1999). *Macromol. Theory Simul., 8*, 391.

[91] Ponomarev, A. L., Sewell, T. D., & Durning, C. J. (2000). *Macromolecules, 33*, 2662.

[92] Wolterink, J. K., Barkema, G. T., & Cohen Stuart, M. A. (2005). *Macromolecules, 38*, 2009.

[93] Smith, G. D., Zhang, Y., Yin, F., & Bedrov, D. (2006). *Langmuir, 22*, 664.

[94] Descas, R., Sommer, J. U., & Blumen, A. (2006). *J. Chem. Phys., 6*, 124, 094701.

[95] Smith, K. A., Vladkov, M., & Barrat, J. L. (2005). *Macromolecules, 38*, 571.

[96] Harmandaris, V. A., Daoulas, K. Ch., & Mavrantzas, V. G. (2005). *Macromolecules, 38*, 5796.

[97] Daoulas, K. Ch., Harmandaris, V. A., & Mavrantzas, V. G. (2005). *Macromolecules, 38*, 5780.

[98] Li, Y., Wei, D., Han, C. C., & Liao, Q. J. (2007). *Chem. Phys., 126*, 204907.

[99] Chremos, A., Glynos, E., Koutsos, V., & Camp, P. (2009). J. *Soft Matter, 5*, 637.

[100] Kallrot, N., & Linse, P. (2007). *Macromolecules, 40*, 4669.

[101] Kallrot, N., Dahlqvist, M., & Linse, P. (2009). *Macromolecules, 42*, 3641.

[102] Reiter, G., Sharma, A., Casoli, A., David, M. O., Khanna, R., & Auroy, P. (1999). *Langmuir, 15*, 2551-2558.

[103] Israelachvili, J. N. (2011). *Intermolecular and Surface Forces, 3rd ed*. London:

Academic Press.

[104] Ivanov, I. B. (1988). *Thin Liquid Films: Fundamentals and Applications*. New York: Marcel Dekker.

[105] Derjaguin, B. V. (1989). *Theory of Stability of Thin Films and Colloids*. New York: Consultants Bureau/Plenum Press.

[106] De Gennes, P. G. (1985). *Rev. Mod. Phys., 57*, 827.

[107] Van Oss, C. J., Chaudhury, M. K., & Good, R. J. (1988). *Chem. Rev., 88*, 927.

[108] Van Oss, C. J. (1993). *Colloids Surf., 78*, 1.

[109] Findenegg, G. H., & Herminghaus, S. (1997). *Curr. Opin. Coll. Interface Sci., 2*, 301.

[110] Brochard-Wyart, F., di Meglio, J. M., Quere, D., & de Gennes, P. G. (1991). *Langmuir, 7*, 335.

[111] Sharma, A. (1993). *Langmuir, 9*, 861-869.

[112] Sharma, A. (1993). *Langmuir, 9*, 3580.

[113] Sharma, A., & Khanna, R. (1998). *Phys. Rev. Lett., 81*, 3463.

[114] Sharma, A., & Jameel, A. T. (1993). *J. Coll. Interface Sci., 161*, 190.

[115] Khanna, R., & Sharma, A. (1997). *J. Coll. Interface Sci., 195*, 42.

[116] Yoo, P. J., Suh, K. Y., & Lee, H. H. (2002). *Macromolecules, 35*, 3205-3212.

[117] Martin, P., & Brochard-Wyart, F. (1998). *Phys. Rev. Lett., 80*, 3296-3299.

[118] Brochard-Wyart, F., Martin, P., & Redon, C. (1993). *Langmuir, 9*, 3682-3690.

[119] Leibler, L., Ajdari, A., Mourran, A., Coulon, G., & Chatenay, D. (1994). In A. Teramoto, M. Kobayashi, T. Norisuje (Eds.), *Ordering in Macromolecular Systems* (301–311). Berlin: Springer-Verlag.

[120] Shull, K. (1994). *Faraday Discuss., 98*, 203.

[121] Martin, J. I., Wang, Z. G., & Schick, M. (1996). *Langmuir, 12*, 2 and 4950.

[122] Service, R. F. (1997). *Science, 278*, 383.

[123] Walheim, S., & Schaffer, E. (1999). *Nature, 283*, 520.

[124] Castro, A. (1981). *U.S. Patent 4*, 247, 498.

[125] Luo, B., Li, Z., Zhang, J., & Wang, X. (2008). *The Fourth Conf. of Aseanian Membrane Soc., 233*, 19.

[126] Jeon, Y. J., Bingzhu, Y., Rhee, J. T., Cheung, D. L., & Jamil, M. (2007). *Macromol. Theo. Simul., 16*(7), 643–659.

[127] Piasini, P., & Zannoni, C. (1998). *Advances in the computer simulation of liquid crystals.* Dordrecht, the Netherlands: Kluwer Academic Publishers.

[128] Baker, R. W. (2000). *Membrane Technology and Applications*. New York: McGraw-Hill.

[129] Mulder, M. (1996). *Basic Principles of Membrane Technology*, 2nd ed. Boston: Kluwer Academic Publishers.

[130] Crawford, G. P., Doane, J. W., & Zumer, S. (1997). In P. J. Collins, J. S. Patel, (Eds.). Handbook of Liquid Crystal Research, Ch. 9. New York: Oxford University Press.

[131] Barton, B. F., Graham, P. D., & McHugh, A. J. (1998). *Macromolecules, 31*, 1672.

[132] Barton, B. F., & McHugh, A. J. (2000). *J. Membr. Sci., 166*, 119.

[133] Graham, P. D., Pervan, A. J., & McHugh, A. J. (1997). *Macromolecules, 30*, 1651.

[134] Chan, P. K. (2002). In A. Karim, C. W. Frank, T. P. Russel, & P. F. Nealey (Eds.), *Comparison of mobility modes in polymer solutions undergoing thermal-induced phase separation*. Mat. Res. Sci. Sym., Polym. Inter. 710, Warrendale, Pennsylvania.

[135] Chan, P. K., & Rey, A. D. (1995). *Macromol. Theory Simul., 4*(5), 873–899.

[136] Chan, P. K., & Rey, A. D. (1995). *Comput. Mater. Sci., 3*, 377.

[137] Higgins, D. A. (2000). *Adv. Mater., 12*, 251.

[138] Chan, P. K., Lee, K. W. D., & Feng, X. (2004). *Chem. Eng. Sci., 59*(7), 1491–1504.

[139] Xue, L. & Han, Y. (2011). *Prog. Polym. Sci., 36*, 269–293.

[140] Charas, A., Ferreira, Q., Farinhas, J., Matos, M., Alcacer, L., & Morgado, J. (2009). *Macromolecules, 42*, 7903–7912.

[141] Zhao, K., Ding, Z., Xue, L. & Han, Y. (2010). *Macromol. Rapid Comm., 31*, 532–538.

[142] Mucha, M. (2003). *Prog. Polym. Sci., 28*, 837–873.

[143] Zhao, K., Zhou, G., Wang, Q., Han, Y., Wang, L., & Ma, D. (2010). *Macromol. Chem. Phys., 211*, 313–320.

[144] Yim, K. H., Zheng, Z., Friend, R. H., Huck, W. T. S., & Kim, J. S. (2008). *Adv. Funct. Mater, 18,* 2897–2904.

[145] Chan, P. K., Tran, T. L., & Rousseau, D. (2005). *Chem. Eng. Sci., 60*, 7153–7159.

[146] Chan, P. K., Lee, K. W. D., & Feng, X. S. (2003). *Macromol. Theory Simul., 12,* 413.

[147] Li, Y. C., Shi, R. P., Wang, C. P., Liu, X. J., & Wang, Y. (2011). *Phys. Rev., E 83,* 041502.

[148] Zhang, W. (2005). *PhD dissertation*. Virginia Polytechnic Institute and State University.

[149] Cahn, J. W. (1961). *Acta Metallurgica, 9*, 795.

[150] Hashimoto, T. (1988). *Phase Transitions, 12*, 47.

[151] Kiran, E., & Liu, K. (2002). *Korean J. Chem. Eng., 19*, 153.

[152] Cui, L., Zhang, Z., Li, X., & Han, Y. (2005). *Polym. Bulletin, 55*, 131–140.

[153] Böltau, M., Walheim, S., Schaffer, E., Mlynek, J., & Steiner, U. (1999). *Science, 283*, 520.

[154] Fink, Y., Winn, J. N., Fan, S., Chen, C., Michel, J., Joannopoulos, J. D., & Thomas, E. L. (1998). *Science, 282*, 679.

[155] Jones, R. A. L., Norton, L. J., Kramer, E. J., Bates, F. S., & Wiltzius, P. (1991). *Phys. Rev. Lett., 66*, 1326.

[156] Rysz, J., Bernasik, A., Ermer, H., Budkowski, A., Brenn, R., Hashimoto, T., & Jedlinski, J. (1997). *Europhys. Lett., 40*, 503.

[157] Rysz, J., Ermer, H., Budkowski, A., Lekka, M., Bernasik, A., Wrobel, S., Brenn, R., Lekki, J., & Jedlinski, J. (1999). *Vacuum, 54*, 303.

[158] Jeon, Y. J. Jamil, M., Lee, H. D., & Rhee, J. T. (2008). *Pramana, 71*(3), 559-572.

[159] Henderson, I. C., & Clarke, N. (2005). *J. Chem. Phys., 123*, 144903.

[160] Chan, P. K., & Rey, A. D. (1996). *Macromolecules, 29*(27), 8934–8941.

[161] Chan, P. K., & Rey, A. D. (1997). *Macromolecules, 30*, 2135.

[162] Chan, P. K. & Jiang, B. T. (2007). *Macromol. Theory Simul., 16*, 690-702.

[163] Chan, P. K., Lee, K. W. D., & Feng, X. S. (2002). *Macromol. Theory Simul., 11*(9), 996–1005.

[164] Hashimoto, T. (1993). In E. L. Thomas (Ed.), *Structure and Properties of Polymers, Vol. 12*. Weinheim: VCH.

[165] Zhang, J., & Nie, J. (2012). *Polym. International, 61*(1) 135–140.

[166] Ullmann, A., Ludmer, Z., & Shinnar, R. (1995). *AIChE Journal, 41*(3), 488–500.

[167] Hashimoto, T., Hayashi, M., Jinnai, H. (2000). *J. Chem. Phys., 112*, 6886.

[168] Hayashi, M., Jinnai, H., Hashimoto, T. (2000). *J. Chem. Phys., 112*, 6897.

[169] Tanaka, H. (1993). *Phys. Rev. E 47*, 2946.

[170] Tanaka, H. (1998). *Phys. Rev. Lett. 81*, 2.

[171] Tanaka, H. (1994). *Phys. Rev. Lett. 72*, 23.

[172] Tanaka, H., & Sigehuzi, T. (2004). *Phys. Rev. E 70*, 051504167.

[173] Li, Y. C., Shi, R. P., Wang, C. P., Liu, X. J., & Wang, Y. (2012). *Modelling Simul. Mater. Sci. Eng., 20,* 075002.

[174] Lee, H. H., Suh, K. Y., & Yoo, P. J. (2002). *Macromolecules, 35*, 3205-3212.

[175] Dalnoki-Veress, K., Forrest, J. A., Stevens, J. R., & Dutcher, J. R. (1996). *J. Polym. Sci., Part B, 34*, 3017-3024.

[176] Tanaka, K., Takahara, A., & Kajiyama, T. (1996). *Macromolecules, 29*, 3232-3239.

[177] Walheim, S., Boltau, M., Mlynek, J., Krausch, G., & Steiner, U. (1997). *Macromolecules, 30*, 4995-5003.

[178] Jeon, Y. J., Bingzhu, Y., Rhee, J. T., Cheung, D. L., & Jamil, M. (2007). *Macromol. Theo. Simul., 16*(7), 643–659.

[179] Chan, P. K. (1997). *PhD dissertation*. Montreal: McGill University.

[180] Hashimoto, T., Itakura, M., & Shimazu N. (1986). *J. Chem. Phys. 85*, 6118.

[181] Henderson, I. C., & Clarke, N. (2004). *Macromolecules, 37*, 1952.

[182] Tran, T. L. (2004). *PhD dissertation*. Toronto: Ryerson University.

[183] Serbutoviez, C., Kloosterboer, J. G., Boots, H. M. J., & Touwslager, F. J. (1996). *Macromolecules, 29* (24), 7690-7698.

[184] Lee, J. C. (1999). *Phys. Rev., 60*(2), 1931–1935.

[185] Zhang, X., Liu, C., Wenbin, G., Zhong, Z., Li, F., Shengping, R., Dong, W., & Weiyou, C. (2008). *Nano/Micro Eng. Molecul. Sys., 3rd IEEE International Conference*. Hainan Island, China.

[186] Marin, L., & Perju, E. (2009). *Phase Transitions, 82*, 507–518.

[187] Li, X., Kanjwal, M. A., Stephansen, K., & Chronakis, I. S. (2012). *Materials Lett., 75*, 189–191.

[188] Hellmann, E. H., Hellmann, G. P., & Rennie, A. R. (1991). *Coll. & Polym. Sci., 269*(4), 343–352.

[189] Hartmut, L. (1995). *Phys. Rev. Lett., 74*(6), 1028–1031.

[190] Dai, M., Song, L., Nie, W., & Zhou, Y. (2013). *J. Coll. Interf. Sci., 391*, 168.

[191] Brown, G., & Chakrabarti, A. (1992). *Phys. Rev. A., 46*(8), 4829–4835.

[192] Jones, R. A. L., Norton, L. J., Kramer, E. J., Bates, F. S., Gehlsen, M. D., Karim, A., Felcher, G. P., & Kleb, R. (1995). *Macromolecules, 28*, 8621.

[193] Guenoun, P., Beysens, D., & Robert, M. (1990). *Phys. Rev. Lett., 65*, 2406.

[194] Wiltzius, P., & Cumming, A. (1991). *Phys. Rev. Lett., 66*, 3000.

[195] Lipowsky, R., & Huse, D. A. (1986). *Phys. Rev. Lett. 57*, 353.

[196] Toral, R. (1991). *Phys. Rev. B, 43*, 3438–3442.

[197] Binder, K. (1995). *Acta Polymerica, 46*(33), 204–225.

[198] Puri, S., & Frisch, H. L. (1997). *J. Phys. Condens. Matter*, *9*, 2109–2133.

[199] Henderson, I. C., & Clarke, N. (2005). *Macromol. Theo. Simul., 14*(7), 435–443.

[200] Yan, L. T., & Xie, X. M. (2007). *J. Chem. Phys. 126*, 064908.

[201] Yan, L. T., Li, J., Li, Y., & Xie, X. M. (2008). *Macromolecules, 41*, 3605–3612.

[202] Yan, L. T., Li, J., & Xie, X. M. (2008). *J. Chem. Phys., 128*(22), 4906.

[203] Rogers, T. M., Elder, K. R., & Desai, R. C. (1988). *Phys. Rev. B, 37*, 9638.

[204] Shang, Y., Kazmer, D., Wei, M., Mead, J., & Barry, C. (2008). *J. Chem. Phys. 128*, 224909.

[205] Yan, L. T., Li, J., Zhang, F., & Xie, X. M. (2008). *J. Rhys. Chem. Phys. B, 112*, 8499.

[206] Nakai, A., Wang, W., Ogasawara, S., Hasegawa, H., & Hashimoto, T. (1996). *Macromolecules, 31*, 5391.

[207] Wang, X., Okada, M., Matsushita, Y., Furukawa, H., & Han, C. C. (2005). *Macromolecules, 38*, 7127.

[208] Yan, L. T., Li, J., Li, Y., & Xie, X. M. (2009). *Polymer, 50*, 2172–2180.

[209] Puri, S., & Binder, K. (2002). *Phys. Rev. E, 66*, 061602.

[210] Marko, J. F. (1993). *Phys Rev E, 48*, 2861.

[211] Brown, G., Chakrabarti, A., & Marko, J. F. (1994). *Phys. Rev. E, 50*(2), 1674–1679.

[212] Geoghegan, M., Ermer, H., Jungst, G., Krausch, G., & Brenn, R. (2000). *Phys. Rev. E, 62*, 940–950.

[213] Nisato, G., Ermi, B. D., Douglas, J. F., & Karim, A. (1999). *Macromolecules, 32*, 2356.

[214] Krausch, G. (1995). *Mater. Sci. Eng. Rep. R.* 14, 1.

[215] Puri, S. (2005). *J. Phys. Condens. Matter., 17*, R101–42.

[216] Marko, J. F., & Siggia, E. D. (1995). *Phys. Rev. E 52*, 2912–2938.

[217] Krausch, G., Kramer, E. J., Bates, F. S., Marko, J. F., Brown, G., & Chakrabarti, A. (1994). *Macromolecules, 27*, 6768–6776.

[218] Bruder, F., & Brenn, R. (1992). *Phys. Rev. Lett., 69*, 624.

[219] Cumming, A., Wiltzius, P., Bates, F. S., & Rosedale, J. H. (1992). *Phys. Rev. A, 45*, 885.

[220] Tanaka, H. (1993). *Phys. Rev. Lett. 70*, 53, 2770.

[221] Krausch, G., Kramer, E. J., Bates, F. S., Marko, J. F., & Dai, C. A. (1993). *Macromolecules, 26*, 5566.

[222] Krausch, G., Kramer, E. J., Bates, F. S., & Dai, C. A. (1993). *Phys. Rev. Lett.,* 71, 3669.

[223] Geoghegan, M., Jones, R. A. L., & Clough, A. S. (1995). *J. Chem. Phys., 103*, 2719.

[224] Karim, A., Slawecki, T. M., Kumar, S. K., Douglas, J. F., Satija, S. K., Han, C. C., Russell, T. P., Liu, Y., Overney, R., Sokolov, J., & Rafailovich, M. H. (1997). *Macromolecules, 31*, 857–862.

[225] Rysz, J., Budkowski, J., Bernasik, A., Klein, J., Kowalski, K., Jedlinski, & J., Fetters, L. J. (2000). *Europhys. Lett., 50*, 35.

[226] Rysz, J., Budkowski, A., Scheffold, F., Klein, J., Fetters, L. J., Bernasik, A., & Kowalski, K. (2000). *Macromol. Symp.,149*, 277.

[227] Budkowski, A. (1999). *Adv. Polym. Sci., 148*, 1.

[228] Cyganik, P., Budkowski, A., Bernasik, A., Bergues, B., Kowalski, K., Rysz, J., Lekki, J., Lekka, M., & Postawa, Z. (2001). *Vacuum, 63*, 307–313.

[229] Nisato, G., Ermi, B. D., Douglas, J. F., Rogers, j. A., & Karim, A. (1998). *Phys. Rev. Lett., 81*, 3900.

[230] Krausch, G., Kramer, E. J., Rafailovich, M. H., & Sokolov. J. (1994). *Appl. Phys. Lett., 64*, 2655.

[231] Walheim, S., Boltau, M., Mlynek, J., Krausch, G., & Steiner, U. (1998). *Nature, 391*, 877.

[232] Budkowski, A., Cyganik, P., Bernasik, A., Bergues, B., Rysz, J., & Brenn, R. (2002). *e-polym., 006*, 1–21.

[233] Rockford, L., Liu, Y., Mansky, P., Russell, T. P., Yoon, M., & Mochrie, S. G. J. (1999). *Phys. Rev. Lett., 82*, 2602.

[234] Kilehorn, L., & Muthukumar, M. (1999). *J. Chem. Phys., 111*, 2259.

[235] Shou, Z., & Chakrabarti, A. (2001). *Polymer, 42*, 6141.

[236] Xue, L., Zhang, J., & Han, Y. (2012). *Prog. in Polym. Sci.*, *37*, 564–594.

[237] Verploegen, E., Mondal, R., Bettinger, C. J., Sok, S., Toney, M. F., & Bao, Z. (2010). *Adv. Funct. Mater., 20*, 3519.

[238] Nmabu, T., Yamuachi, Y., Kushiro, T., & Sakurai, S. (2005). *Faraday Discuss., 28*, 285–298.

[239] Tran-Cong, Q., & Okinaka, J. (1999). *Polym. Eng. Sci., 39*(2), 365–374.

[240] Kohler, W., Krekhov, A., & Zimmermann, W. (2010). *Adv. Polym. Sci., 227*, 145–198.

[241] Jiang, H., Dou, N., Fan, G., Yang, Z., & Zhang, X. (2013). *J. Chem. Phys., 139*(12), 124903–124908.

[242] Voit, A., Krekhov, A., Enge, W., Kramer, L., & Kohler, W. (2005). *Phys. Rev. Lett., 94*, 214501–214504.

[243] Binder, K. (1995). *Adv. Polym. Sci., 138*, 1.

[244] Bates, F. S. (1991). *Science, 251*, 898–904.

[245] Lookman, T., Wu, Y., Alexander, F. J., & Chen, S. (1996). *Phys. Rev. E*, 53, 5513.

[246] Kumaki, J., Hashimoto, T., & Granick, S. (1996). *Phys. Rev. Lett., 77*(10), 1990–1993.

[247] Oh, J., & Rey, A. D. (2001). *Comput. Theor. Polym. Sci., 11*, 205–217.

[248] Bin, Y., Xu, D., & Tang, P. (2010). *Macromolecules, 43*, 5323–5329.

[249] Chan, P. K., & Hong, S. (2010). *Modelling Simul. Mater. Sci. Eng., 18*, 025013.

[250] Chan, P. K., Huang, G., & Kamal, M. R. (2003). *Canadian J. Chem. Eng. 81*(2), 243–257.

[251] Tanaka, H., Yokokawa, T., Abe, H., Hayashi, T., & Nishi. T. (1990). *Phys. Rev. Lett., 65*(25), 3136–3139.

[252] Onuki, A. (1982). *Phys. Rev. Lett., 48*, 753.

[253] Cowie, J. M. G. (1991). *Polymers: Chemistry & physics of modern materials* (2nd ed.). New York: Chapman & Hall.

[254] Utracki, L. A. (1989). *Polymer alloys & blends: Thermodynamics and rheology*. Munich: Hanser Publishers.

[255] Voutsas, E. C., Pappa, G. D., Boukouvalas, C. J. (2004). *Indus. & Eng. Chem., 43*, 1312.

[256] Wakker, A., & Van Dijk, M. A. (1992). *Polym. Network Blends, 2*(3), 123.

[257] Prausnitz, J. M., Lichtenthaler, R. N., & de Azevedo, E. G. (1998). *Molecular thermodynamics of fluid-phase equilibria* (3rd ed.). New Jersey: Prentice Hall.

[258] Tanaka, H. (2000). *J. Phys.: Condensed Matter, 12*, R207.

[259] Flory, P. J. (1953). *Principles of polymer chemistry*. Ithaca, New York: Cornell University Press.

[260] Kurata, M. (1982). *Thermodynamics of polymer solutions*. New York: Hardwood Academic.

[261] Olabisi, O., Robeson, L. M., & Shaw, M. T. (1979). *Polymer-polymer miscibility*.

New York: Academic Press.

[262] Gruner, S. M., Zirkel, A., Urban, V., & Thiyagarajan, P. (2002). *Macromolecules, 35*, 7375–7386.

[263] Riedl, B., & Prud'homme, R. E. (1984). *Polym. Eng. Sci., 24*(17), 1291–1299.

[264] Nishi, T., & Wang, T. T. (1975). *Macromolecules, 8*, 909.

[265] Kwei, T. K., Patterson, G. D., & Wang, T. T. (1976). *Macromolecules, 9*, 780.

[266] Wedroff, J. H. (1980). *J. Poly. Sci., Polym. Lett. Ed., 18*, 439.

[267] Imken, R. L., Paul, D. R., & Barlow, J. W. (1976). *Polym. Eng. Sci., 16,* 593.

[268] Morra, B. S., & Stein, R. S. (1982). *J. Poly. Sci., Polym. Phys. Ed., 20,* 2243.

[269] Roerdink, E., & Challa, G. (1978). *Polymer, 19*, 173.

[270] Aubin, M. & Prud'homme, R. E. (1980). *Macromolecules, 13*, 365.

[271] Harris, J. E., Paul, D. R., & Barlow, J. W. (1983). *Polym. Eng. Sci., 23,* 676.

[272] Clarke, C. J., Eisenberg, A., La Scala, J., Rafailovoch, M. H., Sokolov, J., Li, Z., Qu, S., Nguyen, D., Schwarz, S. A., Strzhemechny, Y., & Sauer, B. B. (1997). *Macromolecules, 30*, 4184–4188.

[273] Roe, R. J., & Zin, W. C. (1980). *Macromolecules, 13*, 1221.

[274] Shull, K. R., & Kramer, E. J. (1990). *Macromolecules, 23*, 4780.

[275] Al-Rawajfeh, A. E., & Mamlook, R. (2008). *Energy Conv. Mangm., 49*, 3405–3408.

[276] Shi, Z. H., & Schreiber, h. P. (1992). *J. App. Polym. Sci., 46,* 787–796.

[277] Fekete, E., Foldes, E., & Pukanszky, B. (2005). *Europ. Polym. J., 41*, 727–736.

[278] Huang, J. C. (2003). *J. App. Polym. Sci., 90,* 671–680.

[279] Chun, y. S., Park, J., Sun, J. B., & Kim, W. N. (2000). *J. Polym. Sci. B: Polym. Phys. 38,* 2072–2076.

[280] Moterio, E. E. C., & Thaumaturgo, C. (1997). *Composition Sci. Tech. 57*, 1159–1165.

[281] Shcherbina, A. A., Gerasimov, V. K., & Chalykh, A. E. (2004). *Russ. Chem. Bul., Int. Ed., 53*(11), 2601–2603.

[282] Kyu, T., & Buddhiranon, S. (2012). *J. Phys. Chem. B, 116*(27), 7795–7802.

[283] Kurata, M. (1982). *Thermodynamics of polymer solutions, Vol. 1*. New York: Harwood Academic Publishers.

[284] Meier, R., Ruderer, M. A., Kaune, G., Diethert, A., Körstgens, V., Roth, S. V. & Buschbaum, P. M. (2011). *J. Phys. Chem. B, 115*, 2899–2909.

[285] De Gennes, P. G. (1976). *J. Chem. Phys. 55*, 572.

[286] Brochard,F., Jouffroy, J., & Levinson, P. (1983). *Macromolecules*, *16*(10), 1638–1641.

[287] Klein, J. (1978). *Nature, 271*, 143–145.

[288] Cahn, J. W. (1965). *J. Chem. Phys., 42*(1), 93–99.

[289] Gunton, J. D., San Miguel, M., & Sahni, P. S. (1983). In C. Domb & J. L. Lebowitz (Eds.), *Phase transitions and critical phenornena*. Vol. 8, Chapt. 3. New York: Academic Press.

[290] Gunton J. D., & Droz, M. (1983). In H. Araki (Ed.), *Lecture notes in physics*. Vol. 183. New York: Springer–Verlag.

[291] Skripov, V. P., & Skripov, A. V. (1979). *Sov. Phys. Usp., 22*(6), 389–410.

[292] Novick-Cohen, A., & Segel, L. A. (1984). *Physica D, 10*(3), 277–298.

[293] Nauman, E. B., & He, D. Q. (2001). *Chem. Eng. Sci., 56*, 1999–2018.

[294] Becker, R. & Doring, W. (1935). *Ann. Phys. (Leipzig) 24*, 719–752.

[295] Lifshitz, I. M., & Slyozov, V. V. (1961). *Phys. Chem. Solids, 19*, 35.

[296] Novick-Cohen, A., (1985). *J. Stat. Phys., 38*, (3–4), 707–723.

[297] Vrentas, J. S., & Duda, J. L. (1979). *AIChE Journal, 25*, 1–24.

[298] Kim, J. Y., & Palffy-Muhoray, P. (1991). *Mol. Cryst. Liq. Cryst., 203*, 93.

[299] Rundman K. B., & Hilliard, J. E. (1967). *Acta. Metd., 15*, 1025.

[300] Kaplan, P. D., Dinsmore, A. D., Yodh, A. G., & Pine, D. J. (1994). *Phys. Rev. E., 50*(6), 48274835.

[301] Glotzer, S. (1995). *Annu. Rev. Comput. Phys., 2*, 1.

[302] Chan, P. K. (2006). *Modelling Simul. Mater. Sci. Eng. 14*, 41–51.

[303] Copetti, M., & Elliott, C. (1990). *Mater. Sci. Tech. 6*, 273.

[304] Okada, M., & Han, C. (1986). *J. Chem. Phys., 85*, 5317.

[305] Langer, J., Baron, M., & Miller, H. (1975). *Phys. Rev. A, 11*, 1417.

[306] Ohnaga, T., Maruta, J., & Inoue, T. (1989). *Polym., 60*, 1945.

[307] Chakrabarti, A., Toral, R., Gunton, J., & Muthukumar, M. (1989). *Phys. Rev. Lett., 63*, 2072.

[308] Chakrabarti, A., Toral, R., Gunton, J., & Muthukumar, M. (1990). *J. Chem. Phys., 92*, 6899.

[309] Brown, G., & Chakrabarti, A. (1993a). *J. Chem. Phys., 98*, 2451.

[310] Matsuoka, T., & Yamamoto, S. (1995). *J. App. Polym. Sci., 57*, 353.

[311] Aksimentiev, A., Holyst, R., & Moorthi, K. (2000). *Macromol. Theo. Simul, 9*, 661.

[312] Ariyapadi, M., & Nauman, E. (1991). In R. Roe (Ed.). *Computer simulation of polymers: Spinodal decomposition in polymer-polymer systems. A two-dimensional computer simulation*. New York: Prentice Hall.

[313] Castellano, C., & Corberi, P. (2000). *Phys. Rev. E, 61*, 3252.

[314] Castellano, C., & Glotzer, S. (1995). *J. Chem. Phys., 103*, 9363.

[315] Kontis, M., & Muthukumar, U. (1992). *Macromolecules, 25*, 1716.

[316] Oh, J., & Rey, A. D. (2000). *Macromol. Theo. Simul., 9*(8), 641–660.

[317] Chan, P. K., Tran, T. L., & Rousseau, D. (2006). *Comput. Mater. Sci., 37*(3), 328–335.

[318] Kramer, E. J., Green, P., & Palmstorm, C. J. (1984). *Polym. 25*, 473.

[319] De Gennes, P. G. (1980). *J. Chem. Phys., 72*, 4756.

[320] Binder, K. (1983). *J. Chem. Phys., 79*, 6387.

[321] Green, P., Palmstrom, C., Mayer, J., & Kramer, E. (1985). *Macromolecules, 18*, 501.

[322] Rouse, P. (1953). *J. Chem. Phys., 21*, 1272.

[323] Cook, H. E. (1970). *Acta Metall. 18*, 297.

[324] Petschek, R., & Metiu, H. (1983). *J. Chem. Phys., 79*, 3443.

[325] Clarke, N., & Buxton, G. A. (2005). *Phys. Rev. E, 72*, 011807.

[326] Puri, S., & Oono, Y. (1987). *Phys. Rev. Lett.,* 58, 836.

[327] Puri, S., & Oono, Y. (1988). *J. Phys. A: Math. Gen.* 21(15), L755–L762.

[328] Chakrabarti, A., & Gunton, J. D. (1988). *Phys. Rev. B, 37*, 3798.

[329] Yeung. C. (1988). *Phys. Rev. Lett. 61*, 9.

[330] Brown, G., Chakrabarti, A. (1993). *J. Chern. Phys.,98*, 2451.

[331] Brown, G., Chakrabarti, A. (1993). *Phys. Rev. E, 4S*, 3705.

[332] Zhu, J., & Chen, L. Q. (l999). *Phys. Rev. E 60*, 4.

[333] Clarke, N. (2004). *Macromolecules, 37*, 1952–1959.

[334] Fialkowski, M., & Holyst, R. (2002). *J. Chern. Phys. 117*, 1886.

[335] Madbouly, S. A., & Ougizawa, T. (2004). *Macromol. Chem. Phys., 205*, 979–986.

[336] Chan, P. K., Kukadiya, S. B., & Mehrvar, M. (2009). *Macromol. Theo. Simul.*, *18*(2), 97–107.

[337] Jinnai, H., Hasegawa, H., Hashimoto, T., & Han, C. C. (1993). *Macromol., 26*, 182–188.

[338] Londono, J. D., & Wignall, G. D. (1997). *Macromol., 30,* 3821–3824.

[339] Shiomi, T., Sato, T., Endo, M., & Imai, K. (1996). *Polym., 37*(11), 2131–2136.

[340] Lipson, J. E. G., Tambasco, M., & Higgins, J. S. (2006). *Macromolecules, 39*, 4860–4868.

[341] Shiomi, T., Sato, T., Katayama, K., & Suzuki, T. (1998). *Polym., 39*(4), 773–780.

[342] Kumar, S. K., Veytsman, B. A., Maranas, J. K., & Crist, B. (1997). *Phys. Rev. Lett., 79*, 2265.

[343] Gujrati, P. D.(2000). *J. Chem. Phys., 112*, 4806.

[344] Crist, B. Kumar, S. K., & Melenkevitz, J. (2000). *Macromolecules, 33*, 6869–6877.

[345] Schmidt, I., & Binder, K. (1985). J. *Physique, 46*, 1631–1644.

[346] Elliott, C. & Songmu, Z. (1986). *Arch. Rational Mech. Analy. 96*(4), 339–357.

[347] Hamdi, S., Schiesser, W. E., & Griffiths, G. W. (2007), *Scholarpedia, 2*(7), 2859–2900.

[348] Sadiku, M. N. O., & Obiozor, C. N. (2000). *Int. J. Elect. Eng. Edu., 37*(3), 282–297.

[349] Witelski, T. P., & Bowen, M. (2003). *Appl. Num. Math., 45*, 331.

[350] Oron, A. (2000). *Phys. Fluids, 12*(7), 1633.

[351] Hindmarsh, A. C., Brown, P. N., Grant, K. E., Lee, S. L., Serban, R., Shumaker, D. E., & Woodward, C. S. (2005). *ACM Trans. Math. Soft., 31*(3), 363–396.

[352] Bahi, J., Charr, J. C., Couturier, R., & Laiymani, D. (2007). *IEEE International Conference on Cluster Computing,* 534–541.

[353] Lorenzetti, D. M., Dols, W. S., Persily, A. K., & Sohn, M. D. (2013). *Building & Environment, 67*, 260–264.

[354] Byrne, G. D., & Hindmarsh, A. C. (1999). *Intl. J. High Performance Comput. Applications, 13*(4), 354–365.

[355] Cohen, S. D., & Hindmarsh, A. C. (1995). *Num. Math. Group, Center for Comput. Sci. & Eng.*

[356] Serban, R., & Hindmarsh, A. C. (2003). *ACM Transactions on Math. Software, V*(N), 1–18.

[357] Hairer, E., & Wanner, G. (1991). *Solving ordinary differential equations II, stiff and differential-algebraic problems.* Berlin, Germany: Springer-Verlag.

[358] Brown, P. N., & Hindmarsh, A. C. (1989). *J. Appl. Math. Comput., 31*, 49–91.

[359] Seban, R., & Hindmarsh, A. C. (2003). *ACM Trans. Math. Soft., V*(N), 1–18.

[360] Lorenzetti, D. M., Dols, W. S., Persily, A. K., & Sohn, M. D. (2013). *Buil. Environ., 67*, 260–264.

[361] Behr, M. Tezduyar, T.E., Aliabadi, S. K., Mittal, S., & Ray, S. E. (1992). *Comput. Meth. Appl. Mech. Eng., 99*, 27–42.

[362] Saad, Y. (1993). *SIAM J. Sci. Comput., 14*, 461–469.

[363] Saad, Y., & Schultz, M. H. (1986). *SIAM J. Sci. Stat. Comput., 7*(3), 856–869.

[364] Karim, A., Slawecki, T. M., Kumar, S. K., Douglas, J. F., Satija, S. K., Han, C. C., Russell, T. P., Liu, Y., Overney, R., Sokolov, J., & Rafailovich, M. H. (1997). *Macromolecules, 31*, 857–862.

[365] Matsuyama, H., Berghmans, S., & Lloyd, D. R. (1999). *Polymer, 40*, 2289.

[366] Matsuyama, H., Berghmans, S., Lloyd, D. R., & Batarseh, M. (1998). *J. Membrane Sci., 142*, 27.

[367] Tanaka, H., Yokokawa, T., Abe, H., Hayashi, T., & Nishi, T. (1990). *Phys. Rev. Lett., 65*(3), 136.

[368] Kyu, T., Mustafa, M., Yang, J. C., Kim, J. Y., & Palffy-Muhoray, P. (1992). *Stud. Polym. Sci., 11*, 245.

[369] Chakrabarti, A. (1992). *Phys. Rev. B, 45*, 9620.

[370] Henderson, I. C., & Clarke, N. (2004). *Macromolecules, 37*, 1952.

[371] Wiltzius, P., Bates, F., & Hefftier, W. (1988). *Phys. Rev. Lett., 60*, 1538.

[372] Hashimoto, T., Itakura, M., & Shimazu N. (1986). *J. Chem. Phys. 85*, 6118.

[373] Chan, P. (1998). *Recent Res. Devel. Macromol. Res., 3*, 439.

[374] Chakrabarti, A., Toral, R., Gunton, J., & Muthukumar, M. (1990). *J. Chem. Phys., 92*, 6899.

[375] Zhang, H., Zhang, J., & Yang, Y. (1995). *Macromol. Theo. Simul., 4*, 1001.

[376] Kim, J. Y., Mustafa, M., Cho, C. H., & Palffy-Muhoray, P. (1992). *Stud. Polym. Sci., 11*, 245.

[377] Inoue, T., & Yamanaka, K. (1990). *J. Mat. Sci., 25*, 241.

[378] Chen, W., Kobayashi, S., Inoue, T., Ohnaga, T., & Ougizawa, T. (1994). *Polymer, 35*, 4015.

[379] Okada, M., Fujimoto, K., & Nose, T. (1995). *Macromolecules, 28*, 1795.

[380] Onuki, A. (2002). *Phase transition dynamics.* Cambridge: Cambridge University Press.

[381] Bray, A.J. (2002). *Adv. Phys. 51*, 481.

[382] Binder, K. (1991). In R.W. Cahn, P. Haasen, & E. J. Kramer (Eds.). *Phase transformation of materials*. Mat. Sci. Tech., Vol. 5, Weinheim: VCH.

[383] Puri, S. & Wadhawan, V. (2009). *Kinetics of phase transitions*. Boca Raton: CRC Press.

[384] Das, S. K., & Majumder, S. (2013). *Phys. Chem. Chem. Phys.*, 15, 13209–13218.

[385] Puri, S., & Binder, K. (2001). *Phys. Rev. Lett., 86*(9), 1797.

[386] Binder, K. & Fratzl, P. (2001). Spinodal Decomposition. In G. Kostorz. (Ed.), *Phase Transformations in Materials*. (409–480). Weinheim: Wiley-VCH.

[387] Puri, S., Das, S. K., & Jaiswal, P. K. (2012). *EPL, 97*, 16005.

[388] Puri, S., Das, S. K., & Jaiswal, P. K. (2012). *Phys. Rev. E 85,* 051137.

[389] Yan, L. T., & Xie, X. M. (2005). *Polymer, 46*, 7684–7694.

[390] Lee, J. C., Sung, J., & Sung, W. (2005). *Phys. Rev., E. 71*, 031805.

[391] Krausch, G., Mlynek, J., Brenn, R., Marko, J. F., & Straub, W. (1994). *Europhys. Lett.,, 28*, 323.

[392] Geoghegan, M., & Krausch, G. (2003). *Prog. Polym. Sci., 28*, 261–302.

[393] Sagui, C., Somoza, A. M., Roland, C., & Desai, R. C. (1993). *J. Phys. A. 26*, L1163.

[394] Jones, R. A. L. (1994). *Polymer, 35*(10), 2160–2166.

[395] Yan, L. T., & Xie, X. M. (2006). *Polymer, 47*, 6472–6480.

[396] Jones, R. A. L., & Kramer, E. J., Bates. (1989). *Phys. Rev. Lett., 62*(3)*,* 280–283.

[397] Schmidt, I., & Binder, K. (1987). *Z. Phys. B, Conden. Matt., 67*, 369–385.

[398] Chan, P. K., Lee, K. W. D., & Kamal, M. R. (2010). *J. Appl. Polym. Sci.,Vol. 117,* 2651–2668.

[399] Chae, J. J., Lee, S. H., & Suh, K. Y. (2011). *Adv. Funct. Mater., 21*, 1147–1153.

[400] Lu, X., Zhang, J., Zhang, C., & Han, Y. (2005). *Macromol. Rapid Commun., 26*, 637–642.

[401] Jamie, E. A. G., Dullens, R. P. A., & Aarts. D. G. A. L. (2011). *J. Phys. Chem. B*, *115*, 13168–13174.

[402] Forsman, J., Woodward, C. E., & Freasier, B. C. (2002). *J. Chem. Phys. 116*(11), 4715–4722.

[403] Cabral, J. T., Higgins, J. S., Yerina, N. A., & Magonov, S. N. (2002). *Macromol., 35*, 1941–1950.

[404] Sato, G., Nishitsuji, S., & Kumaki, J. (2013). *J. Phys. Chem. B, 117*, 9067−9072.

[405] Chan, P. K., Lee, K. W. D., & Kamal, M. R. (2009). *J. Appl. Polym. Sci.,Vol. 111,* 396–407.

[406] Wang, H., & Composto, R. J. (2003). *Interface Sci., 11*, 237–248.

[407] Kargupta, K., & Sharma, A. (2002). *Langmuir, 18*, 1893–1903.

[408] Puri, S., & Binder, K. (1994). *Phys. Rev. E, 49*(6), 5359–5379.

[409] Chen, Z. Y., & Noolandi, J. (1991). *Phys. Rev. Lett., 66*(6), 727–730.

[410] Puri, S., Binder, K., & Frisch, H. L. (1997). *Phys. Rev. E, 56*(6), 6991–7000.

[411] MacDowell, L. G., & Müller, m. (2006). *J. Chem. Phys., 124*, 084907.